CONTROLLED STRESS RHEOMETRY

by

KEVIN GOLDEN
B.Sc. (Hons)

Submitted to the Council for National Academic Awards
in partial fulfilment of the requirements for the
Degree of Doctor of Philosophy

Department of Mathematics and Statistics
Polytechnic South West, Plymouth

October 1990

Carrimed U.K. Ltd

TO MY FAMILY

ACKNOWLEDGEMENTS

I would like to express my sincere gratitude to my supervisors Dr Mansel Davies, and Dr Eirian Jones for their enthusiasm and support throughout the course of these studies. I also gratefully acknowledge the receipt of an S.E.R.C research assistantship during the early part of my research. My thanks also go to the governors of the polytechnic for their award of the research assistantship which enabled me to complete this work.

I wish to thank Carri-Med U.K. Ltd., and in particular Dr Derek Bell, for the technical assistance I recieved during my project.

Thanks are also due to the polytechnic staff who have provided technical support during my project. These thanks are particularly offered to Mike Hall for his valuable assistance during my experimental work.

Finally my appreciation is offered to all those friends who have helped to make my time at the polytechnic, so enjoyable.

CONTROLLED STRESS RHEOMETRY

KEVIN GOLDEN

Abstract

The work in this thesis is concerned with a theoretical and experimental investigation of certain time dependent simple flow situations on a controlled stress rheometer.

We begin by carrying out a viscoelastic analysis of unidirectional combined steady and oscillatory shear flow, that is valid for large oscillatory shear amplitudes. The theory uses a corotational Goddard-Miller model to describe the non-linear relationship between the shear stress and shear rate in the fluid. Our main interest in this work is the description of the reduction in mean shear stress in the fluid due to the fluctuation of the shear rate about a non-zero mean. The effect of elasticity in this flow situation is examined by comparing mean shear stress reduction with that predicted by an inelastic model. A comparison is also made with data obtained on a controlled stress rheometer.

A linear viscoelastic theory which is able to interpret the effect of fluid inertia on pure oscillatory complex viscosity data, is developed for the controlled stress instrument. The relevant equations of motion are solved by numerical methods. A first and second order perturbation technique is used to obtain theoretical expressions for the complex viscosity function for a number of geometries, commonly used to measure dynamic data. The theory is then used to interpret the effect of fluid inertia on experimental dynamic data.

Finally, we carry out a theoretical investigation of the dynamic behaviour of a 'yield stress' material. The generalised Maxwell model is modified, and then used to describe the non-linear viscoelastic dynamic behaviour of 'yield stress' materials.

CONTENTS

Chapter 1

Introduction

Rheology is the study of the deformation and flow of matter. The term was invented by E. C. Bingham in 1929, and is derived from the Greek word 'rheos' meaning 'flow'. The discipline is concerned with the study of material behaviour under a variety of flow conditions. In classical mechanics, the distinction between the flow behaviour of solids and liquids was considered to be quite sharp. The deformation of solids were governed by Hooke's Law describing elastic deformation, and the flow of fluids governed by Newton's Law describing viscous flow. However, it is now well known, that the flow behaviour of many materials do not obey either of these classical laws, but can exhibit both solid-like and fluid-like properties depending on the flow conditions. These materials may be classified as viscoelastic solids if they do not change shape continually when subjected to a constant stress, and as elastico-viscous fluids if they do change shape continually under conditions of constant stress.

The first society dedicated to the study of rheology was the (American) Society of Rheology formed in 1929. This organisation provided an international forum for workers from the fields of physics, engineering, mathematics, and colloidal chemistry. Since this time, interest in the subject has grown to an extent that rheology can justifiably claim to be of fundamental importance to many types of industry, such as the plastics, petroleum, china clay, food, rubber, and textile industries to name but a few. Rheology is also of interest to the clinical sciences with studies into the flow behaviour of body fluids such as blood, mucous, and synovial fluid.

An important area of rheological study is concerned with the measurement of material properties in simple shear flow situations, and is known as rheometry. These measurements may be used directly in the design of efficient flow processes or in quality control assessments. The rheological information obtained from simple rheometrical flow situations can be of use in the development of constitutive equations. These constitutive equations may then be used in conjunction with the stress equations of motion and continuity to predict material behaviour in complex flow situations.

Another important area of rheological study concerns the relationship between observed material behaviour and the microstructure of materials. It is therefore important to be able to consider rheometrical flow situations in which the structure of the material is not destroyed.

A rheometer is a versatile instrument capable of measuring material properties in simple rheometrical flow situations. These instruments are designed so that, either, a deformation is applied to the material and the subsequent forces that are generated measured, or a force is exerted on the material and the subsequent deformation measured.

This thesis is concerned with an experimental and theoretical investigation of certain time dependent simple flow situations, involving elastico-viscous fluids. These flow situations can be generated on a Carri-Med controlled stress rheometer.

In Chapter 2, we describe the formulation of various equations of state for elastico-viscous fluids. Particular emphasis is given to those models that are relevant to the studies carried out in this thesis. We also briefly consider the simple rheometrical flow situations of steady, oscillatory, and combined steady and oscillatory shear flow. The material properties used to characterise the flow behaviour of elastico-viscous fluids in the aforementioned flow situations are discussed.

In Chapter 3, we introduce the subject of controlled stress rheometry. A brief historical account of the development of the controlled stress technique is given, before describing the Carri-Med controlled stress rheometer in detail. We consider the analysis involved in the measurement of the shear viscosity function in steady shear and the complex viscosity function in small amplitude oscillatory shear for this instrument. The analysis is presented for the cone and plate, parallel plate, and concentric cylinder geometries.

In Chapter 4, we carry out a theoretical analysis of the unidirectional shear flow of an elastico-viscous fluid in which the shear rate fluctuates sinusoidally about a non zero mean. One of the aims of this analysis, is to determine the effect of the oscillatory shear component on the mean shear stress produced in the fluid.

A Goddard-Miller model is used to describe the non-linear relationship between the shear stress and the shear rate in the fluid. This corotational model is able to describe large deformations and hence, the analysis is able to consider a flow situation in which the ratio between the oscillatory shear component and the steady shear component is large. Theoretical expressions are also derived to predict the effect of the oscillatory shear rate on the fundamental oscillatory shear stress amplitude and phase. It should be noted, that due to the complexity of the equations involved, mechanical inertia and fluid inertia effects have been ignored in the analysis.

A generalised Newtonian model is used to determine the effect of a combined steady and oscillatory shear rate on the mean shear stress for an inelastic fluid. By comparing predictions from the Goddard-Miller model with predictions from the generalised Newtonian model, we are able to comment on the importance of elasticity in this flow situation.

In Chapter 5, we carry out an experimental programme on the Carri-Med controlled stress rheometer to consider the combined steady and oscillatory shear flow of a 2% solution of polyisobutylene in dekalin. It is possible, via the instrument software, to calculate the applied torque required to produce a given mean shear rate and fundamental oscillatory shear rate amplitude in the fluid. In this manner, we may determine the reduction in the mean shear stress, fundamental oscillatory shear stress amplitude and phase produced in the fluid, due to the presence of the oscillatory component in the shear flow. The experiments will be carried out for large values of the ratio between the oscillatory shear and steady shear components. A comparison will be made between experimental mean shear stress reduction data and theoretical predictions obtained from the Goddard-Miller and generalised Newtonian models.

In Chapter 6, a linear viscoelastic analysis of oscillatory shear flow on the controlled stress rheometer is carried out. The relevant equations of motion are solved exactly using a numerical technique. This analysis is therefore capable of interpreting the effect of fluid inertia on dynamic data. A perturbation analysis which assumes small values of a non-dimensional fluid inertia parameter is also carried out for the linear viscoelastic flow situation to second order accuracy. Theoretical expressions from

both the exact and perturbation analysis are used to investigate the effect of fluid inertia on the complex viscosity function for a variety of flow conditions.

In Chapter 7 an experimental programme is carried out to measure dynamic data for three different elastico-viscous fluids over a frequency range of 0-40 Hz. The theoretical expressions derived in Chapter 6 are used to interpret the effect of fluid inertia on this dynamic data.

In the final chapter, we consider the effect of yield stress on dynamic data. This non-linear viscoelastic behaviour is described in terms of a modified generalised Maxwell model. This model consists of n Maxwell elements connected in parallel with a yield stress component. The theoretical model is then used to investigate the effect of yield stress on the dynamic data. Some of the issues involved in such a comparison are discussed.

Chapter 2

Rheological Equations of State

2.1. Characterisation of elastico-viscous fluids.

The work presented in Chapters 4 to 7, is concerned with the characterisation of elastico-viscous fluids in small amplitude oscillatory and combined steady and oscillatory shear flow. To facilitate the understanding of these studies, we require a description of the material functions normally associated with the characterisation of elastico-viscous fluids in these flow situations.

The stress field in the fluid may be represented by a symmetric covariant tensor σ_{ik}† defined in a spatial coordinate system. The stress in the fluid may be conveniently expressed as

$$\sigma_{ik} = \sigma'_{ik} - pg_{ik} \quad , \tag{2.1.1}$$

where p is an arbitrary isotropic pressure, g_{ik} is the metric tensor associated with the spatial coordinate system, and σ'_{ik} is the extra stress tensor.

In order to relate the deformation in an arbitrary fluid element to the forces producing that deformation, we require an equation of state (or constitutive equation). This equation is used in conjunction with the equations of motion and continuity in the solution of flow problems. The equation of motion is obtained by applying Newton's Law of motion to an arbitrary fluid element (Walters [45]), resulting in the derivation of the following equation,

$$\frac{\partial \sigma_{ik}}{\partial x_k} + \rho f_i = \rho \frac{DV_i}{Dt} \quad , \tag{2.1.2}$$

where $\underline{f}$ is the total body force vector, $\underline{V}$ is the velocity vector and ρ is the density of the fluid. The differential operator

$$\frac{D}{Dt} \equiv \frac{\partial}{\partial t} + V_k \frac{\partial}{\partial x_k} \quad , \tag{2.1.3}$$

is known as the material derivative.

† We use a standard tensor notation, covariant suffices are written below, and contravariant above. Repeated suffices indicate summation.

For incompressible materials, the equation of continuity is given by,

$$\frac{\partial V_k}{\partial x_k} = 0 \quad . \qquad (2.1.4)$$

The flow behaviour of Newtonian liquids in any given flow situation is characterized by the determination of the constant coefficient of viscosity η_0. However, for an elastico-viscous fluid, the viscosity will in general be a function of the shear rate. This viscosity function will be a monotonically decreasing function of shear rate for a shear thinning fluid, and a monotonically increasing function of shear rate for a shear thickening material. In addition to this, we must also consider normal stress effects.

(a). Steady shear flow.

Consider the simple steady flow situation defined by the following velocity distribution V_i in Cartesian coordinates x_i.

$$V_1 = \dot{\gamma} x_2 \quad ; \quad V_2 = 0 \quad ; \quad V_3 = 0 \quad , \qquad (2.1.5)$$

where $\dot{\gamma}$ is the shear rate. The corresponding stress distribution for an elastico-viscous fluid is given by Coleman et al [9] to be

$$\begin{aligned} \sigma_{12} &= \dot{\gamma}\eta(\dot{\gamma}) \\ \sigma_{11} - \sigma_{33} &= \nu_1(\dot{\gamma}) \\ \sigma_{22} - \sigma_{33} &= \nu_2(\dot{\gamma}) \end{aligned} \quad . \qquad (2.1.6)$$

ν_1 and ν_2 are known as the first and second normal stress differences respectively. The behaviour of an elastico-viscous fluid in such a flow situation is characterized by the three material functions η, ν_1, and ν_2. These quantities are all even functions of $\dot{\gamma}$. As $\dot{\gamma}$ tends to zero, the normal stress differences ν_1 and ν_2 both tend to zero, and the shear viscosity η tends to a constant value η_0. This is an indication that elastico-viscous fluids exhibit Newtonian behaviour at low shear rates.

Experimental evidence suggests that first and second normal stress differences are both greater than zero. However, the first normal stress difference is much larger in magnitude than the second

normal stress difference (Walters [45]). The presence of the first normal stress difference in the flow of elastico-viscous fluids, is responsible for some interesting phenomena. One example is the Weissenberg rod climbing effect which is important in mixing problems, (Walters [45]). The first normal stress difference also plays an important role in the die swell effect, (Tanner [35]). This phenomenum is observed when an elastic liquid emerges from an orifice. The diameter of the jet of fluid is seen to increase by several times the size of the orifice diameter.

It should be noted that the material functions $\eta(\dot{\gamma})$ and $\nu_1(\dot{\gamma})$ are restricted by the following relations. For $\eta(\dot{\gamma})$ we have that,

$$\eta(\dot{\gamma}) > 0 \quad \text{for all } \dot{\gamma} \quad , \tag{2.1.7}$$

and that $\dot{\gamma}\eta(\dot{\gamma})$ is a monotonically increasing function of $\dot{\gamma}$.
For $\nu_1(\dot{\gamma})$ we have that,

$$\frac{\nu_1(\dot{\gamma})}{\dot{\gamma}^2}\Big|_{\dot{\gamma}\to 0} > 0 \quad . \tag{2.1.8}$$

(b). Small amplitude oscillatory shear flow.

If we now consider the oscillatory shear flow defined by the following velocity distribution,

$$V_1 = \epsilon x_2 \omega e^{i\omega t} \quad ; \quad V_2 = 0 \quad ; \quad V_3 = 0 \quad . \tag{2.1.9}$$

The corresponding stress distribution when ϵ is small is given by (Walters [45]).

$$\sigma'_{12} = \eta^* \epsilon \omega \, e^{i\omega t} \quad , \tag{2.1.10}$$

where η^* is known as the complex viscosity function. The real and imaginary parts of the complex viscosity function are known as the dynamic viscosity function η' and the dynamic rigidity function G' respectively. We note that in the limit of low shear rates and low frequencies, the apparent viscosity is related to the dynamic viscosity by the equation (Walters [45]).

$$\eta(\dot{\gamma})\big|_{\dot{\gamma}\to 0} = \eta'(\omega)\big|_{\omega\to 0} \quad . \tag{2.1.11}$$

We also note that the first normal stress difference is related to the dynamic rigidity by

$$\left.\frac{\nu_1(\dot\gamma)}{2\dot\gamma^2}\right|_{\dot\gamma\to 0} = \left.\frac{G'(\omega)}{\omega^2}\right|_{\omega\to 0} \quad . \tag{2.1.12}$$

(c). Combined steady and oscillatory shear flow.

Let us consider the parallel superposition of an oscillatory shear component on to the steady shear flow of an elastico-viscous fluid. The velocity distribution for such a flow situation is given by

$$V_1 = \dot\gamma\, x_2 + \epsilon x_2 \omega e^{i\omega t} \; ; \quad V_2 = 0 \; ; \quad V_3 = 0 \quad . \tag{2.1.13}$$

When ϵ is small, the corresponding stress distribution is given by Walters [45],

$$\sigma_{12} = \epsilon\omega\eta_m^* e^{i\omega t} \quad . \tag{2.1.14}$$

We can still characterize the flow behaviour by a complex viscosity function (η_m^*), but this quantity is now a function of both ω and $\dot\gamma$.

For a simple fluid, it can be shown that (Jones and Walters [22]),

$$\eta_m'(\omega,\dot\gamma)\big|_{\omega\to 0} = \frac{d}{d\dot\gamma}\left[\dot\gamma\ \eta(\dot\gamma)\right] \quad , \tag{2.1.15}$$

and that

$$G_m'(\omega,\dot\gamma)\big|_{\omega\to 0} = 0 \quad , \tag{2.1.16}$$

2.2. Formulation of rheological equations of state.

(a). Linear viscoelastic models.

The characterisation of the time dependent flow behaviour of elastico-viscous fluids is greatly simplified if we insist that an arbitrary fluid element can only experience a small deformation from its initial position. Under these conditions we may ignore non-linear effects.

The simplest linear viscoelastic model is the single element Maxwell model (Maxwell [27]), which may be obtained by writing down the relationship between the stress and the rate of strain for a

spring and dashpot† in series. The use of mechanical analogies was a feature of early attempts to model viscoelastic phenomena (Bird et al [5], Ferry [16]). Examples of this type of model are the Jeffries model (Bird et al [5]), and the Voigt model (Ferry [16]).

A dashpot has the same stress/strain rate relationship as a Newtonian fluid. i.e.

$$\sigma'_{ik} = \eta_0 \dot{\gamma}_{ik} \quad , \tag{2.2.1}$$

where the ik^{th} component of the rate of strain tensor $\underline{\dot{\gamma}}$ is given by

$$\dot{\gamma}_{ik} = \left[\frac{\partial v_i}{\partial x_k} + \frac{\partial v_k}{\partial x_i} \right] \quad . \tag{2.2.2}$$

A spring has the same stress/strain relation as an elastic solid. i.e.

$$\sigma'_{ik} = G \gamma_{ik} \quad , \tag{2.2.3}$$

where the ik^{th} component of the strain tensor $\underline{\gamma}$ is given by

$$\gamma_{ik} = \left[\frac{\partial u_i}{\partial x_k} + \frac{\partial u_k}{\partial x_i} \right] \quad . \tag{2.2.2}$$

and u_i describes the displacement, in the i^{th} direction of an element of a solid relative to the unstressed configeration. G is known as the rigidity modulus of the solid.

The single element Maxwell model may be expressed as,

$$\sigma'_{ik} + \lambda_1 \frac{\partial \sigma'_{ik}}{\partial t} = \eta_1 \dot{\gamma}_{ik} \quad , \tag{2.2.5}$$

where

$$\lambda_1 = \eta_1 / G \tag{2.2.6}$$

is a time constant known as the relaxation time. It can easily be seen that in steady shear, equation (2.2.5) reduces to the model for a Newtonian fluid. For rapidly changing stresses, as in high frequency oscillatory shear, the time derivative term dominates the left hand side of the equation. Integration with respect to time

† The dashpot consists of a piston moving in a cylinder containing a fluid of constant viscosity.

yields Hooke's Law. Assuming that σ'_{ik} is finite at time $t=-\infty$, we may rewrite equation (2.2.5) as an integral model. i.e.

$$\sigma'_{ik}(t) = \int_{-\infty}^{t} \left[\frac{\eta_1}{\lambda_1} e^{-(t-t')/\lambda_1} \right] \dot{\gamma}_{ik}(t')\, dt' \quad . \qquad (2.2.7)$$

The function contained within the brackets is known as the relaxation modulus and is denoted by $G(t-t')$. This function enables past events to influence the stress in the fluid at the present time t. The exponential function ensures that events occurring in the recent past have a greater influence on the flow behaviour of the fluid than events that occurred in the distant past. Therefore, the equation of state defined by equation (2.2.7) contains the notion of a fading memory.

Clearly such a simple arrangement as a spring and dashpot in series cannot be expected to describe the complex rheological response of an elastico-viscous fluid. Consequently, more complicated mechanical networks were considered. The most popular of this type of model was the generalised Maxwell model (see figure (2.1)) which may be expressed in both differential and integral forms as follows,

$$\sigma'^{(r)}_{ik} + \lambda_r \frac{\partial \sigma'^{(r)}_{ik}}{\partial t} = \eta_r \dot{\gamma}_{ik} \quad , \qquad (2.2.8)$$

where $\sigma'^{(r)}_{ik}$ is the stress in the r^{th} Maxwell element.

$$\sigma'_{ik} = \sum_{r=1}^{\infty} \sigma'^{(r)}_{ik} \quad . \qquad (2.2.9)$$

and hence from equation (2.2.7) we have

$$\sigma'_{ik}(t) = \int_{-\infty}^{t} \left[\sum_{r=1}^{\infty} \frac{\eta_r}{\lambda_r} e^{-(t-t')/\lambda_r} \right] \dot{\gamma}_{ik}(t')\, dt' \quad . \qquad (2.2.10)$$

This model can be thought of as the linear superposition of an infinite number of Maxwell elements and has been found to describe the linear behaviour of elastico-viscous liquids reasonably well (Bird et al [5]). Both of the empirical models represented by equations (2.2.7) and (2.2.10) are contained within a more general

equation of state, namely the general linear viscoelastic model.

$$\sigma'_{ik}(t) = \int_{-\infty}^{t} G(t-t')\dot{\gamma}_{ik}(t')\, dt' \quad . \qquad (2.2.11)$$

An important example of a linear viscoelastic flow situation is one in which a material is subjected to a small amplitude oscillatory shear deformation, (e.g. Walters and Kemp [43]). The shear stress and shear rate waveforms produced in this flow situation are both sinusoidal but differ in amplitude and phase. The shear stress is given by

$$\sigma'_{ik}(t) = Re\left\{ \sigma_a^0 e^{i\omega t} \right\} \quad , \qquad (2.2.12)$$

and the shear rate waveform is given by

$$\dot{\gamma}_{ik}(t) = Re\left\{ \dot{\gamma}_a^0 e^{i\omega t} \right\} \quad , \qquad (2.2.13)$$

where σ_a^0 and $\dot{\gamma}_a^0$ are the complex shear stress and shear rate amplitudes, and ω is the angular frequency of oscillation. $Re\{\ \}$ denotes the real part of the quantity contained within the brackets. From (Bird et al [5], we see that the complex viscosity function is defined as the ratio between the complex shear stress and shear rate amplitudes. i.e.

$$\eta^* = \frac{\sigma_a^0}{\dot{\gamma}_a^0} \quad . \qquad (2.2.14)$$

If we write this function in terms of its real and imaginary parts, we define the dynamic viscosity η' and the dynamic rigidity G' respectively.

$$\eta^* \equiv \eta' - iG'/\omega \quad . \qquad (2.2.15)$$

The dynamic viscosity and dynamic rigidity functions provide information about the energy dissipated and energy stored in a cyclic deformation. We can see from equation (2.2.14) that a knowledge of the complex viscosity provides a complete characterisation of the linear time dependent behaviour of elastico-viscous fluids.

The measurement of the complex viscosity function is relatively straightforward. Consistent theories for determining η^* exist for

controlled shear strain instruments (e.g. Walters [41], Walters and Kemp [43], Oldroyd [30], Nally [28], and Markovitz [25]), and for controlled stress instruments (e.g. Jones et al [23,24] and Holder [20]).

(b). Codeformational formulation.

We now turn our attention to the development of rheological equations of state that are valid for all types of flow. In 1950, Oldroyd set out certain intuitive principles which rheological equations of state must satisfy [29]. These were that
(i) the behaviour of a material element depends only on its rheological history and not on that of its neighbouring elements.
(ii) The behaviour of a material element does not depend on any rigid-body motion of the material as a whole in space.
(iii) The equation must describe properties independent of the frame of reference.

Oldroyd was able to satisfy principle (iii) by writing the equations in tensorial form. Principles (i) and (ii) were satisfied by the use of a convected coordinate system ξ^j. The convected coordinate system is drawn in the fluid and deforms continuously with it. Hence, an observer in this convected frame of reference experiences no rigid-body motion of the material. Also, this system has the property that a material element ξ^j at time t will be in the same position at all other times. This implies that the rheological history of a material element ξ^j, in a convected reference frame is independent of spatial coordinates, and is therefore independent of the rheological behaviour of any neighbouring elements.

The equations of motion and continuity are both written in terms of a fixed reference frame. Hence, a constitutive equation, formulated in a convected coordinate system, must be expressed in terms of this fixed reference frame. The kinematic and dynamic variables are transformed from one frame to the other using the usual transformation rules for covariant and contravariant tensors [19].

A suitable kinematic variable which is a measure of the deformation of a fluid element at ξ^j is,

$$\epsilon_{ik} = \gamma_{ik}(\xi^j, t') - \gamma_{ik}(\xi^j, t) \quad , \qquad (2.2.18)$$

where γ_{ik} is the metric tensor associated with the convected spatial coordinate system. When we transform the kinematic tensor to the

fixed frame, we obtain the right Cauchy-Green strain tensor C_{ik}.

$$C_{ik} = \frac{\partial x'^{m}}{\partial x^{i}} \frac{\partial x'^{s}}{\partial x^{k}} g_{ms}(x'^{j}) - g_{ik}(x^{j}) \quad , \tag{2.2.19}$$

where g_{ik} is the metric tensor of the fixed coordinate system x^j, and x'^j is the position at time t' of the element that is instantaneously at the point x^i at time t. When there is no deformation in the material,

$$C_{ik} \equiv 0 \quad . \tag{2.2.20}$$

Hence, this variable is useful because small values of C_{ik} correspond to small deformations of the fluid element.

Since the behaviour of a simple fluid depends upon its rheological history, we would intuitively expect the constitutive equation to contain differential and integral operators with respect to time. A differential operator that is independent of any rigid-body motion in space was defined by Oldroyd [29] to be,

$$\frac{\mathcal{D} E_{ik}}{\mathcal{D} t} = \frac{\partial E_{ik}}{\partial t} + v^{r} \frac{\partial E_{ik}}{\partial x^{r}} + \frac{\partial v^{m}}{\partial x^{i}} E_{mk} + \frac{\partial v^{m}}{\partial x^{k}} E_{im} \quad , \tag{2.2.21}$$

where E_{ik} is a symmetric covariant tensor. If we apply this differential operator to the metric tensor g_{ik}, we obtain the rate of strain tensor $\dot{\gamma}_{ik}$.

$$\dot{\gamma}_{ik} = \frac{\mathcal{D} g_{ik}}{\mathcal{D} t} \quad . \tag{2.2.22}$$

For the dynamic variable, we see that the extra stress tensor π'_{ik} in the convected coordinate system is simply transformed to σ'_{ik} in the fixed coordinate system.

The Oldroyd constitutive equation is able to describe observed viscoelastic behaviour qualitatively. The model may be expressed in the form

$$\sigma'_{ik} + \lambda_1 \frac{\mathcal{D}}{\mathcal{D} t} \sigma'_{ik} + \frac{1}{2} \mu_0 \sigma'_{jj} \dot{\gamma}_{ik} - \frac{1}{2} \mu_1 \left[\sigma'_{ij} \dot{\gamma}_{jk} + \sigma'_{kj} \dot{\gamma}_{ji} \right]$$

$$= \eta_0 \left[\dot{\gamma}_{ik} + \lambda_2 \frac{\mathcal{D}}{\mathcal{D} t} \dot{\gamma}_{ik} - \mu_2 \dot{\gamma}_{ij} \dot{\gamma}_{jk} \right] \quad , \tag{2.2.23}$$

where η_0, λ_1, λ_2, μ_0, μ_1, and μ_2 are material constants.

When $\lambda_2 = \mu_0 = \mu_1 = \mu_2 = 0$, we obtain the model

$$\sigma'_{ik} + \lambda_1 \frac{\mathcal{D}}{\mathcal{D}t} \sigma'_{ik} = \eta_0 \dot{\gamma}_{ik} \quad , \qquad (2.2.24)$$

which is an invariant form of Maxwell's linear equation of state.

(c). Corotational formulation.

An alternative approach to satisfying the principles set down by Oldroyd, is by formulating rheological equations of state in a corotational reference frame. Such a frame is described by the orthogonal unit vectors $\underset{\sim}{\overset{\vee}{e}}_i$ which translate with a fluid particle P while rotating with the local angular velocity of the particle. Hence, equations written in this frame will be independent of any rigid-body motion of the fluid. The corotational dynamic and kinematic variables are formulated as functions of time only. This ensures that the behaviour of the fluid particle depends only on its rheological history and not on that of its neighbouring particles.

We again have to transform the dynamic and kinematic variables to a fixed reference frame. This frame is described by the orthogonal unit vectors $\underset{\sim}{e}_i$. It is convenient to choose the corotating frame such that at time $t = t'$, the two frames coincide. At all previous times $t' < t$, the orientation of the corotating frame with respect to the fixed frame is described by the rotation matrix Ω_{ij}. i.e.

$$\underset{\sim}{\overset{\vee}{e}}_i(t') = \sum_j \underline{\Omega}\,(t,t')\underset{\sim}{e}_i(t) \quad . \qquad (2.2.25)$$

Clearly, when $t' = t$,

$$\Omega_{ij}(t,t) = \delta_{ij} \quad , \qquad (2.2.26)$$

where δ_{ij} is the Kronecker delta

$$\delta_{ij} = 1 \quad \text{when} \quad i = j$$
$$= 0 \quad \text{when} \quad i \neq j \qquad (2.2.27)$$

The corotational shear rate tensor $\dot{\gamma}_{ij}$ and the shear stress tensor σ_{ij} may be written in terms of the fixed frame by using the transformation rules defined in (Bird et al [5]).
For all times $t' \leq t$, the fixed frame shear rate tensor is given by

$$\dot{\Gamma}_{ij}(t') = \sum_m \sum_n \Omega_{im}(t,t')\overset{\vee}{\dot{\gamma}}_{mn}(t')\Omega_{jn}(t,t') \quad , \qquad (2.2.28)$$

and the fixed frame shear stress tensor is given by

$$T_{ij}(t') = \sum_m \sum_n \Omega_{im}(t,t')\overset{\nu}{\sigma}_{mn}(t')\Omega_{jn}(t,t') \quad . \qquad (2.2.29)$$

At time t' = t, we may write

$$\dot{\gamma}_{ij} = \overset{\nu}{\dot{\gamma}}_{ij} \quad , \qquad (2.2.30)$$

and

$$\sigma_{ij} = \overset{\nu}{\sigma}_{ij} \quad . \qquad (2.2.31)$$

A corotational derivative which is independent of any rigid body rotation is the Jaumann derivative (Bird et al [5]).

$$\frac{\mathfrak{D}}{\mathfrak{D}t} E_{ij}(t) = \frac{D}{Dt} E_{ij}(t) + \frac{1}{2} \sum_n \left[\omega_{in}(t)E_{nj}(t) - E_{in}(t)\omega_{nj}(t) \right]. \qquad (2.2.32)$$

The Jaumann derivative is made up of the material derivative D/Dt, and a vorticity term.

The simplest viscoelastic corotational model is obtained by formulating a single element Maxwell model in a corotational frame (Bird et al [4,5]). i.e.

$$\sigma'_{ij} + \lambda_1 \frac{\partial \sigma'_{ij}}{\partial t} = \eta_1 \dot{\gamma}_{ij} \quad . \qquad (2.2.33)$$

Transforming the above equation to the fixed frame, we obtain

$$\sigma'_{ij} + \lambda_1 \frac{\mathfrak{D}\,\sigma'_{ij}}{\mathfrak{D}\,t} = \eta_1 \dot{\gamma}_{ij} \qquad (2.2.34)$$

The constitutive equation described by equation (2.2.34) (Zaremba), and two other constant quasi-linear corotational models (Fromm and DeWitt) are described in detail by Bird et al [4,5]. These equations of state are termed quasi-linear because they describe non-linear relations between the stress and rate of strain tensors in the fixed reference frame. However when these equations are written in terms of the analagous quantities in the corotational reference frame, these relations are linear.

The most general quasi-linear corotational viscoelastic constitutive equation is given by the Goddard-Miller model [17]. This model can be thought of as formulating the general linear viscoelastic model in a corotating reference frame and may be

expressed as

$$\sigma_{ik}(t) = \int_{-\infty}^{t} G(t-t')\dot{\Gamma}_{ik}(t')\,dt' \quad . \qquad (2.2.35)$$

The integral defined by equation (2.2.35) is the first term of a memory integral expansion derived by Goddard [18]. The Goddard-Miller model can describe realistic shear viscosity behaviour (Bird et al [4,5]). The model is also capable of describing, qualitatively at least, many elastic effects such as stress overshoot, complex viscosity, elastic recoil, and normal stresses differences (Bird et al [4,5]).

The equation of state described by equation (2.2.35) will be used to investigate the reduction in mean shear stress caused by the parallel superposition of an oscillatory component on to the steady shear flow of an elastico-viscous fluid.

2.3. The generalized Newtonian model.

An equation of state that is able to predict the same viscosity behaviour as the Goddard-Miller model, but is not capable of describing any elastic effects is given by the generalised Newtonian model. This model is obtained by modifying the equation of state for a Newtonian liquid to include a shear rate dependent viscosity function. i.e.

$$\sigma'_{ik} = \eta(\dot{\gamma})\dot{\gamma}_{ik} \quad . \qquad (2.3.1)$$

The non-Newtonian viscosity is a scalar quantity and therefore must only depend on a scalar quantity. It can be shown (Bird et al [5]) that in shear flow, the non-Newtonian viscosity is dependent on the second invariant of the shear rate tensor $\dot{\gamma}_{ik}$. i.e.

$$\dot{\gamma} = \left[\tfrac{1}{2}\,\mathrm{II}_{\dot{\gamma}}\right]^{\frac{1}{2}} \quad , \qquad (2.3.2)$$

where

$$\mathrm{II}_{\dot{\gamma}} = \sum_i \sum_j \dot{\gamma}_{ij}\,\dot{\gamma}_{ji} \quad . \qquad (2.3.3)$$

Many empirical formulae have been proposed to describe the

dependence of the shear viscosity function on the shear rate. Some of those that are relevant to this thesis are described below.

(i). Power law model (Bird et al [5]).

$$\eta(\dot{\gamma}) = m \mid \dot{\gamma} \mid^{n-1} \qquad (2.3.4)$$

where m is known as the consistency index and n is known as the power law index. Clearly, n equal to 1 represents Newtonian behaviour. For $n < 1$, the fluid is shear thinning, increasingly so as n approaches zero. Values of $n > 1$, represent shear thickening behaviour. The consistency index may be determined from the intercept on the viscosity axis.

In figure (2.2) we compare different viscosity models. The linear region of the log-log plot is known as the power law region and is described by equation (2.3.4). The slope of the power law curve is given by (n-1).

The above model is not able to predict the presence of a Newtonian plateau at low shear rates. Therefore, a restriction must be placed on the shear rate range when using a Power Law model.

(ii). Segalman model (Bird et al [5]).

$$\eta(\dot{\gamma}) = \frac{\eta_0 \cos\left[(1-n)\tan^{-1}(\lambda_s\dot{\gamma})\right]}{\left(1 + (\lambda_s\dot{\gamma})^2\right)^{(1-n)/2}} \qquad (2.3.5)$$

The Segalman model is able to describe viscosity data over a wide shear rate range. The constant η_0 is the constant Newtonian viscosity and is obtained from low shear rate viscosity data. The Power Law index is again given by n. λ_s is a time constant known as a relaxation time. This parameter determines the shear rate range over which the fluid exhibits Newtonian behaviour before entering the Power Law region. The shear rate at which this occurs is given by $1/\lambda_s$. One drawback of this model is shown in Figure (2.2). The Segalman shear viscosity curve 'overshoots' the shear viscosity curve predicted by the power law model. This is not a realistic shear viscosity behaviour (Davies et al [10]). We finally note that at higher shear rates, the Segalman model shows similar behaviour to the power law model.

(iii). Carreau model (Bird et al [5]).

$$\eta(\dot{\gamma}) = \eta_0 \, (1 + (\lambda\dot{\gamma})^2)^{(n-1)/2} \quad . \tag{2.3.6}$$

This viscosity model is able to describe viscosity data over a wide shear rate range, but has the advantage of not exhibiting any unrealistic 'overshoot' behaviour. Figure (2.2) shows a comparison of Power Law, Segalman, and Carreau viscosity prediction based on experimental data taken from a 2% solution of polyisobutylene in dekalin.

For some polymeric liquids, a second Newtonian region is observed at high shear rates. Both the Segalman and Carreau models are capable of predicting this second Newtonian region by incorporating a fourth constant η_∞ into the model. e.g. for the Carreau Model,

$$\frac{\eta(\dot{\gamma}) - \eta_\infty}{\eta_0 - \eta_\infty} = (1 + (\lambda\dot{\gamma})^2)^{(n-1)/2} . \tag{2.3.7}$$

(iv). Oldroyd four constant model (Walters and Townsend [44]).

This model predicts a shear rate dependent viscosity of the following form,

$$\eta(\dot{\gamma}) = \eta_0 \, \frac{(1 + \lambda_2 \, \mu_0 \, \dot{\gamma}^2)}{(1 + \lambda_1 \, \mu_0 \, \dot{\gamma}^2)} \quad , \tag{2.3.8}$$

where λ_1, λ_2, and μ_0 are time constants.

The Oldroyd four constant model can qualitatively describe viscosity data over a wide shear rate range. The model predicts a first Newtonian viscosity at low shear rates and a second Newtonian region at high shear rates. At intermediate values of $\dot{\gamma}$, shear thinning behaviour is predicted. The constants λ_1 and λ_2 are restricted by the relation,

$$\lambda_2 \leq \lambda_1 \leq 9\lambda_2 \tag{2.3.9}$$

This means that the maximum difference between the second Newtonian viscosity given by $\eta_0\lambda_2/\lambda_1$, and the first Newtonian viscosity, is 1/9th the magnitude of the first Newtonian viscosity. Experimental evidence (Bird et al [5]), has shown that for polymeric liquids, shear thinning behaviour can lead to much larger reductions in viscosity than this.

2.4. Yield stress.

Many types of material 'appear' to require a critical stress to be exceeded before any deformation or flow can take place. e.g. pastes, dispersions, gels, and concentrated suspensions. This critical stress is commonly known as the yield stress. The work of Barnes and Walters [3], has questioned the concept of a material possessing a yield stress. These workers argue the shear viscosity function of material, is always finite. To support this hypothesis, Barnes and Walters present 'yield stress' data for a commercially available PVA latex adhesive, and a 0.5% solution of Carbopol. This experimental evidence demonstrated that the observed value of yield stress is dependent upon the accuracy of the instrument used to measure it. An important factor in this argument is that of 'time scale'. i.e. providing sufficient time is given, then a material will always deform for any non-zero shear stress. However, many flow processes take place in too short a time for any deformation to be observed. In this context, yield stress remains a useful concept in characterizing the flow behaviour of these materials.

Chapter 8 of this thesis is concerned with the effect of yield stress on dynamic data. We therefore provide a brief discussion here of some of the constitutive equations normally associated with the description of yield stress behaviour.

2.4.1. Bingham model (Bird et al [6]).

$$\sigma = \eta_p \dot{\gamma} + \sigma_y \quad , \qquad (2.4.1)$$

where

$$\sigma_y = \sigma_0 \frac{\dot{\gamma}}{|\dot{\gamma}|} \qquad |\dot{\gamma}| > 0 \quad , \qquad (2.4.2)$$

$$|\sigma_y| < \sigma_0 \qquad \dot{\gamma} = 0 \quad . \qquad (2.4.3)$$

The above two parameter model proposed by Bingham, represents the simplest model for describing the shear stress/shear rate relationship for a yield stress material, (see figure (2.3)). The flow behaviour of a Bingham fluid in steady shear may be characterised by the constant plastic viscosity η_p and the yield stress σ_0. The critical stress value σ_0 is determined by the

intersection of the straight line of the shear stress / shear rate curve with the shear stress axis.

2.4.2. Herschel-Bulkley model (Bird et al [6]).

Another yield stress model which does not allow any deformation unless the yield stress is exceeded, is the Herschel-Bulkley model. This three parameter model describes a plastic viscosity function which is predicted from a power law relation, (see figure (2.3).)

$$\sigma = m\,|\dot{\gamma}|\,\dot{\gamma}\,|^{n-1} + \sigma_y \quad , \qquad (2.4.4)$$

2.4.3 Elastic Bingham model (Yoshimura and Prud'homme [47]).

We now consider a model which describes elastic deformation below the yield stress.

$$\sigma = G\,\gamma_E \qquad |\gamma_E| < \gamma_0 \quad , \qquad (2.4.5)$$

$$\sigma = \eta_p\dot{\gamma} + \sigma_y \qquad |\gamma_E| = \gamma_0 \quad . \qquad (2.4.6)$$

where γ_0 is the yield strain, γ_E is the elastic strain and G is the elastic modulus. At strains below the yield strain, the model behaves as an elastic solid. When the yield strain is exceeded, viscous flow occurs with a constant plastic viscosity η_p. The elastic strain γ_E is stored during the viscous flow and is recovered if the applied shear strain changes direction.

Chapter 3.

An Introduction to Controlled Stress Rheometry.

3.1. Introduction.

Rheometry is concerned with the measurement of material properties in simple flow situations. These measurements may be used directly in the design of efficient flow processes or in quality control assessments. The rheological information obtained from simple rheometrical flow situations can be of use in the development of constitutive equations. These constitutive equations may then be used in conjunction with the stress equations of motion and continuity to predict material behaviour in complex flow situations. Another important area of rheological study concerns the relationship between observed rheological behaviour and the microstructure of materials. Hence, it is important to be able to consider rheometrical flow situations in which the structure of the material is not destroyed.

A rheometer is a versatile instrument capable of determining the material properties of elastico-viscous fluids in simple rheometrical flow situations. These instruments may be of a capillary or a rotational type of design. The work in this thesis is concerned with flow situations that may be generated on a controlled stress rotational rheometer.

In the controlled stress technique, a shear stress is applied to the fluid. An advantage with this flow situation is that the rheometer reacts in sympathy to the fluid properties and does not force the material to deform. This enables accurate low shear data to be measured. An important application of the controlled stress technique, is in the measurement of the yield stress of a material. A controlled stress rheometer is capable of measuring the minimum stress at which the material is observed to deform. It should be noted, that this value of the yield stress, will depend both on the accuracy of the measurement system used and on the amount of time allowed for the experiment to take place.

By contrast, a controlled shear rate rotational instrument (e.g. The Weissenberg Rheogoniometer), imposes a deformation on to the sample and forces the material to move. This obviously has disadvantages when effects such as 'yield stress' are to be measured.

3.2. Historical development of controlled stress rheometry.

In the past, the controlled shear rate technique has been the more popular method for measuring rheological properties. The main reason for this being that it is easier to design an instrument in which the shear rate is controlled than it is to design an instrument in which the shear stress is controlled (Davis et al [14]). The first commercially available controlled stress instrument, was the Stormer viscometer (circa 1920). This instrument is described in detail by Van Wazer et al [40]. The basic geometry was a concentric cylinder geometry in which the inner cylinder was free to rotate under an applied stress and the outer cylinder was fixed. A constant stress was provided by a system of pulleys, strings, and weights (see figure (3.1)). A shear stress was applied to the sample by attaching a known weight to a string and permitting free fall through a distance of about 40 inches. The period of shear was therefore restricted by the distance of travel of the weight. It was possible to use the Stormer viscometer to carry out creep retardation and relaxation experiments. A modification to the Stormer viscometer in which the outer cylinder was rotated and the weight was held stationary was described by The British Food Manufacturing Industries Research Association [7].

In 1951, Oldroyd et al [31] described the use of an air bearing for the accurate centering and support of an inner cylinder inside an outer cylinder. This principle was utilised by Davis, Deer, and Warburton [14] in their development of a concentric cylinder viscometer which was the first of a new generation of controlled stress instruments commonly known as Deer rheometers. This instrument made use of an air bearing turbine system to both centre and support the rotor, and to supply a constant source of stress. The rates of rotation were measured by a stop watch. The very small movements obtained in creep testing were measured by a displacement transducer and displayed as a continuous trace on a UV recorder. Later modifications of this instrument used an induction motor drive system to apply a constant stress to the rotor platen. A schematic diagram of this motor is shown in figure (3.2). A disc supported by an air bearing is situated between two current carrying coils. By varying the current in one of the coils, a torque may be exerted on the disc. This torque is then transmitted to the rotor platen

through a shaft with almost zero friction from the drive head. The Deer rheometer could be used to carry out steady shear flow and creep experiments. However, the induction motor used in the Deer rheometer was not suitable for operation in an oscillatory shear mode due to problems involving electromagnetic inertia [20].

The next development in controlled stress rheometry came with the introduction of the Carri-Med controlled stress rheometer† (figure (3.3)). The experimental programme for this thesis was carried out on a Carri-Med CS100L instrument which allows for a maximum torque of 0.01 Nm to be applied to the rotor.

3.3. Description of The Carri-Med Rheometer.

The Carri-Med rheometer is fully computer controlled. The rheometer may be linked to a microcomputer through an SSM IEEE interface. This enables oscillatory and combined steady and oscillatory shear experiments to be carried out in addition to flow and creep tests. This was therefore the first controlled stress instrument that could be used in an unsteady shear mode of operation (Jones et al [23]). The experimental data is automatically analysed using specially written software. The oscillatory shear-flow analysis was developed by Jones et al [23,24] and Holder [20], and the combined steady and oscillatory shear flow analysis was developed by Davies et al [12].

The stress is applied to the rotor by an electronically controlled induction motor. There are no mechanical connections between the moving and stationary parts of the motor. All rotating parts of the motor are supported by an air bearing. The rotor spindle is hollow, so that a draw rod may be inserted into it. This rod has a screw thread fitted, to which a number of different platens may be attached. The basic geometries incorporated into this apparatus are the cone and plate, parallel plate, concentric cylinder, and double concentric cylinder measuring systems. The bottom plate may be automatically raised or lowered by the computer. The level to which it is raised is set on a micrometer scale. This mechanism controls the parallel plate gap, the concentric cylinder and double concentric cylinder height, and the cone and plate truncation gap.

† Manufactured by Carri-Med UK Ltd, Dorking, Surrey RH4 3YX.

Slight imperfections in the air bearing give rise to a 'wind milling' effect on the rotor. In order to counteract this unwanted rotation, the rheometer calculates the torque required to hold the rotor stationary, effectively 'exerting a zero torque' on the platen. This process is known as biasing, and occurs each time the bottom plate is lowered.

The displacement of the rotor is measured using an optical encoder. This measurement system consists of a circular disc divided into 2500 equal divisions, each marked as a digital location. In between each of these digital positions, the electronics interpolates between each line to give a further 256 divisions per line. The optical encoder therefore has, in total, 640,000 divisions, giving a resolution of the order of 10^{-5} radians.

The temperature control of the experimental apparatus is greatly simplified by having one platen fixed. This stationary platen can then form part of the temperature control system. The Carri-Med rheometer uses a Peltier system to control the temperature of the bottom plate. This system may be used in conjunction with the parallel plate and cone and plate geometries. A circulation jacket should be incorporated into the temperature control system when performing concentric cylinder and double-concentric cylinder experiments. This jacket should be operated at the same temperature as the Peltier system. The Peltier system uses a thermo-electric effect which functions as a heat pump system with no moving parts. This set up enables the temperature to be controlled over a range of 0-99 $^{\circ}$C.

3.4. Steady Shear Flow.

(a). Cone and plate geometry (figure(3.4)).

The fluid is contained between a cone of semi-vertical angle θ_c, and a horizontal flat plate. The radius of the cone (i.e. the distance from the edge to the vertex) is a. The gap angle between the cone and the plate θ_0 is assumed to be small enough to ignore the free surface boundary effect. If the gap angle is small ($\leq 4^{\circ}$), then

the shear rate $\dot{\gamma}_s$ across the gap may be assumed to be constant (Walters and Waters [42]). i.e.

$$\dot{\gamma}_s = \frac{\Omega}{\theta_0} \quad , \tag{3.4.1}$$

where Ω is the angular velocity of the rotor platen. The equation of motion of the cone is given by

$$C = \frac{2\pi a^3}{3} \dot{\gamma}_s \, \eta(\dot{\gamma}_s) \quad , \tag{3.4.2}$$

where C is the applied couple. The shear viscosity function can therefore be determined directly by measuring the angular velocity of the cone.

$$\eta(\dot{\gamma}_s) = \frac{3C\theta_0}{2\pi\Omega a^3} \quad . \tag{3.4.3}$$

(b). Parallel plate geometry (figure (3.5)).

The fluid is contained between two circular parallel plates of radius a and separated by a vertical distance h. The shear rate across the parallel plate gap is dependent on the radial distance r. i.e.

$$\dot{\gamma}_s = \frac{r\Omega}{h} \quad . \tag{3.4.4}$$

The maximum shear rate occurs at the outer edge of the geometry (r=a), and is given by

$$\dot{\gamma}_a = \frac{a\Omega}{h} \quad . \tag{3.4.5}$$

The equation of motion of the top platen is given by the integral,

$$C = 2\pi \int_0^a r^2 \, \dot{\gamma}_s \eta(\dot{\gamma}_s) \, dr \quad . \tag{3.4.6}$$

Substituting for r from equation (3.4.4) into the above integral, and using equation (3.4.5), we obtain

$$\frac{\dot{\gamma}_a{}^3 C}{2\pi a^3} = \int_0^{\dot{\gamma}_a} \dot{\gamma}_s{}^3 \eta(\dot{\gamma}_s) \, d\dot{\gamma}_s \quad . \tag{3.4.7}$$

Differentiating equation (3.4.7) with respect to $\dot{\gamma}_a$ produces the following expression for the shear viscosity function.

$$\eta(\dot{\gamma}_a) = \frac{1}{2\pi a^3}\left[\frac{dC}{d\dot{\gamma}_a} + \frac{3C}{\dot{\gamma}_a}\right] \quad . \qquad (3.4.8)$$

i.e. In order to evaluate the shear viscosity function we must determine the slope of the couple/shear rate curve.

(c) Concentric Cylinder Geometry (Figure (3.6)).

The fluid is contained in an annular gap between two concentric cylinders of radii r_i and r_o ($r_i<r_o$), and height h. When the relative gap, $(r_o - r_i)/r_i$, between the two cylinders is small, we can assume that the shear rate across the gap is constant. (Coleman et al [9]) i.e.

$$\dot{\gamma}_s = \frac{r_i\Omega}{r_o - r_i} \quad . \qquad (3.4.9)$$

The equation of motion of the inner cylinder is given by

$$C = 2\pi r_i^{\,2} h\, \dot{\gamma}_s\, \eta(\dot{\gamma}_s) \quad . \qquad (3.4.10)$$

Hence, the shear viscosity function may be determined directly by measuring the angular velocity of the inner cylinder.

$$\eta(\dot{\gamma}_s) = \frac{C\,(r_o - r_i)}{2\pi\, r_i^{\,3} h\, \Omega} \quad . \qquad (3.4.11)$$

When the relative gap between the two cylinders is large, the analysis is not so straightforward, since the shear rate is now a function of the radial distance r.

A method for obtaining the shear viscosity function from the gradient of the angular velocity/couple curve is presented by Coleman et al [9]. However, this method is only really applicable for very large annular gaps, in which case end effect errors due to the finite dimensions of the measuring system become significant. Clearly, the cone and plate, parallel plate and narrow gap concentric cylinder geometries offer much more convenient methods for determining the shear viscosity function.

(d) Concentric Double Cylinder Geometry (Figure (3.7)).

The analysis for this flow situation is similar to that for the narrow gap concentric cylinder geometry except that there are now two separate annular regions of width $(r_2 - r_1)$ and $(r_4 - r_3)$ respectively. The advantage of this arrangement is that a large area of fluid is in contact with the shearing surface. This results in reduced experimental scatter, which is a particularly important consideration when measuring the rheological properties of thin fluids.

The relative gaps $(r_2 - r_1)/r_1$ and $(r_4 - r_3)/r_3$ are both assumed to be small. Hence, the shear rate across each annular gap can be assumed to be constant (see equation (3.4.9)). The dimensions of the geometry should be chosen so that the shear rate across the inner gap is equal to the shear rate across the outer gap. The couple acting on the rotor cylinder due to the motion of the fluid, is given by

$$C = C_1 + C_2 \quad , \qquad (3.4.13)$$

where

$$C_1 = 2\pi\, r_1^2 h\, \dot{\gamma}_s \eta(\dot{\gamma}_s) \quad , \qquad (3.4.14)$$

and

$$C_2 = 2\pi\, r_3^2 h\, \dot{\gamma}_s\, \eta(\dot{\gamma}_s) \quad , \qquad (3.4.15)$$

i.e.

$$C = 2\pi\, h\, \eta(\dot{\gamma}_s)\Omega \left[\frac{r_1^3}{r_2 - r_1} + \frac{r_3^3}{r_4 - r_3} \right] . \qquad (3.4.16)$$

The shear viscosity may be determined directly from measuring the angular velocity of the rotor platen.

$$\eta(\dot{\gamma}_s) = \frac{C\,(r_2 - r_1)\,(r_4 - r_3)}{2\pi\, h\, \Omega \left[r_1^3(r_4 - r_3) + r_3^3(r_2 - r_1) \right]} . \qquad (3.4.17)$$

3.5. Small Amplitude Oscillatory Shear Flow.

This flow situation is extensively covered in Chapters 6 and 7, and so will only be discussed briefly here. In Chapter 2 we noted that the linear time dependent behaviour of elastico-viscous fluids may be characterised by the complex viscosity function η^*. In practice, this function is a fairly simple quantity to measure. The most important point to note is that the experimental data must be sampled in the linear viscoelastic region. This can be ensured by performing a torque sweep before a dynamic test is carried out. The region where the dynamic viscosity and dynamic rigidity functions are independent of the strain amplitude defines the linear viscoelastic range.

Fluid inertia effects may influence the measurement of the dynamic properties of a fluid. These effects can be particularly severe when measuring the dynamic properties of mobile fluids at high frequencies. Fluid inertia effects can be reduced by using narrow gap geometries to measure the dynamic properties. In this case, the first order correction is usually sufficient to provide accurate dynamic data (Jones et al [24]).

(a). Cone and Plate Geometry.

We consider the small gap angle cone and plate geometry. The dynamic viscosity and dynamic rigidity functions are given to first order accuracy by Holder [20].

$$\eta' = \frac{3C_0 \sin(c)}{2\pi\omega a^3 X_0} \quad , \tag{3.5.1}$$

and

$$G' = \frac{3}{2\pi a^3}\left[\frac{C_0 \cos(c)}{X_0} + I\omega^2\right] + \frac{\omega^2 \rho a^2 \theta_0^{\,2}}{5} \quad , \tag{3.5.2}$$

respectively.

The applied torque amplitude C_0, angular frequency of oscillation ω, cone radius a, fluid density ρ, and gap angle θ_0 are all known quantities. The displacement amplitude X_0 and phase difference c, between the applied torque and angular displacement waveforms are measured as the output from this experiment.

(b). Parallel Plate Geometry.

For a parallel plate measuring system with platens of radius a separated by a vertical distance h, the dynamic viscosity and dynamic rigidity functions are given to first order accuracy by,

$$\eta' = \frac{2hC_0 \sin(c)}{\pi\omega a^4 X_0} \quad , \tag{3.5.3}$$

and

$$G' = \frac{2h}{\pi a^4}\left[\frac{C_0\cos(c)}{X_0} + I\omega^2\right] + \frac{\omega^2\rho h^2}{3} \quad . \tag{3.5.4}$$

(c). Concentric Cylinder Geometry.

For a concentic cylinder measuring system with inner and outer cylinders of height h and radii r_i and r_o respectively, $(r_i<r_o)$, the expressions for the dynamic viscosity and dynamic rigidity functions to first order accuracy are as follows,

$$\eta' = \frac{C_0(r_o^2 - r_i^2)\sin(c)}{4\pi\omega X_o h r_o^2 r_i^2} \quad , \tag{3.5.5}$$

and

$$G' = \frac{(r_o^2 - r_i^2)}{4\pi h r_o^2 r_i^2}\left[\frac{C_0\cos(c)}{X_0} + I\omega^2\right] - \frac{\omega^2\rho r_i^2}{2}\left[\frac{3r_o^2 - r_i^2}{4r_o^2} - \frac{r_o^2 \ln(r_o/r_i)}{r_o^2 - r_i^2}\right] \quad . \tag{3.5.6}$$

(d). Double Concentric Cylinder.

For the double concentric cylinder measuring system with inner and outer annular gaps of width $(r_2 - r_1)$ and $(r_4 - r_3)$ respectively, the dynamic viscosity and dynamic rigidity functions are given to first order accuracy by

$$\eta' = \frac{C_0 \sin(c)}{4\pi\omega X_0 h}\left[\frac{(r_2^2 - r_1^2)(r_4^2 - r_3^2)}{r_1^2 r_2^2(r_4^2 - r_3^2) + r_3^2 r_4^2(r_2^2 - r_1^2)}\right], \qquad (3.5.7)$$

and

$$G' = \frac{1}{4\pi h}\left[\frac{(r_2^2 - r_1^2)(r_4^2 - r_3^2)}{r_1^2 r_2^2(r_4^2 - r_3^2) + r_3^2 r_4^2(r_2^2 - r_1^2)}\right]\left[\frac{C_0\cos(c)}{X_0} + I\omega^2\right]$$

$$- \omega^2\rho\left[r_2^4(r_4^2 - r_3^2)\left[\frac{3r_1^2 - r_2^2}{4} + \frac{r_1^4 \ln(r_1/r_2)}{r_2^2 - r_1^2}\right]\right.$$

$$\left. + \frac{r_3^4(r_2^2 - r_1^2)}{2}\left[\frac{3r_4^2 - r_3^2}{4} + \frac{r_4^4 \ln(r_3/r_4)}{r_4^2 - r_3^2}\right]\right]$$

$$\Big/ \left[r_1^2 r_2^2(r_4^2 - r_3^2) + r_3^2 r_4^2(r_2^2 - r_1^2)\right] . \qquad (3.5.8)$$

Chapter 4

Combined Steady and Oscillatory Shear Flow

4.1 Introduction

In this chapter, we carry out a theoretical analysis of a unidirectional shear flow of an elastico-viscous fluid in which the shear rate fluctuates sinusoidally about a non zero mean. One of the aims of the analysis, is to determine the effect of the oscillatory shear component on the mean shear stress produced in the fluid. In order to understand the motivation behind this work, we shall carry out a review of the previous literature relevant to this flow situation.

It is well documented that when an oscillatory shear component is superimposed on to the steady shear flow of an elastico-viscous fluid, a change in the mean flow rate is observed (Jones and Walters [22], Barnes et al [2], Sundstrom and Kaufman [37], Davies et al [10], Phan-Thien and Dudek [36]). This is to be expected, as the equations describing the relationship between the stress and the strain for these materials are non-linear. It can readily be shown that for a Newtonian fluid, no change in the mean flow rate is predicted (Barnes et al [2]). Depending on the flow conditions considered, the superimposed oscillatory shear component can have either a beneficial or a detrimental effect on the mean flow rate of the fluid (Barnes et al [2], Bullivant [8]). This phenomenum is known as flow enhancement. The sign convention usually adopted is that a positive flow enhancement represents an increase in flow rate, whereas a negative flow enhancement signifies a decrease in this quantity.

A particular flow problem which has recieved a great deal of attention in flow enhancement studies is the flow of an elastico-viscous fluid through a straight pipe of circular cross-section (Walters and Townsend [44], Barnes et al [2], Sundstrom and Kaufman [37], Davies et al [10], Phan-Thien [34]). The pressure gradient generating the flow situation is assumed to fluctuate about a non-zero mean. However, other flow situations have been considered. Jones and Walters (Jones and Walters [22]) have carried out an investigation of the combined steady and oscillatory shear

flow of an elastico-viscous fluid on a Weissenberg rheogoniometer. Recently, Davies et al [12] have demonstrated that a controlled stress rheometer can be used to investigate flow enhancement behaviour.

The flow of an elastico-viscous fluid through a straight pipe of circular cross-section due to a pulsed pressure gradient is a flow situation frequently encountered in industry. Many industrial processes involve pumping non-Newtonian fluids through straight pipes of circular cross-section. It is well known that some mechanical pumps use a reciprocal mechanism which results in a pulsatile pressure gradient. The theoretical work of Barnes et al [2] using a four constant Oldroyd model, predicted that in certain cases where an increase in flow rate was observed, the energy required to maintain the pulsed pressure gradient was, in fact, less than that required to generate the corresponding steady shear flow. This result suggested that it would be of economic advantage to design a pumping mechanism that encouraged a pulsed pressure gradient. This theoretical prediction was however found to be at variance with those of Sundstrom and Kaufman [37] using an Ellis model, and Phan-Thien and Dudek [36], using a non-affine network model, which predicted that the unsteady shear flow would require the greater energy to generate. Phan-Thien and Dudek suggest that the discrepancy between these theoretical predictions may be due to the form of the viscosity function assumed in the Oldroyd model. These workers (Phan-Thien and Dudek [36] used a power law relation to model the shear viscosity of the elastico-viscous fluid.

Barnes, Townsend, and Walters [2] carried out the first detailed investigation into flow enhancement behaviour for the pulsatile pipe flow problem outlined earlier in this introduction. This work was a continuation of earlier theoretical work carried out by Walters and Townsend [44]. Both of these studies considered the situation in which the superimposed oscillatory shear component was sinusoidal in character, and used a four constant Oldroyd model to provide theoretical predictions as to the nature of the flow enhancement effect. These predictions were then compared with experimental data obtained from a conventional pipe flow apparatus. It should be noted that the investigation was restricted to small values of the ratio between the pulsatile pressure gradient amplitude and the steady pressure gradient.

Barnes et al [2] obtained agreement between theory and experiment concerning the variation of flow enhancement with mean pressure gradient for a fixed frequency of pulsation. However, contradictory results were obtained between the theoretical predictions and the experimental data regarding the frequency dependence of the flow enhancement effect. The experimental data indicated that flow enhancement should increase as the frequency of pulsation is increased. The Oldroyd model, however, predicted that flow enhancement should decrease over this frequency range. Davies et al [10] using a Goddard-Miller model, Sundstrom and Kaufman [37] using an Ellis model and Phan-Thien [35] using both a B-KBZ model and a non-affine network model, were all unable to predict the frequency dependence of the Barnes et al experimental data. Furthermore, Sundstrom and Kaufman presented experimental data sampled at low frequencies of pulsation which showed that flow enhancement decreased with increasing frequency. They also showed that the Ellis model was able to predict these experimental results. It was later pointed out by Phan-Thien and Dudek [36], that the Goddard-Miller model and the four constant Oldroyd model are also capable of describing the experimental data taken by Sundstrom and Kaufman. Interestingly, Phan-Thien [34] managed to qualitatively predict the frequency dependence of the flow enhancement data of Barnes et al, using a simple generalized Maxwell model.

In the conventional pipe flow apparatus used by Barnes et al [2], the mean pressure gradient is controlled, and the mean flow rate is measured. In order to compare theory with experiment, the amplitude of the pulsatile pressure gradient must also be measured. This measurement is difficult to obtain accurately, especially at high frequencies, and so can be subject to error. Davies and Chakrabarti [11] overcame this limitation by developing a modified pulsatile pipe flow apparatus. In this modified apparatus, the mean flow rate and the amplitude of the pulsatile pressure gradient are controlled. Hence, with this instrument, measurement of the pulsatile pressure gradient is not required.

The problem of measuring the pulsatile pressure gradient amplitude on the conventional pipe flow apparatus was also raised by Phan-Thien and Dudek [36]. These workers modified the pipe flow apparatus by mounting the pressure transducer directly on to the pressure tap hole in the test section of the pipe flow apparatus. In

the conventional apparatus the transducer is connected to the pressure hole tap via two plastic tubes resulting in a large attenuation of the pulsatile pressure gradient amplitude. This attenuation increases with increasing frequency.

Phan-Thien and Dudek [36] used this modified apparatus to carry out an experimental programme to investigate flow enhancement behaviour. These experimental results showed that flow enhancement decreases with increasing frequency of pulsation. This work also included a theoretical analysis of the flow problem using a non-affine network model. Qualitative agreement was obtained between the experimental flow enhancement data and the theoretical predictions concerning the variation of flow enhancement with both frequency of pulsation and mean pressure gradient. It should be pointed out that, in this investigation, the ratio of the pulsatile pressure gradient amplitude to the steady pressure gradient was small. Consequently, the experimental data obtained by Phan-Thien and Dudek was subject to a large amount of experimental scatter.

The investigations into the pulsatile pipe flow problem described above, have in general been restricted to small pulsatile pressure gradient amplitudes. Consequently, the experimental results obtained from these studies contain some experimental scatter. Davies et al [12] considered the possibility of using the Carri-Med controlled stress rheometer to carry out combined steady and oscillatory shear stress experiments. This instrument can be used to superimpose large amplitude oscillatory displacements on to the steady shear flow of a test fluid. Preliminary experiments, produced results which were in qualitative agreement with the theoretical predictions of Walters and Townsend [44] and Davies et al [10].

Townsend [39] developed a viscoelastic theory based on a four constant Oldroyd model. This theory included the effects of fluid inertia and was valid for large amplitudes of oscillation.

The current project will extend the work of Davies et al [12] by considering the effect of a large sinusoidal fluctuation of the mean shear flow on the mean shear stress produced in the fluid. A corotational Goddard-Miller model is used to describe the non-linear relationship between the shear stress and shear rate for an elastico-viscous fluid. This model is capable of describing large deformations. Due to the complexity of the equations involved, mechanical and fluid inertia effects will be ignored in the analysis.

The generalised Newtonian model will be used to predict the change in mean shear stress for an inelastic fluid. A comparison of the reduction in mean shear stress predicted by the Goddard-Miller and Generalised Newtonian models will provide information concerning the importance of elasticity in this flow situation. As mentioned earlier, the shape of the shear viscosity curve exerts a strong influence on the flow enhancement behaviour of an inelastic fluid. The present study will compare inelastic and viscoelastic flow enhancment predictions for the power law, Carreau, and Segalman models.

4.2. Viscoelastic model.

4.2.1. Constitutive equation.

The constitutive equation for this analysis is provided by the Goddard-Miller model. For this model, relationship between the stress and the strain for an elastico-viscous fluid is given by (Bird et al [4,5]). i.e.

$$\underline{\sigma}'(t) = \int_{-\infty}^{t} G(t-t')\dot{\underline{\Gamma}}(x,t,t')\, dt' \quad , \qquad (4.2.1)$$

where $\underline{\sigma}'(t)$ is the extra stress tensor, $G(t-t')$ is known as the relaxation modulus, and $\dot{\underline{\Gamma}}(x,t,t')$ is the corotational rate of strain of tensor. The formulation together with some of the properties of this model were discussed in detail in Chapter 2.

4.2.2. The geometry.

We consider the combined steady and oscillatory shear flow of a viscoelastic fluid contained in an annular gap between two concentric cylinders of radii r_i and r_o ($r_i<r_o$), (see figure (3.6)). The height of fluid in contact with the cylinders is h. At this stage of the analysis, no assumption is made as to the boundary conditions on the inner and outer cylinders. The theoretical analysis proceeds by assuming that the shear rate $\dot{\gamma}$ in the fluid is of the form

$$\dot{\gamma}(r,t) = \dot{\gamma}_m(1 + \epsilon e^{i\omega t}) \quad , \qquad (4.2.2)$$

where $\dot{\gamma}_m$ is the mean shear rate and ϵ is the ratio between the oscillatory shear rate amplitude and the mean shear rate. In equation (4.2.2), the real part is implied.

All physical quantities are referred to a cylindrical polar coordinate system (r,θ,z). The velocity profile in the fluid is assumed to be of the form

$$V_r = 0 \; ; \quad V_\theta = rF(r) \; ; \quad V_z = 0 \qquad . \tag{4.2.3}$$

Hence the equation of continuity for incompressible fluids is automatically satisfied. i.e.

$$\underline{\nabla} \cdot \underline{V} = 0 \qquad , \tag{4.2.4}$$

The fluid exerts a torque on the upper platen due to the shear stress that is produced in the fluid. Our main interest in this work is to obtain an expression for the mean shear stress produced in the fluid. We will also derive expressions for the fundamental stress amplitude and phase angle.

4.2.3. Derivation of the mean shear stress.

This section will be concerned with a derivation of the mean shear stress for a general relaxation function $G(t-t')$.

The corotational rate of strain tensor is determined for the concentric cyinder geometry in Appendix A. It can be shown that the corotational rate of strain tensors for the parallel plate and small gap angle cone and plate geometries are of the same general form as that described below.

$$\underline{\dot{\Gamma}}(r,t,t') = \begin{bmatrix} -\sin(\varphi) & \cos(\varphi) & 0 \\ \cos(\varphi) & \sin(\varphi) & 0 \\ 0 & 0 & 0 \end{bmatrix} \dot{\gamma}_{\theta r}(r,t') \quad , \tag{4.2.5}$$

where,

$$\varphi = \int_{t'}^{t} \dot{\gamma}_{\theta r}(r,t'')dt'' \qquad . \tag{4.2.6}$$

On examining equation (4.2.5), we see that the shear stress components σ'_{rz}, $\sigma'_{\theta z}$, σ'_{zr}, and $\sigma'_{z\theta}$ are all zero as expected. The

normal stress components σ'_{rr}, $\sigma'_{\theta\theta}$, and σ'_{zz} do not give any contribution to the couple being applied to the upper platen, and therefore will not be considered in this work. The only components of $\dot{\bar{\Gamma}}$ that give rise to shear stresses producing a couple in the fluid are the $\dot{\Gamma}_{\theta r}$ and the $\dot{\Gamma}_{r\theta}$ components.

On substituting equation (4.2.5) in the constitutive equation (4.2.1), we see that the shear stress produced in the fluid is given by

$$\sigma'_{\theta r} = \int_{-\infty}^{t} G(t-t')\cos\left[\int_{t'}^{t} \dot{\gamma}_{\theta r}(t'')dt''\right]\dot{\gamma}_{\theta r}(t')\,dt' \quad , \qquad (4.2.7)$$

where the shear rate $\dot{\gamma}_{\theta r}$ is of the form given in equation (4.2.2). Hence, equation (4.2.7) may be written as

$$\sigma'_{\theta r} = \int_{-\infty}^{t} G(t-t')\cos\left[\dot{\gamma}_m(t-t') - \frac{i\dot{\gamma}_m\epsilon}{\omega}\left[e^{i\omega t} - e^{i\omega t'}\right]\right]\dot{\gamma}_m(1 + \epsilon e^{i\omega t'})\,dt'. \qquad (4.2.8)$$

Let

$$s = t - t' \quad . \qquad (4.2.9)$$

So that equation (4.2.8) becomes

$$\sigma'_{\theta r} = \int_{0}^{\infty} G(s)\cos\left[\dot{\gamma}_m s - \frac{i\dot{\gamma}_m\epsilon}{\omega}\left[e^{i\omega t} - e^{i\omega(t-s)}\right]\right]\dot{\gamma}_m(1 + \epsilon e^{i\omega(t-s)})\,ds \, . \qquad (4.2.10)$$

We may simplify (4.2.10) further by integrating by parts and taking the real part of the resulting expression.

$$\sigma'_{\theta r} = -\int_{0}^{\infty} G'(s)\sin\left[\dot{\gamma}_m s + \frac{\dot{\gamma}_m\epsilon}{\omega}\left[\sin(\omega t) - \sin(\omega(t-s))\right]\right] ds \quad . \qquad (4.2.11)$$

Using simple trigonometric identities we can easily show that the shear stress produced in the fluid is given by

$$\sigma'_{\theta r} = -\int_{0}^{\infty} G'(s)\sin\left[\dot{\gamma}_m s + \frac{\dot{\gamma}_m\epsilon}{\omega}\sin(\omega s/2)\cos(\omega t - \omega s/2)\right] ds \quad . \qquad (4.2.12)$$

The shear stress $\sigma'_{\theta r}$ is periodic in time t. We can therefore express $\sigma'_{\theta r}$ as a Fourier series expansion. i.e.

$$\sigma'_{\theta r}(t) = \frac{a_0}{2} + \sum_{n=1}^{\infty} \left[a_n \cos(n\omega t) + b_n \sin(n\omega t)\right] \quad . \qquad (4.2.13)$$

Clearly the first term is the value of the mean shear stress σ_m, and is given by the formula

$$\sigma_m = \frac{\omega}{2\pi} \int_0^{2\pi/\omega} \sigma'_{\theta r}(t)\, dt \quad . \qquad (4.2.14)$$

On equating equation (4.2.12) and equation (4.2.13), we obtain

$$\sigma_m = -\frac{1}{2\pi} \int_{u=0}^{2\pi} \int_{s=0}^{\infty} G'(s) \sin\left[\dot{\gamma}_m s + \frac{2\dot{\gamma}_m \epsilon}{\omega} \sin(\omega s/2)\cos(u-\omega s/2)\right] ds\, du \ , \qquad (4.2.15)$$

where

$$u = \omega t \quad . \qquad (4.2.16)$$

We may express equation (4.2.15) as

$$\sigma_m = -\int_0^{\infty} G'(s) \sin(\dot{\gamma}_m s) g1\, ds - \int_0^{\infty} G'(s) \cos(\dot{\gamma}_m s) g2\, ds \quad , \qquad (4.2.17)$$

where

$$g1 = \frac{1}{2\pi} \int_0^{2\pi} \cos\left[\frac{2\dot{\gamma}_m \epsilon}{\omega} \sin(\omega s/2)\cos(u-\omega s/2)\right] du \quad , \qquad (4.2.18)$$

and

$$g2 = \frac{1}{2\pi} \int_0^{2\pi} \sin\left[\frac{2\dot{\gamma}_m \epsilon}{\omega} \sin(\omega s/2)\cos(u-\omega s/2)\right] du \quad . \qquad (4.2.19)$$

The integrands defined in g1 and g2 are both periodic functions of period 2π. Hence, if we make the substitution,

$$p = u - \omega s/2 \quad , \qquad (4.2.20)$$

then g1 and g2 become

$$g1 = \frac{1}{2\pi} \int_0^{2\pi} \cos\left[\frac{2\dot{\gamma}_m \epsilon}{\omega} \sin(\omega s/2)\cos(p)\right] dp \quad , \qquad (4.2.21)$$

and

$$g2 = \frac{1}{2\pi}\int_0^{2\pi} \sin\left[\frac{2\dot{\gamma}_m\epsilon}{\omega}\sin(\omega s/2)\cos(p)\right] dp \quad . \quad (4.2.22)$$

Since both integrands are even functions of p, we may write

$$g1 = \frac{1}{\pi}\int_0^{\pi} \cos\left[\frac{2\dot{\gamma}_m\epsilon}{\omega}\sin(\omega s/2)\cos(p)\right] dp \quad , \quad (4.2.23)$$

and

$$g2 = \frac{1}{\pi}\int_0^{\pi} \sin\left[\frac{2\dot{\gamma}_m\epsilon}{\omega}\sin(\omega s/2)\cos(p)\right] dp \quad . \quad (4.2.24)$$

From (Watson [46]), we use the Bessel property.

$$J_0(z) = \frac{1}{\pi}\int_0^{\pi} \cos(z\cos(p))\, dp \quad . \quad (4.2.25)$$

Hence,

$$g1 = J_0\left[\frac{2\dot{\gamma}_m\epsilon}{\omega}\sin(\omega s/2)\right] \quad , \quad (4.2.26)$$

where $J_0(z)$ is a zero order Bessel function of the first kind.
It can be easily shown that

$$\int_0^{\pi} \sin\left[\frac{2\dot{\gamma}_m\epsilon}{\omega}\sin(\omega s/2)\cos(p)\right] dp = 0 \quad . \quad (4.2.27)$$

Hence, we may evaluate the mean shear stress from the formula,

$$\sigma_m = -\int_0^{\infty} G'(s)\sin(\dot{\gamma}_m s) J_0\left[\frac{2\dot{\gamma}_m\epsilon}{\omega}\sin(\omega s/2)\right] ds \quad . \quad (4.2.28)$$

Let the change in mean shear stress due to an imposed oscillation on the steady shear flow of the fluid be E. Therefore

$$E = 1 - \frac{\sigma_m}{\sigma_s} \quad , \quad (4.2.29)$$

where the steady shear stress is given by the integral,

$$\sigma_s = -\int_0^{\infty} G'(s)\sin(\dot{\gamma}_m s)\, ds \quad . \quad (4.2.30)$$

If we integrate equation (4.2.30) by parts, we obtain,

$$\sigma_s = \dot{\gamma}_m \int_0^\infty G(s)\cos(\dot{\gamma}_m s)\, ds \quad . \qquad (4.2.31)$$

From (Bird et al [5]), we see that the viscosity function $\eta(\dot{\gamma})$ and the relaxation modulus G(s) are related by

$$\eta(\dot{\gamma}) = \int_0^\infty G(s)\cos(\dot{\gamma} s)\, ds \quad . \qquad (4.2.32)$$

Hence, the steady shear stress may be evaluated from

$$\sigma_s = \dot{\gamma}_m \eta(\dot{\gamma}_m) \quad . \qquad (4.2.33)$$

4.2.4. Derivation of the fundamental stress amplitude and phase.

The Fourier series expansion given in equation (4.2.13) may be expressed as.

$$\sigma'_{\theta r}(t) = \frac{a_0}{2} + \sum_{n=1}^{\infty} \sigma_{an}\cos(n\omega t - c_n) \quad . \qquad (4.2.34)$$

where σ_{an}, c_n are the n^{th} harmonic amplitude and phase lag of the shear stress waveform.

$$\sigma_{a1} = \left[A_1^2 + B_1^2\right]^{\frac{1}{2}} \quad , \qquad (4.2.35)$$

is the fundamental stress amplitude, and

$$c_1 = \tan^{-1}(B_1 / A_1) \qquad (4.2.36)$$

is the phase lag between the fundamental oscillatory component of shear stress and the oscillatory component of the shear rate.

(a). Derivation of A_1.

From equation (4.2.13), A_1 is given by the integral,

$$A_1 = \frac{\omega}{\pi} \int_0^{2\pi/\omega} \sigma'_{\theta r}(t)\cos(\omega t)\, dt \quad . \qquad (4.2.37)$$

Hence, using equation (4.2.12) we may express A_1 as,

$$A_1 = -\frac{1}{\pi}\int_{u=0}^{2\pi}\int_{s=0}^{\infty} G'(s)\sin\left[\dot{\gamma}_m s + \frac{2\dot{\gamma}_m \epsilon}{\omega}\sin(\omega s/2)\cos(u-\omega s/2)\right]\cos(u)\, ds\, du \,, \tag{4.2.38}$$

where

$$u = \omega t \quad . \tag{4.2.39}$$

We may rewrite equation (4.2.38) as two separate double integrals. i.e.

$$A_1 = -\int_0^{\infty} G'(s)\sin(\dot{\gamma}_m s)h1\, ds - \int_0^{\infty} G'(s)\cos(\dot{\gamma}_m s)h2\, ds \quad , \tag{4.2.40}$$

where

$$h1 = \frac{1}{\pi}\int_0^{2\pi}\cos\left[\frac{2\dot{\gamma}_m \epsilon}{\omega}\sin(\omega s/2)\cos(u-\omega s/2)\right]\cos(u)\, du \quad , \tag{4.2.41}$$

and

$$h2 = \frac{1}{\pi}\int_0^{2\pi}\sin\left[\frac{2\dot{\gamma}_m \epsilon}{\omega}\sin(\omega s/2)\cos(u-\omega s/2)\right]\cos(u)\, du \quad . \tag{4.2.42}$$

The integrals defined in h1 and h2 are both periodic functions of period 2π. Hence if we make the substitution,

$$p = u - \omega s/2 \quad , \tag{4.2.43}$$

then h1 and h2 become

$$h1 = \frac{1}{\pi}\int_0^{2\pi}\cos\left[\frac{2\dot{\gamma}_m \epsilon}{\omega}\sin(\omega s/2)\cos(p)\right]\cos(p+\omega s/2)\, dp \quad , \tag{4.2.44}$$

and

$$h2 = \frac{1}{\pi}\int_0^{2\pi}\sin\left[\frac{2\dot{\gamma}_m \epsilon}{\omega}\sin(\omega s/2)\cos(p)\right]\cos(p+\omega s/2)\, dp \quad . \tag{4.2.45}$$

Evaluation of h1.

Let us first consider h1.

$$h1 = \frac{1}{\pi}\left[\cos(\omega s/2)\int_0^{2\pi}\cos\left[\frac{2\dot{\gamma}_m\epsilon}{\omega}\sin(\omega s/2)\cos(p)\right]\cos(p)\,dp\right.$$

$$\left. - \sin(\omega s/2)\int_0^{2\pi}\cos\left[\frac{2\dot{\gamma}_m\epsilon}{\omega}\sin(\omega s/2)\cos(p)\right]\sin(p)\,dp\right] . \qquad (4.2.46)$$

The first integrand is an even function of p and the second integrand is an odd function of p. Hence, equation (4.2.46) simplifies to

$$h1 = \frac{2\cos(\omega s/2)}{\pi}\int_0^{\pi}\cos\left[\frac{2\dot{\gamma}_m\epsilon}{\omega}\sin(\omega s/2)\cos(p)\right]\cos(p)\,dp \quad . \qquad (4.2.47)$$

It can easily be shown from equation (4.2.47) that

$$h1 = 0 \quad . \qquad (4.2.48)$$

Evaluation of h2.

$$h2 = \frac{1}{\pi}\int_0^{2\pi}\sin\left[\frac{2\dot{\gamma}_m\epsilon}{\omega}\sin(\omega s/2)\cos(p)\right]\cos(p+\omega s/2)\,dp \quad . \qquad (4.2.49)$$

By employing similar arguments to those used to evaluate h1, it can be deduced that the integral defined by equation (4.2.49) reduces to the following expression,

$$h2 = 2\cos(\omega s/2)J_1\left[\frac{2\dot{\gamma}_m\epsilon}{\omega}\sin(\omega s/2)\right] \quad , \qquad (4.2.50)$$

where $J_1(z)$ is a first order Bessel function of the first kind and is defined by the integral (Watson [46]),

$$J_1(z) = \frac{2}{\pi}\int_0^{2\pi}\sin(z\cos(p))\cos(p)\,dp \quad . \qquad (4.2.51)$$

Hence, substituting equations (4.2.48) and (4.2.50) into equation (4.2.40), we obtain A_1 given by

$$A_1 = -2\int_0^{\infty}G'(s)\cos(\dot{\gamma}_m s)\cos(\omega s/2)J_1\left[\frac{2\dot{\gamma}_m\epsilon}{\omega}\sin(\omega s/2)\right]ds \quad . \qquad (4.2.52)$$

(b) Derivation of B_1.

From equation (4.2.13), we see that B_1 is given by

$$B_1 = \frac{\omega}{\pi}\int_0^{2\pi/\omega} \sigma'_{\theta r}(t)\sin(\omega t)\, dt \quad . \quad (4.2.53)$$

Substituting equation (4.2.12) into (4.2.53), we obtain,

$$B_1 = -\frac{1}{\pi}\int_{u=0}^{2\pi}\int_{s=0}^{\infty} G'(s)\sin\left[\dot{\gamma}_m s + \frac{2\gamma_m\epsilon}{\omega}\sin(\omega s/2)\cos(u-\omega s/2)\right]\sin(u)\, ds\, du \quad , \quad (4.2.54)$$

which may be split into two separate double integrals as follows,

$$B_1 = -\int_0^{\infty} G'(s)\sin(\dot{\gamma}_m s)g5\, ds - \int_0^{\infty} G'(s)\cos(\dot{\gamma}_m s)h4\, ds \quad , \quad (4.2.55)$$

where

$$h3 = \frac{1}{\pi}\int_0^{2\pi}\cos\left[\frac{2\dot{\gamma}_m\epsilon}{\omega}\sin(\omega s/2)\cos(u-\omega s/2)\right]\sin(u)\, du \quad , \quad (4.2.56)$$

and

$$h4 = \frac{1}{\pi}\int_0^{2\pi}\sin\left[\frac{2\dot{\gamma}_m\epsilon}{\omega}\sin(\omega s/2)\cos(u-\omega s/2)\right]\sin(u)\, du \quad . \quad (4.2.57)$$

If we analyse the above integrals using similar techniques to those used to evaluate h1 and h2, then we obtain the following results,

$$h3 = 0 \quad , \quad (4.2.58)$$

and

$$h4 = 2\sin(\omega s/2)J_1\left[\frac{2\dot{\gamma}_m\epsilon}{\omega}\sin(\omega s/2)\right] \quad . \quad (4.2.59)$$

Hence, B_1 may be evaluated from the integral,

$$B_1 = -2\int_0^{\infty} G'(s)\cos(\dot{\gamma}_m s)\sin(\omega s/2)J_1\left[\frac{2\dot{\gamma}_m\epsilon}{\omega}\sin(\omega s/2)\right] ds \quad . \quad (4.2.60)$$

From equations (4.2.52) and (4.2.60), we may determine the fundamental stress amplitude and the phase lag defined in equations (4.2.35-36).

4.2.5. Evaluation of integrals using recursive techniques.

The integrals defined by equations (4.2.28), (4.2.38), and (4.2.60) do not lend themselves well to numerical integration. The problem being that the upper limit of integration is infinity, and that the integrands contain the product of two periodic functions. Hence, we would expect convergence for any numerical scheme to be slow and subject to rounding off errors. This section will show an alternative approach where the integrals could be evaluated analytically using recursive techniques.

(a). Fractional reduction in mean shear stress (E).

The inetgral in equation (4.2.28) may be evaluated in the following way. From (Watson [46]), we may express the Bessel function $J_0(z)$ by the infinite series defined below,

$$J_0(z) = \sum_{k=0}^{\infty} \frac{(-1)^k}{(k!)^2} \left[\frac{z}{2} \right]^{2k} , \qquad (4.2.61)$$

which is convergent for all z. Substituting equation (4.2.61) into (4.2.28), we obtain,

$$\sigma_m = -\sum_{k=0}^{\infty} \frac{(-1)^k}{(k!)^2} \left[\frac{\dot{\gamma}_m \epsilon}{\omega}\right]^{2k} \int_0^{\infty} G'(s)\sin(\dot{\gamma}_m s)\sin^{2k}(\omega s/2)\, ds \quad . \qquad (4.2.62)$$

Hence the mean shear stress σ_m can be expressed as a convergent infinite series of integrals. Using trigonometric identities, the mean shear stress may be expressed as

$$\sigma_m = -\sum_{k=0}^{\infty} \frac{(-1)^k}{2^k (k!)^2} \left[\frac{\dot{\gamma}_m \epsilon}{\omega}\right]^{2k} \int_0^{\infty} G'(s)\sin(\dot{\gamma}_m s)(1 - \cos(\omega s))^k\, ds \quad . \qquad (4.2.63)$$

We now define the integral $I_k(\dot{\gamma}_m)$ to be

$$I_k(\dot{\gamma}_m) = -\left[\frac{\epsilon}{2}^2\right]^k \int_0^{\infty} G'(s)\sin(\dot{\gamma}_m s)(1 - \cos(\omega s))^k\, ds \quad . \qquad (4.2.64)$$

$$(k=0,1,2,\ldots)$$

Hence,

$$\sigma_m = \sum_{k=0}^{\infty} \frac{(-1)^k}{(k!)^2} \left[\frac{\dot{\gamma}_m}{\omega}\right]^{2k} I_k(\dot{\gamma}_m) \quad . \qquad (4.2.65)$$

The above series can be shown to be convergent.

Therefore, provided the value of the integral $I_k(\dot{\gamma}_m)$ can be determined for all k, then theoretically we should be able to predict the mean shear stress σ_m.

The integral $I_k(\dot{\gamma}_m)$ in equation (4.2.64) may be expressed in terms of three separate integrals $I_{k-1}(\dot{\gamma}_m)$, $I_{k-1}(\dot{\gamma}_m+\omega)$, and $I_{k-1}(\dot{\gamma}_m-\omega)$. i.e.

$$I_k(\dot{\gamma}_m) = \frac{\epsilon^2}{2}\left[I_{k-1}(\dot{\gamma}_m) - \frac{1}{2} I_{k-1}(\dot{\gamma}_m+\omega) - \frac{1}{2} I_{k-1}(\dot{\gamma}_m-\omega) \right] , \quad (4.2.66)$$

$$(k=1,2,3,\ldots)$$

where

$$I_0(\dot{\gamma}_m) = - \int_0^\infty G'(s)\sin(\dot{\gamma}_m s)\, ds \quad . \quad (4.2.67)$$

Integrating (4.2.67) by parts produces

$$I_0(\dot{\gamma}_m) = \dot{\gamma}_m \int_0^\infty G(s)\cos(\dot{\gamma}_m s)\, ds \quad . \quad (4.2.68)$$

From (Bird et al [5]), we see that the shear viscosity function for the Goddard-Miller model is given by

$$\eta(\dot{\gamma}_m) = \int_0^\infty G(s)\cos(\dot{\gamma}_m s)\, ds \quad , \quad (4.2.69)$$

Hence, equation (4.2.68) becomes

$$I_0(\dot{\gamma}_m) = \dot{\gamma}_m \eta(\dot{\gamma}_m) \quad . \quad (4.2.70)$$

When equation (4.2.66) is used recursively to obtain $I_k(\dot{\gamma}_m)$, we shall need the general result for $I_k(\dot{\gamma}_m \pm r\omega)$, which can be obtained from equation (4.2.66) by replacing $\dot{\gamma}_m$ by $\dot{\gamma}_m \pm r\omega$ to give

$$I_k(\dot{\gamma}_m \pm r\omega) = \frac{\epsilon^2}{2}\left[I_{k-1}(\dot{\gamma}_m \pm r\omega) - \frac{1}{2} I_{k-1}(\dot{\gamma}_m \pm (r+1)\omega) - \frac{1}{2} I_{k-1}(\dot{\gamma}_m \pm (r-1)\omega) \right] ,$$

$$(k=1,2,3,\ldots) \quad (4.2.71)$$

where the starting value for the scheme is

$$I_0(\dot{\gamma}_m \pm r\omega) = (\dot{\gamma}_m \pm r\omega)\eta(\dot{\gamma}_m \pm r\omega) \quad . \quad (4.2.72)$$

The recursive formula (4.2.66) may be used to obtain the mean shear stress σ_m, from equation (4.2.65).

On substituting equation (4.2.65) into equation (4.2.29), we see that the fractional reduction in mean shear stress E, may be obtained from

$$E = 1 - \frac{1}{I_0(\dot{\gamma}_m)} \sum_{k=0}^{\infty} \frac{(-1)^k}{(k!)^2} \left[\frac{\dot{\gamma}_m}{\omega}\right]^{2k} I_k(\dot{\gamma}_m) \quad . \qquad (4.2.73)$$

i.e.

$$E = \frac{1}{I_0(\dot{\gamma}_m)} \sum_{k=1}^{\infty} \frac{(-1)^{k+1}}{(k!)^2} \left[\frac{\dot{\gamma}_m}{\omega}\right]^{2k} I_k(\dot{\gamma}_m) \quad . \qquad (4.2.74)$$

(b) Fundamental Stress Amplitude (σ_{a_1}).

The fundamental stress amplitude produced in the fluid is given by equation (4.2.35). Using the infinite series Bessel identity for $J_1(z)$, given by (Watson [46]).

$$J_1(z) = \frac{z}{2} \sum_{k=0}^{\infty} \frac{(-1)^k}{k!(k+1)!} \left[\frac{z}{2}\right]^{2k} \quad , \qquad (4.2.75)$$

we can show that A_1 and B_1 are given by

$$A_1 =$$

$$- \sum_{k=0}^{\infty} \frac{(-1)^k \ (\dot{\gamma}_m \epsilon/\omega)^{2k+1}}{2^{k+1} k!(k+1)!} \int_0^{\infty} G'(s) \left[\sin((\dot{\gamma}_m + \omega)s) - \sin((\dot{\gamma}_m - \omega)s)\right] \times (1 - \cos(\omega s)) \ ds \quad , \qquad (4.2.76)$$

$$B_1 =$$

$$- \sum_{k=0}^{\infty} \frac{(-1)^k}{2^k k!(k+1)!} \left[\frac{\dot{\gamma}_m \epsilon}{\omega}\right]^{2k+1} \int_0^{\infty} G'(s) \cos(\dot{\gamma}_m s)(1 - \cos(\omega s))^{k+1} \ ds \quad . \qquad (4.2.77)$$

Evaluation of A_1.

We may rewrite the equation for A_1 in equation (4.2.76) as

$$A_1 = \sum_{k=0}^{\infty} \frac{(-1)^k}{k!(k+1)!} \left[\frac{\dot{\gamma}_m}{\omega}\right]^{2k+1} I_k^a(\dot{\gamma}_m) \quad , \qquad (4.2.78)$$

where the integral $I_k^a(\dot{\gamma}_m)$ is defined to be

$$I_k^a(\dot{\gamma}_m) = - \frac{\epsilon^{2k+1}}{2^{k+1}} \int_0^{\infty} G'(s) \left[\sin((\dot{\gamma}_m + \omega)s) - \sin((\dot{\gamma}_m - \omega)s)\right] (1 - \cos(\omega s))^k ds \qquad (4.2.79)$$

It is possible to express $I^a_k(\dot\gamma_m)$ in terms of a recursive formula involving three integrals evaluated at the $(k-1)^{th}$ step. i.e.

$$I^a_k(\dot\gamma_m) = \frac{\epsilon}{2}^2 \left[I^a_{k-1}(\dot\gamma_m) - \frac{1}{2} I^a_{k-1}(\dot\gamma_m+\omega) - \frac{1}{2} I^a_{k-1}(\dot\gamma_m-\omega) \right] . \quad (4.2.80)$$

$(k=1,2,3,\ldots)$

The starting value for this scheme is given by

$$I^a_0(\dot\gamma_m+ r\omega) = - \frac{\epsilon}{2} \int_0^\infty G'(s)\left[\sin((\dot\gamma_m+(r+1)\omega)) - \sin((\dot\gamma_m+(r-1)\omega))\right] ds .$$

$r=0,\pm1,\pm2,\ldots$ (4.2.81)

From (4.2.32),

$$I^a_0(\dot\gamma_m+ r\omega) . = \frac{\epsilon}{2} \left[(\dot\gamma_m+(r+1)\omega)\eta(\dot\gamma_m+(r+1)\omega) - (\dot\gamma_m+(r-1)\omega)\eta(\dot\gamma_m+(r-1)\omega)\right]$$

$r=0,\pm1,\pm2,\ldots$ (4.2.82)

Hence, we have a similar iterative scheme for evaluating A_1 as we employed to work out the fractional reduction in mean shear stress.

Evaluation of B_1.

The equation for B_1 in equation (4.2.77) may be written as

$$B_1 = \sum_{k=0}^{\infty} \frac{(-1)^k}{k!(k+1)!} \left[\frac{\dot\gamma_m}{\omega}\right]^{2k+1} I^b_k(\dot\gamma_m) , \quad (4.2.83)$$

where the integral $I^b(\dot\gamma_m s)$ is defined as

$$I^b_k(\dot\gamma_m) = - \frac{\epsilon^{2k+1}}{2^{k+1}} \int_0^\infty G'(s)\cos(\dot\gamma_m s)(1 - \cos(\omega s))^{k+1} ds . \quad (4.2.84)$$

It can be shown that the integral $I^b_k(\dot\gamma_m)$ satisfies the recursive formula defined below,

$$I^b_k(\dot\gamma_m) = \frac{\epsilon}{2}^2 \left[I^b_{k-1}(\dot\gamma_m) - \frac{1}{2} I^b_{k-1}(\dot\gamma_m+\omega) - \frac{1}{2} I^b_{k-1}(\dot\gamma_m-\omega) \right] , \quad (4.2.85)$$

$k=1,2,3,\ldots$

where the starting value for this iterative scheme is given by

$$I^b_0(\dot\gamma_m+r\omega) = - \epsilon \int_0^\infty G'(s)\cos((\dot\gamma_m+r\omega)s)(1 - \cos(\omega s)) ds . \quad (4.2.86)$$

$r=0,\pm1,\pm2,\ldots$

Integrating (4.2.86) by parts, produces the expression

$$I_0^b(\dot{\gamma}_m+r\omega) = \epsilon \int_0^\infty G(s)\left[(\dot{\gamma}_m+r\omega)\sin((\dot{\gamma}_m+r\omega)s)\right.$$

$$\left. - \frac{1}{2}(\dot{\gamma}_m+(r+1)\omega)\sin((\dot{\gamma}_m+(r+1)\omega)s) - \frac{1}{2}(\dot{\gamma}_m+(r-1)\omega)\sin((\dot{\gamma}_m+(r-1)\omega)s)\right] ds$$

$$r=0,\pm1,\pm2,... \qquad (4.2.87)$$

Hence, in order to obtain $I_0^b(\dot{\gamma}_m+r\omega)$ we need to evaluate integrals of the form

$$Q = \int_0^\infty G(s)\sin((\dot{\gamma}_m+r\omega)s)\, ds \quad , \qquad (4.2.88)$$

$$r=0,\pm1,\pm2,...$$

which is discussed in section (4.2.6)

Finally we define the non-dimensional quantity δ to be the ratio between the fundamental oscillatory stress amplitude and the mean shear stress. i.e.

$$\delta = \frac{\sigma_{a1}}{\sigma_m} \quad . \qquad (4.2.89)$$

and is obtained by evaluating equation (4.2.65) for σ_m and equations (4.2.35), (4.2.78) and (4.2.83) for σ_{a1}.

4.2.6. Non-Newtonian viscosity models.

The relaxation modulus G(s) is related to the shear viscosity function by the following equation (Bird et al [5]),

$$G(s) = \frac{2}{\pi}\int_0^\infty \eta(\dot{\gamma})\cos(\dot{\gamma}s)\, d\dot{\gamma} \quad , \quad s>0 \qquad (4.2.90)$$

This equation can be used to determine G(s) for the following non-Newtonian viscosity models.

(i) Power Law: $\eta(\dot{\gamma}) = m|\dot{\gamma}|^{n-1}$, (4.2.91)

where m and n are material constants.

From (Bird et al[5]), $G(s) = \frac{2m}{\pi s^n}\cos(n\pi/2)\Gamma(n)$. (4.2.92)

(ii) Segalman: $$\eta(\dot\gamma) = \frac{\eta_0 \cos[(1-n)\tan^{-1}(\lambda_s\dot\gamma)}{[1+(\lambda_s\dot\gamma)^2]^{(1-n)/2}} \quad , \quad (4.2.93)$$

where η_0, λ_s, and n are material constants.

From (Bird et al [5]), $$G(s) = \left[\frac{\eta_0}{\lambda_s^{1-n}\Gamma(1-n)}\right]\frac{e^{-s/\lambda_s}}{s^n} \quad . \quad (4.2.94)$$

(iii) Carreau: $$\eta(\dot\gamma) = \frac{\eta_0}{[1+(\lambda\dot\gamma)^2]^{(1-n)/2}} \quad , \quad (4.2.95)$$

where η_0, λ, and n are material constants.

from (Bird et al [5]), $$G(s) = \left[\frac{2^{1+n/2}\eta_0}{\pi^{\frac{1}{2}}\lambda^{1-n/2}\Gamma((1-n)/2)}\right]\frac{K_{-n/2}(s/\lambda)}{s^{n/2}} \quad , \quad (4.2.96)$$

where $K_{-n/2}(s/\lambda)$ is a modified Bessel function.

(a). Mean shear stress reduction (E).

Before we discuss the three non-Newtonian viscosity models, it would be useful to determine the mean shear stress reduction as a function of non-dimensional quantities. We shall need to use the result from equation (4.2.72),

$$\frac{I_0(\dot\gamma_m+r\omega)}{I_0(\dot\gamma_m)} = \left[1+\frac{r\omega}{\dot\gamma_m}\right]\frac{\eta(\dot\gamma_m+r\omega)}{\eta(\dot\gamma_m)} \quad . \quad r=0,\pm1,\pm2,\ldots \quad (4.2.97)$$

(i). Power law model.

For the Power Law model (4.2.91), equation (4.2.97) takes the form

$$\frac{I_0(\dot\gamma_m+r\omega)}{I_0(\dot\gamma_m)} = \left[1+\frac{r\omega}{\dot\gamma_m}\right]\left|1+\frac{r\omega}{\dot\gamma_m}\right|^{n-1} \quad . \quad (4.2.98)$$

$r=0,\pm1,\pm2,\ldots$

The fractional reduction in mean shear stress is a function of $\dot\gamma_m/\omega$ and the power law index n. We note that if equation (4.2.98) is differentiated with respect to $\dot\gamma_m/\omega$, then the resulting function will contain singularities at integer values of $\dot\gamma_m/\omega$. Hence, the slope of the curve of E against $\dot\gamma_m/\omega$ will have an infinite slope for integer values of $\dot\gamma_m/\omega$.

(ii). Segalman model.

For the Segalman model (4.2.93), equation (4.2.98) takes the form

$$\frac{I_0(\dot\gamma_m+r\omega)}{I_0(\dot\gamma_m)} = \left[1 + \frac{r\omega}{\dot\gamma_m}\right]\left[\frac{1 + (\lambda_s\dot\gamma_m)^2}{1 + (\lambda_s\dot\gamma_m)^2(1+r\omega/\dot\gamma_m)^2}\right]^{(1-n)/2}$$

$$\times \frac{\cos[(1-n)\tan^{-1}(\lambda_s\dot\gamma_m(1+r\omega/\dot\gamma_m))]}{\cos[(1-n)\tan^{-1}(\lambda_s\dot\gamma_m)]} \quad . \qquad (4.2.99)$$

Hence, the fractional reduction in mean shear stress is a function of $\dot\gamma_m/\omega$, $\lambda_s\dot\gamma_m$ and n.

(iii) Carreau Model.

For the Carreau model (4.2.95), equation (4.2.98) takes the form

$$\frac{I_0(\dot\gamma_m+r\omega)}{I_0(\dot\gamma_m)} = \left[1 + \frac{r\omega}{\dot\gamma_m}\right]\left[\frac{1 + (\lambda\dot\gamma_m)^2(1+r\omega/\dot\gamma_m)^2}{1 + (\lambda\dot\gamma_m)^2}\right]^{(n-1)/2} . \qquad (4.2.100)$$

(b) Fundamental Stress Amplitude (σ_{a_1}).

It was noted in section (4.2.5) that the iterative scheme for evaluating A_1 was similar to that used for E. Therefore, we will concentrate our discussion on the evaluation of B_1 for different viscosity functions.

(i) Power Law Model.

For the Power Law model, the integral defined by equation (4.2.88), takes the form,

$$Q = \frac{2m}{\pi}\cos(n\pi/2)\Gamma(n)\int_0^\infty G(s)\sin((\dot\gamma_m+r\omega)s)\,ds \quad , \qquad (4.2.101)$$

From (Dwight [15]) we see that the integral defined by equation (4.2.101) is a standard integral of the form

$$\int_0^\infty \frac{1}{s^n}\sin(xs)\,ds = \frac{\pi x^{n-1}}{2\Gamma(n)\sin(n\pi/2)} \quad . \qquad (4.2.102)$$

Hence,

$$Q = m|\dot{\gamma}_m + r\omega|^{n-1}\cot(n\pi/2) \quad . \quad (4.2.103)$$

The fundamental stress amplitude and phase expressions for the power law model are therefore given analytically.

(ii). Segalman model.

For the Segalman model, the integral defined by equation (4.2.88), is given by

$$Q = \left[\frac{\eta_0}{\lambda_s^{1-n}\Gamma(1-n)}\right] \int_0^\infty \frac{e^{-s/\lambda_s}}{s^n} \sin((\dot{\gamma}_m+r\omega)s)\, ds \quad . \quad (4.2.104)$$

From (Dwight [15]) we see that the integral defined in equation (4.2.104) is a standard integral of the form

$$\int_0^\infty \frac{e^{-s/\lambda}}{s^n} \sin(xs)\, ds = \frac{\lambda^{1-n}\sin[(1-n)\tan^{-1}(\lambda x)]}{(1+(\lambda x)^2)^{(1-n)/2}} \quad . \quad (4.2.105)$$

Hence,

$$Q = \frac{\eta_0 \sin[(1-n)\tan^{-1}(\lambda(\dot{\gamma}_m+r\omega))]}{(1+\lambda_2(\dot{\gamma}_m+r\omega)^2)^{(1-n)/2}} \quad . \quad (4.2.106)$$

For the Segalman viscosity model, we have analytical expressions describing the the fundamental stress amplitude and the phase lag.

(iii) Carreau Model.

For the Carreau model, the integral defined by equation (4.2.88) is defined by

$$Q = \left[\frac{2^{1+n/2}\eta_0}{\pi^{\frac{1}{2}}\lambda^{1-n/2}\Gamma((1-n)/2)}\right] \int_0^\infty \frac{K_{-n/2}(s/\lambda)}{s^{n/2}} \sin((\dot{\gamma}_m+r\omega)s)\, ds \quad . \quad (4.2.107)$$

We are unable to solve (4.2.107) analytically. Hence, we do not have analytical expressions for the fundamental stress amplitude and phase lag produced in the fluid for the Carreau viscosity function. However, it is possible to evaluate these quantities numerically. The integral in equation (4.2.107) may be evaluated using a suitable numerical integration technique provided a small enough time step is chosen.

4.3. Inelastic model.

We now consider a model that gives the same viscosity behaviour as the Goddard-Miller model, but does not describe any elastic effects. By comparing theoretical predictions from both models, we can comment on the importance of elasticity in flow enhancement behaviour.

4.3.1. Mean shear stress for an inelastic fluid.

For an inelastic fluid, the shear stress is given by the generalised Newtonian model. i.e.

$$\sigma'_{\theta r}(t) = \dot{\gamma}_{\theta r}(t)\eta(\dot{\gamma}_{\theta r}(t)) \quad . \qquad (4.3.1)$$

Again we impose a combined steady and oscillatory shear rate of the form

$$\dot{\gamma}_{\theta r}(t) = \dot{\gamma}_m(1 + \epsilon\cos(\omega t)) \quad . \qquad (4.3.2)$$

The shear stress is a periodic function of period $2\pi/\omega$ and hence the mean shear stress σ_m is obtained from

$$\sigma_m = \frac{\omega}{2\pi}\int_0^{2\pi/\omega} \sigma_{\theta r}(t)\, dt \quad . \qquad (4.3.3)$$

Substituting equation (4.3.2) into (4.3.3) produces, using $u=\omega t$,

$$\sigma_m = \frac{\dot{\gamma}_m}{2\pi}\int_0^{2\pi}(1 + \epsilon\cos(u))\eta(\dot{\gamma}_m(1 + \epsilon\cos(u)))\, du \quad , \qquad (4.3.4)$$

The expression defined by equation (4.3.4), is independent of frequency as expected.

The fractional reduction in mean shear stress is obtained from equation (4.2.29)

$$E = 1 - \frac{1}{2\pi\eta(\dot{\gamma}_m)}\int_0^{2\pi}(1 + \epsilon\cos(u))\eta(\dot{\gamma}_m(1 + \epsilon\cos(u)))\, du \quad , \qquad (4.3.5)$$

We shall now derive the inelastic mean shear stress reduction for the three non-Newtonian viscosity models considered in this work

(i) Inelastic power law model.

For the power law model,

$$E = 1 - \frac{1}{2\pi}\int_0^{2\pi}(1 + \epsilon\cos(u))\left|1 + \epsilon\cos(u)\right|^{n-1} du \quad , \qquad (4.3.6)$$

The integrand is an even periodic function of period 2π. Hence,

$$E = 1 - \frac{1}{\pi}\int_0^{\pi}(1 + \epsilon\cos(u))\left|1 + \epsilon\cos(u)\right|^{n-1} du \quad , \qquad (4.3.7)$$

(ii) Inelastic Segalman model.

For the Segalman model,

$$E = 1 - \frac{1}{\pi}\int_0^{\pi}(1+\epsilon\cos(u))\left[\frac{1 + (\lambda_s\dot{\gamma}_m)^2}{1 + (\lambda_s\dot{\gamma}_m)^2(1+\epsilon\cos(u))^2}\right]^{(1-n)/2} \times \frac{\cos[(1-n)\tan^{-1}(\lambda_s\dot{\gamma}_m(1+\epsilon\cos(u)))]}{\cos[(1-n)\tan^{-1}(\lambda_s\dot{\gamma}_m)]}\, du \quad . \qquad (4.3.8)$$

(iii) Inelastic Carreau model.

For the Carreau model,

$$E = 1 - \frac{1}{\pi}\int_0^{\pi}(1 + \epsilon\cos(u))\left[\frac{1 + (\lambda\dot{\gamma}_m)^2}{1 + (\lambda\dot{\gamma}_m)^2(1 + \epsilon\cos(u))^2}\right]^{(1-n)/2} du \qquad (4.3.9)$$

The integrands in equations (4.3.7-9) inclusive are all well behaved and can be evaluated using suitable numerical techniques.

4.3.2. Fundamental stress amplitude.

For an inelastic fluid, we would expect the shear stress waveform to be in phase with the shear rate waveform. Hence the quantity B_1 in equation (4.2.35) is equal to zero.
Hence, by substituting equations (4.3.1-2) into equation (4.2.37) we obtain the following equation for the fundamental stress amplitude

$$\sigma_{a1} = \frac{2\dot{\gamma}_m}{\pi} \int_0^{\pi} (1 + \epsilon\cos(u))\ \eta(\dot{\gamma}_m(1 + \epsilon\cos(u)))\ \cos(u)\ du\ . \tag{4.3.10}$$

Normalising this quantity with respect to the mean shear stress σ_m, we obtain

$$\delta = \frac{2 \int_0^{\pi} (1 + \epsilon\cos(u))\ \eta(\dot{\gamma}_m(1 + \epsilon\cos(u)))\ \cos(u)\ du}{\int_0^{\pi} (1 + \epsilon\cos(u))\ \eta(\dot{\gamma}_m(1 + \epsilon\cos(u)))\ du} \tag{4.3.11}$$

The viscosity functions for the power law, Segalman, Carreau models may be substituted into the equation (4.3.11) to obtain the normalised shear stress amplitude by numerical integration.

4.4. Theoretical results and discussion.

In this section, we investigate the reduction of mean shear stress, predicted by the Goddard-Miller model and the generalised Newtonian model, due to the imposition of a sinusoidal shear rate on to a unidirectional steady shear flow. By comparing the predictions of these two models, we are able to comment upon the importance of elasticity in this flow situation. Theoretical curves are generated for three different viscosity functions as described by the power law, Carreau, and Segalman models.

We start this discussion by considering the mean shear stress reduction predicted by the power law viscosity model. This is an important region of the viscosity curve for us to examine because the shear viscosity behaviour of many elastico-viscous fluids can be accurately described, over a wide shear rate range, by a power law model. Figures (4.1) to (4.5) inclusive, show the variation of mean shear stress reduction against the non-dimensional quantity $\dot{\gamma}_m/\omega$ for ϵ values from 0.2 to 2.0. In each of these figures the mean shear

stress reduction is determined for the three values of the power law index, n = 0.3, 0.6, and 0.9.

An important difference between the inelastic and viscoelastic models is that the inelastic power law model predicts that mean shear stress reduction is independent of $\dot{\gamma}_m/\omega$ for all ϵ. All of the figures (4.1) to (4.5) show that as $\dot{\gamma}_m/\omega$ increases, the viscoelastic mean shear stress reduction curves tend towards the constant inelastic value as expected. We note in figures (4.1) and (4.2), that the inelastic mean shear stress reduction for n equal to 0.6 is greater than n equal to 0.3. This result is to be expected, since for small ϵ the inelastic mean shear stress reduction is given by $\epsilon^2 n(1-n)/4$ which has a maximum value at n = 0.5 (Davies et al [10].

We would expect elastic effects to have an important influence on mean shear stress reduction in the region of low $\dot{\gamma}_m/\omega$. In figures (4.1) to (4.5), we observe large differences between the viscoelastic and inelastic predictions in this part of the curve for n equal to 0.3 and for n equal to 0.6. We note that the differences between the two predictions are not very large for n equal to 0.9. This is an expected result because as n approaches unity the flow situation tends to the Newtonian case. It is interesting to note that in the region of $\dot{\gamma}_m/\omega < 1$, the difference between the viscoelastic and inelastic predictions of mean shear stress reduction, decreases as ϵ is increased for a fixed value of n.

Figure (4.1) shows that for small ϵ ($\epsilon = 0.2$), the mean shear stress reduction for the viscoelastic model increases with increasing $\dot{\gamma}_m/\omega$ to a maximum value which occurs just before $\dot{\gamma}_m/\omega$ equal to 1.0. These curves then decrease rapidly towards the constant inelastic prediction. Similar behaviour to this has been observed by other workers (Davies et al [10], Barnes et al [2] and, Phan-Thien and Dudek [36]).

For a fixed value of $\dot{\gamma}_m/\omega$ we see by comparing figures (4.1) to (4.5) that the mean shear stress reduction increases with increasing ϵ. However, if we take ϵ to be constant, then we see that the viscoelastic mean shear stress reduction curves oscillate with a frequency of $\dot{\gamma}_m/\omega$ equal to 1. The amplitude of oscillation decreases as the viscoelastic curves tend to the inelastic prediction. A resonance effect appears to occur at ϵ equal to 1.0. A consequence of this oscillating behaviour, is that the Goddard-Miller model predicts that reduction in mean shear stress may either increase or

decrease with increasing $\dot{\gamma}_m/\omega$. The inelastic model predicts that the reduction in mean shear stress is independent of $\dot{\gamma}_m/\omega$.

In figure (4.5), we note the irregular shape of the viscoelastic mean shear stress reduction curve for ϵ equal to 2, n equal to 0.3. In order to check that the behaviour of this curve is not due to any numerical rounding error, the computer program used was run in both double and quadruple precision.

Let us now consider the reduction in mean shear stress predicted by the Carreau viscosity function. This viscosity model is capable of describing realistic shear viscosity behaviour over a wider shear rate range than the power law model. Another advantage of using this viscosity function in conjunction with the Goddard-Miller model, is that the resulting expression describing mean shear stress reduction (see equation (4.2.100)), does not possess an infinite gradient at integer values of $\dot{\gamma}_m/\omega$.

Figures (4.6) to (4.11) inclusive, examine the effect on mean shear stress reduction of varying $\lambda\omega$, the power law index n, and ϵ for both elastic and inelastic models. In figures (4.6) and (4.7) we vary $\lambda\omega$ from 1.0 to 10.0 for a power law index of 0.3. The values of ϵ considered are 0.8 and 1.2 respectively. This value of the power law index was chosen because it represents a highly shear thinning behaviour. For each value of $\lambda\omega$, the horizontal axis effectively represents a range of $\lambda\dot{\gamma}_m$. e.g. for $\lambda\omega$ equal to 1, $\lambda\dot{\gamma}_m$ takes on values from 0 to 12, whereas for $\lambda\omega$ equal to 10, $\lambda\dot{\gamma}_m$ ranges from 0 to 120. We would therefore expect the Carreau mean shear stress reduction predictions to tend to the power law predictions as $\lambda\omega$ increases. This is clearly shown in figures (4.6) and (4.7).

The mean shear stress reduction shown in figures (4.8) to (4.11) inclusive, is in agreement with the power law mean shear stress reduction curves presented in figures (4.1) to (4.5) except at low values of $\dot{\gamma}_m/\omega$. This is to be expected because the Carreau and the power law viscosity functions are different at low shear rates. For instance, at low $\dot{\gamma}_m/\omega$ the inelastic mean shear stress reduction behaviour predicted by the Carreau model is not constant. However, as $\dot{\gamma}_m/\omega$ increases both the viscoelastic and the inelastic mean shear stress reduction curves from the Carreau model tend to the power law predictions as expected.

In addition to the Carreau and the power law viscosity models, theoretical mean shear stress reduction expressions were also derived

for the Segalman model. Figure (4.12) compares the viscoelastic mean shear stress reduction for each of three viscosity functions discussed in this chapter. Similarly, figure (4.13) compares the inelastic mean shear stress reduction for the same three viscosity functions. It is clear from these two figures that the reduction in mean shear stress is sensitive to the shape of the shear viscosity function.

4.5 Comments.

The flow problem analysed in this chapter was one in which a fluid was subjected to a unidirectional combined steady and oscillatory shear flow. The main interest in this analysis was the derivation of theoretical expressions describing the reduction in the mean shear stress produced by the sinusoidal fluctuation of the shear rate about a non-zero mean. The viscoelastic constitutive equation was supplied by the Goddard-Miller model which is able to describe large deformations. Consequently we were able to carry out a theoretical investigation into mean shear stress reduction for situations where the oscillatory shear component was large compared to the mean shear flow (ϵ).

The theoretical work described above, provided an analytical technique for determining the effect of a large oscillatory shear component on the mean shear flow properties of an elastico-viscous fluid. Similar analytical methods were derived for evaluating the fundamental oscillatory shear stress amplitude, and the phase. However, it should be noted that the fundamental oscillatory shear stress amplitude and phase must be evaluated numerically if the shear viscosity is described by a Carreau model.

Mean shear stress reduction predictions observed for small values of ϵ showed similar behaviour to that obtained by previous workers (Davies et al [10], Barnes et al [2] and, Phan-Thien and Dudek [36]). Townsend [39], used a four constant Oldroyd model to consider the situation of large ϵ for the pulsatile pipe flow problem. This work predicted that the variation of flow enhancement against mean pressure gradient for a fixed value of frequency and ϵ (ϵ=1), does show a peak in the value of the flow enhancement. However, the Townsend results do not show the oscillating behaviour exhibited by the Goddard-Miller model in the current investigation.

It is difficult to make a qualitative comparison between these two sets of results, because the Goddard-Miller model and the Oldroyd four constant model do not predict the same shear viscosity behaviour. It has been previously demonstrated that combined steady and oscillatory shear flow behaviour is sensitive to the shape of the shear viscosity function (Davies et al [10], Phan-Thien and Dudek [36]), Jones and Walters [22].

In Chapter 5, an experimental programme is carried out on a controlled stress rheometer to investigate large ϵ, mean shear stress reduction behaviour for a 2% solution of polyisobutylene in dekalin. The experimental results from the programme will be compared with viscoelastic and inelastic predictions of mean shear stress reduction obtained from the analysis developed in this chapter.

Chapter 5

Combined Steady and Oscillatory Shear Experiments

5.1 Introduction.

Previous workers (Barnes et al [2], Phan-Thien and Dudek [36]), have carried out combined steady and oscillatory shear experiments for small amplitudes of oscillation. These results were then compared with viscoelastic theories using a perturbation analysis for small amplitudes of oscillation. A problem that is encountered with making this small amplitude comparison, is that the experimental data is subject to a degree of experimental scatter, and hence, quantatative agreement between experiment and theory may be difficult to obtain. This chapter will be concerned with making a comparison between theory and experiment for large oscillatory shear amplitudes. Recent developments in the controlled stress rheometer (Davies et al [12]), have enabled combined steady and oscillatory shear experiments to be carried out at large amplitudes of oscillation.

In this chapter, a Carri-Med controlled stress rheometer (CS100L) is used to superimpose an oscillatory shear strain on to the steady shear flow of an elastico-viscous fluid.

5.2. Experimental procedure and results.

The controlled stress rheometer was operated throughout each experiment by an Opus V microcomputer via an IEEE interface. Computer software was used to modify the couple waveform so that a combined steady and oscillatory couple could be applied to the rotor platen. The subsequent displacement of this platen was measured using an optical encoder measuring system. The experiments were carried out at a constant temperature of 23 $^{\circ}$C using both a narrow gap concentric cylinder geometry (r_i=18.5 mm, r_o=20.75 mm, cylinder height=5 cm; fig (3.6)), and a cone and plate geometry (gap angle=1°, radius=2cm; fig (3.4)). The test sample for this programme of experiments was a 2% solution of polyisobutylene in dekalin. This fluid exhibits both shear thinning and elastic properties.

The analysis developed in Chapter 4 was based on a controlled

shear rate theory. However, the experiments were carried out on a controlled stress instrument. Therefore, in order for us to make a comparison between theory and experiment, it was necessary to incorperate a 'feed back loop' into the computer software so that the rheometer behaved as a controlled strain instrument. In order to determine the mean shear stress reduction for each experimental run, a steady shear test was initially performed, followed by a combined steady and oscillatory experiment. The computer software ensured that the required mean shear rate in both cases was the same.

The theory in Chapter 4, requires the knowledge of model parameters n, for the power law model, and n and λ, for the Carreau model. These parameters were obtained by fitting the viscosity functions of these models to the experimental shear viscosity data, as presented in figure (5.1). For the viscosity data shown in this figure, $n = 0.35$, and $\lambda = 4.5\ s^{-1}$. There is a slight discrepancy between the Carreau model viscosity function and the experimental viscosity data at low shear rates. However, most of the combined steady and oscillatory experiments were carried out at mean shear rates in the power law region. Hence, this discrepancy should not affect the mean shear stress predictions.

In figure (5.1), we also present dynamic viscosity for a 2% solution of polyisobutylene in dekalin. It should be noted that the Goddard-Miller model, used in Chapter 4, predicts that the shear viscosity function plotted against shear rate, should be coincident with the dynamic viscosity function plotted against angular frequency. Clearly, this is not the case for a 2% solution of polyisobutylene in dekalin. Interestingly, there is almost a perfect match between the shear viscosity and the magnitude of the complex viscosity, as shown in figure (5.1), which has also been found to be the case for some other materials (Zahorski [48], Bird et al [5]).

In figures (5.2) to (5.6) inclusive, we show mean shear stress reduction curves for the polyisobutylene solution for various values of ϵ (ratio of the oscillatory shear rate amplitude to the mean shear rate). An important feature of the experimental data presented in these figures is the lack of experimental scatter. This figure also shows that for large oscillatory shear rate amplitudes, large mean shear stress reductions are obtained (>50% in some cases).

The mean shear stress reduction data presented in figures (5.2) to (5.4) inclusive, was obtained using a narrow gap concentric cylinder geometry and shows the variation of mean shear stress reduction with the non-dimensional parameter $\dot{\gamma}_m/\omega$. The range of $\dot{\gamma}_m/\omega$ considered, was governed by the limitations of the instrument for the particular geometry concerned. In each experimental run, both the angular frequency and ϵ were held constant. The experiments were repeated for different values of ϵ. Figures (5.2-4) all show that, under these conditions, the magnitude of the mean shear stress reduction increases monotonically with increasing mean shear rate and oscillatory shear rate amplitude. For the experimental mean shear stress reduction data shown in these figures, we see that the effect of increasing ϵ for a constant value of $\dot{\gamma}_m/\omega$ is to increase the mean shear stress reduction effect. The theoretical predictions in figures (5.2-4) will be discussed in section (5.3).

In figures (5.5) and (5.6), the measurement system used is that of a 1° gap angle cone and plate set-up. The mechanical inertia of the cone and plate system is less than that for the concentric cylinder system. There is also less surface contact with the fluid. Hence, the cone and plate system, enables an extended range of $\dot{\gamma}_m/\omega$ to be considered. These experimental curves again show that mean shear stress reduction increases monotonically with increasing $\dot{\gamma}_m/\omega$ as ω and ϵ are held constant.

The viscoelastic power law theory, developed in Chapter 4, predicts that the mean shear stress reduction should only be a function of the power law index n, $\dot{\gamma}_m/\omega$, and ϵ. Since, both ϵ and n are held constant for figures (5.5-6), the reduction in mean shear stress predicted by these experiments, should be a function of $\dot{\gamma}_m/\omega$ only. This prediction is supported by the experimental data shown in figures (5.5-6). The frequency of oscillation for the experimental results shown in figure (5.5) was 2 Hz and was reduced to 1 Hz for the experiments carried out in figure (5.6). If we compare the experimental mean shear stress reductions obtained for $\dot{\gamma}_m/\omega \triangleq 4$, and $\dot{\gamma}_m/\omega \triangleq 9$, we see that

($\dot{\gamma}_m/\omega \triangleq 4$; [E(freq=2 Hz) = 0.375 , E(freq=1 Hz) = 0.388]
$\dot{\gamma}_m/\omega \triangleq 9$; [E(freq=2 Hz) = 0.462 , E(freq=1 Hz) = 0.473].)

This result confirms that the experiments were carried out in the power law region.

Also shown in figure (5.5), is experimental data taken from a controlled stress rheometer by Davies et al [12]. The frequency of oscillation in the Davies et al data was 4 Hz. We can see that good agreement is obtained between the two sets of data when plotted against $\dot{\gamma}_m/\omega$. The Davies et al data mean shear stress reduction data contained some experimental scatter. This was probably due to the inaccuracy of the snail cam device used to measure the angular displacement.

5.3. Theoretical Comparison.

The theoretical expressions derived in Chapter 4 (equations (4.2.74) and (4.3.9)), in conjunction with a Carreau viscosity function (4.2.95), were used to generate viscoelastic and inelastic mean shear stress reduction curves for the figures (5.2-7).

We begin by considering the variation of mean shear stress reduction with $\dot{\gamma}_m/\omega$ in figures (5.2-6). The angular frequency ω, and the ratio ϵ, are both held constant. For low values of $\dot{\gamma}_m/\omega$, we would expect elastic effects to play an important role in determining the combined steady and oscillatory flow behaviour of the fluid. However, as $\dot{\gamma}_m/\omega$ is increased, the importance of elasticity in determining flow behaviour should diminish. This prediction is consistent with the behaviour of the viscoelastic and inelastic curves presented in these figures, in that the viscoelastic curve tends to the inelastic curve as expected.

For each of the figures (5.2-6), discrepancies are observed between the experimental mean shear stress reduction data and both the viscoelastic and inelastic theoretical curves. The experimental mean shear stress reduction data increases monotonically with increasing $\dot{\gamma}_m/\omega$, and does not display any of the oscillating behaviour of the viscoelastic model. This oscillating behaviour appears to be an artifact of the Goddard-Miller model and is unlikely to arise in more realistic viscoelastic models. Even though the Goddard-Miller model has not given agreement with experimental behaviour at low values of $\dot{\gamma}_m/\omega$, we would expect the model to give reasonable predictions of experimental data at large values of $\dot{\gamma}_m/\omega$. The reason being that all viscoelastic models must tend to the inelastic model as the frequency of oscillation tends to zero. However some discrepancies still occur between theory and experiment

at large values of $\dot{\gamma}_m/\omega$. We therefore conclude that the theoretical discrepancy is not entirely due to the viscoelastic model used.

A possible reason for the discrepancies discussed, is that the theory was based on the assumption that the oscillatory component of the shear rate waveform was sinusoidal. In our experiments on the controlled stress rheometer, the shear waveform was observed to be non-sinusoidal (see figure (5.9)). This is to be expected for non-Newtonian fluids.

It is not a simple matter to use the Goddard-Miller viscoelastic model to determine the mean shear rate enhancement for a combined steady and oscillatory shear stress situation. However, we are able to examine this flow problem for the inelastic model. Since the experiments were carried out at mean shear rates which were in the power law region, a power law viscosity function was considered. This analysis is presented in section (5.4). The corrected inelastic predictions for the controlled stress situation are shown in figures (5.2-7).

The cone and plate mean shear stress reduction results from the inelastic controlled stress analysis, in figure (5.6), appear to show an improved prediction of the experimental data at large $\dot{\gamma}_m/\omega$. In figure (5.6), the experimental data does appear to be tending to the inelastic correction as $\dot{\gamma}_m/\omega$ is increased. However, in the results for the concentric cylinder, in figures (5.2-4), it is difficult to see whether an improvement in the discrepancy between theory and experiment has been made, since the range of $\dot{\gamma}_m/\omega$ is restricted.

In figure (5.7), we consider the variation of mean shear stress reduction with ϵ, for a fixed value of $\dot{\gamma}_m/\omega$ and ω ($\dot{\gamma}_m/\omega$=1.0). Again, we observe differences between the inelastic and viscoelastic curves, and the experimental data. However, it should be pointed out that the viscoelastic model does qualitatively predict the correct behaviour regarding the variation of mean shear stress reduction with ϵ. The differences between the inelastic model and the experimental data were to be expected for the low value of $\dot{\gamma}_m/\omega$ considered in this experiment.

In figure (5.8) we consider the variation of the inelastic mean shear stress reduction with ϵ for the controlled stress and the controlled strain analysis. The theoretical predictions from these

two theories are compared with the small ϵ mean shear stress reduction predicted by an inelastic power law model (Davies et al [10]). The mean shear stress reduction predicted by the three models are in agreement at values of $\epsilon \leq 1.0$, as expected. However, there are clear differences between the controlled stress and controlled strain analysis for values of $\epsilon > 1.0$. Therefore, our assumption of a sinusoidal oscillatory component of the shear rate, was subject to error and must be taken into account in the theory. We would expect to have a similar type of error for the viscoelastic theory

5.4. Comparison between controlled stress and controlled strain inelastic analyses.

Most of the experimental work in this chapter, was carried out at mean shear rates, which were in the power law region of the shear viscosity curve of a 2% solution of polyisobutylene in dekalin. We therefore use a power law viscosity function to describe the shear viscosity behaviour of the inelastic model considered in this section. For an inelastic power law fluid, the relationship between shear stress and shear rate is given by the generalised Newtonian model as,

$$\sigma = m\dot{\gamma}|\dot{\gamma}|^{n-1} \quad . \tag{5.4.1}$$

Hence, the shear rate may be expressed in terms of the shear stress by

$$\dot{\gamma} = m^{-\frac{1}{n}} \sigma|\sigma|^{\frac{1}{n}-1} \quad . \tag{5.4.2}$$

We begin by considering an inelastic controlled strain analysis for the combined steady and oscillatory shear flow problem outlined in this work. From equation (4.3.7), we see that if the shear rate in the fluid is assumed to be of the form,

$$\dot{\gamma} = \dot{\gamma}_m(1 + \epsilon\cos(\omega t)) \quad , \tag{5.4.3}$$

where ϵ is the ratio between the amplitude $\dot{\gamma}_{a_1}$ of the oscillatory component of the shear rate, and the mean shear rate $\dot{\gamma}_m$, then the inelastic power law model, gives the following expression for the

mean shear stress reduction E.

$$E = 1 - \frac{\omega}{\pi} \int_0^{\pi/\omega} (1 + \epsilon\cos(\omega t)) \left|1 + \epsilon\cos(\omega t)\right|^{n-1} dt \quad . \qquad (5.4.4)$$

However, the experimental flow situation considered in this work, is one in which the stress is the controlled variable. A shear stress is applied to the fluid of the form

$$\sigma = \sigma_m (1 + \delta \cos(\omega t)) \quad . \qquad (5.4.5)$$

where δ is the ratio between ampliude σ_{a1}, of the oscillatory component of the shear stress, and the mean shear stress σ_m.

$$\delta = \frac{\sigma_{a1}}{\sigma_m} \quad . \qquad (5.4.6)$$

The shear rate produced in the fluid will now be non-sinusoidal. i.e.

$$\dot{\gamma} = \dot{\gamma}_m + \sum_{i=1}^{\infty} \dot{\gamma}_{ai} \cos(\omega t) \quad . \qquad (5.4.7)$$

The mean shear rate $\dot{\gamma}_m$ and the fundamental oscillatory shear rate ammpliude $\dot{\gamma}_m$ may be obtained via a Fourier series analysis, as follows

$$\dot{\gamma}_m = \frac{\omega}{\pi} \left[\frac{\sigma_m}{m}\right]^{\frac{1}{n}} \int_0^{\pi/\omega} (1 + \delta\cos(\omega t)) \left|1 + \delta\cos(\omega t)\right|^{\frac{1}{n} - 1} dt \ , \qquad (5.4.8)$$

and

$$\dot{\gamma}_{a1} = \frac{\omega}{2\pi} \left[\frac{\sigma_m}{m}\right]^{\frac{1}{n}} \int_0^{\pi/\omega} (1 + \delta\cos(\omega t)) \left|1 + \delta\cos(\omega t)\right|^{\frac{1}{n} - 1} \cos(\omega t)\, dt \ . \qquad (5.4.9)$$

The inelastic controlled stress prediction of mean shear stress reduction E, is subsequently obtained from the equation

$$E = 1 - \frac{\sigma_m}{\sigma_s} \quad , \qquad (5.4.10)$$

where σ_s is given by the inelastic power law model.

$$\sigma_s = m \dot{\gamma}_m \left|\dot{\gamma}_m\right|^{n-1} \quad . \qquad (5.4.11)$$

Due to the presence of second and higher order terms in the shear rate waveform (5.4.7), the mean shear stress predicted in equation (5.4.11) for the controlled stress analysis, will differ from the prediction of mean shear stress reduction obtained from the controlled strain analysis in equation (5.4.4)

5.5. Comments.

In this chapter, we have presented experimental mean shear stress reduction data obtained from a Carri-Med controlled stress rheometer. These combined steady and oscillatory shear experiments were carried out for large oscillatory shear amplitudes, (ϵ>1). It is important to point out the lack of experimental scatter in the mean shear stress reduction data. This should facilitate any future comparison between theoretical and experimental predictions for mean shear stress reduction. It should also be noted that large reductions in the mean shear stress were observed for large oscillatory shear amplitudes. In figure (5.5), it was shown that good agreement is obtained between the current mean shear stress reduction data and the data of Davies et al [12].

The viscoelastic model qualitatively predicts the correct trend regarding the variation of mean shear stress reduction with ϵ. However, large discrepancies were observed between the experimental and theoretical predictions for the variation of mean shear stress reduction with both ϵ and $\dot{\gamma}_m/\omega$. The viscoelastic analysis assumes that the shear rate waveform is sinusoidal. Figure (5.9) clearly shows that this assumption is incorrect. This result is to be expected, since polyisobutylene is a non-Newtonian fluid. However, if we consider the corrected inelastic prediction for mean shear stress reduction, we see that the inclusion of second and higher harmonics in the shear rate waveform does not adequately describe the discrepancies between the experimental and theoretical predictions. We would expect any corrected viscoelastic curves to tend to the inelastic curves as $\dot{\gamma}_m/\omega$ is increased. Clearly, the experimental mean shear stress reduction data would have to start decreasing with increasing $\dot{\gamma}_m/\omega$ if the experimental data is to coincide with the corrected inelastic prediction at high values of $\dot{\gamma}_m/\omega$. We have no evidence to support this type of behaviour. It is true that mechanical inertia effects were ignored in the development of the

corrected inelastic theory. However, the experimental data presented in figures (5.5) and (5.6) suggested that mechanical inertia effects were not significant for this programme of experiments.

The Goddard-Miller model is not able to adequately describe the combined steady and oscillatory shear flow behaviour of elastico-viscous fluids. The model is capable of describing realistic shear viscosity behaviour or realistic dynamic viscosity behaviour, but is unable to describe both behaviours simultaneously. This may be an important consideration for the accurate modelling of combined steady and oscillatory flow behaviour.

Chapter 6

Fluid Inertia Effects in Controlled Stress Oscillation (Theory).

6.1. Introduction.

This chapter is concerned with the effect of fluid inertia on experimental oscillatory shear data taken from a controlled stress rheometer. A linear viscoelastic theory has been developed which includes the effect of fluid inertia for the parallel plate, cone and plate, concentric cylinder, and double concentric cylinder geometries. The time dependent behaviour of a material undergoing a linear viscoelastic deformation may be characterised by the complex viscosity function η^*. Small amplitude oscillatory shear experiments were first performed on applied strain rheometers such as the Weissenberg rheogoniometer. Many workers, Maude and Walters [26], Oldroyd [30], Walters [41], Walters and Kemp [43], Nally [28], and Markovitz [25], have studied the effect of fluid inertia on oscillatory shear data taken from this instrument. This topic is comprehensively covered by Walters in Rheometry [45].

It was first shown that the controlled stress rheometer could be operated in an oscillatory stress mode by Jones et al [24]. These workers developed a linear viscoelastic theory for the cone and plate geometry which excluded the effect of fluid inertia. Fluid inertia effects were first considered by Holder [20] and by Jones et al [24]. The former, working on a Deer rheometer, developed a linear viscoelastic theory for the cone and plate and parallel plate geometries. This theory included a first order fluid inertia correction for the cone and plate geometry, and an exact fluid inertia correction for the parallel plate geometry. However, due to problems of electromagnetic inertia in the induction motor used to drive the Deer rheometer, Holder was unable to verify these theoretical expressions with experimental results. Jones et al [24] developed first order fluid inertia corrections for the parallel plate, cone and plate, and concentric cylinder geometries. An experimental program was carried out using a Carri-Med controlled stress rheometer on a highly elastic fluid and a slightly elastic fluid. Their results indicated that over a frequency range of 0-10 Hz, fluid inertia effects were small for the cone and plate and

parallel plate geometries when testing a 2% solution of polyacrylamide in water. It was also shown that fluid inertia effects should be taken into account in the concentric cylinder geometry especially for high density mobile fluids.

The aim of present work is to consider the effect of fluid inertia on dynamic data obtained from the Carri-Med controlled stress rheometer. This chapter will concentrate on developing a linear viscoelastic theory capable of interpreting experimental data over a wide frequency range. The theory will assume that the fluid under consideration is incompressible. For each geometry, the equations of motion will be solved exactly using a numerical technique. The perturbation solution to the equations of motion will be extended to second order accuracy.

6.2. Parallel plate.

6.2.1. Governing equations.

All physical quantities are referred to cylindrical polar coordinates (r,θ,z). The parallel plate geometry is defined by two coaxial horizontal flat plates of radius a, separated by a vertical distance h as shown in fig (3.5). An oscillatory couple is applied to the top platen forcing it to make small amplitude angular oscillations of amplitude X_0 and frequency ω about the z-axis. The bottom platen remains stationary. The generalised linear equation of state for elastico-viscous liquids,

$$\sigma_{ij} = \eta^*\dot{\gamma}_{ij} - pg_{ij} \quad , \tag{6.2.1}$$

will be used, where σ_{ij} is the stress tensor, $\dot{\gamma}_{ij}$ is the rate of strain tensor, g_{ij} is the metric tensor, and p is the isotropic pressure.

The complex viscosity η^* is defined by (2.2.15) to be,

$$\eta^* \equiv \eta' - iG'/\omega \quad . \tag{6.2.2}$$

Following the analysis of previous workers, Walters and Kemp [43], Holder [20], and Jones et al [24], the non-zero physical velocity component is assumed to be,

$$V_{(\theta)} = rF(z)e^{i\omega t} \quad , \tag{6.2.3}$$

which identically satisfies the equation of continuity for incompressible fluids (equation (2.1.4). This velocity profile gives rise to one non-zero component of the rate-of-strain tensor (Bird et al [5],

$$\dot{\gamma}_{\theta z} = r \frac{dF(z)}{dz} e^{i\omega t} \quad . \tag{6.2.4}$$

which can be used in equation (6.2.1) to determine the θz-component of the stress tensor. i.e.

$$\sigma_{\theta z} = r \frac{dF(z)}{dz} \eta^* e^{i\omega t} \quad . \tag{6.2.5}$$

Substituting (6.2.3) and (6.2.5) into the relevant equation of motion (2.1.2),

$$\rho\left[\frac{\partial v_\theta}{\partial t} + v_r \frac{\partial v_\theta}{\partial r} + \frac{v_\theta}{r} \frac{\partial v_\theta}{\partial \theta} + v_z \frac{\partial v_\theta}{\partial z} + \frac{v_r v_\theta}{r} \right]$$

$$= \frac{1}{r^2} \frac{\partial}{\partial r}\left[r^2 \sigma_{\theta r}\right] + \frac{1}{r} \frac{\partial}{\partial \theta} \sigma_{\theta\theta} + \frac{\partial}{\partial z} \sigma_{\theta z} - \frac{1}{r} \frac{\partial p}{\partial \theta} \quad , \tag{6.2.6}$$

we obtain the second order ordinary differential equation,

$$\frac{d^2F(z)}{dz^2} + \alpha^2 F(z) = 0 \quad , \tag{6.2.7}$$

which must be solved subject to the boundary conditions,

$$F(h) = i\omega X_0 \quad , \tag{6.2.8}$$

$$F(0) = 0 \quad . \tag{6.2.9}$$

The complex parameter α^2 defined by Walters[45],

$$\alpha^2 = \frac{-i\omega\rho}{\eta^*} \quad , \tag{6.2.10}$$

governs the magnitude of fluid inertia effects, where ρ is the liquid density. The solution to (6.2.7) subject to the boundary conditions (6.2.8) and (6.2.9) is given by,

$$F(z) = \frac{i\omega X_0 \sin(\alpha z)}{\sin(\alpha h)} \quad . \tag{6.2.11}$$

The equation of motion of the top platen is

$$C - C_F = I\ddot{X} \quad , \tag{6.2.12}$$

where C is the applied couple, C_F is the couple acting on the top platen due to the motion of the fluid, I is the moment of inertia of the top platen, and $\ddot{X}$ is the angular acceleration.

The applied couple may be written as,

$$C = C_0 e^{i(\omega t+c)} \quad , \tag{6.2.13}$$

where C_0 is the amplitude, and c phase lag of the motion of the top platen behind the input couple.

The angular deformation X of the parallel plate resulting from a sinusoidal applied couple C can be expressed as

$$X = X_0 e^{i\omega t} \quad . \tag{6.2.14}$$

Hence the angular acceleration of the top platen is given by,

$$\ddot{X} = -\omega^2 X_0 e^{i\omega t} \quad . \tag{6.2.15}$$

The couple exerted on the top platen due to the motion of the fluid is

$$C_F = 2\pi \int_0^a r^2 \sigma_{\theta z}|_{z=h} dr \quad , \tag{6.2.16}$$

where the θz-component of the stress tensor is obtained by substituting (6.2.11) into (6.2.5). C_F is therefore given by,

$$C_F = \frac{i\omega\pi a^4 X_0 \alpha \cot(\alpha h)\eta^* e^{i\omega t}}{2} \quad . \tag{6.2.17}$$

We may express the equation of motion of the top platen as,

$$\eta^* C(\alpha^2) = C_0 e^{ic} + I\omega^2 X_0 \quad , \tag{6.2.18}$$

where,

$$C(\alpha^2) = \frac{i\omega\pi a^4 X_0 \alpha \cot(\alpha h)}{2} \quad . \tag{6.2.19}$$

The complex viscosity η^* can now be determined by solving equation (6.2.18) in conjunction with equation (6.2.19). These equations are able to interpret the full effect of fluid inertia on the complex viscosity function and must be solved numerically. A computer algorithm based on a rapidly convergent iterative scheme has been written for this purpose. However, for some flow situations fluid inertia effects are small. Hence a perturbation technique may be used to solve these equations analytically.

6.2.2. Perturbation method of solution.

Consider equation (6.2.19) which defines the complex trancendental function $C(\alpha^2)$. The function $(\alpha h)\cot(\alpha h)$ may be expanded in powers of $(\alpha h)^2$ terms, and hence,

$$C(\alpha^2) = \frac{i\omega\pi a^4 X_0}{2h}\left[1 - \frac{(\alpha h)^2}{3} - \frac{(\alpha h)^4}{45} \right] \quad . \qquad (6.2.20)$$

where terms of order $(\alpha h)^6$ and higher order terms have been ignored. Similarly the complex viscosity function η^* may be expanded in the following form,

$$\eta^* = \eta_0^* + (\alpha h)^2\eta_1^* + (\alpha h)^4\eta_2^* \quad . \qquad (6.2.21)$$

However, from (6.2.10) we see that the non-dimensional fluid inertia parameter $(\alpha h)^2$ is a function of η^*. In particular,

$$(\alpha h)^2 = \frac{-i\omega\rho h^2}{\eta^*} \quad . \qquad (6.2.22)$$

If we define $(\alpha_0 h)^2$ to be

$$(\alpha_0 h)^2 = \frac{-i\omega\rho h^2}{\eta_0^*} \quad , \qquad (6.2.23)$$

then it can easily be shown by substituting (6.2.21) into (6.2.22) that $(\alpha h)^2$ may be expanded in terms of $(\alpha_0 h)^2$, as follows

$$(\alpha h)^2 \triangleq (\alpha_0 h)^2 - (\alpha_0 h)^4\eta_1^*/\eta_0^* \quad , \qquad (6.2.24)$$

and

$$(\alpha h)^4 \triangleq (\alpha_0 h)^4 \quad . \qquad (6.2.25)$$

where terms of order $(\alpha_0 h)^6$ have been ignored. Consequently the expansions given by (6.2.20-21) become,

$$C(\alpha_0^2) \triangleq \frac{i\omega\pi a^4 X_0}{2h}\left[1 - \frac{(\alpha_0 h)^2}{3} - (\alpha_0 h)^4\left[\frac{1}{45} - \frac{\eta_1^*}{3\eta_0^*}\right]\right] \quad , \qquad (6.2.26)$$

and

$$\eta^* \triangleq \eta_0^* + (\alpha_0 h)^2\eta_1^* + (\alpha_0 h)^4(\eta_2^* - \eta_1^{*2}/\eta_0^*) \quad , \qquad (6.2.27)$$

respectively.

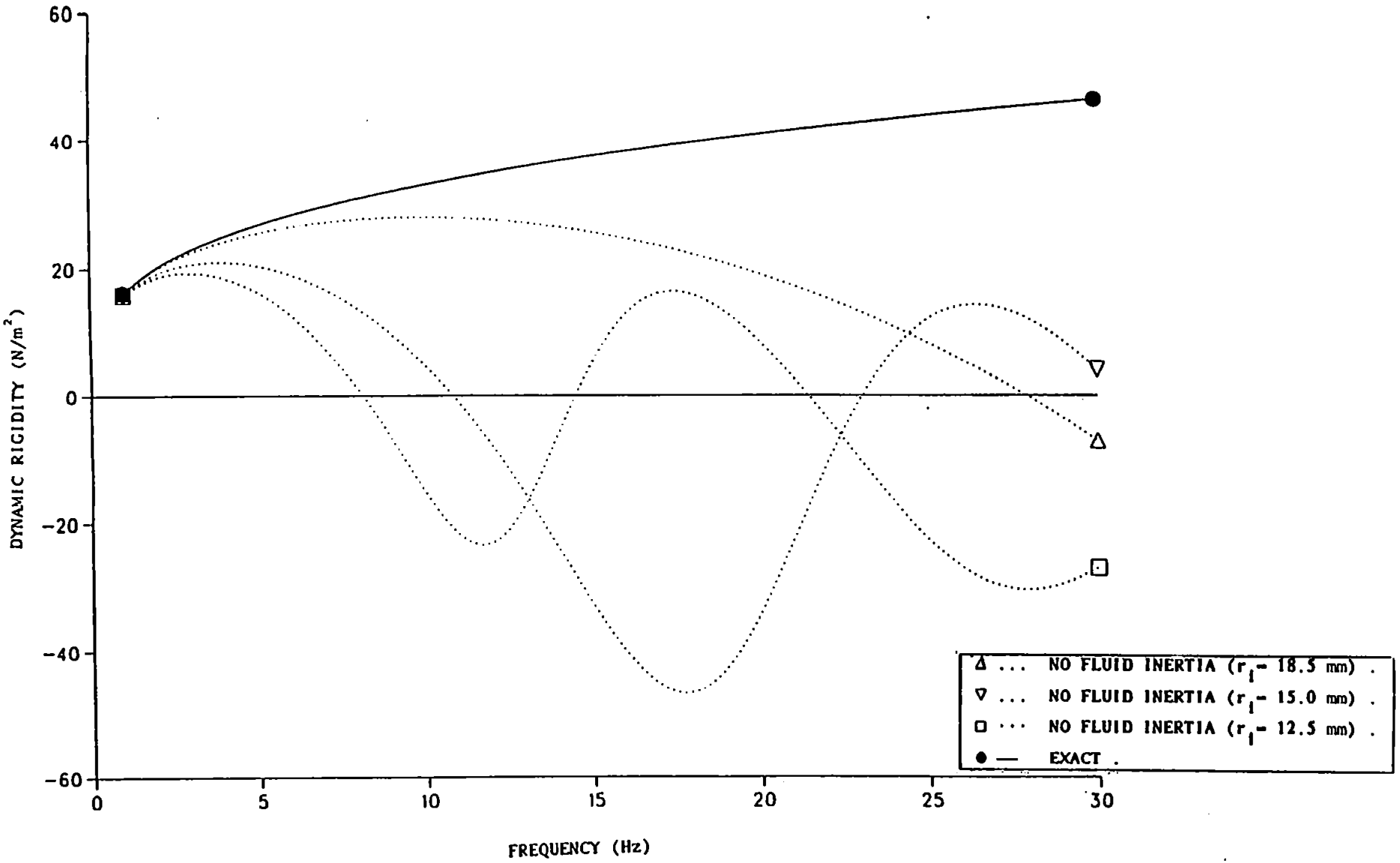
60
40
20
0
-20
-40
-60
0
5
10
15
20
25
30
DYNAMIC RIGIDITY (N/m²)
FREQUENCY (Hz)
△ ... NO FLUID INERTIA (r₁ = 18.5 mm)
▽ ... NO FLUID INERTIA (r₁ = 15.0 mm)
□ ... NO FLUID INERTIA (r₁ = 12.5 mm)
● — EXACT

Clearly the simplest situation we are able to consider is when fluid inertia effects are negligible. (i.e. $\alpha^2=0$). Under this assumption the equation of motion (6.2.18) of the top platen reduces to,

$$\eta_0^* = \frac{2h}{i\omega\pi a^4 X_0}\left[C_0 e^{ic} + I\omega^2 X_0 \right] \quad . \qquad (6.2.28)$$

The real and imaginary parts of the complex viscosity are called the dynamic viscosity and the dynamic rigidity respectively. These linear viscoelastic functions are related to the experimental displacement amplitude and phase data by the expressions,

$$\eta_0' = \frac{2hC_0\sin(c)}{\omega\pi a^4 X_0} \quad , \qquad (6.2.29)$$

and

$$G_0' = \frac{2h}{\pi a^4}\left[\frac{C_0\cos(c)}{X_0} + I\omega^2 \right] \quad . \qquad (6.2.30)$$

The phase angle c must therefore lie in the range,

$$0 \leqslant c \leqslant \pi \quad . \qquad (6.2.31)$$

The mechanical inertia of the system is governed by the term $I\omega^2$ and has no effect on the dynamic viscosity.

We are now in a position to derive expressions for the first and second order complex viscosity coefficients. It can be seen by comparing (6.2.18) and (6.2.28) that the complex viscosity η^* and the zero order approximation to the complex viscosity η_0^* are related by,

$$\eta^* C(\alpha^2) = \eta_0^* \frac{i\omega\pi a^4 X_0}{2h} \quad . \qquad (6.2.32)$$

Hence by using (6.2.20-27) and equating coefficients, we find that the complex viscosity is given by,

$$\eta^* \triangleq \eta_0^*\left[1 + \frac{(\alpha_0 h)^2}{3} + \frac{(\alpha_0 h)^4}{45} \right] \quad . \qquad (6.2.33)$$

Let the first and second order approximations to the complex viscosity be $\eta^*_{(1)}$ and $\eta^*_{(2)}$ respectively. Jones et al [24] have derived the first order fluid inertia correction for this geometry in an earlier investigation.

Consider equation (6.2.33), which to first order accuracy is,

$$\eta^*_{(1)} = \eta^*_0 - \frac{i\omega\rho h^2}{3} \quad . \tag{6.2.34}$$

The first order approximation has no real component and therefore the zero order dynamic viscosity function remains unchanged. i.e.

$$\eta'_{(1)} = \eta'_0 \quad . \tag{6.2.35}$$

However, the zero order dynamic rigidity function is increased by an amount $\omega\rho h^2/3$.

$$G'_{(1)} = G'_0 + \frac{\omega^2\rho h^2}{3} \quad . \tag{6.2.36}$$

The first order fluid inertia corrections (6.2.35-36) have previously been derived by Jones et al [24]. Equation (6.2.36) shows that the first order fluid inertia correction is dependent on the system geometry only and is independent of fluid properties. It should be noted that η^*_1 is proportional to h^2. Hence, by varying the gap size, in experiments, the influence of fluid inertia may be determined.

The second order fluid inertia approximation may be obtained from equation (6.2.33), and is given by

$$\eta^*_{(2)} = \eta^*_0 - \frac{i\omega\rho h^2}{3} - \frac{\omega^2\rho^2 h^4}{45\eta^*_0} \quad . \tag{6.2.37}$$

i.e.

$$\eta^*_{(2)} = \eta^*_0 - \frac{i\omega\rho h^2}{3} - \frac{1}{45}\left[\frac{\omega\rho h^2}{|\eta^*_0|}\right]^2(\eta'_0 + iG'_0/\omega) \quad , \tag{6.2.38}$$

where,

$$|\eta^*_0| = \left[\eta'^2_0 + (G'_0/\omega)^2\right]^{\frac{1}{2}} \quad . \tag{6.2.39}$$

Taking real and imaginary parts we see that the dynamic viscosity η'_0 is decreased by a value of $(\eta'_0/45)(\omega\rho h^2/|\eta^*_0|)^2$.

$$\eta'_{(2)} = \eta'_0\left[1 - \frac{1}{45}\left[\frac{\omega\rho h^2}{|\eta^*_0|}\right]^2\right] \quad . \tag{6.2.40}$$

The dynamic rigidity $G'_{(2)}$ is given by,

$$G'_{(2)} = G'_0\left[1 + \frac{1}{45}\left[\frac{\omega\rho h^2}{|\eta^*_0|}\right]^2\right] + \frac{\omega^2\rho h^2}{3} \quad . \tag{6.2.41}$$

The second order fluid inertia correction depends on both the system geometry and on the fluid properties. Expressions defined by equations (6.2.29-30),(6.2.35-36), and (6.2.40-41) may be used to produce dynamic data from experimental displacement amplitude and phase data measurements, provided fluid inertia effects are not too large.

6.2.3. Exact method of solution.

If fluid inertia effects are large, it is not possible to obtain an analytical solution to the couple equation (6.2.18). By multiplying both sides of (6.2.32) by a complex factor $-1/i\omega\rho h^2$, the resultant equation is non-dimensional and may be written in the form,

$$(\alpha_0 h)^2 = (\alpha h)\tan(\alpha h) \quad . \tag{6.2.42}$$

This equation may be solved numerically using a Newton-Raphson technique. To avoid the discontinuity in $\tan(\alpha h)$ as αh approaches $k\pi/2$, $k = \pm 1, \pm 3, \ldots$, we rewrite this equation as,

$$(\alpha h)\sin(\alpha h) - (\alpha_0 h)^2\cos(\alpha h) = 0 \quad . \tag{6.2.43}$$

Let

$$f(\alpha h) = (\alpha h)\sin(\alpha h) - (\alpha_0 h)^2\cos(\alpha h) \quad . \tag{6.2.44}$$

The complex parameter $(\alpha_0 h)^2$ is known experimentally. (αh) can now be determined by solving equation (6.2.43) numerically using the iterative procedure (Jennings [21]).

$$z_{k+1} = z_k - \frac{f(z_k)}{f'(z_k)} \quad , \; k = 0,1,2,\ldots \tag{6.2.45}$$

where z_0 is an initial value for αh. It should be noted that the solution to equation (6.2.43) is multivalued and hence, care must be taken in the initial choice of (αh) to ensure that the scheme converges to the correct solution.

6.3. Cone and plate.

6.3.1. Governing equations.

All physical quantities are referred to spherical polar coordinates (r,θ,φ). The cone and plate geometry is defined by two coaxial instrument members; a cone of semi-vertical angle θ_c and a flat horizontal plate of radius r as shown in figure (3.4). The angle between the cone and the plate, denoted θ_0, is assumed to be small ($\leq 4^{\circ}$). A couple is applied to the cone forcing it to make small amplitude angular oscillations of amplitude X_0 and frequency ω about the φ-axis. The bottom platen remains stationary. We again use the generalised linear equation of state for elastico-viscous liquids defined by (6.2.1). i.e.

$$\sigma_{ij} = \eta^*\dot{\gamma}_{ij} - pg_{ij} \quad . \tag{6.3.1}$$

Following the analysis of previous workers, Holder [20] and Jones et al [24], the non-zero physical velocity component is assumed to be,

$$V_{(\varphi)} = F(r,\theta)e^{i\omega t} \quad , \tag{6.3.2}$$

which identically satisfies the equation of continuity (2.1.4), for incompressible fluids. The velocity profile (6.3.2) gives rise to two non-zero components of the shear rate tensor. These are (Bird et al [5]),

$$\dot{\gamma}_{\theta r} = \left[\frac{\partial F(r,\theta)}{\partial r} - \frac{F(r,\theta)}{r} \right] e^{i\omega t} \quad , \tag{6.3.3}$$

and

$$\dot{\gamma}_{\theta\varphi} = \frac{1}{r}\left[\frac{\partial F(r,\theta)}{\partial \theta} - F(r,\theta)\cot(\theta) \right] e^{i\omega t} \quad . \tag{6.3.4}$$

The corresponding components of the stress tensor are given by

$$\sigma_{\theta r} = \left[\frac{\partial F(r,\theta)}{\partial r} - \frac{F(r,\theta)}{r} \right] \eta^* e^{i\omega t} \quad , \tag{6.3.5}$$

and

$$\sigma_{\theta\varphi} = \frac{1}{r}\left[\frac{\partial F(r,\theta)}{\partial \theta} - F(r,\theta)\cot(\theta) \right] \eta^* e^{i\omega t} \quad . \tag{6.3.6}$$

Substituting (6.3.2) and (6.3.5-6) into the relevant equation of motion (see equation (2.1.2)),

$$\rho\left[\frac{\partial V_\varphi}{\partial t} + V_r \frac{\partial V_\varphi}{\partial r} + \frac{V_\varphi}{r} \frac{\partial V_\varphi}{\partial \theta} + \frac{V_\varphi}{r\sin(\theta)} \frac{\partial V_\varphi}{\partial \varphi} + \frac{V_r V_\varphi}{r} + \frac{V_\theta V_\varphi}{r} \cot(\theta) \right]$$

$$= \frac{1}{r^3} \frac{\partial}{\partial r}\left[r^3 \sigma_{r\varphi}\right] + \frac{1}{r\sin(\theta)} \frac{\partial}{\partial \theta}\left[\sigma_{\theta\varphi}\sin(\theta)\right] + \frac{1}{r\sin(\theta)} \frac{\partial}{\partial \varphi} \sigma_{\varphi\varphi} + \frac{\sigma_{\theta\varphi}\cot(\theta)}{r}$$

$$- \frac{1}{r\sin(\theta)} \frac{\partial p}{\partial \varphi} \quad , \qquad (6.3.7)$$

we obtain the second order partial differential equation,

$$\frac{\partial}{\partial r}\left[r^2 \frac{\partial F(r,\theta)}{\partial r}\right] + \frac{1}{\sin(\theta)}\left[\sin(\theta)\frac{\partial F(r,\theta)}{\partial \theta}\right] - \frac{F(r,\theta)}{\sin^2(\theta)} = -(\alpha r)^2 F(r,\theta) \quad , \qquad (6.3.8)$$

where α is defined in equation (6.2.10).
Equation (6.3.8) must be solved subject to the boundary conditions

$$F(r,\theta_c) = i\omega r X_0 \sin(\theta_c) \qquad (6.3.9)$$

$$F(r,0) = 0 \quad . \qquad (6.3.10)$$

Nally [28] has solved the above partial differential equation using a separation of variables technique. The general solution may be written as,

$$F(r,\theta) = r^{-\frac{1}{2}} \sum_{n=1}^{\infty} J_{n+\frac{1}{2}}(\alpha r)\left[A_n P'_n(\cos(\theta)) + B_n Q'_n(\cos(\theta)) \right] \quad , \qquad (6.3.11)$$

where $J_{n+\frac{1}{2}}(\alpha r)$ is a Bessel function of the first kind of order $(n+1/2)$, $P_n(\cos(\theta))$ and $Q_n(\cos(\theta))$ are zero order Legendre functions of the first and second kind of degree n, and ' denotes differentiation with respect to θ. A_n and B_n are arbitrary constants to be determined from the boundary conditions (6.3.9-10). We shall need to use the following result from Watson[46],

$$(\alpha r)^{3/2} = 2^{3/2} \sum_{n=1,3}^{\infty} \frac{(n+1/2)\Gamma(1+n/2)}{[(n-1)/2]!} J_{n+\frac{1}{2}}(\alpha r) \quad , \qquad (6.3.12)$$

where from [28] we define the gamma function Γ to be,

$$\Gamma(k+\tfrac{1}{2}) = \frac{1\ 3\ 5\ 7\ \ldots.(2k-1)}{2^k} \Gamma(1/2) \quad . \qquad (k=1,2,3,\ldots) \qquad (6.3.13)$$

$F(r,\theta_c)$ may be expanded in terms of $J_{n+1/2}$ by substituting (6.3.12) into (6.3.9) to give

$$F(r,\theta_c) = i\omega X_0 r^{-\frac{1}{2}} \alpha^{-\frac{3}{2}} \sin(\theta_c) \sum_{n=1,3}^{\infty} a_n J_{n+\frac{1}{2}}(\alpha r) \quad , \tag{6.3.14}$$

where,

$$a_n = 2^{3/2} \frac{(n+1/2)\Gamma(1+n/2)}{[(n-1)/2]!} \quad . \tag{6.3.15}$$

Using the properties of the Legendre functions (Abramovitz and Segun [1], we see that the solution (6.3.11) to the differential equation (6.3.8) satisfies the boundary conditions (6.3.10) and (6.3.14) provided,

$$A_n = 0 \qquad \text{for all } n \quad , \tag{6.3.16}$$

$$B_n = 0 \qquad n \text{ even} \quad , \tag{6.3.17}$$

and

$$B_n = \frac{i\omega X_0 a_n \sin(\theta_c)\alpha^{-3/2}}{Q_n'(\cos(\theta_c))} \qquad n \text{ odd} \quad . \tag{6.3.18}$$

Hence equation (6.3.11) becomes,

$$F(r,\theta) = r^{-\frac{1}{2}} \alpha^{-\frac{3}{2}} \sum_{n=1,3}^{\infty} a_n J_{n+\frac{1}{2}}(\alpha r) R_n(\theta) \quad , \tag{6.3.19}$$

where,

$$R_n(\theta) = \frac{i\omega X_0 \sin(\theta_c)\, Q_n'(\cos(\theta))}{Q_n'(\cos(\theta_c))} \quad . \tag{6.3.20}$$

The equation of motion of the cone is given by,

$$C_0 e^{i(\omega t+c)} - C_F = -I\omega^2 X_0 e^{i\omega t} \quad , \tag{6.3.21}$$

where I is now the moment of inertia of the cone. The couple acting on the cone due to the motion of the fluid is given by,

$$C_F = -2\pi \sin^2(\theta_c) \int_0^a r^2 \sigma_{\theta\varphi}|_{\theta=\theta_c} dr \quad . \tag{6.3.22}$$

Equation (6.3.6) describes the $\theta\varphi$-component of the stress tensor from which C_F may be determined. i.e.

$$C_F = -2\pi\sin^2(\theta_c)\alpha^{-3}\sum_{n=1,3}^{\infty} a_n\left[R_n'(\theta) - R_n(\theta)\cot(\theta) \right]_{\theta=\theta_c} H_{n+\frac{1}{2}}(\alpha r)\eta^* e^{i\omega t}, \tag{6.3.23}$$

where

$$H_{n+\frac{1}{2}}(\alpha a) = \int_0^{\alpha a} (\alpha r)^{1/2} J_{n+\frac{1}{2}}(\alpha r)\, d(\alpha r) \quad . \tag{6.3.24}$$

The equation of motion of the cone may therefore be expressed as,

$$\eta^* C(\alpha^2) = C_0 e^{ic} + I\omega X_0^2 \quad . \tag{6.3.25}$$

where the complex function $C(\alpha^2)$ is given by,

$$C(\alpha^2) = -2\pi\sin^2(\theta_c)\alpha^{-3}\sum_{n=1,3}^{\infty} a_n\left[R_n'(\theta) - R_n(\theta)\cot(\theta) \right]_{\theta=\theta_c} H_{n+\frac{1}{2}}(\alpha r) \quad . \tag{6.3.26}$$

Equation (6.3.25) may be used to determine the complex viscosity exactly. A computer algorithm has been written to solve equation (6.3.25) numerically by employing essentially the same iterative technique as described in section (6.2.3). This scheme is discussed in section (6.3.3)

6.3.2 Perturbation method of solution.

If we assume that fluid inertia effects are small, then from Maude and Walters [26], we see that the solution to (6.3.8) may be expanded in powers of $(\alpha r)^2$ terms. i.e.

$$F(r,\theta) \doteq F_0(r,\theta) + (\alpha r)^2 F_1(r,\theta) + (\alpha r)^4 F_2(r,\theta) \quad , \tag{6.3.27}$$

where terms of order $(\alpha r)^6$ have been ignored.

If we use the Bessel function property (Watson [46]),

$$J_{n+\frac{1}{2}}(\alpha r) = \sum_{m=0}^{\infty} \frac{(-1)^m (\alpha r/2)^{n+2m+\frac{1}{2}}}{m!\Gamma(n+m+3/2)} \quad . \tag{6.3.28}$$

in equation (6.3.19) we obtain by collecting coefficients the expression for $F(r,\theta)$ below

$$F(r,\theta) \triangleq r\left[R_1(\theta) + \frac{(\alpha r)^2}{10}\left[R_3(\theta) - R_1(\theta) \right] + (\alpha r)^4\left[\frac{R_5(\theta)}{504} - \frac{R_3(\theta)}{180} + \frac{R_1(\theta)}{280} \right] \right] . \quad (6.3.29)$$

This solution is the same as that obtained by Holder[20].

When fluid inertia effects are ignored,

$$F(r,\theta) \triangleq rR_1(\theta) . \quad (6.3.30)$$

which when used in conjunction equations (6.3.6) and (6.3.22), gives the following expression C_F.

$$C_F = \frac{2\pi a^3 \sin^2(\theta_c)}{3}\left[R_1'(\theta) - R_1(\theta)\cot(\theta) \right]_{\theta=\theta_c} \eta_0^* e^{i\omega t} . \quad (6.3.31)$$

When fluid inertia effects are not ignored, then in order to simplify the equations, it is convenient to assume that the gap angle θ_0, is small. Using the properties of Legendre functions (Abramovitz and Segun [1]), it can be shown that equation (6.3.29) may be written as,

$$F(r,\theta) \triangleq \frac{i\omega r X_0}{\theta_0}\left[(\pi/2-\theta) + \frac{(\alpha r)^2}{6}\left[(\pi/2-\theta)\theta_0^2 - (\pi/2-\theta)^3 \right] + (\alpha r)^4\left[\frac{7}{360}(\pi/2-\theta)\theta_0^4 - \frac{1}{36}(\pi/2-\theta)^3\theta_0^2 + \frac{1}{120}(\pi/2-\theta)^5 \right] \right] . \quad (6.3.32)$$

Substituting equations (6.3.6) and (6.3.32) into equation (6.3.22), C_F is now given by,

$$C_F \triangleq \frac{2\pi i\omega a^3 X_0}{3\theta_0}\left[1 - \frac{1}{5}(\alpha a\theta_0)^2 - \frac{1}{105}(\alpha a\theta_0)^4 \right] . \quad (6.3.33)$$

Hence from (6.3.25),

$$C(\alpha^2) \triangleq \frac{2\pi i\omega a^3 X_0}{3\theta_0}\left[1 - \frac{1}{5}(\alpha a\theta_0)^2 - \frac{1}{105}(\alpha a\theta_0)^4 \right] . \quad (6.3.34)$$

When fluid inertia effects are ignored, the equation of motion of the cone reduces to, on substitution of equation (6.3.34) into equation (6.3.25), the following expression for η_0^* ,

$$\eta_0^* = \frac{3\theta_0}{2\pi i\omega a^3 X_0}\left[C_0 e^{ic} + I\omega^2 X_0 \right] \quad . \tag{6.3.35}$$

Taking real and imaginary parts we see that the dynamic viscosity is given by,

$$\eta_0' = \frac{3\theta_0 C_0 \sin(c)}{2\pi\omega a^3 X_0} \quad , \tag{6.3.36}$$

and the dynamic rigidity is given by,

$$G_0' = \frac{3\theta_0}{2\pi a^3 X_0}\left[C_0\cos(c) + I\omega^2 X_0 \right] \quad . \tag{6.3.37}$$

For the case when fluid inertia effects are included, we see by substituting equation (6.3.34) into the couple equation (6.3.25) and equating with equation (6.3.25) that

$$\eta^* \doteq \eta_0^*\left[1 + \frac{(\alpha_0 a\theta_0)^2}{3} + \frac{(\alpha_0 a\theta_0)^4}{105} \right] \quad . \tag{6.3.38}$$

The first and second order approximations to the complex viscosity function may be obtained from (6.3.38).

Substituting (6.3.35) into (6.3.38) yields the first order approximation,

$$\eta_{(1)}^* = \eta_0^* - \frac{i\omega\rho a^2\theta_0^2}{5} \quad . \tag{6.3.39}$$

Taking real and imaginary parts, we see that the dynamic rigidity function is now given by,

$$G_{(1)}' = G_0' + \frac{\omega^2\rho a^2\theta_0^2}{5} \quad . \tag{6.3.40}$$

The dynamic viscosity function is unaffected by first order fluid inertia effects.

The second order approximation, is given from equation (6.3.8) to be

$$\eta_{(2)}^* = \eta_{(1)}^* - \frac{1}{105}\left[\frac{\omega^2\rho^2 a^4\theta_0^4}{\eta_0^*}\right] \quad . \tag{6.3.41}$$

Taking real and imaginary parts we see that the dynamic viscosity is given by,

$$\eta'_{(2)} = \eta'_0\left[\, 1 - \frac{1}{105}\left[\frac{\omega^2\rho^2a^4\theta_0^4}{|\eta_0^*|}\right]\right] \quad , \qquad (6.3.42)$$

and that the dynamic rigidity is given by,

$$G'_{(2)} = G'_{(1)} + G'_0\ \frac{1}{105}\left[\frac{\omega^2\rho^2a^4\theta_0^4}{|\eta_0^*|}\right] \quad , \qquad (6.3.43)$$

where

$$|\eta_0^*| = \left[\eta_0'^2 + (G'_0/\omega)^2\right]^{\frac{1}{2}} \quad . \qquad (6.3.44)$$

6.3.3. Exact method of solution.

When fluid inertia effects are included in the analysis, the couple equation is given by (6.3.25). The couple equation for the case when fluid inertia effects are ignored in the analysis is obtained by substituting equation (6.3.31) into equation (6.3.21). i.e.

$$\frac{2\pi a^3\sin^2(\theta_c)}{3}\left[\, R'_1(\theta) - R_1(\theta)\cot(\theta)\,\right]_{\theta=\theta_c}\eta_0^* = C_0e^{ic} + I\omega^2X_0 \quad . \qquad (6.3.45)$$

By comparing equation (6.3.45) with (6.3.25), we see that η^* and η_0^* are related by the following equation.

$$\eta_0^* = \frac{3\eta^*}{(\alpha a)^3}\sum_{n=1,3}^{\infty} a_nL_n(\theta)|_{\theta=\theta_c}\ H_{n+\frac{1}{2}}(\alpha a) \quad , \qquad (6.3.46)$$

where the function $L_n(\theta)$ is defined by,

$$L_n(\theta) =$$

$$\left[\frac{Q_n''(\cos(\theta)) - Q_n'(\cos(\theta))\cot(\theta)}{Q_n'(\cos(\theta_c))}\right] \Big/ \left[\frac{Q_1''(\cos(\theta)) - Q_1'(\cos(\theta))\cot(\theta)}{Q_1'(\cos(\theta_c))}\right] \quad . \qquad (6.3.47)$$

Multiplying both sides of (6.3.46) by a complex factor $-1/i\omega\rho a^2$ leads to the non-dimensional equation,

$$(\alpha a)^5 - 3(\alpha_0 a)^2 \sum_{n=1,3}^{\infty} a_n L_n(\theta)\big|_{\theta=\theta_c} H_{n+\frac{1}{2}}(\alpha a) = 0 \quad , \qquad (6.3.48)$$

which is to be solved using the same iterative scheme as set out in section (6.2.3). At the $(k+1)^{th}$ iteration,

$$(\alpha a)_{k+1} = (\alpha a)_k - \frac{f((\alpha a)_k)}{f'((\alpha a)_k)} \quad , \quad k = 0,1,2,\ldots \qquad (6.3.49)$$

The function $f(\alpha a)$ is defined by,

$$f(\alpha a) = (\alpha a)^5 - (\alpha_0 a)^2 \sum_{n=1,3}^{\infty} a_n L_n(\theta)\big|_{\theta=\theta_c} H_{n+\frac{1}{2}}(\alpha a) \quad . \qquad (6.3.50)$$

The non-dimensional complex parameter $(\alpha_0 a)^2$ may be determined experimentally. For each value of this parameter, we must find a value of αa which satisfies (6.3.48). The first and second derivatives of the nth order Legendre function may be evaluated using the following stable forward recursive relations,

$$Q_n'(\cos(\theta)) = \frac{2n-1}{n-1}\cos(\theta)Q_{n-1}'(\cos(\theta)) - \frac{n}{n-1}Q_{n-2}'(\cos(\theta)) \quad ,$$

$$n=2,3,4.. \qquad (6.3.51)$$

and

$$Q_n''(\cos(\theta)) = \frac{2n-1}{n-1}\left[\cos(\theta)Q_{n-1}''(\cos(\theta)) - \sin(\theta)Q_{n-1}'(\cos(\theta))\right]$$

$$- \frac{n}{n-1}Q_{n-2}''(\cos(\theta)) \qquad n=2,3,4,.. \quad . \qquad (6.3.52)$$

where ' refers to differentiation with respect to θ.

We note the recursive formula for evaluating the Bessel function $J_{n+\frac{1}{2}}(\alpha a)$,

$$J_{n+1/2}(\alpha a) = \frac{2n-1}{\alpha a} J_{n-1/2}(\alpha a) - J_{n-3/2}(\alpha a), \qquad (6.3.53)$$

This formula is unstable recursing in the forward direction, but stable when recursing backwards . A scheme for evaluating $J_{n+\frac{1}{2}}(\alpha a)$ due to Miller and presented by Olver can be found in [32].

The integral represented by $H_{n+\frac{1}{2}}(\alpha a)$ may be evaluated by means of a stable forward recursive relation.

$$H_{n+1/2}(\alpha a) = \frac{n}{n-1} H_{n-3/2}(\alpha a) - \frac{2n-1}{n-1} (\alpha a)^{1/2} J_{n-1/2}(\alpha a), \quad n=2,3,4,.. \tag{6.3.54}$$

This formula is obtained by subtstituting equation (6.3.53) into equation (6.3.24) and integrating by parts.

6.4. Concentric cylinders.

6.4.1. Governing equations.

All physical quantities are referred to cylindrical polar coordinates (r,θ,z). The concentric cylinder geometry consists of two coaxial cylinders of height h and radii r_i and r_o respectively $(r_o>r_i)$, as shown in figure (3.6). A couple is applied to the inner cylinder forcing it to make small amplitude angular oscillations of amplitude X_0 and frequency ω about the z-axis. The outer cylinder remains stationary.

We again use the generalised linear equation of state for elastico-viscous liquids defined in section (6.2).

$$\sigma_{ij} = \eta^*\dot{\gamma}_{ij} - pg_{ij} \quad . \tag{6.4.1}$$

Following the analysis of Jones et al [24], the non-zero physical velocity component is assumed to be,

$$V_\theta = rF(r)e^{i\omega t} \quad , \tag{6.4.2}$$

which identically satisfies the equation of continuity (2.1.4), for incompressible fluids. This velocity profile gives rise to one non-zero component of the shear rate tensor (Bird et al [5]),

$$\dot{\gamma}_{\theta r} = r\frac{dF(r)}{dr}e^{i\omega t} \quad , \tag{6.4.3}$$

which can be substituted into equation (6.4.1) to obtain the corresponding component of the stress tensor,

$$\sigma_{\theta r} = r\frac{dF(r)}{dr}\eta^* e^{i\omega t} \quad . \tag{6.4.4}$$

Substituting (6.4.1) and (6.4.3) into the relevant equation of motion,

$$\rho\left[\frac{\partial V_\theta}{\partial t} + V_r\frac{\partial V_\theta}{\partial r} + \frac{V_\theta}{r}\frac{\partial V_\theta}{\partial \theta} + V_z\frac{\partial V\theta}{\partial z} + \frac{V_r V_\theta}{r} \right]$$

$$= \frac{1}{r^2}\frac{\partial}{\partial r}\left[r^2\sigma_{\theta r}\right] + \frac{1}{r}\frac{\partial}{\partial \theta}\sigma_{\theta\theta} + \frac{\partial}{\partial z}\sigma_{\theta z} - \frac{1}{r}\frac{\partial p}{\partial \theta} \quad , \qquad (6.4.5)$$

leads to the second order ordinary differential equation,

$$\frac{d}{dr}\left[r^3\frac{dF(r)}{dr}\right] + \alpha^2 r^3 F(r) = 0 \quad . \qquad (6.4.6)$$

The solution to this differential equation must satisfy the following boundary conditions.

$$F(r_i) = i\omega X_0 \quad , \qquad (6.4.7)$$

$$F(r_o) = 0 \quad . \qquad (6.4.8)$$

It can be shown that it is possible to rewrite (6.4.6) in the form,

$$r^2\frac{d^2G(r)}{dr^2} + r\frac{dG(r)}{dr} + (\alpha^2 r^2 - 1)G(r) = 0 \quad , \qquad (6.4.9)$$

where,

$$G(r) = rF(r) \quad . \qquad (6.4.10)$$

Equation (6.4.9) is an example of Bessel's equation and has a general solution,

$$G(r) = AJ_1(\alpha r) + BY_1(\alpha r) \quad , \qquad (6.4.11)$$

where $J_1(\alpha r)$ and $Y_1(\alpha r)$ are first order Bessel functions of the first and second kind respectively, and A and B are arbitrary constants to be determined from the boundary conditions (6.4.7-8). The solution G(r) satisfies (6.4.7-8) provided A and B are given by,

$$A = \frac{-i\omega X_0 r_i Y_1(\alpha r_o)}{J_1(\alpha r_o)Y_1(\alpha r_i) - Y_1(\alpha r_o)J_1(\alpha r_i)} \quad , \qquad (6.4.12)$$

and

$$B = \frac{i\omega X_0 r_i J_1(\alpha r_o)}{J_1(\alpha r_o)Y_1(\alpha r_i) - Y_1(\alpha r_o)J_1(\alpha r_i)} \quad . \qquad (6.4.13)$$

Hence,

$$F(r) = \frac{i\omega X_0 r_i}{r}\left[\frac{Y_1(\alpha r)J_1(\alpha r_o) - J_1(\alpha r)Y_1(\alpha r_o)}{J_1(\alpha r_o)Y_1(\alpha r_i) - Y_1(\alpha r_o)J_1(\alpha r_i)}\right] \quad . \qquad (6.4.14)$$

The equation of motion of the inner cylinder is,

$$C_0 e^{i(\omega t+c)} - C_F = -I\omega^2 X_0 e^{i\omega t} \quad , \tag{6.4.15}$$

where the couple acting on the inner cylinder due to the motion of the fluid is given by,

$$C_F = -2\pi h r_i^2 \sigma_{\theta r}|_{r=r_i} \quad . \tag{6.4.16}$$

The θr-component of the stress tensor may be determined by substituting (6.4.14) into (6.4.4). i.e.

$$\sigma_{\theta r}|_{r=r_i} = i\omega X_0 \alpha r_i \left[\frac{Y_1(\alpha r_0)J_2(\alpha r_i) - J_1(\alpha r_0)Y_2(\alpha r_i)}{J_1(\alpha r_0)Y_1(\alpha r_i) - Y_1(\alpha r_0)J_1(\alpha r_i)}\right]\eta^* e^{i\omega t} \quad . \tag{6.4.17}$$

The equation of motion of the inner cylinder may be expressed as,

$$\eta^* C(\alpha^2) = C_0 e^{ic} + I\omega^2 X_0 \quad , \tag{6.4.18}$$

where,

$$C(\alpha^2) = 2\pi i\omega X_0 h\alpha r_i^3 \left[\frac{J_1(\alpha r_0)Y_2(\alpha r_i) - Y_1(\alpha r_0)J_2(\alpha r_i)}{J_1(\alpha r_0)Y_1(\alpha r_i) - Y_1(\alpha r_0)J_1(\alpha r_i)}\right] \quad . \tag{6.4.19}$$

and I is now the moment of inertia of the inner cylinder. Equation (6.4.19) must be solved numerically to determine the complex viscosity function η^*. However, it is possible to derive an approximate analytical expression providing we assume that fluid inertia effects are small.

6.4.2. Perturbation method of solution.

It is convenient to define the following non-dimensional quantity

$$\mu = \frac{r}{r_o} \quad , \tag{6.4.20}$$

On substitution of μ into equation (6.4.6), we obtain the differential equation,

$$\frac{d}{d\mu}\left[\mu^3 \frac{dF(\mu)}{d\mu}\right] + (\alpha r_0)^2 \mu^3 F(\mu) = 0 \quad , \tag{6.4.21}$$

the solution to which must satisfy the boundary conditions

$$F(r_i/r_o) = i\omega X_0 \quad , \tag{6.4.22}$$

and

$$F(1) = 0 \quad . \tag{6.4.23}$$

By expanding the solution to (6.4.21) in powers of $(\alpha r_o)^2$ terms, we obtain,

$$F(\mu) \triangleq F_0(\mu) + (\alpha r_o)^2 F_1(\mu) + (\alpha r_o)^4 F_2(\mu) \quad , \tag{6.4.24}$$

where $(\alpha r_o)^2$ is considered small enough to ignore terms of order $(\alpha r_o)^6$. On substitution of the expansion (6.4.24) into (6.4.21), we obtain three second order ordinary differential equations that must be solved subject to the boundary conditions (6.4.22-23). These are,

$$\frac{d}{d\mu}\left[\mu^3 \frac{dF_0(\mu)}{d\mu}\right] = 0 \quad , \tag{6.4.25}$$

$$\frac{d}{d\mu}\left[\mu^3 \frac{dF_1(\mu)}{d\mu}\right] = -\mu^3 F_0(\mu) \quad , \tag{6.4.26}$$

$$\frac{d}{d\mu}\left[\mu^3 \frac{dF_2(\mu)}{d\mu}\right] = -\mu^3 F_1(\mu) \quad . \tag{6.4.27}$$

The above equations enable us to determine the zero, first, and second order coefficients F_0, F_1, and F_2 respectively. Substituting F_0, F_1, and F_2 into equation (6.4.24), we obtain

$$\begin{aligned} F(\mu) \triangleq\ & \frac{i\omega X_0 r_i^2}{r_o^2 - r_i^2}\left[\frac{1}{\mu^2} - 1\right. \\ & + \frac{1}{8}(\alpha r_o)^2\left[\mu^2 - 4\ln(\mu) + \left[\frac{4r_i^2\ln(r_i/r_o)}{r_o^2 - r_i^2} + \frac{r_i^2}{r_o^2}\right]\left[\frac{1}{\mu^2} - 1\right] - 1\right] \\ & + \frac{1}{16}(\alpha r_o)^4\left[\frac{\mu^4}{12} - \mu^2\ln(\mu) + \frac{\mu^2}{2} + \left[\frac{r_i^2\ln(r_i/r_o)}{r_o^2 - r_i^2} + \frac{r_i^2}{r_o^2}\right]\left[\ln(\mu) - \frac{\mu^2}{4}\right]\right] \\ & - \frac{r_i^2}{r_o^2 - r_i^2}\left[\frac{r_i^2}{r_o^2}\ln(r_i/r_o)\left[1 + \frac{4r_i^2\ln(r_i/r_o)}{r_o^2 - r_i^2}\right] + \frac{3r_i^2}{4r_o^2} - \frac{r_i^4}{6r_o^4} - \frac{7}{12}\right]\left[\frac{1}{\mu^2} - 1\right] \\ & \left. - \frac{7}{12} + \frac{1}{4}\left[\frac{r_i^2\ln(r_i/r_o)}{r_o^2 - r_i^2} + \frac{r_i^2}{r_o^2}\right]\right] \quad . \end{aligned} \tag{6.4.28}$$

The couple acting on the inner cylinder due to the motion of the fluid is given by equation (6.4.16) to be

$$C_F = -2\pi r_i^2 \sigma_{\theta r}|_{\mu = r_i/r_o} , \tag{6.4.29}$$

where $\sigma_{\theta r}$ is given by equation (6.4.4),

$$\sigma_{\theta r} = \mu \frac{dF(\mu)}{d\mu} \eta^* e^{i\omega t} . \tag{6.4.30}$$

The couple C_F can therefore be determined by substituting (6.4.28) and (6.4.30) into (6.4.29). i.e.

$$C_F = \frac{4\pi i\omega X_0 h r_i^2 r_o^2}{r_o^2 - r_i^2}\left[1 + (\alpha r_o)^2 C_1 + (\alpha r_o)^4 C_2\right]\eta^* e^{i\omega t} , \tag{6.4.31}$$

where the first and second order coefficients are given by,

$$\left.\begin{aligned} C_1 &= \frac{r_i^2}{2r_o^2}\left[\frac{3r_o^2 - r_i^2}{4r_o^2} + \frac{r_o^2 \ln(r_i/r_o)}{r_o^2 - r_i^2}\right] , \\ \text{and} \\ C_2 &= \frac{r_i^2}{32r_o^2}\left[\frac{4r_i^2 \ln(r_i/r_o)}{r_o^2 - r_i^2}\left[1 + \frac{2r_o^2 \ln(r_i/r_o)}{r_o^2 - r_i^2}\right]\right. \\ &\quad \left. - \frac{(7r_o^2 - r_i^2)(r_o^2 - r_i^2)}{6r_o^4}\right] \end{aligned}\right\} \tag{6.4.32}$$

respectively.

If we substitute equation (6.4.31) into equation (6.4.15), and then express the resulting equation in the form given by equation (6.4.18), we obtain the following expression for $C(\alpha^2)$.

$$C(\alpha^2) = \frac{4\pi i\omega X_0 h r_i^2 r_o^2}{r_o^2 - r_i^2}\left[1 + (\alpha r_o)^2 C_1 + (\alpha r_o)^4 C_2\right] , \tag{6.4.33}$$

where C_1 and C_2 are defined by equation (6.4.32).

If we ignore fluid inertia effects, then on substituting equation (6.4.33) into equation (6.4.18), we obtain the following expression for η_0^*

$$\eta_0^* = \frac{r_o^2 - r_i^2}{4\pi i\omega X_0 h r_i^2 r_o^2}\left[C_0 e^{ic} + I\omega^2 X_0\right] . \tag{6.4.34}$$

Taking real and imaginary parts, we obtain the following expressions for the dynamic viscosity η_0' and the dynamic rigidity G_0'.

$$\eta_0' = \frac{C_0(r_o^2 - r_i^2)\sin(c)}{4\pi\omega X_0 h r_i^2 r_o^2} \quad , \tag{6.4.35}$$

and

$$G_0' = \frac{(r_o^2 - r_i^2)}{4\pi h r_i^2 r_o^2}\left[\frac{C_0\cos(c)}{X_0} + I\omega^2\right] \quad . \tag{6.4.36}$$

For the case when fluid inertia effects are included, we see by substituting equation (6.4.33) into the couple equation (6.4.18) and equating with equation (6.4.34) that

$$\eta^* \triangleq \eta_0^*\left[1 - (\alpha_0 r_o)^2 C_1 - (\alpha_0 r_o)^4 C_2\right] \quad , \tag{6.4.37}$$

where C_1 and C_2 are given by (6.4.32).

To first order accuracy, the complex viscosity is given by

$$\eta^*_{(1)} = \eta_0^*\left[1 - (\alpha_0 r_o)^2 C_1\right] \quad . \tag{6.4.38}$$

Hence, from (6.4.32)

$$\eta^*_{(1)} = \eta_0^* + \frac{i\omega\rho r_i^2}{2}\left[\frac{3r_o^2 - r_i^2}{4r_o^2} + \frac{r_o^2 \ln(r_i/r_o)}{r_o^2 - r_i^2}\right] \quad . \tag{6.4.39}$$

Clearly the dynamic viscosity is unaffected by first order fluid inertia effects. However the dynamic rigidity is now given by,

$$G'_{(1)} = G_0' - \frac{\omega^2\rho r_i^2}{2}\left[\frac{3r_o^2 - r_i^2}{4r_o^2} + \frac{r_o^2 \ln(r_i/r_o)}{r_o^2 - r_i^2}\right] \quad . \tag{6.4.40}$$

The second order approximation to the complex viscosity is also obtained from equation (6.4.37).

$$\eta^*_{(2)} = \eta^*\left[1 - (\alpha_0 r_o)^2 C_1 - (\alpha_0 r_o)^4 C_2\right] \quad . \tag{6.4.41}$$

Hence,

$$\eta^*_{(2)} = \eta^*_0 + \frac{i\omega\rho r_i^2}{2}\left[\frac{3r_o^2 - r_i^2}{4r_o^2} + \frac{r_o^2\ln(r_i/r_o)}{r_o^2 - r_i^2}\right]$$

$$+ \frac{(\omega\rho r_i r_o)^2}{32\eta^*_0}\left[\frac{4r_i^2\ln(r_i/r_o)}{r_o^2 - r_i^2}\left[1 + \frac{2r_o^2\ln(r_i/r_o)}{r_o^2 - r_i^2}\right]\right.$$

$$\left. - \frac{(7r_o^2 - r_i^2)(r_o^2 - r_i^2)}{6r_o^4}\right] \quad . \qquad (6.4.42)$$

By taking the real and imaginary parts of (6.4.42), we obtain the dynamic viscosity,

$$\eta'_{(2)} = \eta'_0\left[1 + \frac{1}{32}\left[\frac{\omega\rho r_i r_o}{|\eta^*_0|}\right]^2\left[\frac{4r_i^2\ln(r_i/r_o)}{r_o^2 - r_i^2}\left[1 + \frac{2r_o^2\ln(r_i/r_o)}{r_o^2 - r_i^2}\right]\right.\right.$$

$$\left.\left. - \frac{(7r_o^2 - r_i^2)(r_o^2 - r_i^2)}{6r_o^4}\right]\right] \quad , \qquad (6.4.43)$$

and the dynamic rigidity,

$$G'_{(2)} = G'_{(1)} - \frac{G'_0}{32}\left[\frac{\omega\rho r_i r_o}{|\eta^*_0|}\right]^2\left[\frac{4r_i^2\ln(r_i/r_o)}{r_o^2 - r_i^2}\left[1 + \frac{2r_o^2\ln(r_i/r_o)}{r_o^2 - r_i^2}\right]\right.$$

$$\left. + \frac{(7r_o^2 - r_i^2)(r_o^2 - r_i^2)}{6r_o^4}\right] \quad . \qquad (6.4.44)$$

6.4.3. Exact method of solution.

As with the previous geometries considered, we find that for large fluid inertia effects we must solve the couple equation (6.4.18) numerically. By comparing (6.4.18) and (6.4.34) we are able to deduce that η^*_0 and η^* are related by the expression,

$$\eta^*_0 = \frac{\alpha r_i \eta^*(r_o^2 - r_i^2)}{2r_o^2}\left[\frac{J_1(\alpha r_o)Y_2(\alpha r_i) - Y_1(\alpha r_o)J_2(\alpha r_i)}{J_1(\alpha r_o)Y_1(\alpha r_i) - Y_1(\alpha r_o)J_1(\alpha r_i)}\right] \quad . \qquad (6.4.45)$$

Multiplying both sides of (6.4.45) by a complex factor $-1/i\omega\rho$ leads to the equation,

$$\alpha_0^2(r_o^2 - r_i^2)\frac{r_i}{r_o} = 2\alpha r_0\left[\frac{J_1(\alpha r_o)Y_1(\alpha r_i) - Y_1(\alpha r_o)J_1(\alpha r_i)}{J_1(\alpha r_o)Y_2(\alpha r_i) - Y_1(\alpha r_o)J_2(\alpha r_i)}\right] \quad . \qquad (6.4.46)$$

This equation is valid for all fluid inertia effects and will be solved numerically using the iterative procedure described in section (6.2.3) and defined at the $(k+1)^{th}$ iteration to be,

$$z_{k+1} = z_k - \frac{f(z_k)}{f'(z_k)} \quad , \tag{6.4.47}$$

where,

$$z_k = (\alpha r_0)^2 \quad , \tag{6.4.48}$$

and

$$f(z) = z\left[J_1(z)Y_1(r_i z/r_o) - Y_1(z)J_1(r_i z/r_o)\right] - \frac{\alpha_0^2 r_i (r_o^2 - r_i^2)}{2r_0}\left[J_1(z)Y_2(r_i z/r_o) - Y_1(z)J_2(r_i z/r_o)\right] \tag{6.4.49}$$

The Bessel functions of the first and second kind $J_n(z)$ and $Y_n(z)$, may be evaluated using the following recursive relation,

$$J_{n+1}(z) = \frac{2n}{z} J_n(z) - J_{n-1}(z) \quad , \tag{6.4.50}$$

This relation is stable when the recursive relationship is applied in the forward direction for $Y_n(z)$, but unstable when applied in the forward direction for $J_n(z)$. The Bessel function of the first kind must be evaluated using (6.4.50) in the reverse direction.

6.5. Double concentric cylinder.

6.5.1 Governing equations.

All physical quantities are referred to cylindrical polar coordinates (r,θ,z). The double concentric cylinder geometry differs from the concentric cylinder geometry in that the rotor cylinder is situated between inner and outer stator cylinders. This forms two coaxial annular regions as shown in figure (3.7). A couple is applied to the rotor cylinder forcing it to make small amplitude angular oscillations of amplitude X_0 and frequency ω about the z-axis.

In the theory, the flow of the fluid contained in the inner annular region is considered separately from the flow of the fluid in the outer annular region. The equations of motion and the velocity profile for each annular region are identical to those describing the

flow of a fluid in a concentric cylinder geometry (section (6.4)). The boundary conditions, however will be different.

The equation of state is defined by equation (6.2.1). i.e.

$$\sigma_{ij} = \eta^{*}\dot{\gamma}_{ij} - pg_{ij} \quad . \tag{6.5.1}$$

The starting point of our analysis of this flow situation is the second order ordinary differential equation defined by (6.4.6). i.e.

$$\frac{d}{dr}\left[r^{3}\frac{dF(r)}{dr}\right] + \alpha^{2}r^{3}F(r) = 0 \quad . \tag{6.5.2}$$

It was shown in section (6.4) that the general solution to this differential equation is given by,

$$F(r) = \frac{1}{r}\left[AJ_{1}(\alpha r) + BY_{1}(\alpha r)\right] \quad , \tag{6.5.3}$$

where $J_{1}(\alpha r)$ and $Y_{1}(\alpha r)$ are first order Bessel functions of the first and second kind respectively, and A and B are arbitrary constants to be determined by satisfying the boundary conditions.

Let the radii of the rotor surface and stationary surface of the inner annulus be r_{2} and r_{1} respectively ($r_{2}>r_{1}$). For the outer annulus, r_{3} is the radius of the rotor surface and r_{4} is the radius of the stationary surface ($r_{4}>r_{3}$) (see figure (3.7)).

Let us first consider the flow of the fluid in the inner annulus. The general solution (6.5.3) to the differential equation (6.5.2), must satisfy the boundary conditions,

$$F(r_{1}) = 0 \quad , \tag{6.5.4}$$

$$F(r_{2}) = i\omega X_{0} \quad , \tag{6.5.5}$$

where as for the outer annulus the boundary conditions, to be satisfied are

$$F(r_{3}) = i\omega X_{0} \quad , \tag{6.5.6}$$

$$F(r_{4}) = 0 \quad . \tag{6.5.7}$$

If we let the radius of the rotor for each annular region be r_{m} and the radius of the stator be r_{s} ,then the two sets of boundary

conditions defined by equations (6.5.6-7) may be covered by the single set below,

$$F(r_m) = i\omega X_0 \quad , \tag{6.5.8}$$

$$F(r_s) = 0 \quad . \tag{6.5.9}$$

Expressed in this form, these boundary conditions are identical to the boundary conditions (6.4.7-8) for the concentric cylinder geometry. Therefore, from equations (6.4.12-13) we see that the constants A and B must be given by,

$$A = \frac{-i\omega X_0 r_m Y_1(\alpha r_s)}{J_1(\alpha r_s)Y_1(\alpha r_m) - Y_1(\alpha r_s)J_1(\alpha r_m)} \quad , \tag{6.5.10}$$

and

$$B = \frac{i\omega X_0 r_m J_1(\alpha r_s)}{J_1(\alpha r_s)Y_1(\alpha r_m) - Y_1(\alpha r_s)J_1(\alpha r_m)} \quad . \tag{6.5.11}$$

Hence the solution to equation (6.5.2) subject to the boundary conditions defined by (6.5.8-9) is,

$$F(r) = \frac{i\omega X_0 r_m}{r}\left[\frac{Y_1(\alpha r)J_1(\alpha r_s) - J_1(\alpha r)Y_1(\alpha r_s)}{J_1(\alpha r_s)Y_1(\alpha r_m) - Y_1(\alpha r_s)J_1(\alpha r_m)}\right] \quad . \tag{6.5.12}$$

The equation of motion of the rotor cylinder is,

$$C_0 e^{i(\omega t+c)} - C_F = -I\omega^2 X_0 e^{i\omega t} \quad , \tag{6.5.13}$$

where I is the moment of inertia of the rotor cylinder.

The couple acting on the middle cylinder due to the motion of the fluid is given by the sum,

$$C_F = C_{Fi} + C_{Fo} \quad . \tag{6.5.14}$$

C_{Fi} is the couple acting on the rotor cylinder due to the motion of the fluid in the inner annulus,

$$C_{Fi} = -2\pi h r_2^2 \sigma_{\theta r}|_{r=r_2} \quad , \tag{6.5.15}$$

and C_{Fo} is the couple acting on the rotor cylinder due to the motion of the fluid in the outer annulus.

$$C_{Fo} = 2\pi h r_3^2 \sigma_{\theta r}|_{r=r_3} \quad . \tag{6.5.16}$$

Using equation (6.4.17) we can deduce that

$$\sigma_{\theta r}|_{r=r_2} = i\omega X_0 \alpha r_2 \left[\frac{Y_1(\alpha r_1)J_2(\alpha r_2) - J_1(\alpha r_1)Y_2(\alpha r_2)}{J_1(\alpha r_1)Y_1(\alpha r_2) - Y_1(\alpha r_1)J_1(\alpha r_2)}\right]\eta^* e^{i\omega t} \quad , \quad (6.5.17)$$

and that

$$\sigma_{\theta r}|_{r=r_3} = i\omega X_0 \alpha r_3 \left[\frac{Y_1(\alpha r_4)J_2(\alpha r_3) - J_1(\alpha r_4)Y_2(\alpha r_3)}{J_1(\alpha r_4)Y_1(\alpha r_3) - Y_1(\alpha r_4)J_1(\alpha r_3)}\right]\eta^* e^{i\omega t} \quad . \quad (6.5.18)$$

The equation of motion of the rotor cylinder (6.5.13) may be expressed as

$$\eta^* C(\alpha^2) = C_a e^{ic} + I\omega^2 X_0 \quad , \quad (6.5.19)$$

where

$$C(\alpha^2) = 2\pi i\omega X_0 h\alpha\left[r_2^3\left[\frac{J_1(\alpha r_1)Y_2(\alpha r_2) - Y_1(\alpha r_1)J_2(\alpha r_2)}{J_1(\alpha r_1)Y_1(\alpha r_2) - Y_1(\alpha r_1)J_1(\alpha r_2)}\right]\right.$$

$$\left. - r_3^3\left[\frac{J_1(\alpha r_4)Y_2(\alpha r_3) - Y_1(\alpha r_4)J_2(\alpha r_3)}{J_1(\alpha r_4)Y_1(\alpha r_3) - Y_1(\alpha r_4)J_1(\alpha r_3)}\right]\right] \quad . \quad (6.5.20)$$

Equation (6.5.19) is valid for all fluid inertia effects and must be solved numerically if we wish to use it to determine the complex viscosity function η^*.

6.5.2. Perturbation method of solution.

Consider the equation of motion of the rotor cylinder. From equation (6.5.13),

$$C_F = (C_0 e^{ic} + I\omega^2 X_0)e^{i\omega t} \quad , \quad (6.5.21)$$

By considering equations (6.4.31-32) inclusively, we are able to deduce that the couple acting on the rotor cylinder due to the flow of the fluid contained in the inner and outer annuli may be approximated by the following expressions. For the inner annulus we have,

$$C_{Fi} \triangleq \frac{4\pi i\omega X_0 h r_1^2 r_2^2}{r_2^2 - r_1^2}\left[1 + (\alpha r_2)^2 C_{1i} + (\alpha r_2)^4 C_{2i}\right]\eta^* e^{i\omega t} \quad , \quad (6.5.22)$$

where,

$$C_{1i} = \frac{1}{2}\left[\frac{3r_1^2 - r_2^2}{4r_1^2} + \frac{r_1^2 \ln(r_1/r_2)}{r_2^2 - r_1^2}\right] \quad , \quad (6.5.23)$$

and

$$C_{2i} =$$

$$\frac{r_1^2}{32r_2^2}\left[\frac{4r_2^2\ln(r_1/r_2)}{r_2^2 - r_1^2}\left[1 + \frac{2r_1^2\ln(r_1/r_2)}{r_2^2 - r_1^2}\right] + \frac{(7r_1^2 - r_2^2)(r_2^2 - r_1^2)}{6r_1^4}\right] \quad . \quad (6.5.24)$$

For the outer annulus,

$$C_{Fo} \triangleq \frac{4\pi i\omega X_0 h r_3^2 r_4^2}{r_4^2 - r_3^2}\left[1 + (\alpha r_4)^2 C_{1o} + (\alpha r_4)^4 C_{2o}\right]\eta^* e^{i\omega t} \quad , \quad (6.5.25)$$

where,

$$C_{1o} = \frac{r_3^2}{2r_4^2}\left[\frac{3r_4^2 - r_3^2}{4r_4^2} + \frac{r_4^2\ln(r_3/r_4)}{r_4^2 - r_3^2}\right] \quad , \quad (6.5.26)$$

and

$$C_{2o} =$$

$$\frac{r_3^2}{32r_4^2}\left[\frac{4r_3^2\ln(r_3/r_4)}{r_4^2 - r_3^2}\left[1 + \frac{2r_4^2\ln(r_3/r_4)}{r_4^2 - r_3^2}\right] - \frac{(7r_4^2 - r_3^2)(r_4^2 - r_3^2)}{6r_4^4}\right] \quad . \quad (6.5.27)$$

Hence the total couple acting on the rotor cylinder is given by,

$$C_F \triangleq 4\pi i\omega X_0 h\left[\frac{r_1^2 r_2^2}{r_2^2 - r_1^2} + \frac{r_3^2 r_4^2}{r_4^2 - r_3^2}\right]\left[1 + (\alpha r_4)^2 C_1 + (\alpha r_4)^4 C_2\right]\eta^* e^{i\omega t} \quad ,$$

(6.5.28)

where,

$$C_1 = \left[r_2^4(r_4^2 - r_3^2)\left[\frac{3r_1^2 - r_2^2}{4} + \frac{r_1^4\ln(r_1/r_2)}{r_2^2 - r_1^2}\right]\right.$$

$$\left. + \; r_3^4(r_2^2 - r_1^2)\left[\frac{3r_4^2 - r_3^2}{4} + \frac{r_4^4\ln(r_3/r_4)}{r_4^2 - r_3^2}\right]\right]$$

$$\Big/ \left[2r_4^2(r_1^2 r_2^2(r_4^2 - r_3^2) + r_3^2 r_4^2(r_2^2 - r_1^2))\right] \quad , \quad (6.5.29)$$

and

$$C_2 =$$

$$\left[r_1^4 r_2^4 (r_4^2 - r_3^2)\left[\frac{r_2^2 \ln(r_1/r_2)}{r_2^2 - r_1^2}\left[1 + \frac{2r_1^2 \ln(r_1/r_2)}{r_2^2 - r_1^2}\right] + \frac{(7r_1^2 - r_2^2)(r_2^2 - r_1^2)}{6r_1^4}\right]\right.$$

$$+ r_3^4 r_4^4 (r_2^2 - r_1^2)\left[\frac{r_3^2 \ln(r_3/r_4)}{r_4^2 - r_3^2}\left[1 + \frac{2r_4^2 \ln(r_3/r_4)}{r_4^2 - r_3^2}\right] - \frac{(7r_4^2 - r_3^2)(r_4^2 - r_3^2)}{6r_4^4}\right]$$

$$\left. \Big/ \left[32r_4^4 (r_1^2 r_2^2 (r_4^2 - r_3^2) + r_3^2 r_4^2 (r_2^2 - r_1^2))\right]\right. \quad . \quad . \quad (6.5.30)$$

From (6.4.37) we can show that the complex viscosity may be expanded in powers of $(\alpha_0 r_4)^2$ terms.

$$\eta^* \triangleq \eta_0^*\left[1 - (\alpha_0 r_4)^2 C_1 - (\alpha_0 r_4)^4 C_2\right] \quad , \quad (6.5.31)$$

where $(\alpha_0 r_4)^2$ is considered small enough to ignore terms of order $(\alpha_0 r_4)^6$. The coefficients C_1 and C_2 are given by (6.5.29-30). If we ignore fluid inertia effects, then the equation of motion of the rotor cylinder reduces to

$$\left[\frac{r_1^2 r_2^2}{r_2^2 - r_1^2} + \frac{r_3^2 r_4^2}{r_4^2 - r_3^2}\right] 4\pi i\omega X_0 h\eta_0^* = C_0 e^{ic} + I\omega^2 X_0 \quad . \quad (6.5.32)$$

Hence the complex viscosity is given by,

$$\eta_0^* = \frac{1}{4\pi i\omega h}\left[\frac{(r_2^2 - r_1^2)(r_4^2 - r_3^2)}{r_1^2 r_2^2 (r_4^2 - r_3^2) + r_3^2 r_4^2 (r_2^2 - r_1^2)}\right]\left[\frac{C_0 e^{ic}}{X_0} + I\omega^2\right] \quad . \quad (6.5.33)$$

Taking real and imaginary parts we obtain the following expressions for dynamic viscosity,

$$\eta_0' = \frac{C_0 \sin(c)}{4\pi\omega X_0 h}\left[\frac{(r_2^2 - r_1^2)(r_4^2 - r_3^2)}{r_1^2 r_2^2 (r_4^2 - r_3^2) + r_3^2 r_4^2 (r_2^2 - r_1^2)}\right] \quad , \quad (6.5.34)$$

and the dynamic rigidity,

$$G_0' = \frac{1}{4\pi h}\left[\frac{(r_2^2 - r_1^2)(r_4^2 - r_3^2)}{r_1^2 r_2^2 (r_4^2 - r_3^2) + r_3^2 r_4^2 (r_2^2 - r_1^2)}\right]\left[\frac{C_0 \cos(c)}{X_0} + I\omega^2\right] \quad . \quad (6.5.35)$$

The first and second order fluid inertia corrections to the complex viscosity function are obtained by substituting equations (6.5.29-30) into equation (6.5.31). The first order fluid inertia correction is given by

$$\eta^*_{(1)} = \eta^*_0 + i\omega\rho r_4^2 C_1 \quad . \tag{6.5.36}$$

Taking real and imaginary parts provides the following expression for the dynamic rigidity function.

$$G'_{(1)} = G'_0 - \omega^2\rho r_4^2 C_1 \quad . \tag{6.5.37}$$

There is no first order fluid inertia correction to the dynamic viscosity function. The second order fluid inertia correction is given by

$$\eta^*_{(2)} = \eta^*_{(1)} + \frac{\omega^2\rho^2 r_4^4}{\eta^*_0} C_2 \tag{6.5.38}$$

Taking real and imaginary parts, we see that the dynamic viscosity is now given by

$$\eta'_{(2)} = \eta'_0\left[1 + \left[\frac{\omega\rho r_4^2}{|\eta^*_0|}\right]^2 C_2\right] \quad , \tag{6.5.39}$$

and that the dynamic rigidity is given by

$$G'_{(2)} = G'_{(1)} - \left[\frac{\omega\rho r_4^2}{|\eta^*_0|}\right]^2 C_2 G'_0 . \tag{6.5.40}$$

6.5.3. Exact method of solution.

Consider the couple equation (6.5.19)

$$\eta^* C(\alpha^2) = C_0 e^{ic} + I\omega^2 X_0 \quad ,$$

where from (6.5.20),

$$C(\alpha^2) = 2\pi i\omega X_0 h\alpha\left[r_2^3\left[\frac{J_1(\alpha r_1)Y_2(\alpha r_2) - Y_1(\alpha r_1)J_2(\alpha r_2)}{J_1(\alpha r_1)Y_1(\alpha r_2) - Y_1(\alpha r_1)J_1(\alpha r_2)}\right] - r_3^3\left[\frac{J_1(\alpha r_4)Y_2(\alpha r_3) - Y_1(\alpha r_4)J_2(\alpha r_3)}{J_1(\alpha r_4)Y_1(\alpha r_3) - Y_1(\alpha r_4)J_1(\alpha r_3)}\right]\right] .$$

Comparing equations (6.5.20) and (6.5.33) we see that η^* and η_0^* are related by the following equation.

$$\eta_0^*\left[\frac{r_1^2r_2^2}{r_2^2 - r_1^2} + \frac{r_3^2r_4^2}{r_4^2 - r_3^2}\right] = \frac{\alpha\eta^*}{2}\left[r_2^3\left[\frac{J_1(\alpha r_1)Y_2(\alpha r_2) - Y_1(\alpha r_1)J_2(\alpha r_2)}{J_1(\alpha r_1)Y_1(\alpha r_2) - Y_1(\alpha r_1)J_1(\alpha r_2)}\right]\right.$$

$$\left. - r_3^3\left[\frac{J_1(\alpha r_4)Y_2(\alpha r_3) - Y_1(\alpha r_4)J_2(\alpha r_3)}{J_1(\alpha r_4)Y_1(\alpha r_3) - Y_1(\alpha r_4)J_1(\alpha r_3)}\right]\right] \quad (6.5.41)$$

Multiplying both sides of (6.5.41) by a complex factor $-1/i\omega\rho$ leads to the non-dimensional equation

$$2(\alpha r_4)\left[\frac{r_1^2r_2^2(r_4^2 - r_3^2) + r_3^2r_4^2(r_2^2 - r_1^2)}{r_3^2(r_2^2 - r_1^2)(r_4^2 - r_3^2)}\right]$$

$$= \alpha_0^2 r_3 r_4\left[\left[\frac{r_2}{r_3}\right]^3\left[\frac{J_1(\alpha r_1)Y_2(\alpha r_2) - Y_1(\alpha r_1)J_2(\alpha r_2)}{J_1(\alpha r_1)Y_1(\alpha r_2) - Y_1(\alpha r_1)J_1(\alpha r_2)}\right]\right.$$

$$\left. - \left[\frac{J_1(\alpha r_4)Y_2(\alpha r_3) - Y_1(\alpha r_4)J_2(\alpha r_3)}{J_1(\alpha r_4)Y_1(\alpha r_3) - Y_1(\alpha r_4)J_1(\alpha r_3)}\right]\right] \quad (6.5.42)$$

This equation is valid for all fluid inertia effects and will be solved numerically using the iterative procedure outlined in section (6.2.3) and defined at the $(k+1)^{th}$ iteration to be,

$$z_{k+1} = z_k - \frac{f(z_k)}{f'(z_k)} \qquad k = 0,1,2,\ldots \quad (6.5.43)$$

where

$$z = (\alpha r_4)^2 \quad (6.5.44)$$

and

$$f(z) = \alpha_0^2 r_3 r_4\left[\left[\frac{r_2}{r_3}\right]^3\left[\frac{J_1(zr_1/r_4)Y_2(zr_2/r_4) - Y_1(zr_1/r_4)J_2(zr_2/r_4)}{J_1(zr_1/r_4)Y_1(zr_2/r_4) - Y_1(zr_1/r_4)J_1(zr_2/r_4)}\right]\right.$$

$$\left. - \left[\frac{J_1(z)Y_2(zr_3/r_4) - Y_1(z)J_2(zr_3/r_4)}{J_1(z)Y_1(zr_3/r_4) - Y_1(z)J_1(\alpha r_3/r_4)}\right]\right]$$

$$- 2z\left[\frac{r_1^2r_2^2(r_4^2 - r_3^2) + r_3^2r_4^2(r_2^2 - r_1^2)}{r_3^2(r_2^2 - r_1^2)(r_4^2 - r_3^2)}\right] \quad (6.5.45)$$

The Bessel functions of the first and second kind $J_n(z)$ and $Y_n(z)$ may be determined via the recursive relation defined by (6.4.50).

6.6. Complex modulus and argument for α^2.

For all geometries considered in this chapter, the parameter α^2 governs fluid inertia effects. From equation (6.2.10), this complex quantity may be written in terms of its complex modulus and argument as follows,

$$\alpha^2 = \frac{\omega\rho}{|\eta^*|} e^{i\delta} \quad , \tag{6.6.1}$$

where $\tan(\delta)$ is defined as the loss tangent (Ferry [16]) and is given by,

$$\tan(\delta) = \frac{\eta'\omega}{G'} \quad . \tag{6.6.2}$$

The loss tangent is a non-dimensional quantity and is a measure of the ratio of the energy dissipated to the energy stored in a periodic deformation. A purely viscous flow is represented by $\tan(\delta)$ being equal to infinity where as setting $\tan(\delta)$ to zero represents a purely elastic deformation. Consequently, the complex argument of α^2 must lie in the range,

$$0 \leqslant \delta \leqslant \pi/2 \quad . \tag{6.6.3}$$

By varying $\omega\rho/|\eta^*|$ over this range of δ, we define a region in which theoretically we are able to examine the effect of fluid inertia on the flow properties of any type of material undergoing a linear viscoelastic deformation.

6.7. Theoretical results and discussion.

In this section we discuss the effect of fluid inertia on the complex viscosity function η^* for the parallel plate, cone and plate, and concentric cylinder geometries. At the present time, dynamic data taken from rheometrical instruments is usually not fully corrected for fluid inertia effects. In this discussion theoretical results will be presented in a form which will provide the experimentalist with an indication of whether the rheometer dynamic data needs to be corrected for fluid inertia.

We shall first discuss fluid inertia effects for the parallel plate system. In figure (6.1) we plot the zero, first, and second order approximations to $(\alpha h)^2$ together with the exact value of this

quantity. Except in the region of magnitudes ($\omega\rho h^2/|\eta^*| \pm 0.05$), large differences occur if fluid inertia effects are not taken into account. However, the first order approximation provides good agreement with the exact value of $(\alpha h)^2$ over the complete range of δ for $\omega\rho h^2/|\eta^*|$ less or equal to 1.0. The accuracy of the perturbation method is further improved if we include second order fluid inertia terms in our calculations. In figure (6.2), a wider range of $\omega\rho h^2/|\eta^*|$ is considered up to a value of 2.0. In this range differences occur between the exact and first and second order approximations.

In order to see the effect of fluid inertia on the complex magnitude and argument, we present figures (6.3-11) inclusive. In these figures a region has been defined in which the area has been divided into eight equal segments in the δ-direction while $\omega\rho h^2/|\eta^*|$ has been divided in increments of five percent. The input grids for all of these figures represent the parameter $(\alpha h)^2$ in which fluid inertia effects have been fully taken into account.

In figures (6.3) to (6.5) the output grid represents the situation where fluid inertia effects have been ignored. Hence any differences between these results demonstrates the full effect of fluid inertia on $(\alpha h)^2$. We can immediately see that the deformation of the output grid with respect to the exact value of $(\alpha h)^2$ is dependent upon both $\omega\rho h^2/|\eta^*|$ and δ. This deformation is greater as δ tends to zero. This is because fluid inertia has a far greater effect on the dynamic rigidity than on the dynamic viscosity. It can be seen from figure (6.4), that the error incurred in $\omega\rho h^2/|\eta^*|$ as a consequence of ignoring fluid inertia effects is less than five percent for all δ, provided $\omega\rho h^2/|\eta^*|$ is less than 0.15. Clearly, as δ approaches $\pi/2$, the range of $\omega\rho h^2/|\eta^*|$ for which we can obtain the five percent accuracy is extended.

It should be noted from figure (6.6), that for $\omega\rho h^2/|\eta^*|$ less or equal to 0.4, second and higher order fluid inertia effects are negligible. Hence we can assume that the differences between the zero order and exact grids in figures (6.4) and (6.5), are due to first order fluid inertia effects. Since first order fluid inertia effects do not influence the dynamic viscosity function, we can deduce that these differences are due to changes in the dynamic rigidity. The result of including fluid inertia in the theory for evaluating $(\alpha h)^2$, is to reduce the magnitude of the complex modulus

$\omega\rho h^2/|\eta^*|$ and to cause a shift in the complex argument δ towards the real axis. Both of these observations are consistent with an increase in the dynamic rigidity function as predicted by equation (6.2.36).

Regions of the zero order grid for which δ is greater than $\pi/2$ may only be explained by negative values of experimental dynamic rigidity data. Figures (6.3) to (6.5), all show that this type of error is corrected by including fluid inertia in the theory.

In figures (6.6) to (6.8), the output grid has been obtained using the first order perturbation method described in section (6.2.2). As previously stated, the first order expressions accurately describe fluid inertia effects provided $\omega\rho h^2/|\eta^*|$ is less or equal to 0.4 . For values of $\omega\rho h^2/|\eta^*|$ greater than 0.4, the effect of fluid inertia is to decrease the magnitude of $\omega\rho h^2/|\eta^*|$ as δ approaches zero, but to increase this quantity as δ approaches $\pi/2$. This is because second and higher order fluid inertia effects influence both the dynamic viscosity and the dynamic rigidity.

Figures (6.7) and (6.8) show large fluid inertia effects occurring as $\omega\rho h^2/|\eta^*|$ is increased to a value of 2.5. As δ tends to either of its limiting values, the error in $\omega\rho h^2/|\eta^*|$ increases.

The output grids for figures (6.9) to (6.11) have been calculated using the second order perturbation method. Figure (6.9) shows that providing $\omega\rho h^2/|\eta^*|$ is less than 0.8 then third and higher order fluid inertia effects are negligible irrespective of the value of δ. We see by comparing figure (6.9) with figure (6.6) that as expected, for small fluid inertia effects, the second order perturbation method provides a more accurate approximation of $(\alpha h)^2$ than the first order method. Figures (6.10) and (6.11) show that this is not necessarily true for larger fluid inertia effects. In figure (6.11), we see that it is possible for at least two values of $(\alpha h)^2$ to be mapped to a single value of $(\alpha_2 h)^2$, and hence to single values $(\alpha_0 h)^2$ and $(\alpha_1 h)^2$. This was predicted by equation (6.2.42) and shows how important it is to provide the numerical scheme defined by (6.2.45) with an accurate initial value.

In the case of the cone and plate geometry we consider the effect of fluid inertia on the complex non-dimensional parameter $(\alpha a\theta_0)^2$. The theoretical curves presented in figures (6.12-13) inclusive, demonstrate fluid inertia effects for the cone and plate geometry. The discrepancies between the input and output curves in

figures (6.12-13), represent the full effect of fluid inertia on $(\alpha a\theta_0)^2$. These figures confirm that the effect of fluid inertia on these quantities follows the same trend as observed for the parallel plate geometry. Figure (6.14) shows the first order fluid inertia approximation for the cone and plate geometry. As expected, this approximation is in better agreement with $(\alpha a\theta_0)^2$ than that provided by the zero order approximation. In the case of the concentric cylinder geometry, figure (6.15) shows a similar effect of fluid inertia on $(\alpha(r_o-r_i))^2$.

Chapter 7

Fluid Inertia Effects in Controlled Stress Oscillation (Experiments).

7.1 Introduction

The aim of this chapter is to show the effects of fluid inertia on experimental dynamic data taken from a Carri-Med controlled stress rheometer. A frequency range of up to 40 Hz was used. The experimental programme will comprise of small amplitude oscillatory shear experiments carried out on three different fluids. These are as follows; a highly elastic 2% solution of polyisobutylene in dekalin, silicone (30 Ns/m^2), which is a slightly elastic fluid, and polybutene, which has a slightly non-Newtonian dynamic viscosity and a small but measurable dynamic rigidity.

Increasing the angular frequency of an oscillatory shear experiment, results in an increase in the magnitude of both mechanical inertia and fluid inertia effects. The mechanical inertia of the rotor platen used must be known accurately, otherwise large errors can occur particularly in the dynamic rigidity data, since mechanical inertia effects are proportional to the square of the angular frequency. In order to accurately predict the mechanical inertia of the system the controlled stress rheometer may be calibrated by carrying out an oscillatory test in air. The full effect of fluid inertia on the dynamic properties of the test sample may be interpreted using the theoretical analysis developed in Chapter 6.

A previous experimental programme on the controlled stress rheometer, carried out by, Jones et al [24], was restricted to a frequency range of 1 Hz to 10 Hz. The effect of fluid inertia on their dynamic data, obtained for a 2% solution of polyisobutylene in dekalin, was interpreted using first order fluid inertia corrections. The experiments were performed using cone and plate, parallel plate, and concentric cylinder geometries. These experiments showed that, for the frequency range considered, a first order fluid inertia correction was capable of adequately describing fluid inertia effects for the cone and plate and parallel plate geometries. However, discrepancies between this experimental data and data sampled on the concentric cylinder geometry suggested that

higher order fluid inertia corrections are required for this geometry.

The current experimental programme will also consider a 2% solution of polyisobutylene in dekalin. As previously mentioned this fluid is a highly elastic mobile fluid, and consequently we would expect fluid inertia effects to be greater for this material than for either the polybutene or the silicone when tested at the same frequencies of oscillation. Dynamic measurements will be carried out for all three of the aforementioned measurement system geometries.

7.2 Experimental Set Up and Procedure.

The experimental apparatus, was essentially the same as that described in Chapter 5. A torque was applied to the rotor platen in the form of a digitised sinusoidal waveform, the frequency of which was set by the use of a timer card in the microcomputer. The maximum resolution of the sinusoidal waveform was governed by the condition that the elapsed time between successive points cannot be less than 250 μs. This resulted in a mean resolution of 400 points per cycle at 10 Hz and a mean resolution of 100 points per cycle at 40 Hz.

The output displacement waveform was measured digitally using an optical encoder measuring system. The displacement amplitude and phase lag between the input and output displacement waveforms were obtained from the software by evaluating the fourier series coefficients through a numerical integration procedure. The data was sampled over a large number of cycles to ensure accurate evaluation of the displacement amplitude and phase lag particularly at high frequencies of oscillation. The maximum number of cycles that could be applied, was governed by the storage capacity of the microcomputer which allowed for the storage of a maximum of 12000 data points. The sinusoidal torque was initially applied to the rotor platen for a number of 'settling' cycles before sampling took place. This was to allow time for the flow field in the fluid to reach a periodic state.

Throughout the experimental programme, the rheometer was operated in auto strain mode. This means that for a frequency sweep experiment the measured strain amplitude was kept constant. The torque required to produce the required strain amplitude was automatically calculated by the rheometer software. The theory developed in Chapter 6 is only valid provided the data is measured in the linear viscoelastic region. This implies a restriction on the

strain or torque amplitude and is dependent on the type of fluid considered. The dynamic properties of the fluid should be independent of strain or torque amplitude. Therefore a torque amplitude sweep was carried out before each experiment in order to determine the strain amplitude required for the data to lie in the linear viscoelastic region. The theory developed in Chapter 6 is also based on the assumption that the fluid under consideration is incompressible. Hence, care was taken to ensure that no bubbles were present in the fluid before sampling commenced.

The dynamic properties of these fluids should be independent of the measurement system geometry. Hence, in order to validate the theoretical expressions developed in Chapter 6 (equations (6.2.42), (6.3.48), and (6.4.46)), the experiments were carried out on the cone and plate, parallel plate, and concentric cylinder geometries. The cone and plate geometry had a 2° gap angle. The platens for the parallel plate geometry were of radius 2cm, and the gap between the platens varied from 250 μm to 1000μm. Three different set-ups were used for the concentric cylinder geometries. The radius of the stator (outer) cylinder was kept at 20.75 mm throughout the programme. The annular gap was varied by changing the rotor (inner) cylinder. Three different rotor cylinders were used of radii 18.5mm, 15.0 mm, and 12.5 mm.

7.3 Results and discussion.

7.3.1 A 2% solution of polyisobutylene in dekalin.

Figure (7.1) shows the variation of dynamic viscosity and dynamic rigidity with frequency for a 2% solution of polyisobutylene in dekalin up to a frequency of 30 Hz. A comparison is made between dynamic data obtained from a cone and plate geometry (gap angle=2°), a parallel plate geometry (gap=0.25 mm), and a concentric cylinder geometry (gap=2.25 mm). These curves were obtained from the raw displacement amplitude and phase data using the exact fluid inertia theory developed in Chapter 6. The experiments were carried out at a constant temperature of 20°C.

The dynamic viscosity shows excellent agreement between the three different geometries for the frequency range considered. There is little difference between the dynamic rigidity data obtained from

the cone and plate geometry and that obtained from the parallel plate geometry up to 30 Hz. The concentric cylinder dynamic rigidity data is in good agreement with the cone and plate and parallel plate data up to 20 Hz. However, at higher frequencies, from 20 Hz to 30 Hz, the concentric cylinder geometry predicts a lower value of the dynamic rigidity function than that obtained from the other two geometries. The concentric cylinder experimental data was found to be reproducible when the experiment was repeated with different batches of the fluid. Hence, it is unlikely that the trend of the concentric cylinder dynamic rigidity data is due to experimental scatter.

The concentric cylinder geometry experiment was repeated for the three different annular gaps. In figure (7.2) we see that agreement is obtained for the dynamic viscosity data between the narrow and medium gaps up to 30 Hz. Reasonable agreement is obtained between these two geometries and the large gap geometry up to 22 Hz. However, from 22 Hz to 30 Hz, the dynamic viscosity function predicted by the large gap geometry begins to increase slightly with frequency. According to the parallel plate and cone and plate data, the dynamic viscosity should be a monotonically decreasing function of frequency. It is also noted that a small step in the large gap dynamic viscosity data occurs between 10 Hz and 11 Hz which is probably due to end effects.

The dynamic rigidity data from figure (7.2) shows that agreement is obtained between all three annular gaps up to a frequency of 9 Hz, and just between the narrow and medium gap geometries up to 13 Hz. It should be noted that there are two sudden steps in the dynamic rigidity function predicted by the large gap geometry. These occur at frequencies of 10 Hz and 23 Hz. There is also a kink in the dynamic rigidity function predicted by the medium gap geometry. This kink occurs between 10 Hz and 20 Hz and is much smoother than the steps in the large gap dynamic rigidity function. This behaviour proved to be reproducible for different samples and for different strain amplitudes ranging from 1 to 10 milli radians.

A possible cause of the discrepancies between the concentric cylinder data and that obtained from the other two geometries in figure (7.1), and between the different concentric cylinder annular gaps in figure (7.2), could be due to end effects. The linear viscoelastic theory developed in Chapter 6 assumes that the

dimensions of the shearing surfaces are infinite. However, when applying this theory to interpret experimental data, end effects due to the finite dimensions of the measurement system geometry are ignored.

The rotor cylinder in the concentric cylinder geometry, has an air cavity situated on the bottom surface in order to reduce the area of this bottom surface in contact with the fluid. This cavity also makes it easier to set up the experiment without introducing bubbles into the sample. However, there is still a small area of the bottom surface in contact with the fluid. This part of the cylinder subsequently forms a shearing surface that is neglected in the theoretical analysis. It is also possible for a small amount of fluid to enter the air cavity thus creating another shearing surface on the inner wall of this cylinder. These shearing surfaces exert an extra drag on the rotor cylinder resulting in a reduction in the displacement amplitude of this member.

We must also note that, the fluid in contact with the bottom surface of the rotor cylinder is subject to fluid inertia effects. As stated previously, this shearing surface is not taken into account in the theory. Therefore, any end correction must take into account fluid inertia effects.

Another contributing factor to the discrepancies observed in the concentric cylinder dynamic data, could be temperature effects. The temperature of the experiment was controlled by maintaining the ram plate (see figure (3.6)) at the required setting. It was not possible to obtain a temperature jacket for the purpose of ensuring that the temperature was constant throughout the sample. Hence, a small temperature gradient might exist across the platen gap, giving rise to incorrect dynamic data.

In figures (7.3) and (7.4), we consider the effect of fluid inertia on dynamic data obtained from a large gap concentric cylinder geometry (gap=8.25 mm). Fluid inertia effects are clearly important for both the dynamic viscosity and dynamic rigidity calculations. It should be noted that if fluid inertia effects are not taken into account in figure (7.3), then the dynamic viscosity data show an apparent shear thickening followed by a shear thinning behaviour as frequency is increased. Similarly in figure (7.4), the dynamic rigidity data show an apparent structure breakdown followed by a structure recovery as frequency is increased. Similar observations

can be made about the dynamic viscosity and dynamic rigidity data presented in figures (7.5) and (7.6) for the medium gap concentric cylinder geometry (gap=5.75 mm).

We again draw attention to the discrepancies in the exact dynamic rigidity data at 10 Hz and 23 Hz for the large gap concentric cylinder (figure (7.5)), and at 15 Hz for the medium gap concentric cylinder (figure (7.6)). The equation, (6.4.46), used to interpret the effect of fluid inertia on dynamic data contain periodic functions which can lead to multi-valued solutions. In order to check that the numerical scheme employed to solve the equation for the concentric cylinder system, (6.4.47), converged to the correct solution, we substituted exact values of the dynamic viscosity and dynamic rigidity back into equation (6.4.46). This equation was then used to predict the uncorrected dynamic data.

The predictions from this theoretical exercise are presented in figures (7.7) and (7.8). The corrected dynamic data was based on the assumption that dynamic viscosity and dynamic rigidity predicted by the cone and plate geometry in figure (7.1) is accurately predicted. This data was then fitted with a power law relationship, (see figure (7.9)).

The theoretical curves presented in figures (7.7) and (7.8) for medium and large concentric cylinder gaps, clearly show the oscillating nature of the dynamic data when fluid inertia effects are not included. It should be noted that the uncorrected dynamic curves are in very good agreement with the uncorrected experimental data presented in figures (7.3) to (7.6) inclusive, which confirms that our numerical scheme converged to the right solution for fluid inertia effects.

In figures (7.10) and (7.11), we consider dynamic data from the narrow gap concentric cylinder geometry. The uncorrected dynamic viscosity and dynamic rigidity curves are in very good agreement with the theoretical predictions shown in figures (7.7) and (7.8). Also displayed in these figures, are the first and second order fluid inertia corrections for the dynamic data. It should be noted that the first order fluid inertia correction does not affect the dynamic viscosity function. Figure (7.10) shows that fluid inertia has a small effect on the the dynamic viscosity data up to 30 Hz. The small discrepancies between the exact and uncorrected data in the frequency range of 25 Hz to 30 Hz, are adequately described by the

second order fluid inertia correction. In figure (7.11), we see that the first order fluid inertia correction is in good agreement with the exact data up to 20 Hz. The second order fluid inertia correction is now in agreement with the exact data up to 24 Hz.

In figure (7.12), good agreement is obtained between the dynamic viscosity and dynamic rigidity functions obtained from the 0.25 mm and 0.5 mm gap parallel plate geometries. The effect of fluid inertia on the dynamic data for the 0.5 mm gap geometry is considered in figure (7.13). Fluid inertia effects up to 30 Hz, may be adequately described using the first order correction. Similarly, fluid inertia effects on the cone and plate geometry (figure (7.14)), for the frequency range considered, may be adequately described by the the first order correction.

7.3.2. Silicone (30 Ns/m^{-2}).

Figures (7.15) to (7.20) inclusive show the variation of dynamic data with frequency for silicone up to a frequency of 40 Hz. The full effect of fluid inertia on the dynamic data has been taken into account. These experiments were carried out at a constant temperature of 25 C. In figure (7.15), we compare dynamic data obtained from the three types of geometry considered in this work. The dimensions of the geometries used in figure (7.15) are as defined in figure (7.1). It should be noted that over the frequency range considered, the dynamic data shows virtually no experimental scatter. Excellent agreement is obtained between both the dynamic viscosity and the dynamic rigidity obtained from the cone and plate and parallel plate geometries. The concentric cylinder results, however, do differ slightly from the predictions of the other two geometries. In order to consider the concentric cylinder geometry in greater detail, we vary the annular gap, (figure (7.16)). Again we observe discrepancies between the dynamic data predicted by the three gaps. The value of both the dynamic viscosity and the dynamic rigidity data at a given value of the frequency, increases as the annular gap increases. Possible reasons for the discrepancies in both figure (7.15) and (7.16) were discussed earlier in connection with the 2% solution of polyisobutylene in dekalin results. In figure (7.17), very good agreement is obtained between the dynamic data from a 0.25 mm, 0.5 mm, and a 1 mm parallel plate gap.

From figures (7.18) to (7.20), we can clearly see that, as

expected, fluid inertia effects are smaller for silicone than for the 2% solution of polyisobutylene in dekalin. We see that for the large gap concentric cylinder geometry (figure (7.18)), and the 1 mm gap parallel plate geometry, (figure (7.19)), the effect of fluid inertia on the dynamic data over the frequency range considered, can be adequately described by a first order correction. The cone and plate results displayed in figure (7.20), show that fluid inertia effects are not important for this geometry over the frequency range considered.

7.3.3 Polybutene.

In figures (7.21) to (7.23), we present dynamic data for polybutene up to a frequency of 30 Hz. This material possesses a slightly non-Newtonian dynamic viscosity. These experiments were carried out at a constant temperature of 20 C. The comparison between exact dynamic data obtained from the cone and plate geometry, and the 0.5 mm and 1 mm parallel plate gap geometries, shows good agreement for the dynamic viscosity data predicted by the three geometries. However, for the dynamic rigidity, slight differences between 1 mm gap parallel plate data and that obtained from the other two geometries are observed at frequencies between 25 Hz and 30 Hz. As mentioned previously, contributary factors to this discrepancy could be edge effects or temperature effects. Figures (7.22) and (7.23) show that the effect of fluid inertia on the dynamic properties of polybutene are small for the parallel plate and cone and plate geometries considered in this work.

7.4. Comments.

In this experimental programme a Carri-Med controlled stress rheometer was used to measure the dynamic properties of three different fluids over a frequency range of 0.01 Hz to 30 Hz, (up to 40 Hz for silicone (30 Ns/m^2)). Previous work by Jones et al [24], was restricted to a maximum frequency of 10 Hz and therefore fluid inertia effects were not as large as those observed in this work. The linear viscoelastic analysis carried out in Chapter 6 was used to interpret the effect of fluid inertia on the dynamic data over the frequency range considered. This analysis should predict dynamic viscosity and dynamic rigidity data that is independent of the

measurement system geometry. In general, good agreement was obtained between the dynamic data obtained from the different geometries considered in this work, an exception to this being, the concentric cylinder dynamic rigidity data measured at frequencies of oscillation greater than 25 Hz.

Discrepancies were observed between the dynamic rigidity data predicted by the concentric cylinder geometries, and that predicted by the parallel plate and cone and plate geometries for both the 2% solution of polyisobutylene in dekalin and the silicone sample. Discrepancies were also observed in the dynamic data for these fluids predicted by the different concentric cylinder annular gaps. It is possible, that these discrepancies could be due to end effects or temperature effects. The influence of end effects on the dynamic data, could be reduced by the use of a double concentric cylinder geometry. As shown in figure (3.7), there is only a small area of the rotor platen in contact with the fluid that is not included in the theoretical analysis for this geometry.

As expected, the largest fluid inertia effects were observed in experiments involving the polyisobutylene solution. The dynamic data for the 2% solution of polyisobutylene in dekalin was sampled up to a frequency of 30 Hz. The fluid inertia effects observed for the parallel plate (gap=0.25 mm, 0.5 mm) and the cone and plate (gap angle=2°) geometries were small and could be adequately described by the first order fluid inertia theory.

The dynamic data obtained from the large and medium gap concentric cylinder geometries demonstrated that large fluid inertia effects can cause the uncorrected dynamic viscosity and dynamic rigidity data to oscillate when plotted against frequency. We were able to predict this oscillatory behaviour theoretically using the analysis developed in Chapter 6. Good agreement was obtained between these theoretical predictions and the experimental results.

The work contained in this chapter has been accepted for publication in Revista Portuguesa de Hemorreologia.

Chapter 8

Yield stress effects in controlled stress oscillation.

8.1. Introduction.

In this final chapter, we are concerned with the theoretical description of the non-linear effect of yield stress on viscoelastic dynamic behaviour. As discussed previously in Chapter 2, a yield stress model provides a useful approximation for the description of the flow behaviour of many types of material e.g. gels, slurries, pastes, concentrated dispersions.

The yield stress model predicts an infinite shear viscosity at zero shear rates. Real materials, however, have a finite zero shear viscosity and hence a Newtonian viscosity region. It therefore follows that it is theoretically possible to obtain dynamic data in the linear viscoelastic region. In practice this is not possible, since the strain amplitudes required for dynamic data to be taken in the linear viscoelastic region, are too small to be accurately measured on rheometrical instruments.

The motivation for the work carried out in this chapter was provided by dynamic experiments in which a Carri-Med controlled stress rheometer was used to apply a sinusoidal torque to a 'yield stress' material. A typical displacement waveform obtained from these experiments is displayed in figure (8.1). The non-sinusoidal displacement waveform shows ranges of applied stress over which the change in displacement is very small ($< 10^{-5}$ radians). This observation is commonly known as 'flat topping'. This will occur in the region where the applied torque does not exceed the yield stress of the material. Following the ideas of Barnes and Walters [3] on the non-existence of yield stress, an alternative explanation of 'flat topping' can be ascribed to the shear thinning properties of the material (Perkins [33]). In figure (8.2) the complex viscosity is clearly torque amplitude dependent. We therefore have a non-linear viscoelastic flow situation.

Previous work relevant to the problem of describing the dynamic response of 'yield stress' materials has been carried out by Yoshimura and Prud'homme [47]. These workers modified the two parameter Bingham model (Bird et al [6]), to include recoverable

elastic strain below the yield stress or yield strain. This modified model is called the elastic Bingham model (see Chapter 2). The model describes elastic deformation below the yield stress. Above the yield stress, the model describes viscous flow characterised by a constant plastic viscosity and a yield stress. The flow situation considered by Yoshimura and Prud'homme [47] was one in which a sinusoidal shear strain was applied to the fluid.

The work carried out in this chapter, makes use of the concept of yield stress to describe the non-linear viscoelastic dynamic behaviour displayed in figure (8.1). The model is presented in figure (8.3) and differs from that of Yoshimura and Prud'homme [47] in that it is not able to predict elastic deformation below the yield stress. However, the model has the advantage of reducing to a generalised linear viscoelastic model when the yield stress is zero.

It is convenient to characterise the dynamic response of these so called 'yield stress' materials in terms of a plastic complex viscosity and the yield stress. We can think of the plastic complex viscosity as being analagous to the plastic shear viscosity in steady shear flow. It should be noted in this model that the plastic complex viscosity will be independent of oscillatory stress amplitude.

8.2. Description of the model.

The model is shown diagramatically in figure (8.3). It consists of n Maxwell elements connected in parallel with a yield stress component. The model will not deform unless the applied stress exceeds some critical stress value. The condition for flow to occur is that the magnitude of the difference between the applied stress, σ, and the sum of the stresses in the Maxwell elements, $\sum_i \sigma_i$, must be equal to the yield stress σ_0. i.e.

$$\left| \sigma - \sum_{i=1}^{n} \sigma_i \right| = \sigma_0 \quad . \qquad (8.2.1)$$

The stress response of the model is made up of the sum of the stresses in the Maxwell elements σ_i, and the stress in the yield stress element σ_y. i.e.

$$\sigma = \sum_{i=1}^{n} \sigma_i + \sigma_y \quad . \qquad (8.2.2)$$

When a stress is initially applied to the model, the stresses in the Maxwell elements are completely relaxed. Hence, the condition for initial flow to occur is given by,

$$\left| \sigma \right| > \sigma_0 \quad . \qquad (8.2.3)$$

(a). Response of Maxwell elements.

Referring to section (2.2), equations (2.2.5) to (2.2.10) inclusive, we see that in the i^{th} Maxwell element, the stress is related to the shear rate by the following first order linear differential equation in σ_i.

$$\sigma_i + \lambda_i \dot{\sigma}_i = \eta_i \dot{\gamma} \quad , \quad i=1,2,\ldots,n \quad , \qquad (8.2.4)$$

where the dot denotes differentiation with respect to time.

By solving this differential equation we obtain the shear stress σ_i in terms of the shear rate and is given by

$$\sigma_i = \int_{-\infty}^{t} \frac{\eta_i}{\lambda_i} e^{-(t-t')/\lambda_i} \dot{\gamma}(t')\, dt' \quad . \qquad (8.2.5)$$

The total stress in the n Maxwell elements is therefore given by

$$\sum_{i=1}^{n} \sigma_i = \int_{-\infty}^{t} G(t-t')\, \dot{\gamma}(t')\, dt' \quad . \qquad (8.2.6)$$

where the relaxtion modulus G(t-t') for n Maxwell elements is given by

$$G(t-t') = \sum_{i=1}^{n} \frac{\eta_i}{\lambda_i} e^{-(t-t')/\lambda_i} \quad . \qquad (8.2.7)$$

When an oscillatory stress is applied to the fluid, there will be ranges of applied stress for which the flow condition (8.2.1) is not satisfied and the shear rate will therefore be zero. During this part of the periodic cycle, we see from equation (8.2.4) that in the i^{th} Maxwell element stress relaxation takes place according to the equation

$$\sigma_i = \frac{A_i}{\lambda_i} e^{-t/\lambda_i} \quad , \quad \dot{\gamma} = 0 \quad , \qquad (8.2.8)$$

The total stress for n Maxwell elements is

$$\sum_{i=1}^{n} \sigma_i = \sum_{i=1}^{n} \frac{A_i}{\lambda_i} e^{-t/\lambda_i} \quad , \quad \dot{\gamma} = 0 \quad , \qquad (8.2.9)$$

where the A_i's are arbitrary constants which can be determined from the condition that the stresses σ_i must be continuous for all time t.

(b). Response of yield stress element (σ_y).

When the shear rate is non-zero, then the stress in the yield stress element will have one of two values, $\pm\sigma_0$. i.e.

$$\sigma_y = \frac{\dot{\gamma}(t)}{|\dot{\gamma}(t)|} \sigma_0 \quad , \quad \dot{\gamma}(t) \neq 0 \quad . \qquad (8.2.10)$$

However, when the shear rate is zero, then σ_y is indeterminate but must satisfy the condition

$$|\sigma_y| < \sigma_0 \quad , \quad \dot{\gamma}(t) = 0 \quad . \qquad (8.2.11)$$

Substituting equations (8.2.6), (8.2.9) and (8.2.10) into equation (8.2.2), we obtain the equation of state for the model presented in fiqure (8.3) and is given by

$$\sigma = \begin{cases} \int_{-\infty}^{t} G(t-t')\, \dot{\gamma}(t')\, dt' + \sigma_0 \frac{\dot{\gamma}(t)}{|\dot{\gamma}(t)|} & , \quad \dot{\gamma}(t) \neq 0 \quad . \\ \sum_{i=1}^{n} \frac{A_i}{\lambda_i} e^{-t/\lambda_i} + \sigma_y & , \quad \dot{\gamma}(t) = 0 \quad . \end{cases} \qquad (8.2.12)$$

where G(t-t') is given in equation (8.2.7), σ_y satisfies the condition (8.2.11) and A_i,s are constants which are determined from satisfying the condition that the stress in each Maxwell element is continuous. We shall now use this equation of state in the flow situation encountered on the Carri-med controlled stress rheometer.

8.3. Solution of the equation of motion.

In a controlled stress rheometer The fluid is contained between two platens. One platen, the stator, is fixed and the other platen, the rotor, is free to rotate under an applied couple. The theory will assume that the shear rate throughout the measurement system gap is constant. Hence, this analysis is valid for the small gap angle cone and plate geometry and the narrow annular gap concentric cylinder geometry. In order to obtain a basic understanding of the solution to the theoretical equations we shall only be concerned with the theory for the case when mechanical inertia of the rotor is ignored.

Consider a sinusoidal torque being applied to the upper rotor of the form

$$C = C_0 \sin(\omega t), \qquad t>0 \quad . \tag{8.3.1}$$

When the mechanical inertia of the rotor is ignored then on applying the equation of motion to the upper platen, the shear stress applied to the sample is also sinusoidal and is given by

$$\sigma = \sigma_a \sin(\omega t), \qquad t>0 \quad . \tag{8.3.2}$$

where σ_a is the stress amplitude and is related to the torque amplitude by the formula

$$C_0 = F_\sigma \sigma_a \quad . \tag{8.3.3}$$

F_σ is known as the platen geometry shear stress factor.

Substituting for the stress σ from equation (8.3.2) into the equation of state (8.2.12) we have for the case when $\dot\gamma \neq 0$

$$\sigma_a \sin(\omega t) = \int_{-\infty}^{t} G(t-t')\,\dot\gamma(t')\,dt' + \sigma_0 \frac{\dot\gamma(t)}{|\dot\gamma(t)|} \quad , \quad \dot\gamma(t)\neq 0 \tag{8.3.4}$$

In order to determine the shear rate and shear strain waveforms it is necessary to formulate this equation in its differential form. This is obtained by applying the differential operator $\prod_{i=1}^{n}(1+\lambda_i d/dt)$ to equation (8.3.4) to give the following $(n-1)^{th}$ order linear differential equation in $\dot\gamma$

$$\sum_{k=1}^{n} \eta_k \prod_{\substack{i=1 \\ i\neq k}}^{n} \left[1 + \lambda_i \frac{d}{dt}\right]\dot\gamma = \prod_{i=1}^{n} \left[1 + \lambda_i \frac{d}{dt}\right]\sigma_a \sin(\omega t) - \sigma_0 \frac{\dot\gamma(t)}{|\dot\gamma(t)|} \quad , \quad \gamma(t)\neq 0 \tag{8.3.5}$$

This equation can now be solved to produce the shear rate and hence produce the shear strain. The solution to this equation is discussed in the following section.

8.3.1. Determination of the shear rate function

Equation (8.3.5) can be solved by considering the solution as the sum of two parts; the complementary function (CF) and the particular integral (PI). i.e.

$$\dot{\gamma} = \dot{\gamma}_{CF} + \dot{\gamma}_{PI} \quad . \tag{8.3.6}$$

(a). The complementary function.

The complementary function for equation (8.3.5) is obtained by solving the homogeneous differential equation

$$\sum_{k=1}^{n} \eta_k \prod_{\substack{i=1 \\ i\neq k}}^{n} \left[1 + \lambda_i \frac{d}{dt} \right] \dot{\gamma} = 0 \quad . \tag{8.3.7}$$

We may assume $\dot{\gamma}_{CF}$ to be of the form

$$\dot{\gamma}_{CF} = \sum_{k=1}^{n} c_k e^{m_k t} \quad . \tag{8.3.8}$$

where c_k and m_k are constants.
Substituting (8.3.8) into (8.3.7) we have

$$\sum_{k=1}^{n} \frac{\eta_k}{(1 + \lambda_k m)} \prod_{i=1}^{n} (1 + \lambda_i m) = 0 \quad . \tag{8.3.9}$$

Since the term $\prod_{i=1}^{n} (1+\lambda_i m) \neq 0$ then equation (8.3.9) simplifies to

$$\sum_{k=1}^{n} \frac{\eta_k}{(1 + \lambda_k m)} = 0 \quad . \tag{8.3.10}$$

This equation is a (n-1)th order polynomial in m and can be solved to produce the (n-1) roots m_i (i=1,2,..,n-1).

(b). The particular integral.

To obtain the particular integral to equation (8.3.5) it is convenient to express this equation in complex number form. i.e.

$$\sum_{k=1}^{n} \eta_k \prod_{\substack{i=1 \\ i\neq k}}^{n} \left[1 + \lambda_i \frac{d}{dt}\right] \dot{\gamma} = C_a \mathrm{Im}\left[\prod_{i=1}^{n} \left[1 + j\lambda_i\omega\right] e^{j\omega t}\right] - \sigma_0 \frac{\dot{\gamma}(t)}{|\dot{\gamma}(t)|} \quad , \quad \dot{\gamma}(t)\neq 0 \tag{8.3.11}$$

where Im denotes of imaginary part of the quantity contained within the square brackets.

We may assume a particular integral of the form

$$\dot{\gamma}_{PI} = \mathrm{Im}\left[B\, e^{j\omega t} \right] + C \quad . \tag{8.3.12}$$

where B and C are constants.

Substituting equation (8.3.12) into equation (8.3.11) and equating sinusoidal terms the complex constant B must satisfy the equation

$$B \sum_{k=1}^{n} \frac{\eta_k}{(1 + j\lambda_k\omega)} = \sigma_a \quad . \tag{8.3.13}$$

To simplify this equation it is convenient to define the plastic complex viscosity η_p^* by

$$\eta_p^* = \eta_p' - j\frac{G_p'}{\omega} = \sum_{k=1}^{n} \frac{\eta_k}{(1 + j\lambda_k\omega)} \quad . \tag{8.3.14}$$

This definition is normally associated with the complex viscosity predicted by the Generalised Maxwell linear viscoelastic model. However, we now have a yield stress element incorporated into the model and so the above quantity can no longer be thought of as the complex viscosity function.

Using the above definition for plastic complex viscosity we may rewrite equation (8.3.13) for the constant B as

$$B = \frac{\sigma_a}{\eta_p^*} \quad . \tag{8.3.15}$$

To obtain the constant C in equation (8.3.12) we substitute equation (8.3.12) into equation (8.3.11) and equate the constant terms to give

$$C = -\frac{\sigma_0 \dot{\gamma}}{\eta_0 |\dot{\gamma}|} \quad . \tag{8.3.16}$$

where η_0 is defined by the equation

$$\eta_0 = \sum_{k=1}^{n} \eta_k \quad . \tag{8.3.17}$$

Substituting for the constants B and C from equations (8.3.15) and (8.3.16) respectively into (8.3.12) the particular integral is

$$\dot{\gamma}_{PI} = \mathrm{Im}\left[\frac{\sigma_a}{\eta_p^*} e^{j\omega t} \right] - \frac{\sigma_0}{\eta_0} \frac{\dot{\gamma}}{|\dot{\gamma}|} \quad . \tag{8.3.18}$$

The general solution to the differential equation (8.3.5) can now be obtained by substituting equations (8.3.8) and (8.3.18) into (8.3.6) to give

$$\dot{\gamma} = \sum_{i=1}^{n-1} c_i e^{m_i t} + \mathrm{Im}\left[\frac{\sigma_a}{\eta_p^*} e^{j\omega t} \right] - \frac{\sigma_0}{\eta_0} \frac{\dot{\gamma}}{|\dot{\gamma}|} \quad , \quad \dot{\gamma} \neq 0 \tag{8.3.19}$$

Over any one particular cycle of oscillation there will be two regions of time in which in which the shear rate is zero. i.e. there will be a region of time in which $\dot{\gamma} > 0$ and a region of time in which $\dot{\gamma} < 0$. If we denote the time region for the case $\dot{\gamma} > 0$ by $t_1 \leq t < t_2$ and the time region for the case $\dot{\gamma} < 0$ by $t_3 \leq t < t_4$, then the shear rate in equation (8.3.19) over any one cycle of oscillation may be written as

$$\dot{\gamma} = \begin{cases} 0 & , \quad t_4 - 2\pi/\omega \leq t < t_1 \\ \sum_{i=1}^{n-1} c_i e^{m_i t} + \mathrm{Im}\left[\frac{\sigma_a}{\eta_p^*} e^{j\omega t} \right] - \frac{\sigma_0}{\eta_0} & , \quad t_1 \leq t < t_2 \\ 0 & , \quad t_2 \leq t < t_3 \\ \sum_{i=1}^{n-1} c_i e^{m_i t} + \mathrm{Im}\left[\frac{\sigma_a}{\eta_p^*} e^{j\omega t} \right] + \frac{\sigma_0}{\eta_0} & , \quad t_3 \leq t < t_4 \end{cases} \tag{8.3.20}$$

It should be noted, that the complementary function (8.3.8) has to be included in the general solution (8.3.20). This complementary function is usually associated with transient terms which are important in start-up flow, but which normally decay to zero after a sufficient time has elapsed. However, for the flow problem considered in this work, the complementary function does not disappear, even when the flow has reached its periodic state. The exception to this situation, is the case of a single Maxwell element, (n=1). For this case, the differential equation reduces to an analytical expression for the shear rate and will be discussed later.

In the expression for the shear rate in equation (8.3.20) we shall need to obtain the three sets of constants m_i, c_i, (i=1,2,...,n-1) and t_m, (m=1,2,3,4). The constants m_i have been discussed previously and are determined from the roots to the $(n-1)^{th}$ order polynomial (8.3.10). The derivation of the constants c_i and t_m are discussed in section (8.3.3) and are obtained numerically by satisfying relevant boundary conditions. In general these constants will be different in value for each cycle of oscillation until the periodic state has been reached.

8.3.2. Derivation of the fundamental shear rate amplitude

In order for us to be able to calculate the complex viscosity function for our model shown in figure (8.3) we shall need to evaluate the fundamental amplitude and phase of the shear rate waveform derived in equation (8.3.20).

We use a Fourier series analysis to determine the fundamental amplitude and phase of the shear rate expression presented in equation (8.3.20). We show that it is possible to obtain an analytical expression for the fundamental amplitude and phase for the shear rate waveform in terms of the contants m_i, c_i, (i=1,2,...,n-1) and t_m, (m=1,2,3,4) which appear in equation (8.3.20).

The Fourier series expansion for the shear rate expression obtained in equation (8.3.20) may be written as

$$\dot{\gamma} = \frac{1}{2} a_0 + \sum_{i=1}^{\infty} a_i \cos(\omega t) + b_i \sin(\omega t) \qquad (8.3.21)$$

The fundamental amplitude for the shear rate is therefore given by

$$c_1 = \left[a_1^2 + b_1^2 \right]^{\frac{1}{2}} , \qquad (8.3.22)$$

and the phase difference α between the applied stress and the fundamental harmonic of the shear rate waveform is given by

$$\tan(\alpha) = \frac{b_1}{a_1} \quad . \tag{8.3.23}$$

It is convenient to rewrite equation (8.3.21) in complex form to give

$$\dot{\gamma} = \frac{1}{2} d_0 + \sum_{i=1}^{\infty} d_i e^{j\omega t} \tag{8.3.24}$$

where $d_0 = a_0$, and $d_i = a_i + jb_i$ is the complex amplitude of the i^{th} harmonic. Hence the fundamental complex amplitude d_1 for the shear rate waveform may be obtained from evaluating the integral

$$d_1 = \frac{\omega}{\pi} \int_0^{2\pi/\omega} \dot{\gamma}(t)\ e^{j\omega t} dt \quad . \tag{8.3.25}$$

where $\dot{\gamma}$ is given by equation (8.3.20)

In equation (8.3.20) we see that ,over any one period of oscillation, the non zero shear rate times lie in the intervals $t_1 \leqslant t < t_2$ and $t_3 \leqslant t < t_4$. Hence equation (8.3.25) become

$$d_1 = \frac{\omega}{\pi} \int_{t_1}^{t_2} \dot{\gamma}(t)\ e^{j\omega t} dt + \frac{\omega}{\pi} \int_{t_3}^{t_4} \dot{\gamma}(t)\ e^{j\omega t} dt \quad . \tag{8.3.26}$$

We shall only be interested in the fundamental amplitude when a sufficient number of cycles of oscillation has ocurred. i.e. when the solution has reached it's periodic state. When this occurs it can be shown by symmetry that t_3 and t_4 are related to t_1 and t_2 by

$$\left.\begin{aligned} t_3 &= t_1 + \frac{\pi}{\omega} \\ \text{and} \qquad t_4 &= t_2 + \frac{\pi}{\omega} \end{aligned}\right\} \tag{8.3.27}$$

On making the substitution $u = t - \pi/\omega$ in the second integral in equation (8.3.26) and using equation (8.3.27) the complex amplitude in equation (8.3.26) reduces to

$$d_1 = \frac{2\omega}{\pi} \int_{t_1}^{t_2} \dot{\gamma}(t)\ e^{j\omega t}\ dt \quad , \tag{8.3.28}$$

Substituting for $\dot{\gamma}$ from equation (8.3.20) into equation (8.3.28) we have

$$d_1 = \frac{2\omega}{\pi} \int_{t_1}^{t_2} \left[\sum_{i=1}^{n-1} c_i e^{m_i t} + \mathrm{Im}\left[\frac{\sigma_a}{\eta_p^*} e^{j\omega t} \right] - \frac{\sigma_0}{\eta_0} \right] e^{j\omega t} \, dt \quad . \tag{8.3.29}$$

Using the complex number result

$$\mathrm{Im}[z] = \frac{1}{2j} \left[z - \bar{z} \right] \quad , \tag{8.3.30}$$

where $\bar{z}$ is the complex conjugate of z, then equation (8.3.29) may be written as

$$d_1 = \frac{2\omega}{\pi} \int_{t_1}^{t_2} \left[\sum_{i=1}^{n-1} c_i e^{(m_i + j\omega)t} + \frac{\sigma_a}{2j\eta_p^*} e^{2j\omega t} - \frac{\sigma_a}{2j\bar{\eta}_p^*} - \frac{\sigma_0}{\eta_0} e^{j\omega t} \right] dt \tag{8.3.31}$$

Evaluating the integral in equation (8.3.31) produces the analytical expression,

$$d_1 = \frac{2\omega}{\pi} \left[\sum_{i=1}^{n-1} \frac{c_i}{(m_i + j\omega)} e^{(m_i + j\omega)t} - \frac{\sigma_a}{4\omega\eta_p^*} e^{2j\omega t} - \frac{\sigma_a t}{2j\bar{\eta}_p^*} - \frac{\sigma_0}{j\omega\eta_0} e^{j\omega t} \right]_{t_1}^{t_2} . \tag{8.3.32}$$

Taking real and imaginary parts of d_1 provides analytical expessions for a_1 and b_1 respectively.

$$a_1 = \frac{2\omega}{\pi} \left[\sum_{i=1}^{n-1} \frac{c_i \cos(\omega t - \beta_i)}{(m_i^2 + \omega^2)^{\frac{1}{2}}} e^{m_i t} - \frac{\sigma_a}{4\omega|\eta_p^*|} \left[\cos(2\omega t + \delta) - \frac{2G't}{|\eta_p^*|} \right] \right.$$

$$\left. - \frac{\sigma_0}{\omega\eta_0} \sin(\omega t) \right]_{t_1}^{t_2} . \tag{8.3.33}$$

and

$$b_1 = \frac{2\omega}{\pi} \left[\sum_{i=1}^{n-1} \frac{c_i \sin(\omega t - \beta_i)}{(m_i^2 + \omega^2)^{\frac{1}{2}}} e^{m_i t} - \frac{\sigma_a}{4\omega|\eta_p^*|} \left[\sin(2\omega t + \delta) - \frac{2\eta' t}{|\eta_p^*|} \right] \right.$$

$$\left. + \frac{\sigma_0}{\omega\eta_0} \cos(\omega t) \right]_{t_1}^{t_2} . \tag{8.3.34}$$

where

$$\tan(\beta_i) = \frac{\omega}{m_i} \quad , \tag{8.3.35}$$

and

$$\tan(\delta) = \frac{\eta'_p \omega}{G'_p} \quad . \tag{8.3.36}$$

The fundamental amplitude and phase for the shear rate waveform is determined by substituting equations (8.3.33) and (8.3.34) into equations (8.3.22) and (8.3.23).

8.3.3. Derivation of the constants c_i and t_i in equation (8.3.20)

In order to determine the constants c_i and t_i we first consider the simplest case of a single Maxwell element in parallel with a yield stress component. In this case, the complementary function in equation (8.3.20) vanishes, and hence, we only need to determine the constants t_i. We shall then discuss the more general case of n Maxwell elements in parallel with an yield stress component.

(a). Single Maxwell element.

To facilitate the explanation concerning the derivation of the constants t_i, we present the periodic shear rate waveform (figure (8.4)), in advance of the discussion concerning the determination of these constants.

For the single element model, equation (8.3.20) simplifies to

$$\dot{\gamma} = \begin{cases} 0 & , \quad t_4 - 2\pi/\omega \leq t < t_1 \\ \mathrm{Im}\left[\dfrac{\sigma_a}{\eta^*_p} e^{j\omega t} \right] - \dfrac{\sigma_0}{\eta_1} & , \quad t_1 \leq t < t_2 \\ 0 & , \quad t_2 \leq t < t_3 \\ \mathrm{Im}\left[\dfrac{\sigma_a}{\eta^*_p} e^{j\omega t} \right] + \dfrac{\sigma_0}{\eta_1} & , \quad t_3 \leq t < t_4 \end{cases} \tag{8.3.37}$$

We shall now discuss the procedure that is carried out to obtain the unknown constants t_i. As we progress from one time region to the next time region we shall need to monitor the stress in the Maxwell

element. This stress has to be continuous for all time t. This information is necessary in the calculation of the constants t_1 and t_3 in each cycle of oscillation.

To calculate the times t_i, we will need to consider the four time ranges in the first cycle. However, the first time range in the initial cycle of oscillation is a special case in that the stress in the Maxwell element is zero. Consequently, in order to obtain for a general cycle we shall also need to discuss the first time range in the second cycle. We now consider the first cycle of oscillation;

(i). $0 \leq t < t_1$.

In this time range, the model will not deform until the flow condition (8.2.1) is satisfied. This occurs at time t_1, which on the first cycle is given analytically by equation (8.2.3). i.e.

$$t_1 = \frac{1}{\omega} \sin^{-1}\left[\frac{\sigma_0}{\sigma_a} \right] \quad . \tag{8.3.38}$$

(ii). $t_1 \leq t < t_2$.

Over this range of times, the model deforms with a shear rate that is greater than zero. Hence from equation (8.3.37) the shear rate is given by

$$\dot{\gamma} = \mathrm{Im}\left[\frac{\sigma_a}{\eta_p^*} e^{j\omega t} \right] - \frac{\sigma_0}{\eta_1} \quad . \tag{8.3.39}$$

Throughout this deformation, there is a non-zero stress in the Maxwell element. The magnitude of this stress while the shear rate is positive, may be obtained from equation (8.2.1). i.e.

$$\sigma_1 = \sigma_a \sin(\omega t) - \sigma_0 \quad . \tag{8.3.40}$$

During this period, the applied stress increases to its maximum value at $t=\pi/2\omega$, before decreasing as the time t_2 is approached. When t_2 is reached, the applied stress has decreased by such an extent that the flow condition is no longer satisfied. At this point, the shear rate is zero. The time t_2 is determined by solving equation (8.3.39) with $\dot{\gamma} = 0$. i.e.

$$\mathrm{Im}\left[\frac{\sigma_a}{\eta_p^*} e^{j\omega t} \right] - \frac{\sigma_0}{\eta_1} = 0 \quad . \tag{8.3.41}$$

This equation can be solved analytically.

(iii). $t_2 \leq t < t_3$.

In this time range, the flow condition (8.2.1) is not satisfied and so no further deformation of the model takes place until time t_3 is reached. During this range, the applied stress decreases to zero at $t=\pi/\omega$, but then increases in magnitude as we approach t_3. Time t_3 is obtained by satisfying the flow condition (8.2.1) below

$$\sigma_a \sin(\omega t) - \sigma_1(t) = -\sigma_0 \quad , \tag{8.3.42}$$

where $\sigma_1(t)$ is the stress in the Maxwell element which relaxes according to equation (8.2.8) and is given by

$$\sigma_1(t) = A_1 e^{-t/\lambda_1} \quad . \tag{8.3.43}$$

The constant A_1 is determined by satisfying the condition that the stress σ_1 must be continuous at all times. At time t_2, σ_1 is given by

$$\sigma_1(t_2) = \sigma_a \sin(\omega t_2) + \sigma_0 \quad . \tag{8.3.44}$$

On substitution of equation (8.3.43) with $t = t_2$, into equation (8.3.44), we obtain A_1. Substituting equation (8.3.43) into equation (8.3.42), we obtain an equation in t which must be solved numerically to give the time t_3

(iv) $t_3 \leq t < t_4$.

Over this range of times, the model deforms according to equation (8.3.37). i.e.

$$\dot{\gamma} = \mathrm{Im}\left[\frac{\sigma_a}{\eta_p^*} e^{j\omega t} \right] + \frac{\sigma_0}{\eta_1} \quad . \tag{8.3.45}$$

The shear rate is now negative, and hence, the stress σ_1 is obtained from equation (8.2.1), and given by,

$$\sigma_1 = \sigma_a \sin(\omega t) - \sigma_0 \quad . \tag{8.3.46}$$

The magnitude of the applied stress increases to a maximum value at $t=3\pi/2\omega$, before again decreasing to zero at $t=2\pi/\omega$ to complete a full cycle. However, at $t=t_4$, the applied stress falls below the critical stress required for the flow condition to be satisfied. The time at which this occurs is determined by solving equation (8.3.45) with the

shear rate equal to zero. i.e.

$$\mathrm{Im}\left[\frac{\sigma_a}{\eta_p^*}e^{j\omega t}\right] + \frac{\sigma_0}{\eta_1} = 0 \quad . \qquad (8.3.47)$$

This is an equation in t which can be solved analytically to produce the time t_4.

(v). $t_4 \leq t < t_1+2\pi/\omega$.

In this time range, the flow condition (8.2.1) is not satisfied and so no further deformation of the model takes place until time $t_1+2\pi/\omega$ is reached. During this range, the applied stress decreases to zero at $t=2\pi/\omega$, but then increases in magnitude as we approach $t_1+2\pi/\omega$. Time $t_1+2\pi/\omega$ is obtained by satisfying the flow condition (8.2.1) below

$$\sigma_a \sin(\omega t) - \sigma_1(t) = \sigma_0 \quad , \qquad (8.3.48)$$

where $\sigma_1(t)$ is the stress in the Maxwell element which relaxes according to equation (8.2.8) and is given by

$$\sigma_1(t) = A_1 e^{-t/\lambda_1} \quad . \qquad (8.3.49)$$

The constant A_1 is determined by satisfying the condition that the stress σ_1 must be continuous at all times. At time t_4, σ_1 is given by

$$\sigma_1(t_4) = \sigma_a \sin(\omega t_4) - \sigma_0 \quad . \qquad (8.3.50)$$

On substitution of equation (8.3.49) with $t = t_4$, into equation (8.3.50), we obtain A_1. Substituting equation (8.3.49) into equation (8.3.48), we obtain an equation in t which must be solved numerically to give the time t_1

(b) The generalised model (n Maxwell elements).

The procedure for determining the shear rate waveform is similar to that for the single Maxwell element model. However, the complementary function is now present in the expression for the shear rate and so we have to determine the constants m_i and c_i. The constants m_i are the roots to equation (8.3.10) as discussed earlier. Before we discuss the four time ranges separately we shall need to use a formula which predicts the magnitude of the discontinuity that arises in the shear rate predictions. This formula is produced in the following way.

Substituting equation (8.3.2) into equation (8.2.1) we have

$$\sum_{i=1}^{n} \sigma_i = \sigma_a \sin(\omega t) + \sigma_0 \frac{\dot{\gamma}}{|\dot{\gamma}|} \quad , \qquad \gamma \neq 0 \ . \tag{8.3.51}$$

On differentiating equation (8.3.51) with respect to t we have

$$\sum_{i=1}^{n} \dot{\sigma}_i = \sigma_a \omega \cos(\omega t) \ , \qquad \dot{\gamma} \neq 0 \ . \tag{8.3.52}$$

Dividing equation (8.2.4) throughout by λ_i and summing terms we obtain an expression for the shear rate given by

$$\dot{\gamma} = \frac{1}{\eta_0} \left[\sum_{i=1}^{n} \frac{\sigma_i}{\lambda_i} + \sum_{i=1}^{n} \dot{\sigma}_i \right] \ . \tag{8.3.53}$$

Substituting for equation (8.3.52) into equation (8.3.53) we have

$$\dot{\gamma} = \frac{1}{\eta_0} \left[\sum_{i=1}^{n} \frac{\sigma_i}{\lambda_i} + \omega \sigma_a \cos(\omega t) \right] \ . \tag{8.3.54}$$

If we monitor the stresses in the Maxwell elements in each time range, then equation (8.3.54) can be used to obtain the magnitude of the discontinuity in the shear rate at times t_1 and t_3 . In order to monitor the stresses in the Maxwell elements for the time ranges when $\dot{\gamma} \neq 0$, we shall need to obtain a formula which expresses the stress in the Maxwell element in terms of the shear rate function. This formula can be obtained by solving the differential equation (8.2.4), to give

$$\sigma_i = e^{-t/\lambda_i} \int \frac{\eta_i}{\lambda_i} e^{t/\lambda_i} \dot{\gamma}(t) \, dt + E_i \ , \qquad (i=1,2,..,n) \tag{8.3.55}$$

where E_i is a constant of integration.

To simplify the discussion we shall only consider two Maxwell elements in the derivation of the constants c_i and t_i . We now discuss the shear rate waveform for the different time regions.

(i). $0 \leq t < t_1$.

In this time range, the model will not deform until the flow condition (8.2.1) is satisfied. This occurs at time t_1 , which on the first cycle of oscillation is given by

$$t_1 = \frac{1}{\omega} \sin^{-1}\left[\frac{\sigma_0}{\sigma_a} \right] \quad . \tag{8.3.56}$$

Since the shear rate is zero in this region then the stresses in the two Maxwell elements are also zero.

$$\text{i.e.} \qquad \sigma_i = 0 \quad , (i=1,2) \quad \text{for} \quad \dot{\gamma} = 0 \tag{8.3.57}$$

In particular the stresses in the Maxwell elements will be zero at time t_1.

(ii). $t_1 \leq t < t_2$.

In this time range the model deforms with a shear rate which is greater than zero. Hence from equation (8.3.20) the shear rate is given by

$$\dot{\gamma} = c_1 e^{m_1 t} + \text{Im}\left[\frac{\sigma_a}{\eta_p^*} e^{j\omega t} \right] - \frac{\sigma_0}{\eta_0} \quad , \tag{8.3.58}$$

Since the stresses in the Maxwell elements is known to be zero at time t_1, then the shear rate at time t_1 can be determined from equation (8.3.54). Hence, $\dot{\gamma}(t_1)$ is now known and the constant c_1 can be determined from equation (8.3.58). The shear rate for this time range is then known from equation (8.3.58) for all time t. The time t_2 can now be obtained solving equation (8.3.58) for the case when $\dot{\gamma} = 0$ to obtain an equation in time t. This equation has to be solved numerically to obtain the time t_2.

To monitor the stresses in the Maxwell elements, in this time region, we can obtain an analytical solution for these stresses by substituting for equation (8.3.58) into equation (8.3.55). In equation (8.3.55) the constant E_i would be known by satisfying the stress continuity at time t_1. Hence, the Maxwell element stresses are known, in this time region, for all time t.

(iii). $t_2 < t < t_3$.

In this time range, the flow condition (8.2.1) is not satisfied, and so no further deformation of the model takes place until time t_3 is reached. The stresses in the Maxwell elements relax according to equation (8.2.8). The constants A_i are determined by satisfying the condition that the stresses σ_i are continuous at time t_2. On substituting equation (8.2.8) into the equation

$$\sigma_a \sin(\omega t) = \sigma_1 + \sigma_2 - \sigma_0 \quad , \qquad (8.3.59)$$

we obtain an equation in t which can be solved to obtain the time t_3.

Using symmetry arguments the procedure for determining the constants c_i and t_i, in the remaining time ranges, are similar to those discussed above.

8.4. Effect of yield stress on dynamic data.

The fundamental amplitude and phase of the shear strain waveform predicted by the modified generalised Maxwell model may be determined using a Fourier series analysis. By substituting these quantities into the normal expressions for the complex viscosity function from the linear viscoelastic theory, this model may be used to theoretically show the effect of yield stress on the complex viscosity function η^*. Consider the shear rate and shear strain waveforms shown in figures (8.4) and (8.5) respectively. The shear strain curve predicted by the model is of the same general shape as the experimental waveform presented in figure (8.1). However, one difference between these waveforms, is the presence of discontinuities in the slope of theoretical curve at times t_1 and t_3 which are not present in the experimental displacement waveform. This difference is due to the influence of mechanical inertia effects in the experimental flow situation. These effects have been ignored in the theoretical analysis. The fundamental amplitude and phase angle for the theoretical curves may be determined by a Fourier series analysis as described in section (8.3). This information may then be used to predict the complex viscosity behaviour that would be obtained from a viscoelastic material possessing a Bingham yield stress. The following curves were determined using a single Maxwell element.

Figures (8.6) and (8.7) show the variation of normalised dynamic viscosity and normalised dynamic rigidity with respect to normalised angular frequency. The dynamic viscosity was normalised with respect to the zero frequency value of the plastic dynamic viscosity, and similarly, the dynamic rigidity with respect to the zero frequency value of the plastic dynamic rigidity. In figure (8.6), the Δ=0 curve, represents the variation of plastic dynamic viscosity with frequency. This curve is the same as the dynamic viscosity predicted by the generalised Maxwell model. (i.e. σ_0=0 in the modified generalised Maxwell model). The effect of yield stress is to increase the predicted value of the dynamic viscosity. The larger the yield stress, the larger the effect. We can make similar comments about the effect of yield stress of dynamic rigidity behaviour. i.e. the effect of yield stress is to increase the value of the dynamic rigidity.

Figures (8.8) and (8.9), show the variation of normalised dynamic viscosity and normalised dynamic rigidity against normalised torque amplitude. The torque amplitude is normalised with respect to yield stress. Hence, the effect of yield stress on these dynamic properties should decrease as normalised torque amplitude increases. The horizontal curve at $\eta'/\eta'_p = 1$, represents the plastic dynamic viscosity function which is independent of torque amplitude, by definition. This quantity can also be thought of as representing linear viscoelastic behaviour. The non-linear viscoelastic behaviour of the normalised dynamic viscosity is clearly shown in its dependence upon the torque amplitude. The same observation is found in figure (8.9) with the normalised dynamic rigidity behaviour. It should be noted that the modified generalised Maxwell model does predict the correct trend regarding the torque amplitude dependence of the dynamic viscosity and dynamic rigidity as was observed experimentally in figure (8.2).

8.5. Comments.

The aim of this chapter was to describe the non-linear effect of yield stress on viscoelastic dynamic behaviour. The modified generalised Maxwell model considered in this work, is able to characterise this non-linear viscoelastic behaviour in terms of a plastic complex viscosity and a yield stress. The plastic complex

viscosity has the property of being independent of strain amplitude provided the strain amplitude is sufficiently small. For situations when the yield stress component in the modified generalised Maxwell model is zero, then the plastic complex viscosity is equal to the complex viscosity.

It has been shown, that the model does predict the correct trend regarding the torque amplitude dependence of dynamic data as observed using a Carri-Med controlled stress rheometer.(see figures (8.2), (8.10), and (8.11)). However, it should be noted, that no direct comparison between the theoretical predictions of this model and experimental data has as yet been undertaken. Such a comparison would require curve fitting the theoretical expression (8.3.20) to the experimental shear rate data in order to determine the model constants η_i, λ_i, and σ_0. Current work being carried out at Plymouth Polytechnic South West, is concerned with determining a suitable curve fitting technique for working out the value of these constants. It should be noted that, mechanical inertia effects have been ignored in the analysis presented in this chapter. It is not difficult to show that it is possible to obtain analytical expressions for the shear rate and shear strain waveforms when mechanical inertia effects are included in the theory. However, the constants c_i, t_i, and m_i are now likely to be more difficult to obtain.

Part of the work carried out in this chapter, has been published by Davies, Golden, and Jones [13].

Appendix A.

Derivation of the corotating rate of strain sensor $\dot{\underline{\Gamma}}$ (Bird et al [5]).

The aim of this section is to present the theory for evaluating the components of the corotating rate of strain tensor $\dot{\underline{\Gamma}}$ for the flow problem discussed in Chapter 4. All quantities are referred to a cylindrical polar coordinate system (r,θ,z). From Bird et al [5], (equation 7.3-5), $\dot{\underline{\Gamma}}$ is given by the relation

$$\dot{\underline{\Gamma}}\,(r,t,t') = \left[\, \underline{\Omega}\,(t,t')\cdot\dot{\underline{\gamma}}\,(t')\cdot\underline{\Omega}^{\dagger}\,(t,t') \,\right] \quad , \qquad (A.1)$$

where $\underline{\Omega}\,(t,t')$ describes the local rotation of a fluid particle as it moves along its path from time t' to t. $\dagger$ denotes the transpose.

This section will be considered in two parts. The first part will consider the determination of the rotation tensor $\underline{\Omega}\,(t,t')$. The second part will consider the derivation of the rate of strain tensor $\dot{\underline{\gamma}}(t')$ at some past time t'. The problem of formulating equations of state in curvilinear coordinates will be discussed.

(i) Determination of the Rotation Tensor $\underline{\Omega}\,(t,t')$

The rotation tensor $\underline{\Omega}\,(t,t')$ describes the orientation of the corotating reference frame $\underline{\check{e}}_i$ with respect to the fixed frame $\underline{e}_i$. The corotating frame is chosen so that at time t' = t, the two frames coincide. We may write

$$\underline{\check{e}}_i\,(t') = \left[\, \underline{e}_i \,.\, \underline{\Omega}\,(t,t') \,\right] \quad . \qquad (A.2)$$

The components of the rotation tensor $\underline{\Omega}\,(t,t')$ will be evaluated for the unidirectional shear flow of an elastico-viscous fluid contained in the annular gap of a concentric cylinder geometry with inner cylinder radius r_i and outer cylinder radius r_o. The cylinder height is h. The velocity distribution in the fluid is defined by,

$$V_r = 0 \;;\; V_\theta = r\,F(r,t') \;;\; V_z = 0 \quad . \qquad (A.3)$$

At time t', the rate of strain tensor $\dot{\underline{\gamma}}\,(t')$ and the vorticity

tensor $\underline{\omega}$ (t') are given by

$$\dot{\underline{\gamma}}\ (t') = \nabla\ \underline{V}\ (t') + \left[\nabla\ \underline{V}\ (t')\right]^{\dagger} \quad , \qquad (A.4)$$

and

$$\underline{\omega}\ (t') = \nabla\ \underline{V}\ (t') - \left[\nabla\ \underline{V}\ (t')\right]^{\dagger} \quad , \qquad (A.5)$$

respectively. To evaluate the components of these two tensors in cylindrical polar coordinates, we refer to Bird et al [5] (Appendix A). We see from equation (A.3) that the only non-zero components of the rate of strain and vorticity tensors , rate of strain tensor are the θr and $r\theta$ components.

$$\dot{\gamma}_{\theta r} = r\ \frac{dF(r,t')}{dr} \quad , \qquad (A.6)$$

and

$$\omega_{r\theta} = \frac{1}{r}\ \frac{d}{dr}\left[r^2 F(r,t')\ \right] \quad . \qquad (A.7)$$

The rotation of the $\overset{v}{\underline{e}}_i$ frame depends on the local angular velocity $\underline{W}$ of the particle. From Bird et al [5], (eqn. 7.1-4),

$$\underline{W} = \tfrac{1}{2}\left[\nabla \times \underline{V}\ \right] \quad . \qquad (A.8)$$

For the velocity field (A.3),

$$\underline{W} = \tfrac{1}{2}\ (0,\ 0,\ \omega_{r\theta}) \quad . \qquad (A.9)$$

Hence, we have a rotation of the fluid about the z-axis. Let α be the angle of rotation of the fluid particle about the z-axis such that at time t' = t, the corotating frame coincides with the fixed frame. By making use of elementary geometric arguments (Bird et al [5], section (7.6)), together with the equation A.2, the rotation tensor $\underline{\Omega}$ (t,t') for this flow problem is,

$$\underline{\Omega}\ (t,t') = \begin{bmatrix} \cos(\alpha) & -\sin(\alpha) & 0 \\ \sin(\alpha) & \cos(\alpha) & 0 \\ 0 & 0 & 1 \end{bmatrix} \quad . \qquad (A.10)$$

Note that when $\alpha = 0$, i.e. at time t'=t, the above matrix reduces to

$$\underline{\Omega}\ (t,t') = \begin{bmatrix} 1 & 0 & 0 \\ 0 & 1 & 0 \\ 0 & 0 & 1 \end{bmatrix} \quad , \qquad (A.11)$$

thus satisfying equation (A.2)

The local angular velocity of the fluid particle about the z-axis is $\frac{1}{2}\,\omega_{r\theta}$. Hence, α the angle, through which the z-axis is rotated from time t' to t is, given by the differential equation

$$\frac{d\alpha}{dt'} = -\tfrac{1}{2}\,\omega_{r\theta} \qquad . \qquad (A.12)$$

Integrating the above equation with respect to t', and satisfying the condition that when t' = t then $\alpha = 0$, we obtain an expression for the angle of rotation as follows,

$$\alpha\,(t,t') = \tfrac{1}{2}\int_{t'}^{t} \omega_{r\theta}\,(t'')\,dt'' \qquad (A.13)$$

(ii). Derivation of the rate of strain tensor $\dot{\underline{\gamma}}$ (t').

(a). The curvilinear co-ordinate System (r,θ,z).

Due to the geometries considered, we shall need to formulate our equations of state in curvilinear coordinates. Therefore, the theory must take into account the change in orientation of the curvilinear coordinate system as the fluid moves along its path from time t' to t. We describe the curvilinear coordinate system by an orthogonal set of unit vectors $\dot{\underline{e}}_i$. The $\dot{\underline{e}}_i$ frame changes its orientation as the fluid particle P travels along its path from time t' to t. This affects the components of the rate of strain tensor $\dot{\underline{\gamma}}$ (t') which has to be written in terms of the fixed frame $\underline{e}_i$. When we evaluate the rate of strain tensor from equation (A.4), we obtain it in terms of the $\dot{\underline{e}}_i$ frame. We choose the $\dot{\underline{e}}_i$ frame so that at time t' = t, the $\dot{\underline{e}}_i$ and $\underline{e}_i$ frames coincide.

At time t', the two reference frames are related by the equation below (Bird et al [5], eqn (7.6.2)),

$$\dot{\underline{e}}_i = \left[\, \underline{e}_i \cdot \underline{\Lambda}\,(t,t') \,\right] \qquad . \qquad (A.14)$$

The change in orientation of the curvilinear coordinate system is therefore described by the $\underline{\Lambda}$ tensor.

(b). Determination of the rate of strain tensor $\dot{\underline{\gamma}}$ (t')

From equation (A.4) we may write down the components of the rate of strain tensor $\dot{\underline{\gamma}}$ (t') at some past time t' referred to the $\dot{\underline{e}}_i$ frame. i.e.

$$\dot{\underline{\gamma}}\ (t') = \begin{bmatrix} 1 & 0 & 0 \\ 0 & 1 & 0 \\ 0 & 0 & 1 \end{bmatrix} \dot{\gamma}_{r\theta} \quad , \qquad (A.15)$$

where is given by equation (A.6).

The equations of fluid motion and continuity are written in a fixed frame. We must therefore transform the equations of state from the corotating reference frame to a fixed frame. Before we can write the rate of strain tensor in terms of the fixed frame, we must determine the components of the $\underline{\Lambda}$ tensor. From time t' to time t, the $\dot{\underline{e}}_i$ frame rotates through an angle β. Using elementary geometric arguments, we can show that

$$\underline{\Lambda}\ (t,t') = \begin{bmatrix} \cos(\beta) & -\sin(\beta) & 0 \\ \sin(\beta) & \cos(\beta) & 0 \\ 0 & 0 & 1 \end{bmatrix} \qquad (A.16)$$

The $\dot{\underline{e}}_i$ frame rotates with angular velocity F(r,t') from time t' to t. Therefore, the rate of change of β with respect to t' is given by

$$\frac{d\beta}{dt'} = - F(r,t') \qquad (A.17)$$

Satisfying the condition that when t' = t then $\beta = 0$, and integrating equation (A.17) with respect to t', we obtain an expression for β (t,t').

$$\beta\ (t,t') = \int_{t'}^{t} F(r,t'')\ dt'' \qquad (A.18)$$

Equation (A.15) may be rewritten in terms of the unit vectors ($\dot{\underline{e}}_r$, $\dot{\underline{e}}_\theta$, $\dot{\underline{e}}_z$). i.e.

$$\dot{\underline{\gamma}}\ (t') = (\dot{\underline{e}}_r \dot{\underline{e}}_\theta + \dot{\underline{e}}_\theta \dot{\underline{e}}_r)\ \dot{\gamma}_{r\theta} \quad . \qquad (A.19)$$

Using equation (A.14), the rate of strain tensor may be expressed in terms of the fixed frame. i.e.

$$\dot{\underline{\gamma}}\,(t') = \left[(\underline{e}_r \cdot \underline{\Lambda}\,(t,t'))(\underline{e}_\theta \cdot \underline{\Lambda}\,(t,t')) + (\underline{e}_\theta \cdot \underline{\Lambda}\,(t,t'))(\underline{e}_r \cdot \underline{\Lambda}\,(t,t')) \right] \dot{\gamma}_{r\theta}\,(t') \qquad (A.20)$$

which provides the result

$$\dot{\underline{\gamma}}\,(t') = \begin{bmatrix} \sin(2\beta) & \cos(2\beta) & 0 \\ \cos(2\beta) & -\sin(2\beta) & 0 \\ 0 & 0 & 0 \end{bmatrix} \dot{\gamma}_{r\theta}\,(t') \qquad (A.21)$$

On substitution of equations (A.10) and (A.21) into equation (A.1) we obtain the components of the corotating rate of strain tensor.

$$\dot{\underline{\Gamma}}\,(r,t,t') = \begin{bmatrix} \cos(\alpha) & -\sin(\alpha) & 0 \\ \sin(\alpha) & \cos(\alpha) & 0 \\ 0 & 0 & 0 \end{bmatrix} \begin{bmatrix} \sin(2\beta) & \cos(2\beta) & 0 \\ \cos(2\beta) & -\sin(2\beta) & 0 \\ 0 & 0 & 0 \end{bmatrix} \times \begin{bmatrix} \cos(\alpha) & \sin(\alpha) & 0 \\ -\sin(\alpha) & \cos(\alpha) & 0 \\ 0 & 0 & 0 \end{bmatrix} \dot{\underline{\gamma}}\,(t') \quad . \qquad (A.22)$$

i.e.

$$\dot{\underline{\Gamma}}\,(r,t,t') = \begin{bmatrix} -\sin(2(\alpha-\beta)) & \cos(2(\alpha-\beta)) & 0 \\ \cos(2(\alpha-\beta)) & \sin(2(\alpha-\beta)) & 0 \\ 0 & 0 & 0 \end{bmatrix} \dot{\gamma}_{r\theta}(t') \qquad (A.23)$$

Now, equations (A.13) and (A.14) can be used to yield an expression for $(\alpha-\beta)$. i.e.

$$\alpha-\beta = \tfrac{1}{2} \int_t^{t'} r \frac{dF(r,t'')}{dr}\, dt'' \quad . \qquad (A.24)$$

Hence,

$$2(\alpha-\beta) = \int_t^{t'} \dot{\gamma}_{r\theta}(r,t'')\, dt'' \quad . \qquad (A.25)$$

The corotating rate of strain tensor $\dot{\underline{\Gamma}}\,(r,t,t')$ is therefore given by

$$\dot{\underline{\Gamma}}\,(r,t,t') = \begin{bmatrix} -\sin(\varphi(r,t'')) & \cos(\varphi(r,t'')) & 0 \\ \cos(\varphi(r,t'')) & \sin(\varphi(r,t'')) & 0 \\ 0 & 0 & 0 \end{bmatrix} \dot{\gamma}_{r\theta}(t') \quad , \qquad (A.26)$$

where

$$\varphi\ (r,t") = \int_{t}^{t'} \dot{\gamma}_{r\theta}(r,t")\ dt" \qquad . \qquad (A.27)$$

References

[1] Abramovitz, M. and I. Segan, "Handbook of Mathematical Functions", Dover Publications, New York, (1968).

[2] Barnes, H. A., P. Townsend, and K. Walters, Rheol. Acta., **10**, 517, (1971).

[3] Barnes, H. A., and K. Walters, Rheol. Acta, **24**, 323, (1985).

[4] Bird, R. B., O. Hassager, and S. I. Abdel-Khalik, AIChE. J., **20**, No. 6, 1041, (1974).

[5] Bird, R. B., R. C. Armstrong, and O. Hassager, "Dynamics of Polymeric Liquids", Vol. 1, Fluid Mechanics, J. Wiley & Sons, (1977).

[6] Bird, R. B., G. C. Dai, and B. J. Yarusso, Rev. Chem. Eng., **1**, No. 1, (1983).

[7] British Food Manufacturing Industries Research Association, "Physics Exhibition Handbook (London: Institute of Physics and Physical Society)", 1962.

[8] Bullivant, S. A., PhD Thesis, Plymouth Polytechnic, (1977).

[9] Coleman B. D., H. Markovitz, and W. Noll, "Viscometric Flows of Non-Newtonian Fluids", Springer-Verlag, (1966).

[10] Davies, J. M., S. Bhumiratana, and R. B. Bird, JNNFM., **3**, 237, (1977/78).

[11] Davies, J. M. and A. Chakrabarti, Proc. 4th Int. Congress on Rheology, **2**, 217, (1978).

[12] Davies, J. M., T. E. R. Jones, and E. J. Carter., J.N.N.F.M, **23**, 73, (1987).

[13] Davies, J. M., K. Golden, and T. E. R. Jones, Proc. 3rd European Rheology Conference, 120, (1990).

[14] Davis, J. J., S. S. Deer and B. Warburton, J. Phys. E, Series 2, Vol. 1, (1968).

[15] Dwight, H. B., "Tables of Integrals and other Mathematical Data", 4th Ed, Macmillan, (1961).

[16] Ferry, J. D., "Viscoelastic Properties of Polymers", 3rd Ed, J. Wiley & Sons, (1980).

[17] Goddard, J. D., and C. Miller, Rheol. Acta., 5, 177, (1966).

[18] Goddard, J. D., Trans. Soc. Rheol., 11, 381, (1967).

[19] Goodbody, A. M., "Cartesian Tensors", J. Wiley & Sons, (1982).

[20] Holder, E. F., M.Sc Thesis, U.C.W. Aberystwyth, (1982).

[21] Jennings, W., "First Course in Numerical Methods", Macmillan, (1964).

[22] Jones, T. E. R., and K. Walters, J. Phys. A, 4, 85, (1971).

[23] Jones, T. E. R., J. M. Davies, and H. A. Barnes, Proc. 8th Int. Congress on Rheology, 4, 45, (1984).

[24] Jones, T. E. R., J. M. Davies, and A. Thomas, Rheol. Acta., 26, 14, (1987).

[25] Markovitz, H., J. App. Phys., 23, 1070-77.

[26] Maude, A. D., and K. Walters, Nature, 200, 914, (1964).

[27] Maxwell, J. C., Phil. Trans. Roy. Soc. Lon., A157, 49, (1867).

[28] Nally, M. C., Brit. J. Appl. Phys., 16, 1023, (1965).

[29] Oldroyd, J. G., Proc. Roy. Soc., A, Vol. 200, 523, (1950).

[30] Oldroyd, J. G., Quart. Journ. Mech. and Applied Math., 4, 271 (1951).

[31] Oldroyd, J. G., D. J. Strawbridge, and B. A. Toms, Proc. Phys. Soc B., 64, 44, (1951).

[32] Olver, F. W. J., "Mathematical Tables", 6, H. M. Stationers, (London).

[33] Perkins. T. J. P., PhD Thesis, U.C.W. Aberystwyth, (1987).

[34] Phan-Thien, N., J.N.N.F.M., 4, 167, (1978).

[35] Phan-Thien, N., J. Rheol., 25(3), 293, (1981).

[36] Phan-Thien, N., and J. Dudek, JNNFM., 11, 147, (1982).

[37] Sundström, D. W., and A. Kaufman., Ind. Eng. Chem., Process Des. Dev., 16, 320, (1977).

[38] Tanner, R. I., "Engineering Rheology", Rev Ed, Oxf. Univ. Press, (1988).

[39] Townsend P., Rheol. Acta., 12, 13, (1973).

[40] Van Wazer, J. R., J. W. Lyons, K. W. Kim, and R. E. Colwell, "Viscosity and Flow Measurement", London: Interscience, (1963).

[41] Walters, K., Quart. J. Mech. and App. Math., 14, Pt. 4, 431, (1961).

[42] Walters, K., and N. D. Waters, "Polymer Systems: deformation and flow.", Macmillan, (1968).

[43] Walters, K. and R. A. Kemp., Rheol. Acta., 7, 1, (1968).

[44] Walters, K., and P. Townsend, Proc. 5th Int. Cong. Rheol., 4, 471, (1970).

[45] Walters, K., "Rheometry", Chapman and Hall, (1975).

[46] Watson, G. N., "A Treatise on the Theory of Bessel Functions", 2nd Ed, Camb. Univ. Press, (1966).

[47] Yoshimura, A.S., R. K. Prud'homme, Rheol. Acta., 26, 428, (1987).

[48] Zahorski, S., "Mechanics of Viscoelastic Fluids", Martinus Nijhoff Pub., (1981).

NOMENCLATURE

(x_1, x_2, x_3)	: cartesian coorinates
(r, θ, z)	: cylindrical coordinates
(r, θ, ψ)	: spherical coordinates
(ξ_1, ξ_2, ξ_3)	: convected coordinates
a	: cone radius, platen radius
a_n	: fourier series coefficients of $\cos(n\omega t)$
$\|a\|$	: magnitude of a
b_n	: fourier coefficients of $\sin(n\omega t)$
c	: phase angle
c_i	: constant in modified generalised Maxwell model theory
C	: Couple/Torque
C_F	: Couple acting on rotor platen due to fluid
C_0	: Couple/Torque amplitude
C_{ik}	: right Cauchy-Green tensor
$\frac{d}{dt}$	: total derivative
$\frac{\partial}{\partial t}$	: partial derivative
$\frac{D}{Dt}$	: material derivative
$\overline{\overline{t}}$	: Jaumann derivative
$\underline{\underline{t}}$	: Oldroyd derivative
$\underline{e}_i$	: orthogonal unit vectors (fixed frame)
$\underline{e}_i$	: orthogonal unit vectors (corotating frame)
E	: mean shear stress reduction
f_i	: total body force vector
F_σ	: platen geometry shear stress factor
g_{ik}	: metric tensor (fixed frame)
$G(t-t')$	: relaxation function
G'	: dynamic rigidity (pure oscillatory shear)

G'_m	: dynamic rigidity (combined steady and oscillatory shear)
G'_p	: plastic dynamic rigidity
$G'_0, G'_{(1)}, G'_{(2)}$	: dynamic rigidity from fluid inertia perturbation theory (zero, first, and second order fluid inertia effects)
G'_i	: rigidity coefficient (Maxwell element)
h	: parallel plate gap, cylinder height
i, j	: $\sqrt{(-1)}$
$Im[\ ]$	: imaginary part of complex number
I	: mechanical inertia of rotor
J_n	: n^{th} order Bessel function of the first kind
$K_{-n/2}$	: n^{th} order modified Bessel function
ln	: naperian logarithm
m	: constant (power law model)
m_i	: constant (modified generalised Maxwell model)
n	: power law index
p	: isotropic pressure
P_n	: Legendre function of the second kind (degree n)
Q_n	: Legendre function of the first kind (degree n)
$r_i, r_0, r_1, r_2, r_3, r_4$	: cylinder radii
$Re[\ ]$	: real part of complex number
s	: time
t	: time
t_i	: time constant (modified generalised Maxwell model)
T_{ik}	: corotating stress tensor (fixed frame)
u_i	: displacement vector components
v_i	: velocity vector components
Y_n	: n^{th} order Bessel function of the second kind (order n)
z	: complex number
$\bar{z}$	: complex conjugate

α : angle of rotation

α : fluid inertia parameter

$\alpha_0, \alpha_1, \alpha_2$: fluid inertia paramers from perturbation theory (zero, first, and second order)

γ_0 : yield strain

γ_E : elastic strain

γ_{ik} : rate of strain tensor (fixed frame)

$\dot{\gamma}_m$: mean shear rate

$\dot{\gamma}_s$: steady shear rate

$\dot{\gamma}_{ik}$: rate of strain tensor (fixed frame)

$\dot{\gamma}_a^0$: complex shear rate amplitude

$\dot{\gamma}_{a_1}$: oscillatory shear rate amplitude

$\tan(\delta)$: loss tangent

δ : ratio between fundamental oscillatory shear stress amplitude and mean shear stress

δ_{ik} : kronecker delta

Δ : ratio between yield stress and shear stress amplitude

ϵ : oscillatory strain amplitude (Chapter 2)

ϵ : ratio between fundamental oscillatory shear rate amplitude and mean shear rate

ϵ_{ik} : strain tensor (convected frame)

η : shear viscosity

η_0 : zero shear viscosity

η_∞ : infinite shear viscosity

η_p : plastic shear viscosity

η_i : viscosity coefficient (generalised Maxwell model)

η' : dynamic viscosity (pure oscillatory shear)

η'_m : dynamic viscosity (combined steady and oscillatory shear)

η'_p : plastic dynamic viscosity

$\eta_0', \eta_1', \eta_2'$: dynamic viscosity from perturbation theory

η^* : complex viscosity (pure oscillatory shear)

η_p^* : plastic complex viscosity

$\eta_0^*, \eta_1^*, \eta_2^*$: complex viscosity from perturbation theory (zero, first, second order)

Θ_c : cone angle

Θ_0 : gap angle

λ : relaxation time (Carreau model)

λ_l : relaxation time (Maxwell element)

λ_s : relaxation time (Segalman model)

λ_1, λ_2 : relaxation time (Oldroyd models)

Λ_{ij} : rotation matrix

μ_0, μ_1, μ_2 : Oldroyd model constants

ν_1 : first normal stress difference in steady simple shear

ν_2 : second normal stress difference in steady simple shear

$\prod_{i=1}^{n}$: product sign

Π'_{ik} : extra stress tensor (convected frame)

ρ : fluid density

σ_{ik} : total stress tensor

σ'_{ik} : extra stress tenssor

σ'_{ik} : extra stress tenssor (corotaing frame)

σ_a^0 : complex shear stress amplitude

σ_m : mean shear stress

σ_0 : yield stress value

σ_y : stress in yield stress element

σ_{a_1} : fundamental oscillatory shear stress amplitude

$\sum_{i=1}^{n}$: summation sign

ω_{ik} : vorticity tensor

Ω : angular velocity

Ω_{ik} : rotation matrix

ψ : angular displacement

ψ_0 : displacement amplitude

$\Pi_{\dot{\gamma}}$: second invariant of rate of strain tensor

∇ : del operator

! : factorial sign

FIGURE (2.1)

The Generalised Maxwell Model.

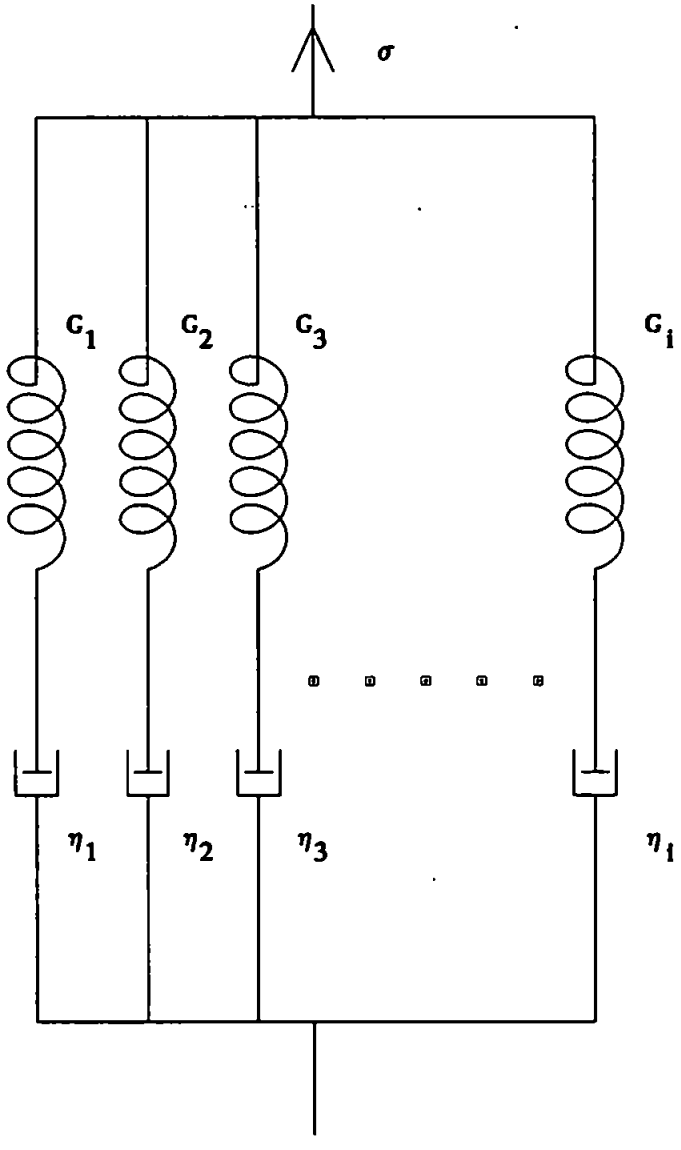
σ
G1
G2
G3
Gi
η1
η2
η3
ηi

FIGURE (2.2)

Variation of normalised viscosity ($\eta(\dot{\gamma})/\eta_0$) with normalised shear rate ($\lambda\dot{\gamma}$) for different viscosity models (n = 0.3).

(i). Power Law Model.

(ii). Segalman Model.

(iii). Carreau Model.

(iv). Newtonian Model.

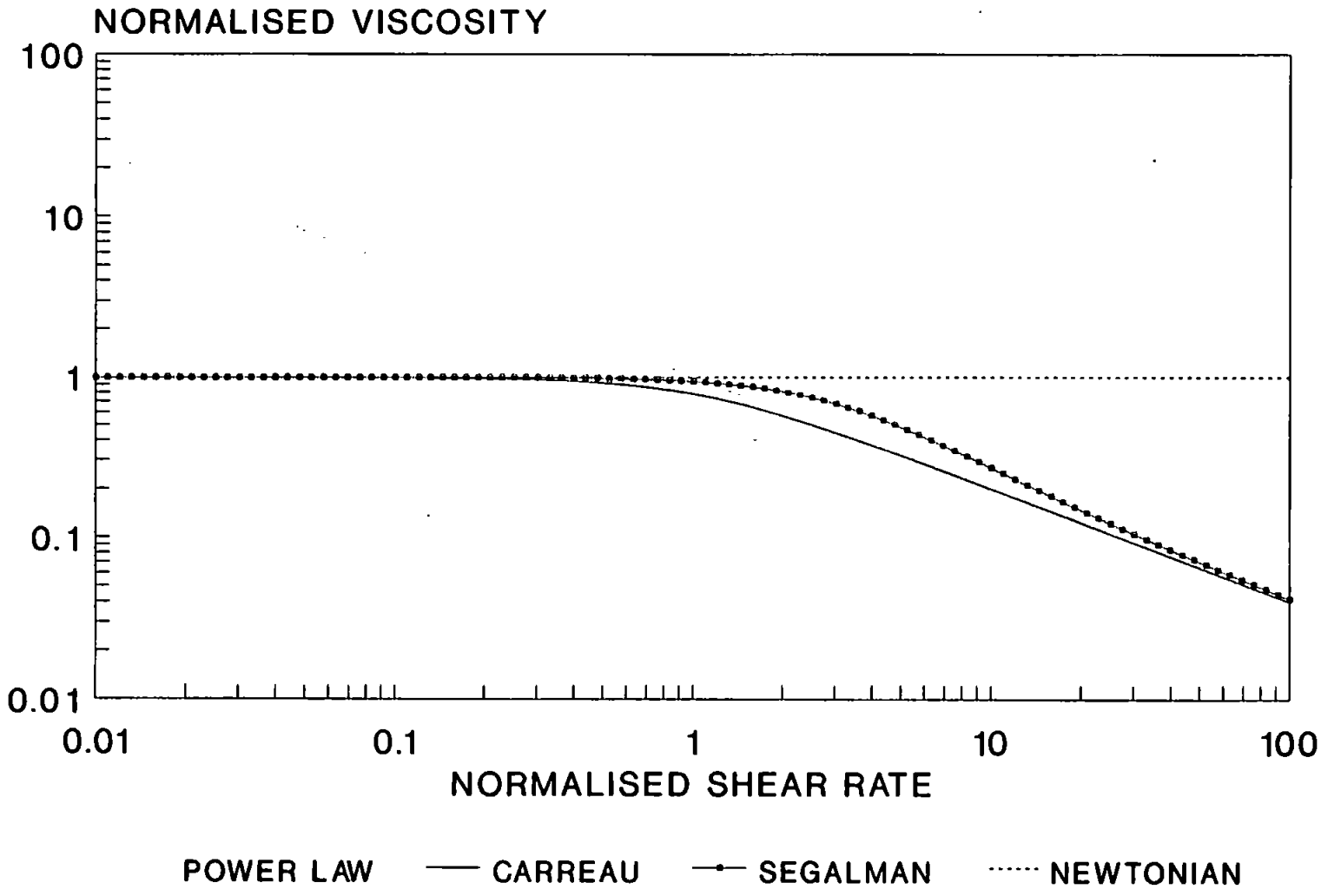
NORMALISED VISCOSITY
100
10
1
0.1
0.01
0.01
0.1
1
10
100
NORMALISED SHEAR RATE
POWER LAW
CARREAU
SEGALMAN
NEWTONIAN

FIGURE (2.3)

Variation of shear stress with shear rate for

(i). The Bingham Model.

(ii). The Herschel-Bulkley Model.

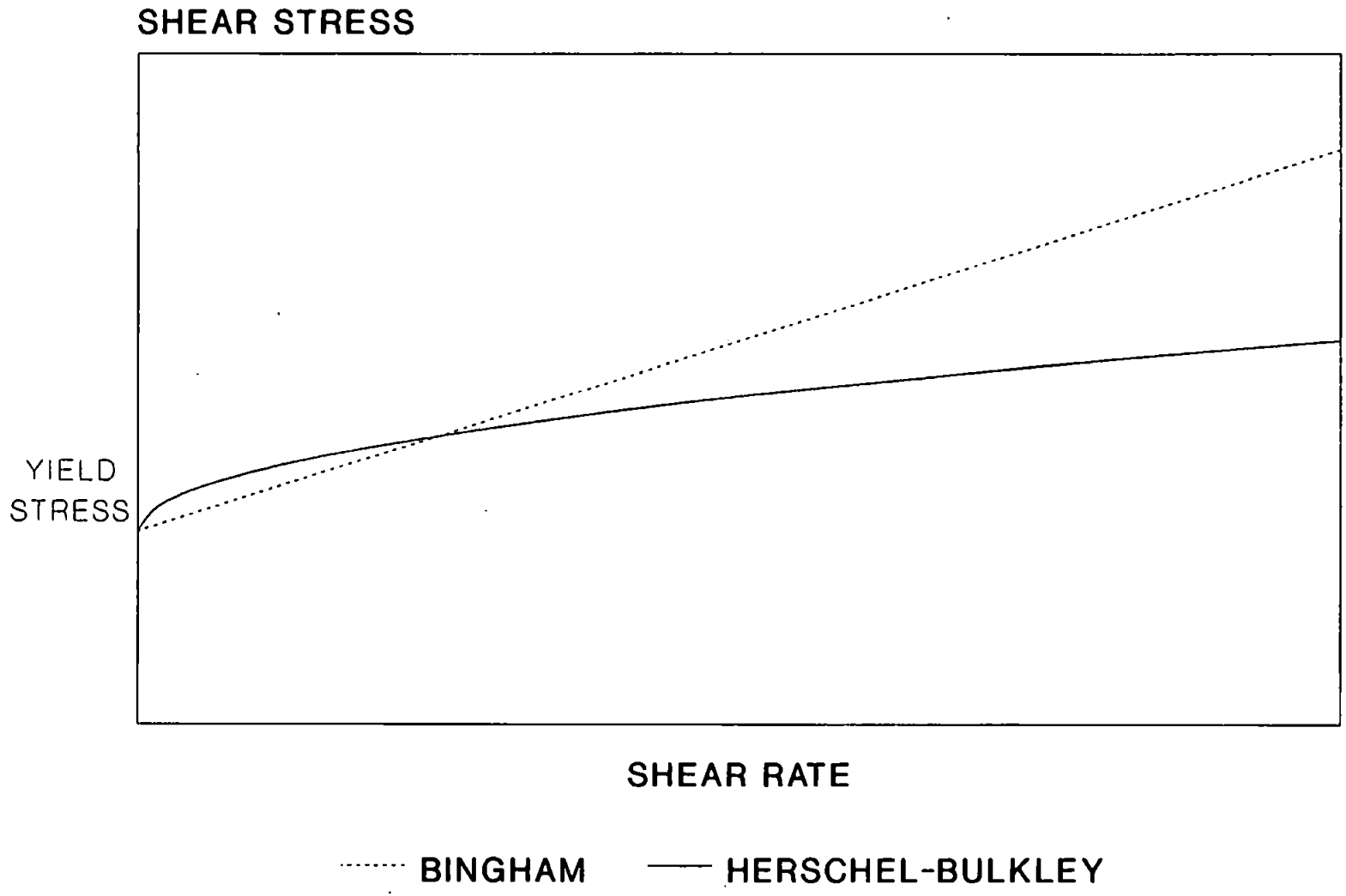
SHEAR STRESS
YIELD STRESS
SHEAR RATE
BINGHAM
HERSCHEL-BULKLEY

FIGURE (3.1)

The Stormer Viscometer.

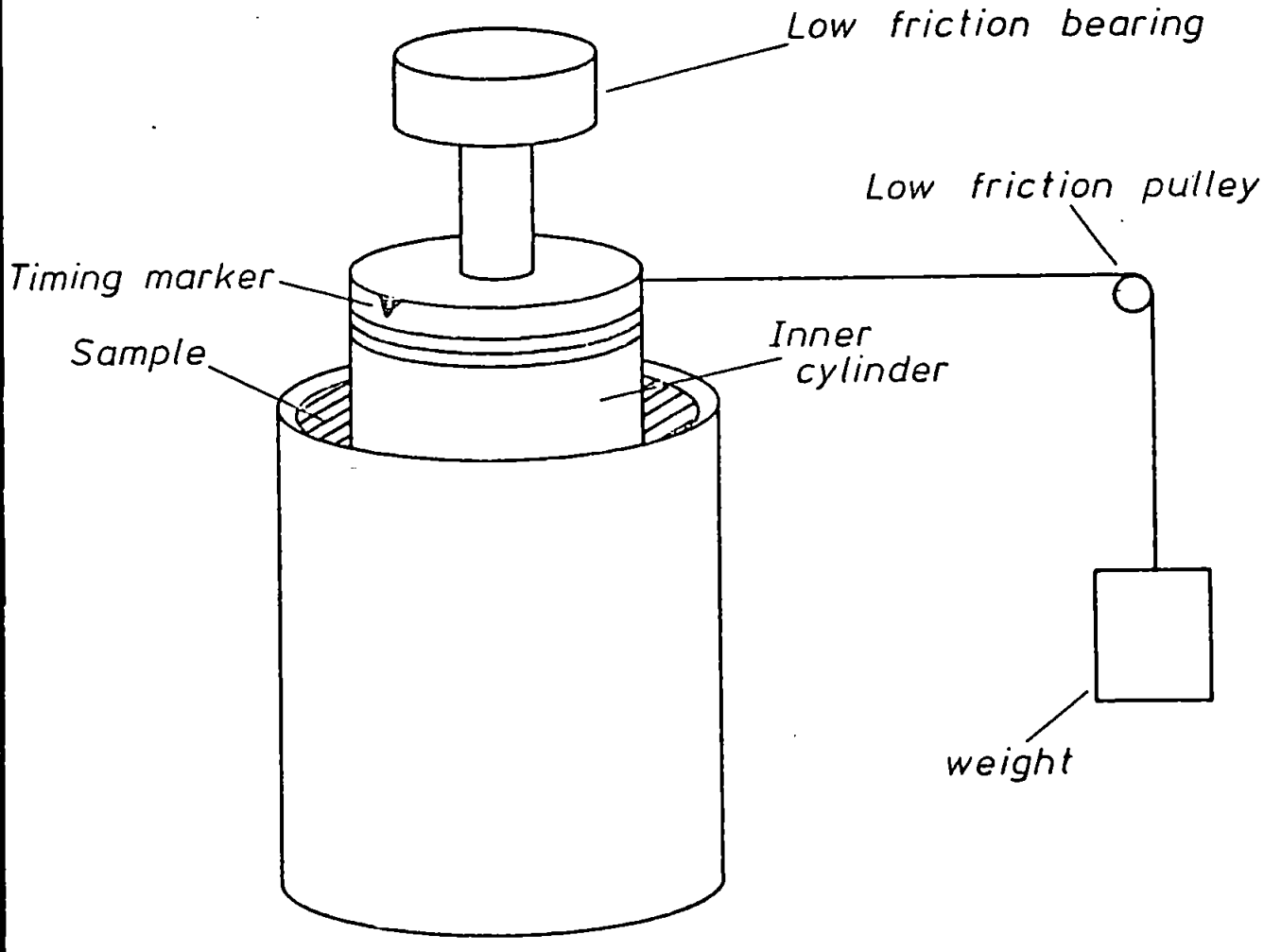
Low friction bearing
Low friction pulley
Timing marker
Sample
Inner cylinder
weight

FIGURE (3.2)

Schematic diagram of the air-bearing in the Deer Rheometer.

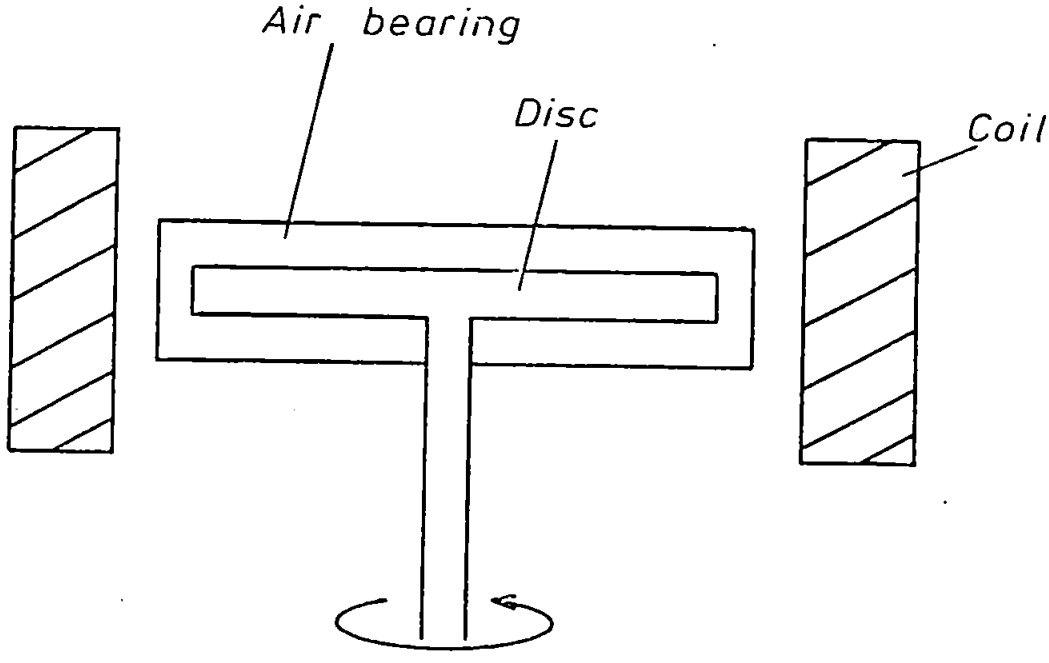
Air bearing
Disc
Coil

FIGURE (3.3)

The Carri-Med Contolled Stress Rheometer.

1. Stand base.
2. Bearing support pillar.
3. Air bearing housing.
4. Air bearing-located axially and radially.
5. Motor drive spindle.
6. Upper measurement member-cone & plate or parallel plate or concentric cylinder.
7. Drive motor stator.
8. Optical encoder measurement system.
9. I.E.E.E. interface.
10. Automatic sample presentation system.
11. Mains switch.
12. Draw rod - retains measurement system.
13. Moveable top cover.
14. L.E.D. Display.
15. Adjustable levelling feet.
16. Height adjusting micrometer scale.
17. Gap setting micrometer scale.
18. Bottom plate of measurement system - raised or lowered on a dry bearing - temperature controlled by a Peltier system.
19. Digital input / output optical encoder interface.
20. Gap setting indicator light and lead.

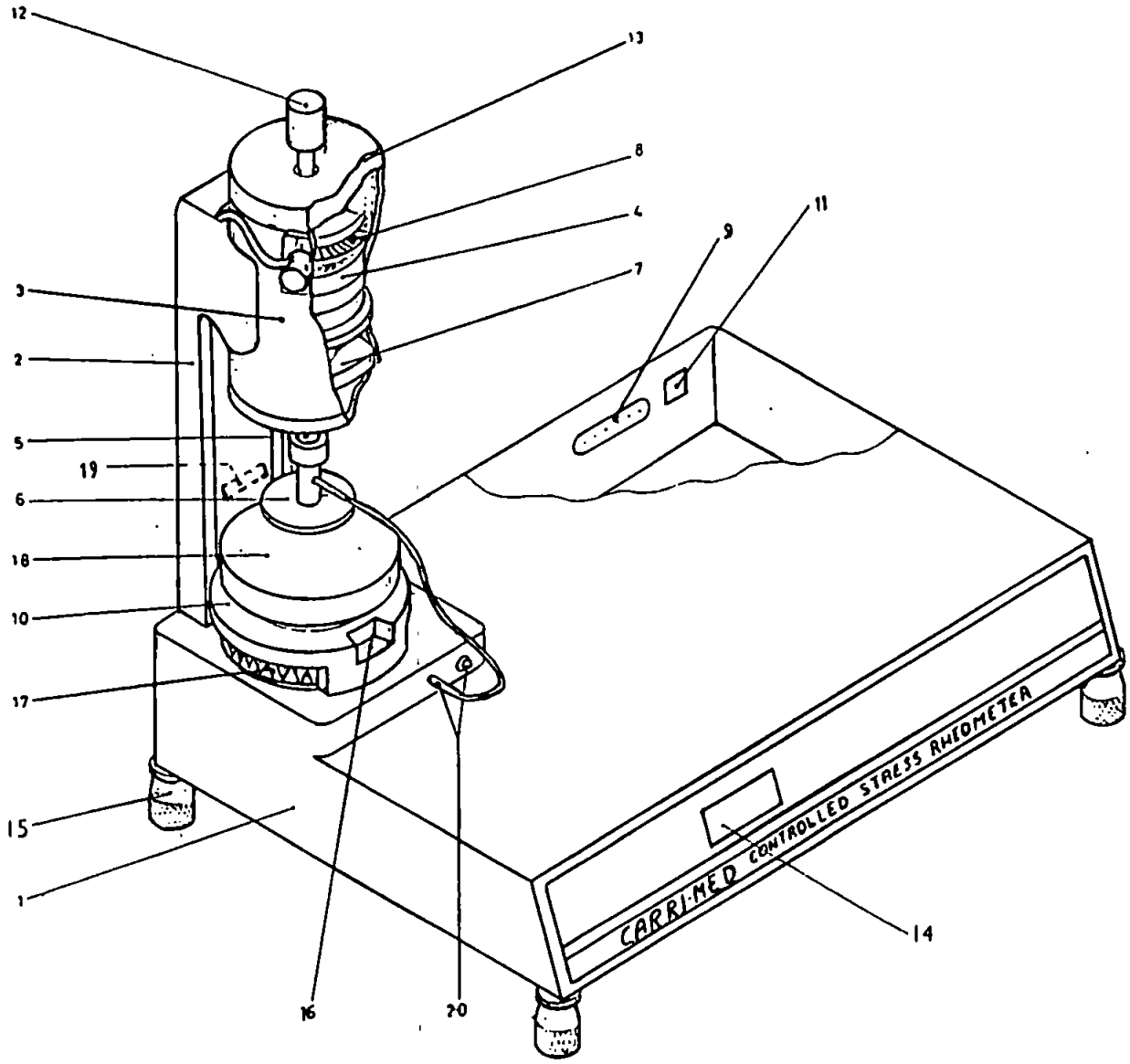
12
13
8
4
9
11
7
3
2
5
19
6
18
10
17
15
1
16
20
14
CARRI-MED CONTROLLED STRESS RHEOMETER

FIGURE (3.4)

The cone and plate system on the Carri-Med controlled stress rheometer.

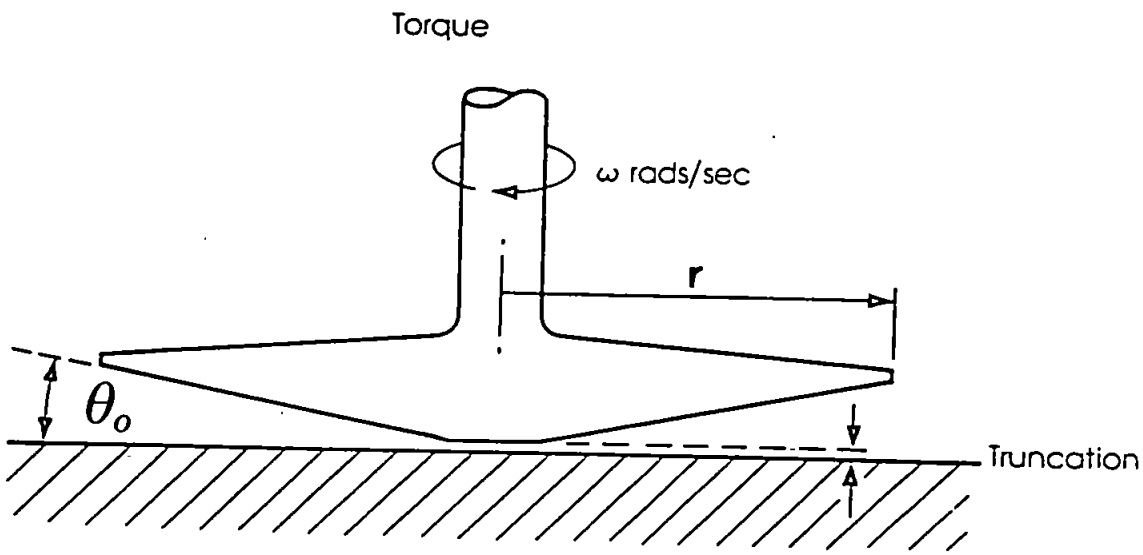
Torque
ω rads/sec
r
θ_o
Truncation

FIGURE (3.5)

The parallel plate system on the Carri-Med controlled stress rheometer.

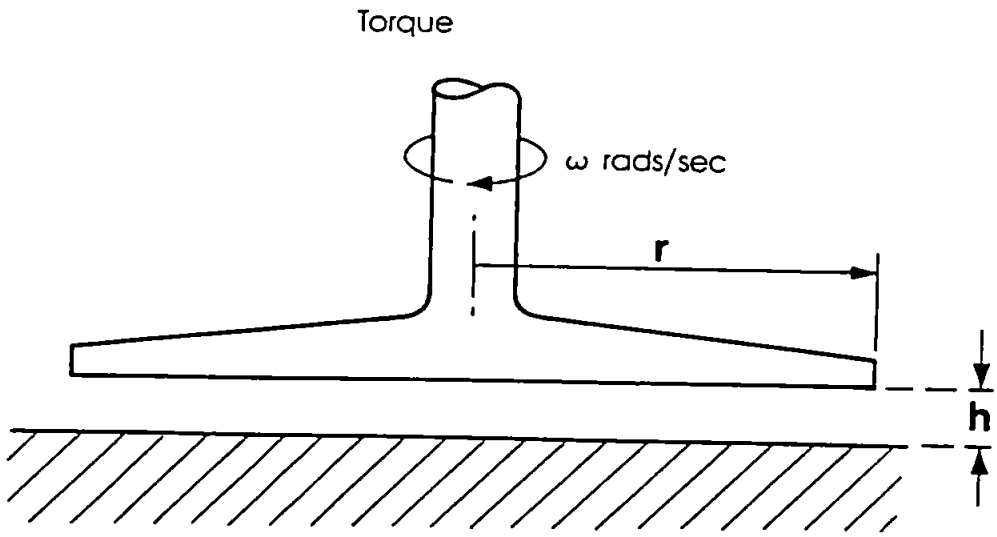
Torque
ω rads/sec
r
h

FIGURE (3.6)

The concentric cylinder system on the Carri-Med controlled stress rheometer.

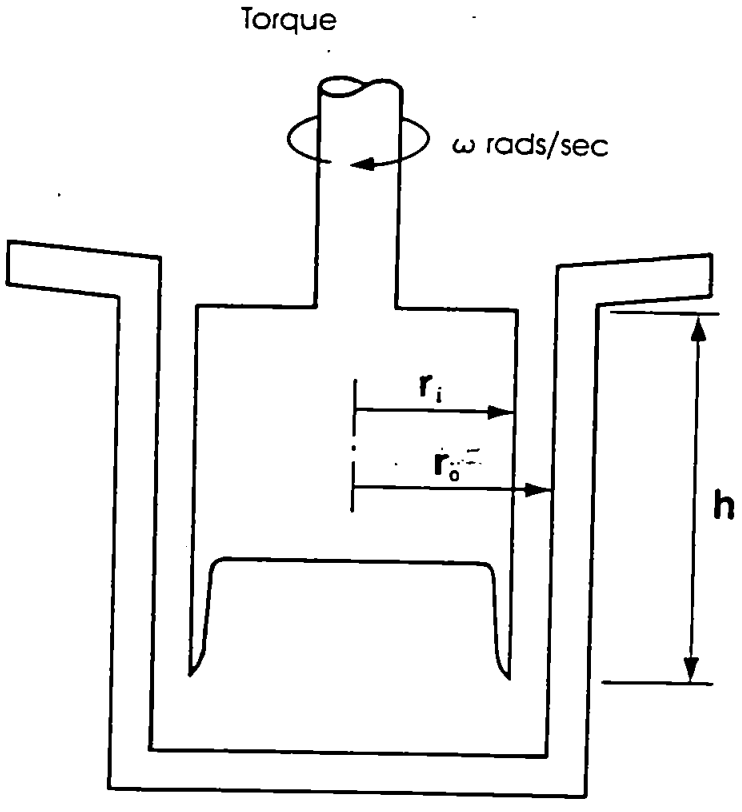
Torque
ω rads/sec
r_i
r_o
h

FIGURE (3.7)

The double concentric cylinder system on the Carri-Med controlled stress rheometer.

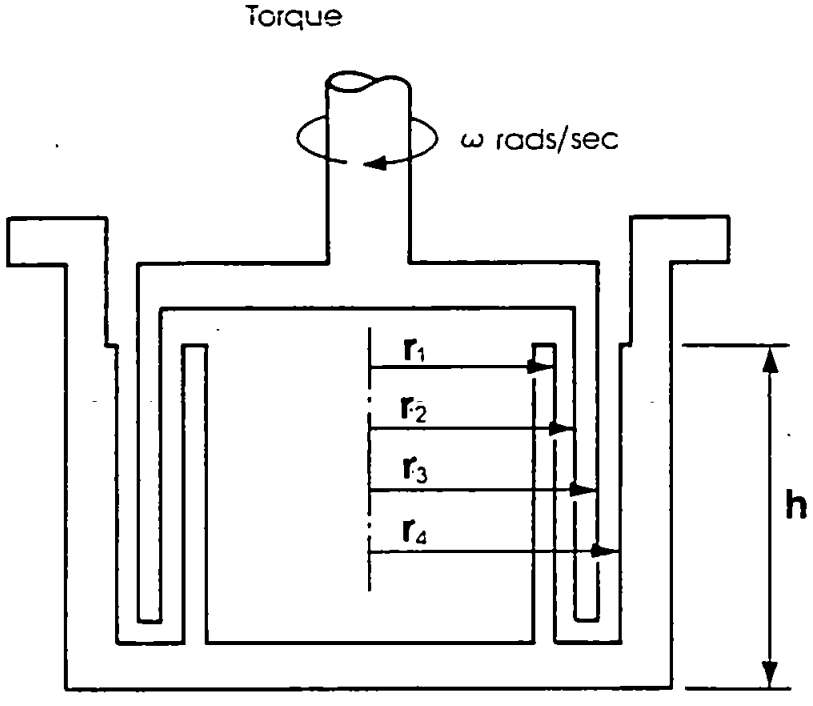
Torque
ω rads/sec
r1
r2
r3
r4
h

FIGURE (4.1)

Combined Steady and Oscillatory Shear Flow.

Variation of mean shear stress reduction $(\sigma_s - \sigma_m)/\sigma_s$ with $\dot{\gamma}_m/\omega$ for a power law model ($n = 0.3, 0.6, 0.9$; $\epsilon = 0.2$).

(i). Goddard-Miller Model (viscoelastic).

(ii). Generalised Newtonian Model (inelastic).

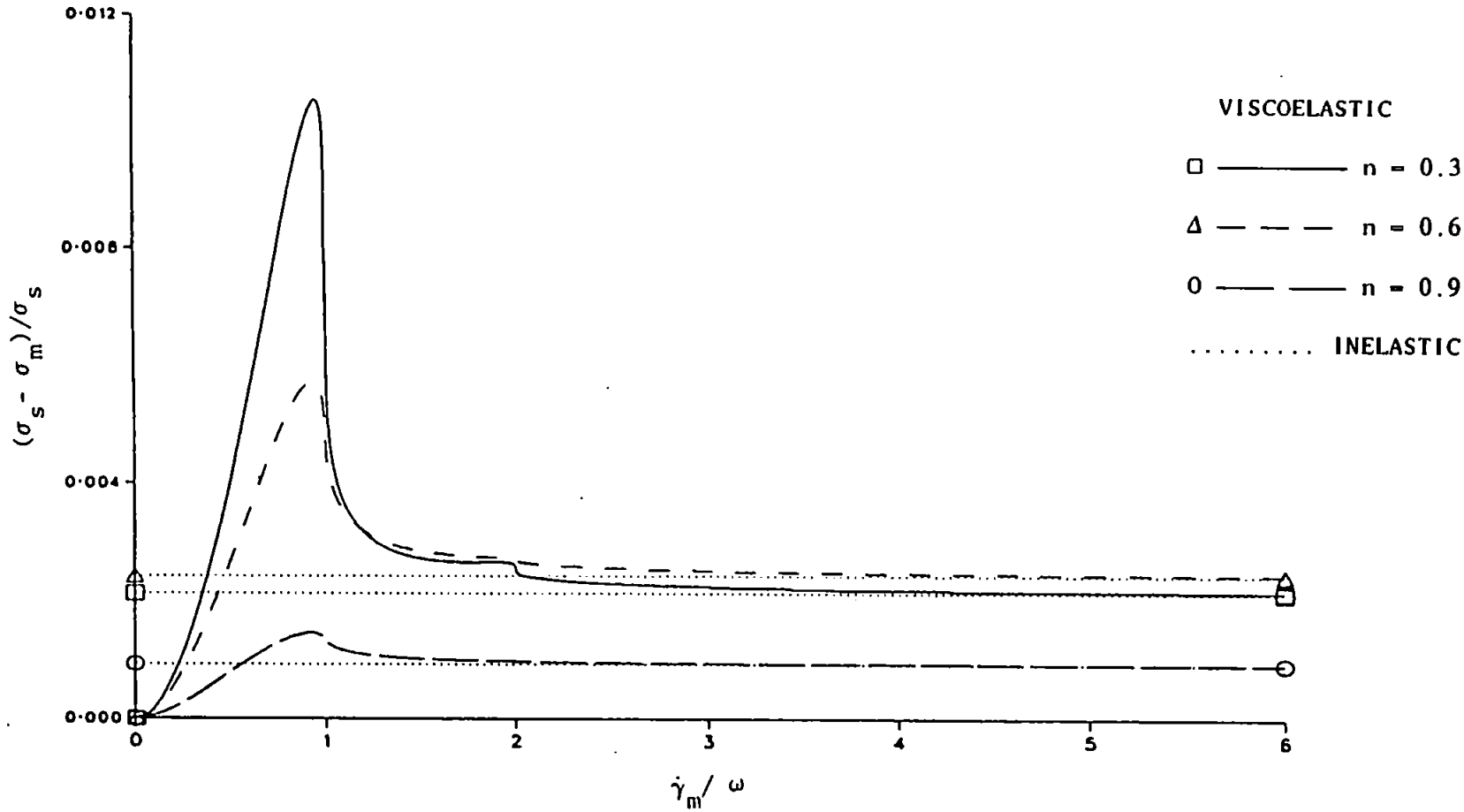
0·012
0·008
0·004
0·000
$(\sigma_s - \sigma_m)/\sigma_s$
0
1
2
3
4
5
6
$\dot{\gamma}_m/\omega$
VISCOELASTIC
n = 0.3
n = 0.6
n = 0.9
INELASTIC

FIGURE (4.2)

Combined Steady and Oscillatory Shear Flow.

Variation of mean shear stress reduction $(\sigma_s - \sigma_m)/\sigma_s$ with $\dot{\gamma}_m/\omega$ for a power law model ($n = 0.3, 0.6, 0.9$; $\epsilon = 0.8$).

(i). Goddard-Miller Model (viscoelastic).

(ii). Generalised Newtonian Model (inelastic).

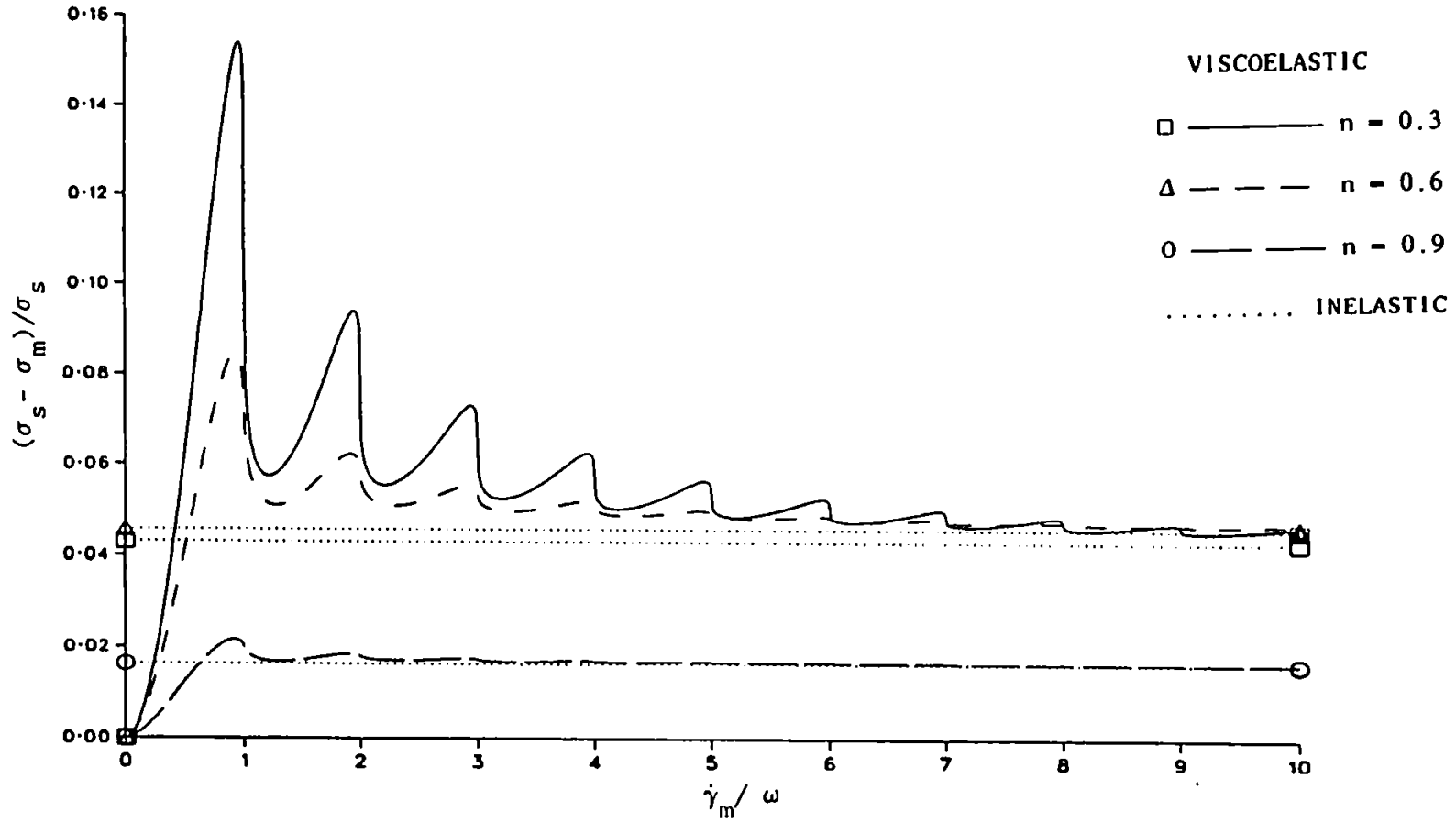
VISCOELASTIC
□ n = 0.3
Δ n = 0.6
O n = 0.9
..... INELASTIC
$(\sigma_s - \sigma_m)/\sigma_s$
$\dot{\gamma}_m/\omega$
0·00
0·02
0·04
0·06
0·08
0·10
0·12
0·14
0·16
0
1
2
3
4
5
6
7
8
9
10

FIGURE (4.3)

Combined Steady and Oscillatory Shear Flow.

Variation of mean shear stress reduction $(\sigma_s - \sigma_m)/\sigma_s$ with $\dot{\gamma}_m/\omega$ for a power law model (n = 0.3, 0.6, 0.9; ϵ = 1.0).

(i). Goddard-Miller Model (viscoelastic).

(ii). Generalised Newtonian Model (inelastic).

EFFECT OF OSCILLATION ON THE STEADY FLOW PROPERTIES OF NON-NEWTONIAN FLUIDS (POWER LAW VISCOSITY BEHAVIOUR).

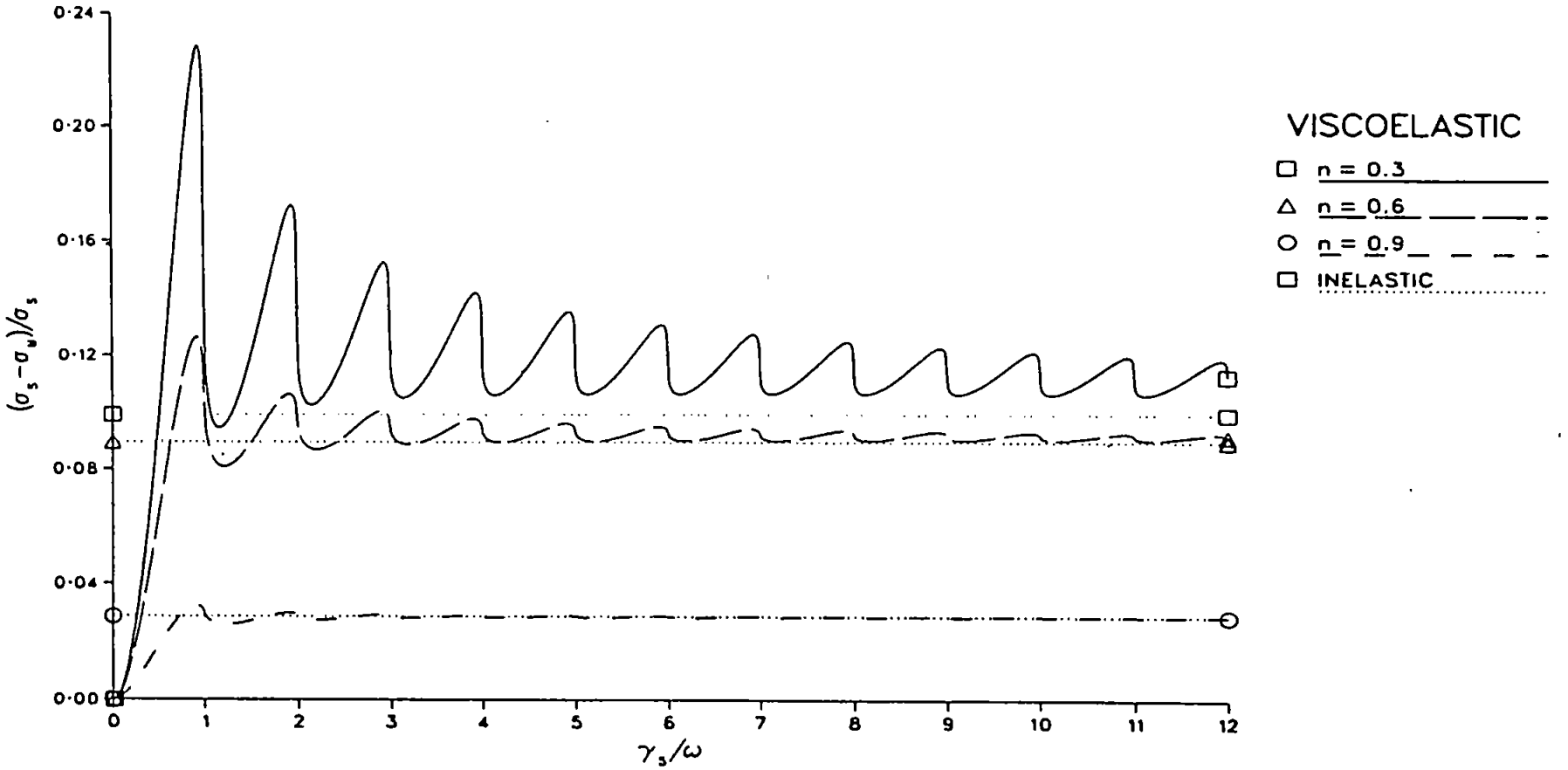

FIGURE (4.4)

Combined Steady and Oscillatory Shear Flow.

Variation of mean shear stress reduction $(\sigma_s - \sigma_m)/\sigma_s$ with $\dot{\gamma}_m/\omega$ for a power law model ($n = 0.3, 0.6, 0.9$; $\epsilon = 1.4$).

(i). Goddard-Miller Model (viscoelastic).

(ii). Generalised Newtonian Model (inelastic).

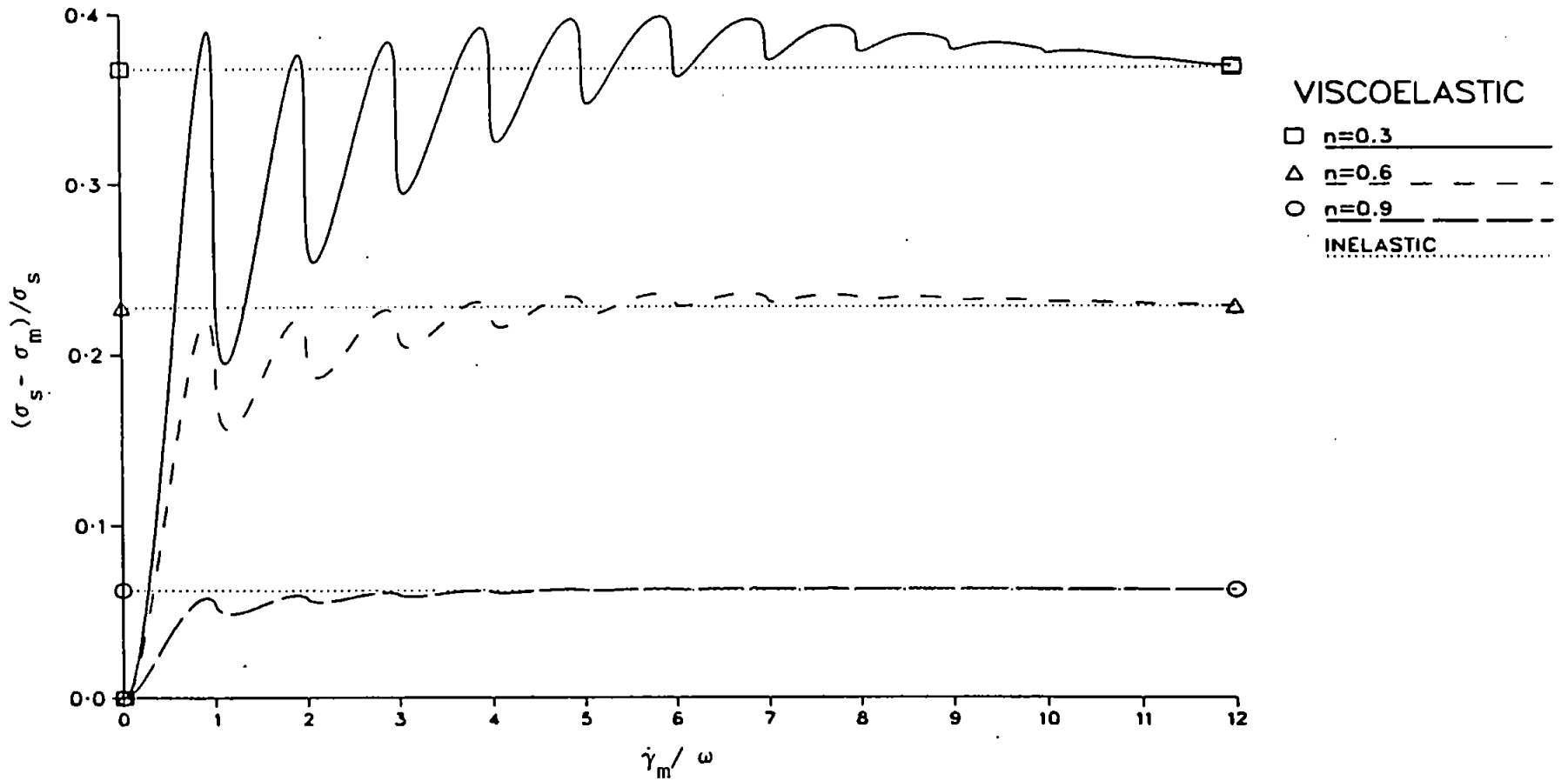
0·4
0·3
0·2
0·1
0·0
$(\sigma_s - \sigma_m)/\sigma_s$
0
1
2
3
4
5
6
7
8
9
10
11
12
$\dot{\gamma}_m/\omega$
VISCOELASTIC
n=0.3
n=0.6
n=0.9
INELASTIC

FIGURE (4.5)

Combined Steady and Oscillatory Shear Flow.

Variation of mean shear stress reduction $(\sigma_s - \sigma_m)/\sigma_s$ with $\dot{\gamma}_m/\omega$ for a power law model (n = 0.3, 0.6, 0.9; ϵ = 2.0).

(i). Goddard-Miller Model (viscoelastic).

(ii). Generalised Newtonian Model (inelastic).

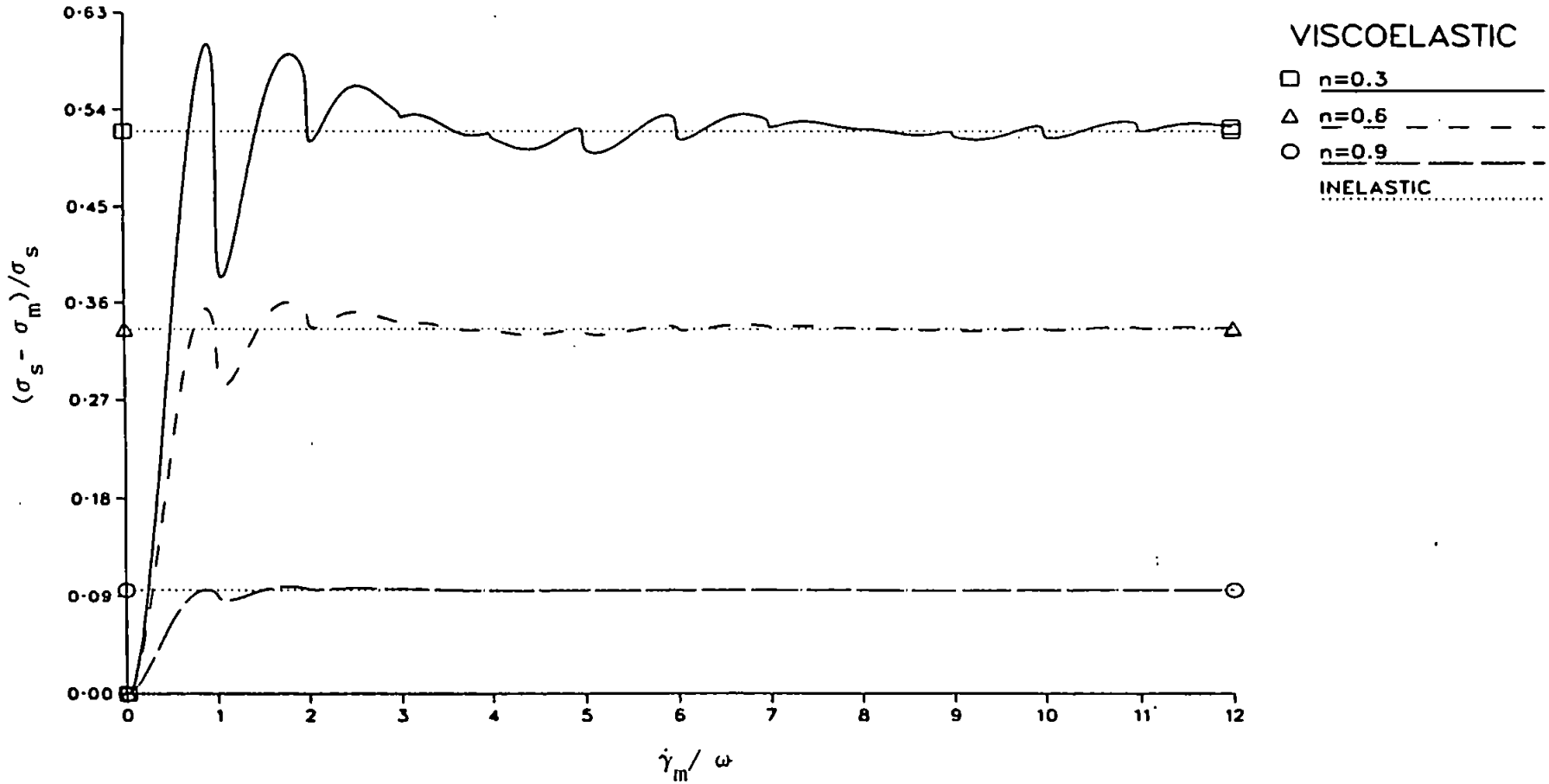
0·63
0·54
0·45
0·36
0·27
0·18
0·09
0·00
0
1
2
3
4
5
6
7
8
9
10
11
12
$(\sigma_s - \sigma_m)/\sigma_s$
$\dot{\gamma}_m/\ \omega$
VISCOELASTIC
n=0.3
n=0.6
n=0.9
INELASTIC

FIGURE (4.6)

Combined Steady and Oscillatory Shear Flow.

Variation of mean shear stress reduction $(\sigma_s - \sigma_m)/\sigma_s$ with $\dot{\gamma}_m/\omega$ for a Carreau model ($\lambda\omega$ = 1.0, 2.0, 5.0, 10.0; n = 0.3; ϵ = 0.8).

(i). Goddard-Miller Model (viscoelastic).

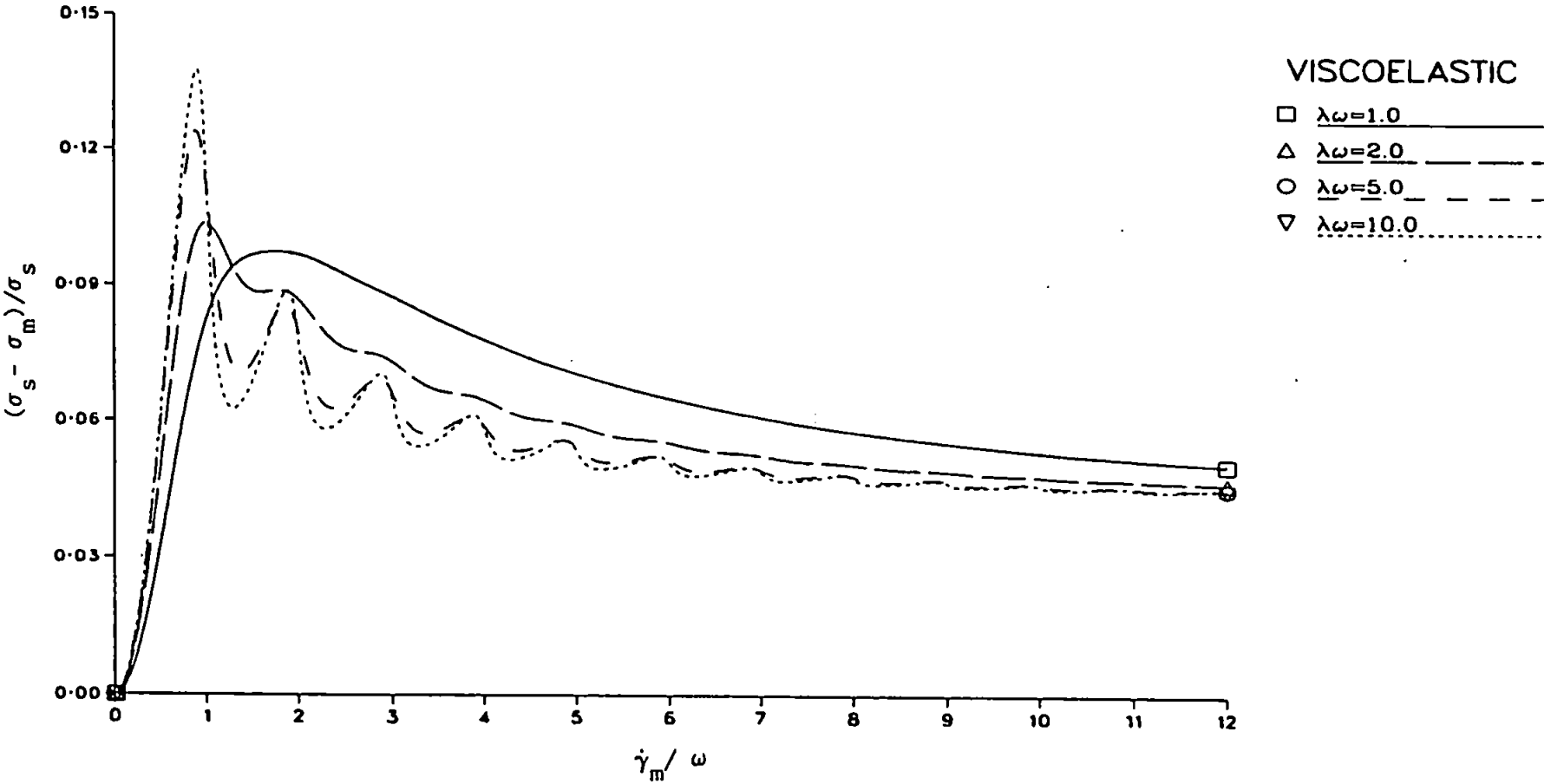
VISCOELASTIC
λω=1.0
λω=2.0
λω=5.0
λω=10.0
0·15
0·12
0·09
0·06
0·03
0·00
0
1
2
3
4
5
6
7
8
9
10
11
12
$(\sigma_s - \sigma_m)/\sigma_s$
$\dot{\gamma}_m/\ \omega$

FIGURE (4.7)

Combined Steady and Oscillatory Shear Flow.

Variation of mean shear stress reduction $(\sigma_s - \sigma_m)/\sigma_s$ with $\dot{\gamma}_m/\omega$ for a Carreau model ($\lambda\omega$ = 1.0, 2.0, 5.0, 10.0; n = 0.3; ϵ = 1.2).

(i). Goddard-Miller Model (viscoelastic).

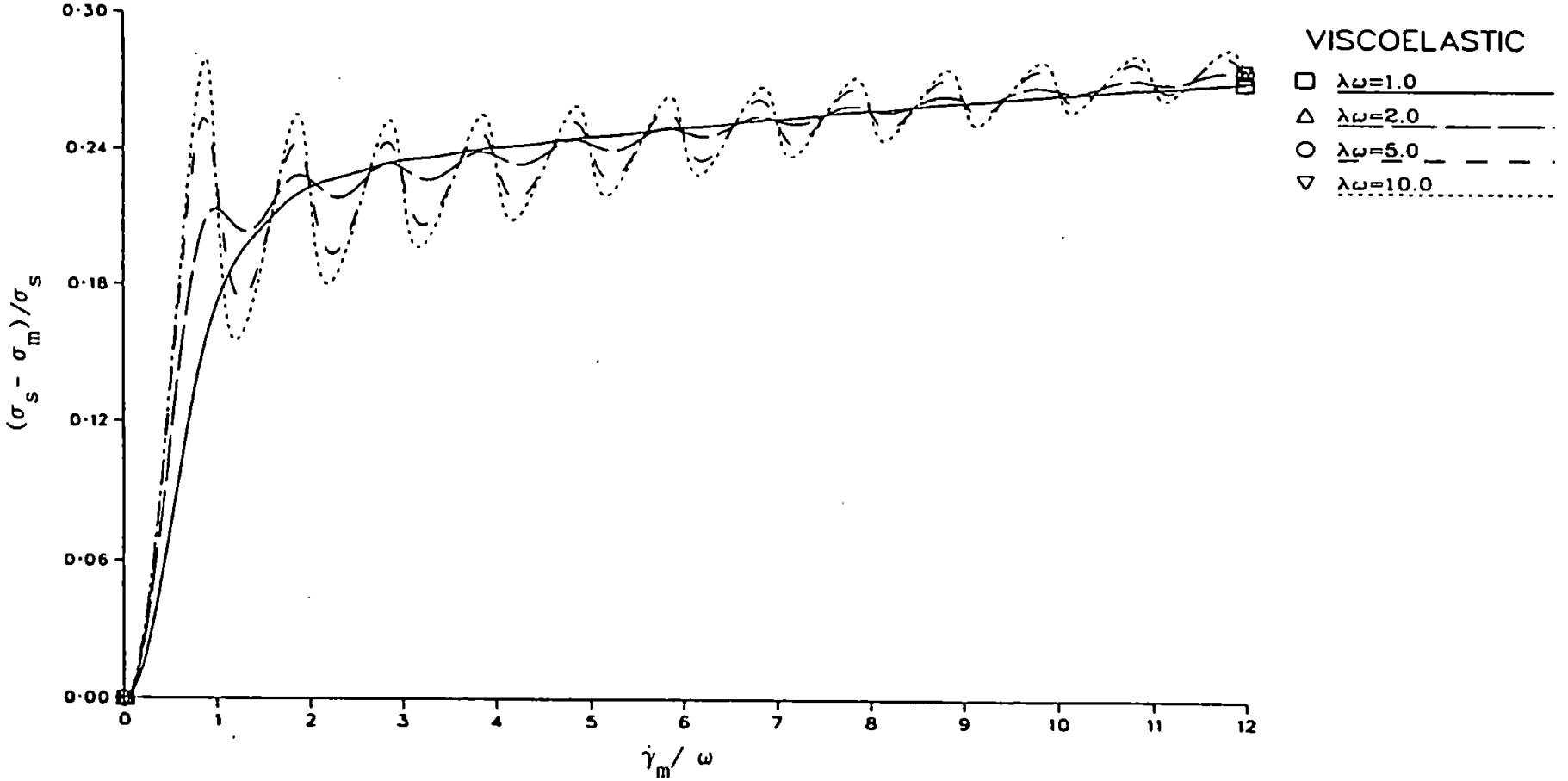
VISCOELASTIC
λω=1.0
λω=2.0
λω=5.0
λω=10.0
0·30
0·24
0·18
0·12
0·06
0·00
0
1
2
3
4
5
6
7
8
9
10
11
12
$(\sigma_s - \sigma_m)/\sigma_s$
$\dot{\gamma}_m/\omega$

FIGURE (4.8)

Combined Steady and Oscillatory Shear Flow.

Variation of mean shear stress reduction $(\sigma_s - \sigma_m)/\sigma_s$ with $\dot{\gamma}_m/\omega$ for a Carreau model ($\lambda\omega = 5.0$; $n = 0.2, 0.4, 0.6, 0.8$; $\epsilon = 1.5$).

(i). Goddard-Miller Model (viscoelastic).

(ii). Generalised Newtonian Model (inelastic).

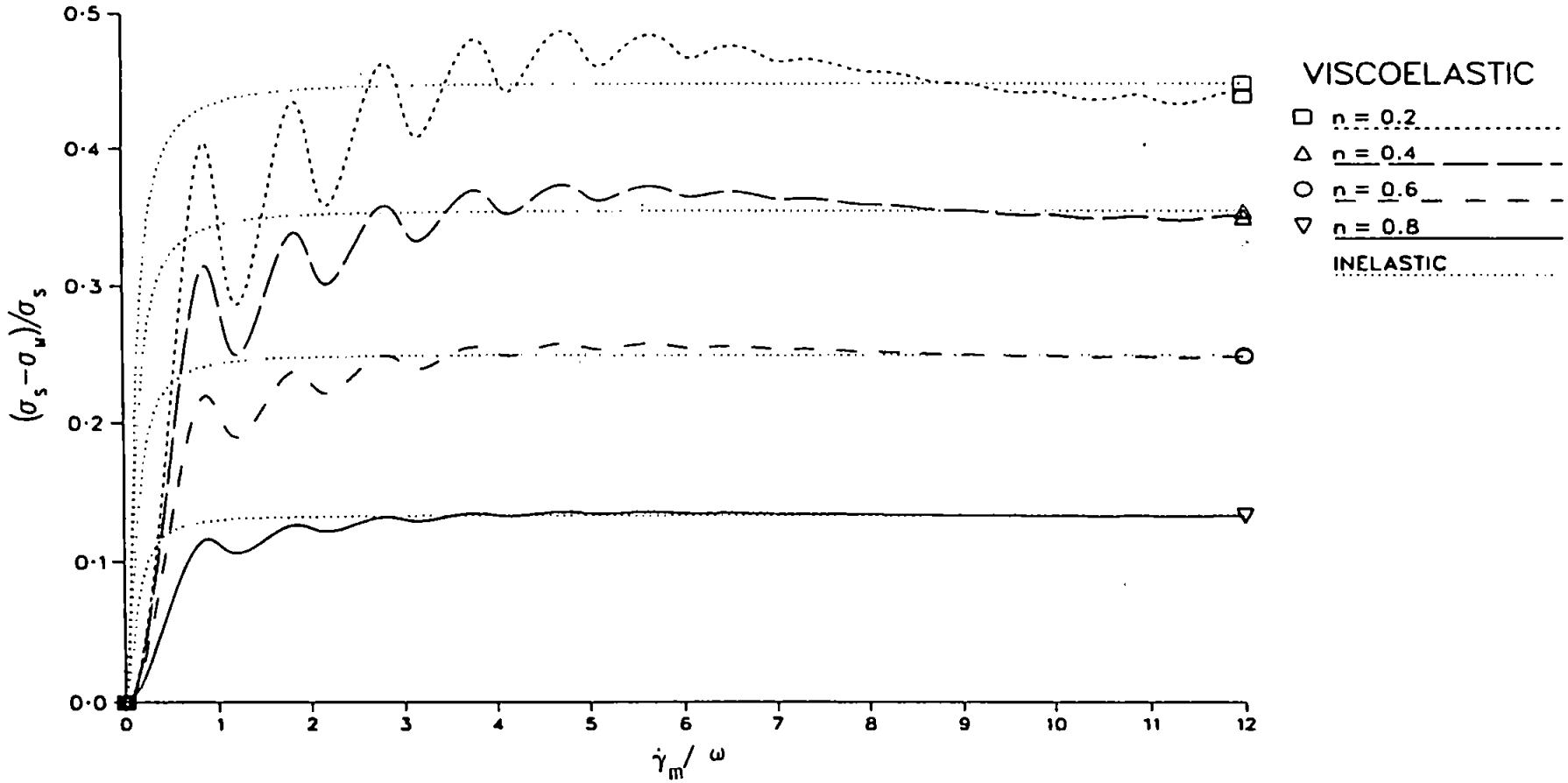
0·5
0·4
0·3
0·2
0·1
0·0
0
1
2
3
4
5
6
7
8
9
10
11
12
$(\sigma_s - \sigma_u)/\sigma_s$
$\dot{\gamma}_m / \omega$
VISCOELASTIC
n = 0.2
n = 0.4
n = 0.6
n = 0.8
INELASTIC

FIGURE (4.9)

Combined Steady and Oscillatory Shear Flow.

Variation of mean shear stress reduction $(\sigma_s - \sigma_m)/\sigma_s$ with $\dot{\gamma}_m/\omega$ for a Carreau model ($\lambda\omega = 5.0$; $n = 0.2, 0.4, 0.6, 0.8$; $\epsilon = 3.0$).

(i). Goddard-Miller Model (viscoelastic).

(ii). Generalised Newtonian Model (inelastic).

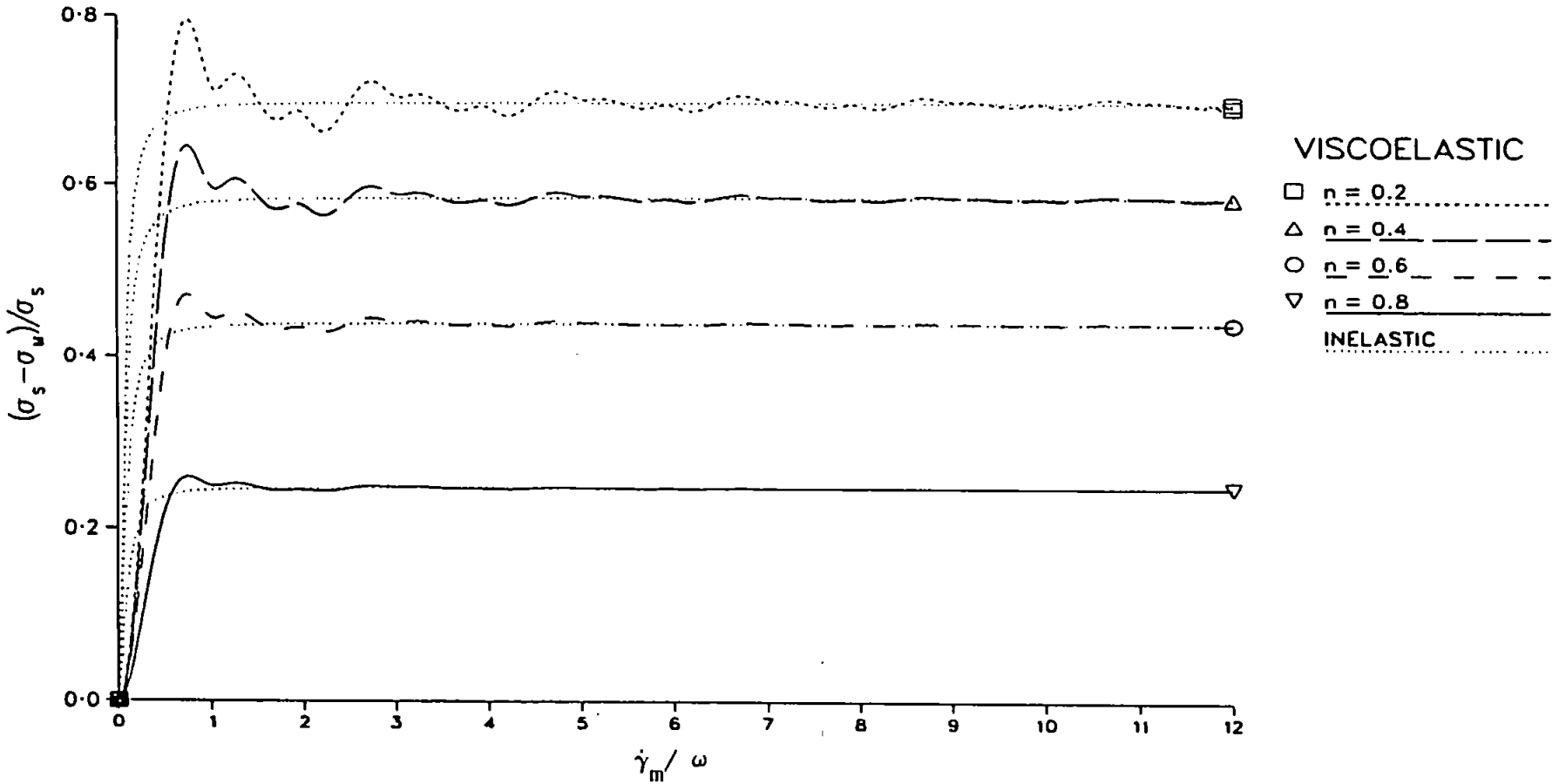
0·8
0·6
0·4
0·2
0·0
0
1
2
3
4
5
6
7
8
9
10
11
12
$(\sigma_s - \sigma_w)/\sigma_s$
$\dot{\gamma}_m / \omega$
VISCOELASTIC
n = 0.2
n = 0.4
n = 0.6
n = 0.8
INELASTIC

FIGURE (4.10)

Combined Steady and Oscillatory Shear Flow.

Variation of mean shear stress reduction $(\sigma_s - \sigma_m)/\sigma_s$ with $\dot{\gamma}_m/\omega$ for a Carreau model ($\lambda\omega = 5.0$; $\epsilon = 0.2, 0.5, 0.8, 1.0$; $n = 0.3$).

(i). Goddard-Miller Model (viscoelastic).

(ii). Generalised Newtonian Model (inelastic).

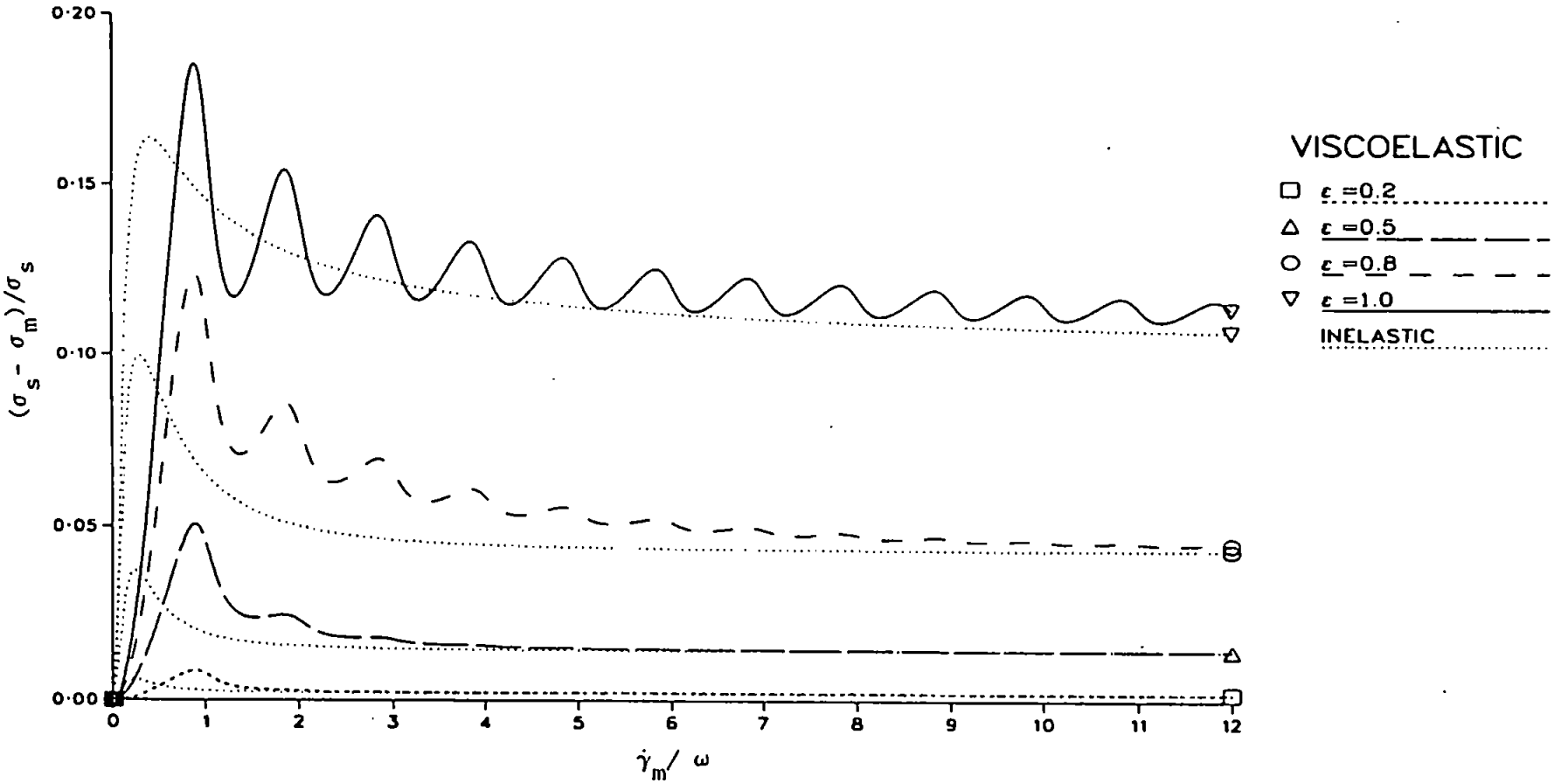
0·20
0·15
0·10
0·05
0·00
$(\sigma_s - \sigma_m)/\sigma_s$
0
1
2
3
4
5
6
7
8
9
10
11
12
$\dot{\gamma}_m/\ \omega$
VISCOELASTIC
ε =0.2
ε =0.5
ε =0.8
ε =1.0
INELASTIC

FIGURE (4.11)

Combined Steady and Oscillatory Shear Flow.

Variation of mean shear stress reduction $(\sigma_s - \sigma_m)/\sigma_s$ with $\dot{\gamma}_m/\omega$ for a Carreau model ($\lambda\omega = 5.0$; $\epsilon = 1.0, 1.5, 2.0, 2.5$; $n = 0.3$).

(i). Goddard-Miller Model (viscoelastic).

(ii). Generalised Newtonian Model (inelastic).

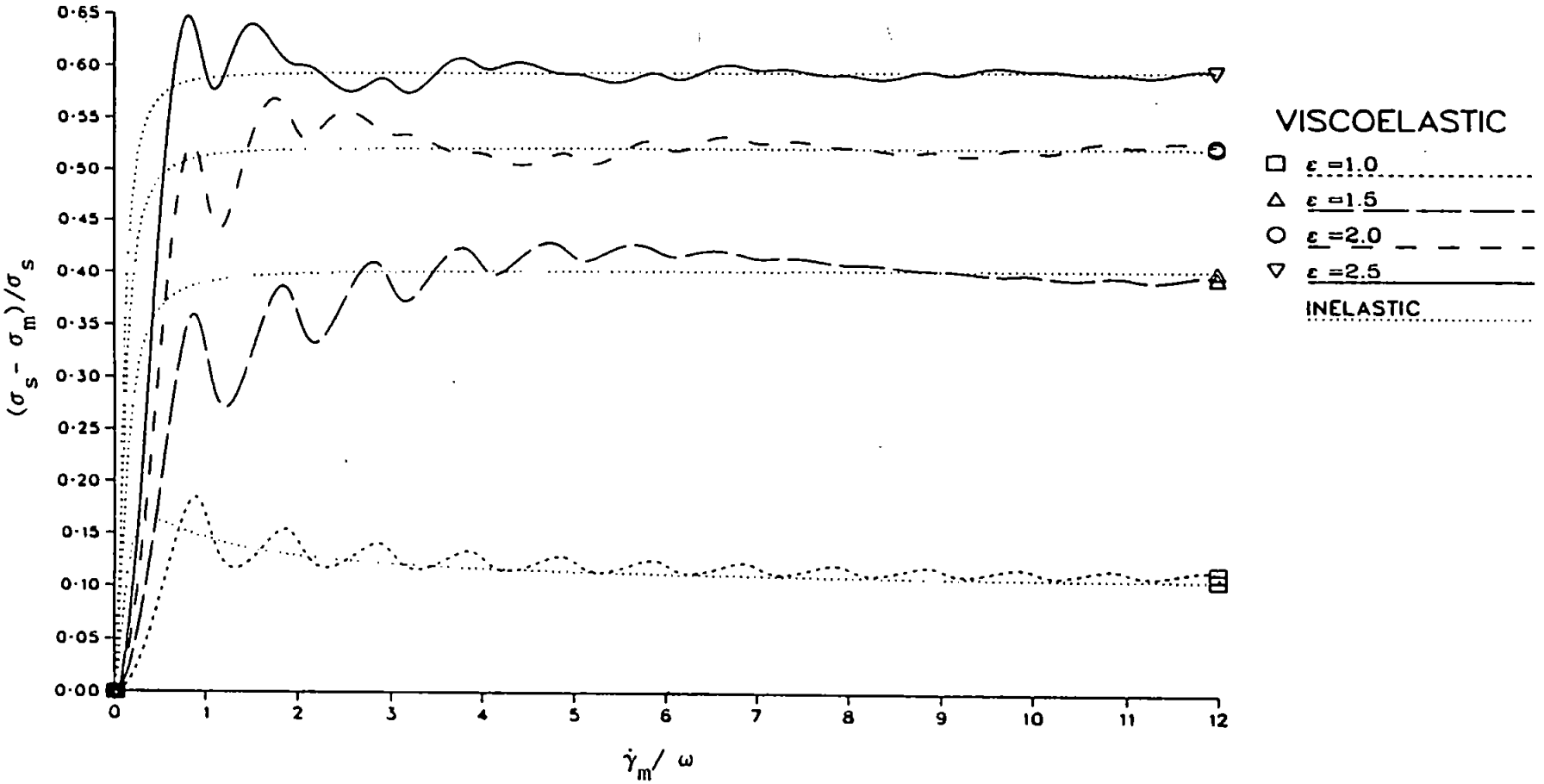
0·65
0·60
0·55
0·50
0·45
0·40
0·35
0·30
0·25
0·20
0·15
0·10
0·05
0·00
$(\sigma_s - \sigma_m)/\sigma_s$
0
1
2
3
4
5
6
7
8
9
10
11
12
$\dot{\gamma}_m/\ \omega$
VISCOELASTIC
ε =1.0
ε =1.5
ε =2.0
ε =2.5
INELASTIC

FIGURE (4.12)

Combined Steady and Oscillatory Shear Flow.

Variation of mean shear stress reduction $(\sigma_s - \sigma_m)/\sigma_s$ with $\dot{\gamma}_m/\omega$ for a Goddard-Miller Model (viscoelastic), ($n = 0.3$; $\epsilon = 1.5$; $\lambda\omega = 5.0$).

(i). Power Law Model

(ii). Carreau Model.

(iii). Segalman Model.

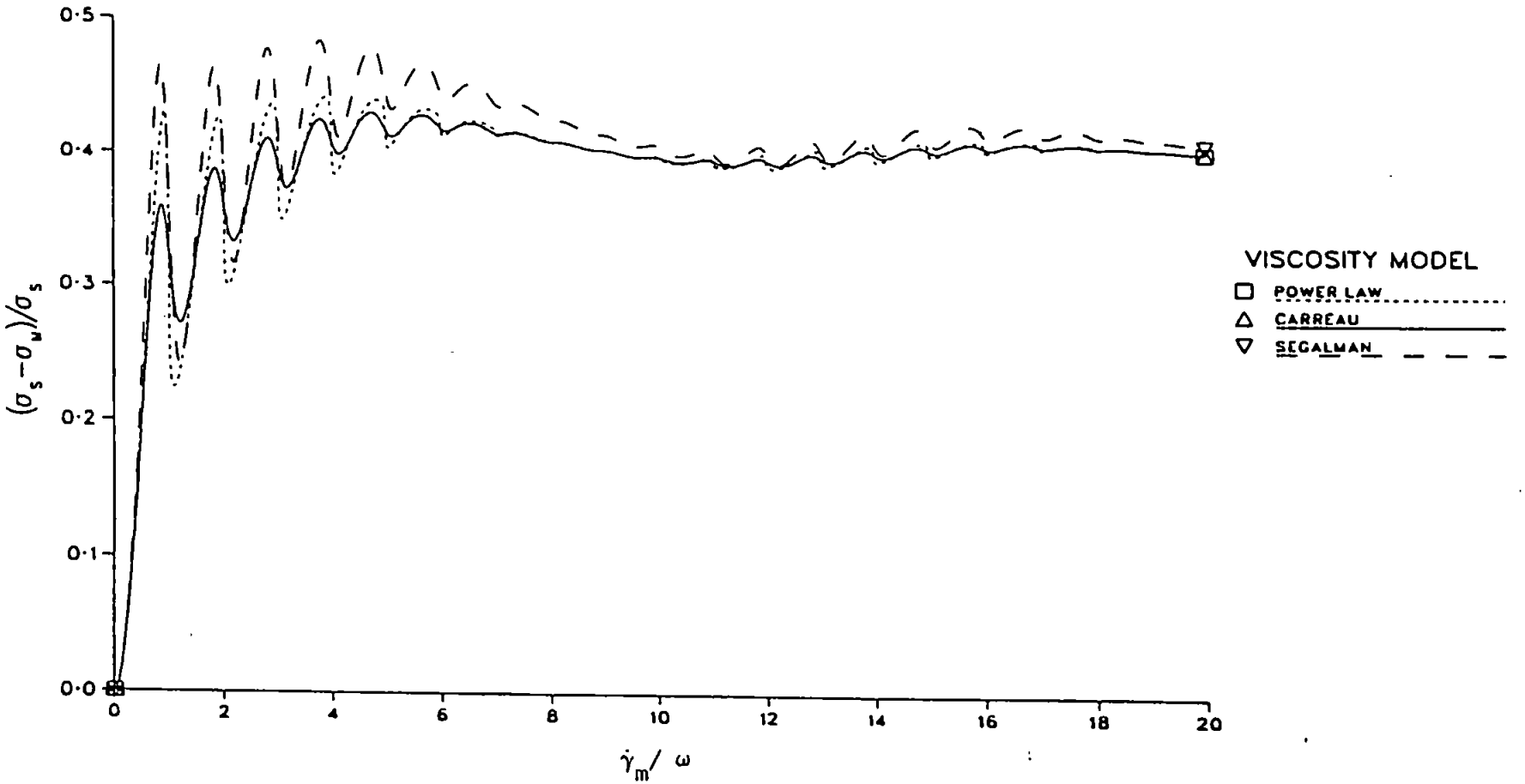
0·5
0·4
0·3
0·2
0·1
0·0
$(\sigma_s - \sigma_w)/\sigma_s$
0
2
4
6
8
10
12
14
16
18
20
$\dot{\gamma}_m / \omega$
VISCOSITY MODEL
POWER LAW
CARREAU
SEGALMAN

FIGURE (4.13)

Combined Steady and Oscillatory Shear Flow.

Variation of mean shear stress reduction $(\sigma_s - \sigma_m)/\sigma_s$ with $\dot{\gamma}_m/\omega$ for a Generalised Newtonian Model (inelastic), ($n = 0.2$; $\epsilon = 1.5$; $\lambda\omega = 5.0$).

(i). Power Law Model.

(ii). Carreau Model.

(iii). Segalman Model.

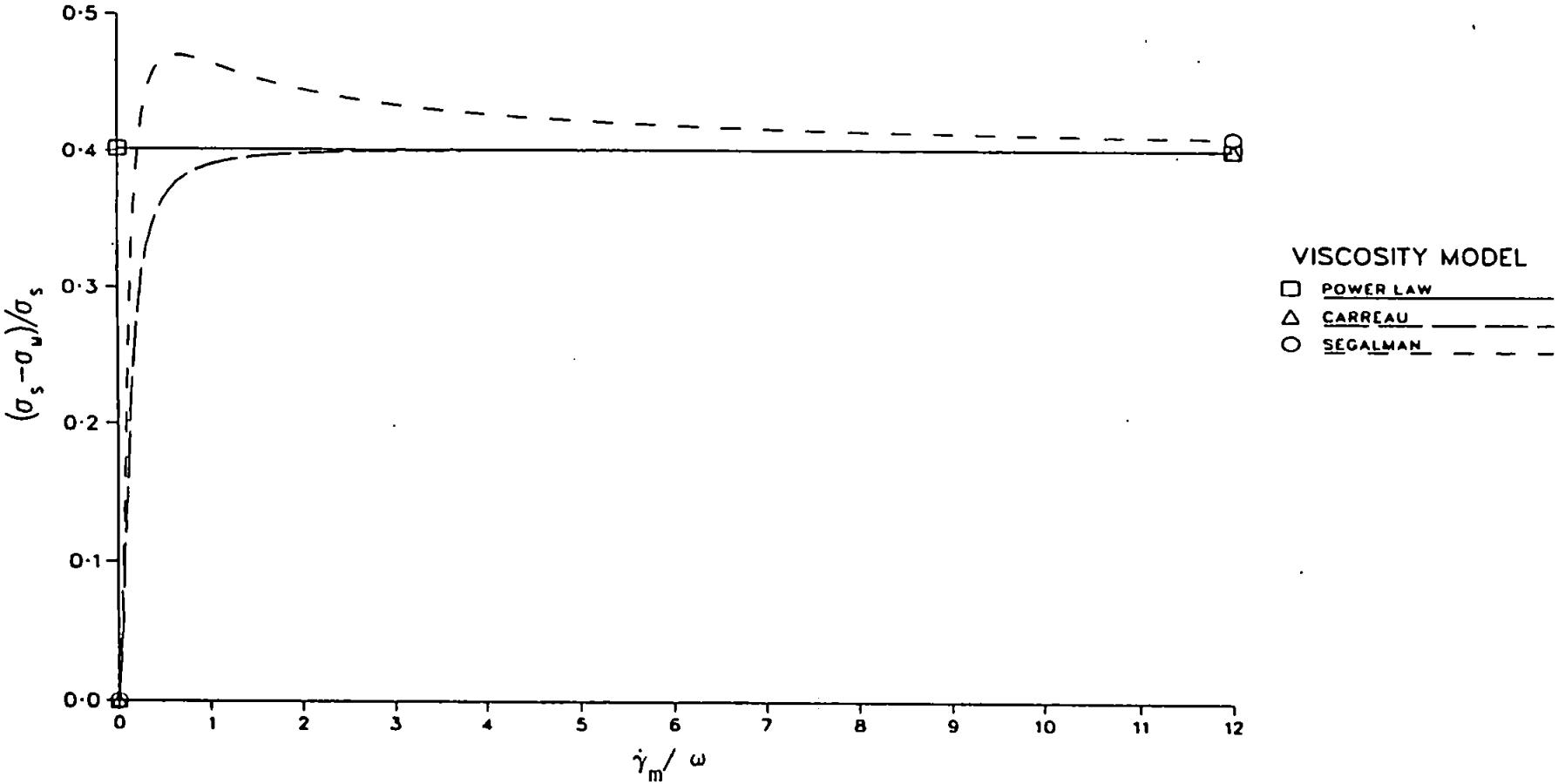
0·5
0·4
0·3
0·2
0·1
0·0
$(\sigma_s - \sigma_\infty)/\sigma_s$
0
1
2
3
4
5
6
7
8
9
10
11
12
$\dot{\gamma}_m / \omega$
VISCOSITY MODEL
POWER LAW
CARREAU
SEGALMAN

FIGURE (5.1)

Viscosity behaviour of a 2% solution of polyisobutylene in dekalin.

(i). Experimental shear viscosity data.

(ii). Experimental dynamic viscosity data.

(iii). Magnitude of complex viscosity.

(iv). Carreau fit to shear viscosity data.
(η_0 = 28 Ns/m^2; n = 0.35; λ =4.5 s^{-1}).

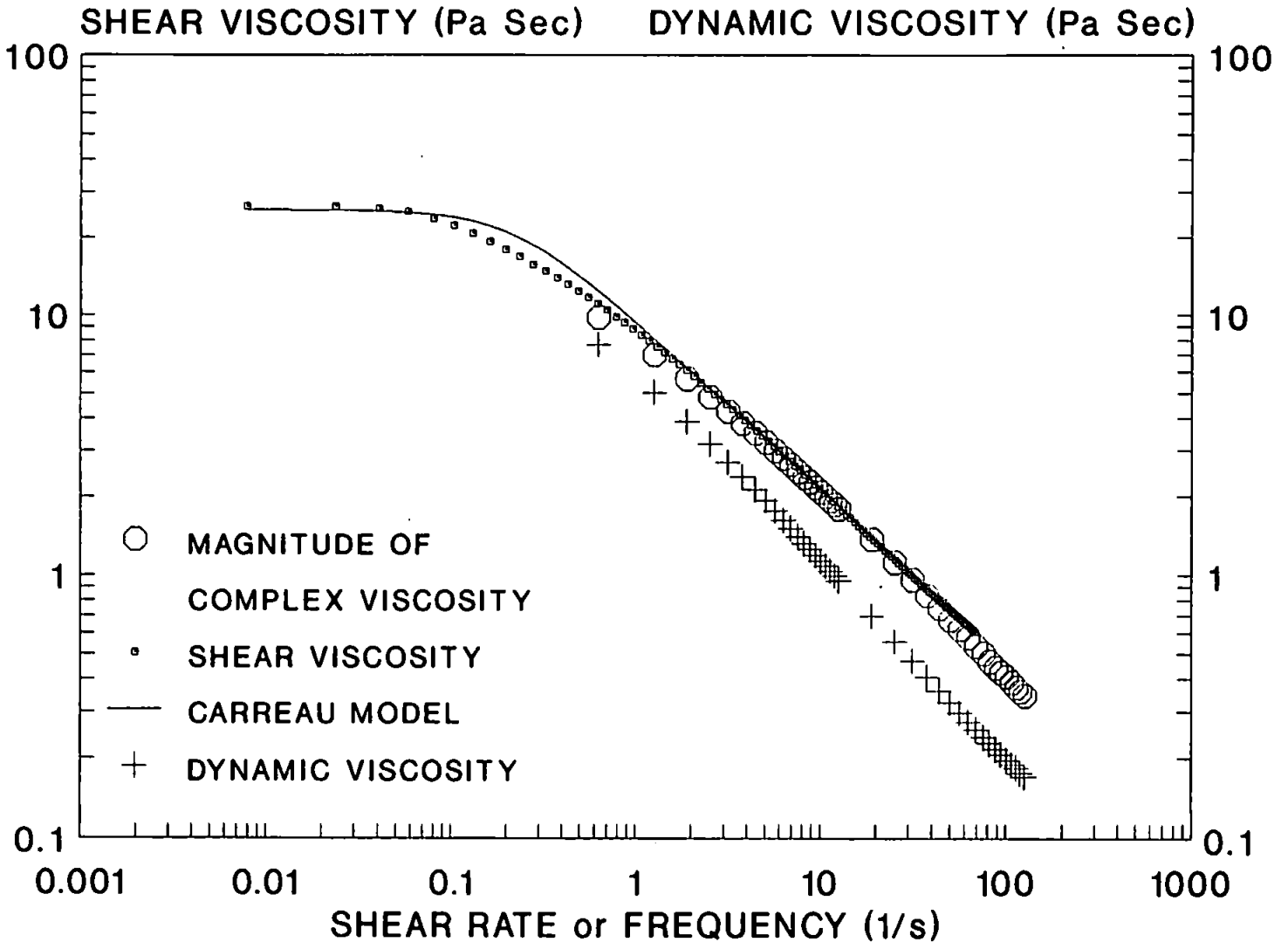
SHEAR VISCOSITY (Pa Sec)
DYNAMIC VISCOSITY (Pa Sec)
100
10
1
0.1
MAGNITUDE OF
COMPLEX VISCOSITY
SHEAR VISCOSITY
CARREAU MODEL
DYNAMIC VISCOSITY
0.001
0.01
0.1
1
10
100
1000
SHEAR RATE or FREQUENCY (1/s)

FIGURE (5.2)

Combined Steady and Oscillatory Shear Flow.

Variation of mean shear stress reduction $(\sigma_s - \sigma_m)/\sigma_s$ with $\dot{\gamma}_m/\omega$, (ϵ = 0.8; freq = 2 Hz).

(i). Experimental data (concentric cylinder geometry, r_i = 18.5 mm, r_o = 20.75 mm).

(ii). Goddard-Miller model (viscoelastic).

(iii). Generalised Newtonian model (inelastic).

(iv). Controlled stress inelastic correction.

Model constants (based on Carreau fit to shear viscosity curve), (n=0.35; λ =4.5 s^{-1}).

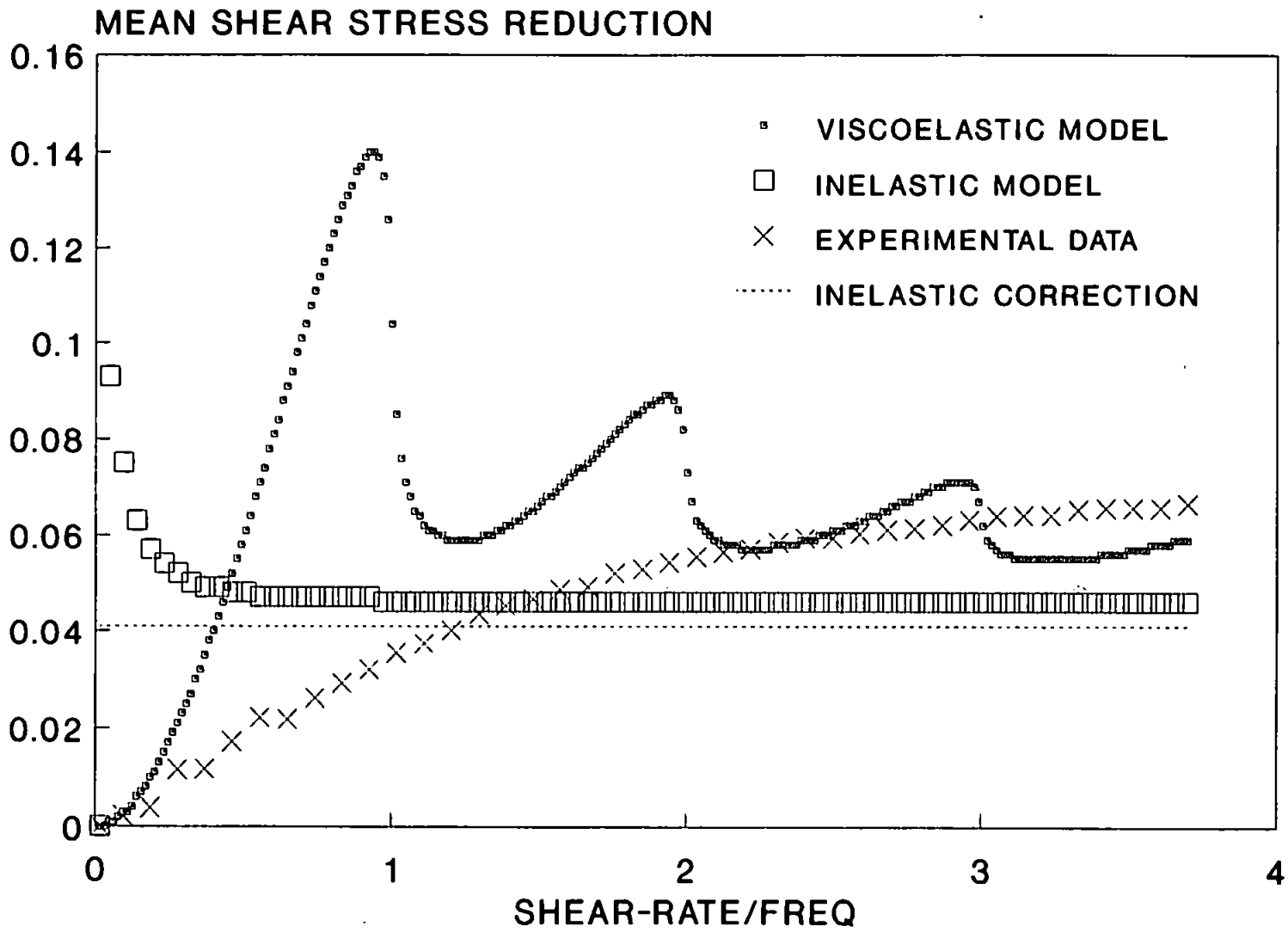
MEAN SHEAR STRESS REDUCTION
0.16
0.14
0.12
0.1
0.08
0.06
0.04
0.02
0
0
1
2
3
4
SHEAR-RATE/FREQ
VISCOELASTIC MODEL
INELASTIC MODEL
EXPERIMENTAL DATA
INELASTIC CORRECTION

FIGURE (5.3)

Combined Steady and Oscillatory Shear Flow.

Variation of mean shear stress reduction $(\sigma_s - \sigma_m)/\sigma_s$ with $\dot{\gamma}_m/\omega$, (ϵ = 1.2; freq = 2 Hz).

(i). Experimental data (concentric cylinder geometry, r_i = 18.5 mm, r_o = 20.75 mm).

(ii). Goddard-Miller model (viscoelastic).

(iii). Generalised Newtonian model (inelastic).

(iv). Controlled stress inelastic correction.

Model constants (based on Carreau fit to shear viscosity curve), (n=0.35; λ =4.5 s^{-1}).

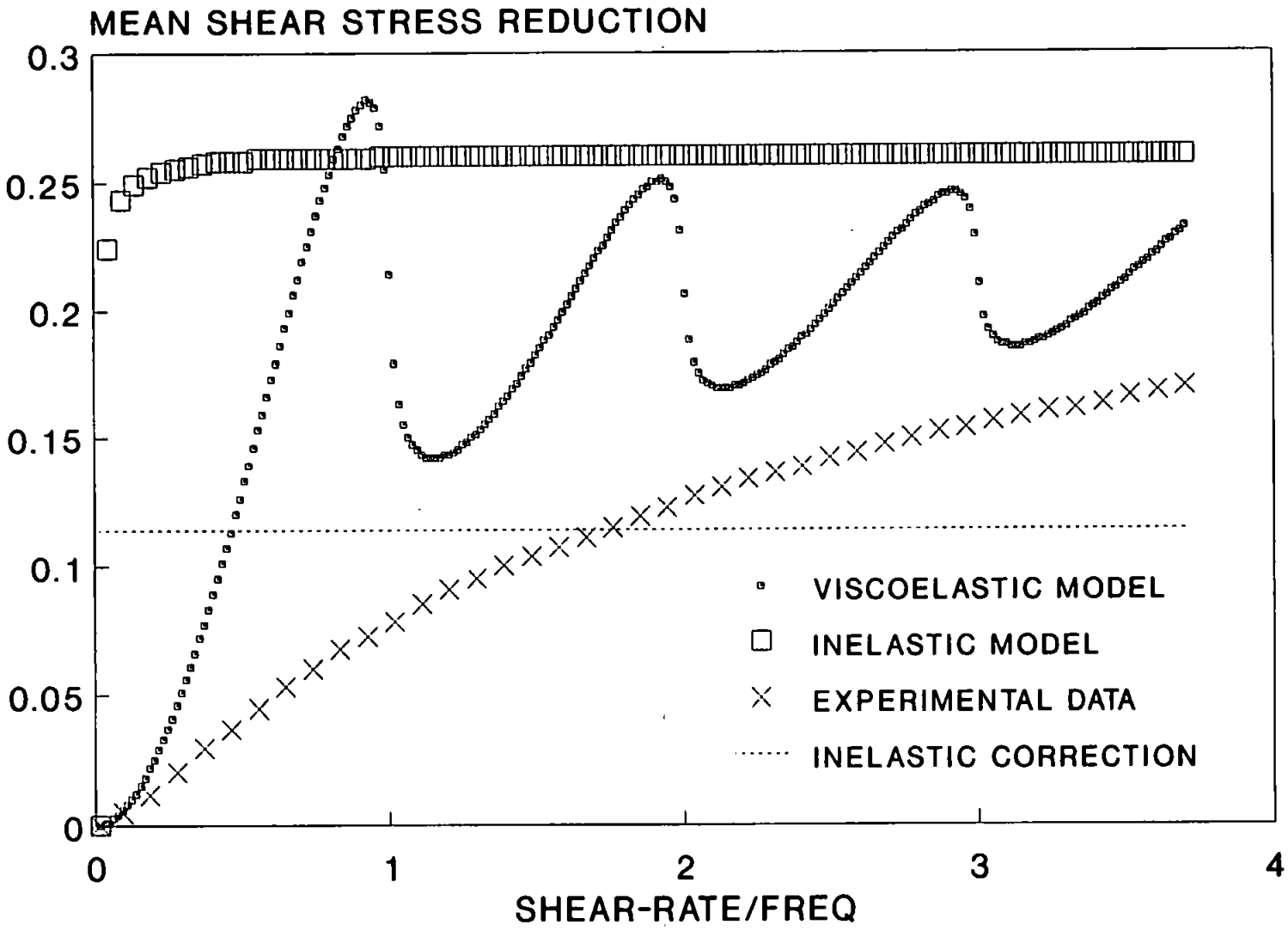
MEAN SHEAR STRESS REDUCTION
0.3
0.25
0.2
0.15
0.1
0.05
0
0
1
2
3
4
SHEAR-RATE/FREQ
VISCOELASTIC MODEL
INELASTIC MODEL
EXPERIMENTAL DATA
INELASTIC CORRECTION

FIGURE (5.4)

Combined Steady and Oscillatory Shear Flow.

Variation of mean shear stress reduction $(\sigma_s - \sigma_m)/\sigma_s$ with $\dot{\gamma}_m/\omega$, (ϵ = 1.5; freq = 2 Hz).

(i). Experimental data (concentric cylinder geometry, r_i = 18.5 mm, r_o = 20.75 mm).

(ii). Goddard-Miller model (viscoelastic).

(iii). Generalised Newtonian model (inelastic).

(iv). Controlled stress inelastic correction.

Model constants (based on Carreau fit to shear viscosity curve), (n=0.35; λ = 4.5 s^{-1}).

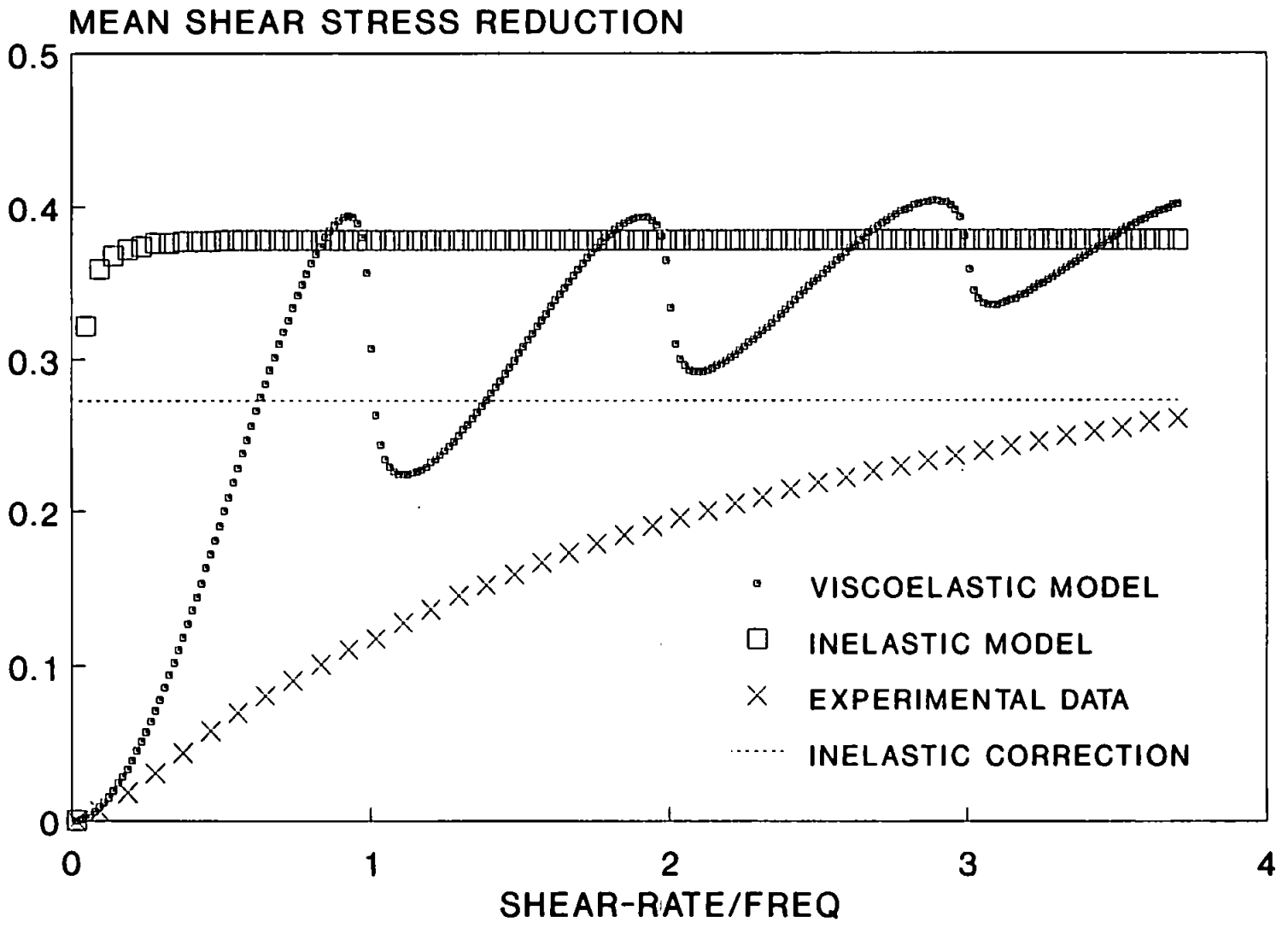
MEAN SHEAR STRESS REDUCTION
0.5
0.4
0.3
0.2
0.1
0
0
1
2
3
4
SHEAR-RATE/FREQ
VISCOELASTIC MODEL
INELASTIC MODEL
EXPERIMENTAL DATA
INELASTIC CORRECTION

FIGURE (5.5)

Combined Steady and Oscillatory Shear Flow.

Variation of mean shear stress reduction $(\sigma_s - \sigma_m)/\sigma_s$ with $\dot{\gamma}_m/\omega$, (ϵ = 2.0; freq = 2 Hz).

(i). Experimental data (cone and plate geometry, $\theta_0 = 1^{\cdot}$, a = 2 cm).

(ii). Experimental data (Davies et al [12], cone and plate geometry, $\theta_0 = 2^{\cdot}$, a = 2 cm, freq = 4 Hz).

(iii) Goddard-Miller model (viscoelastic).

(iv). Generalised Newtonian model (inelastic).

(v). Controlled stress inelastic correction.

Model constants (based on Carreau fit to shear viscosity curve), (n=0.35; $\lambda = 4.5\ s^{-1}$).

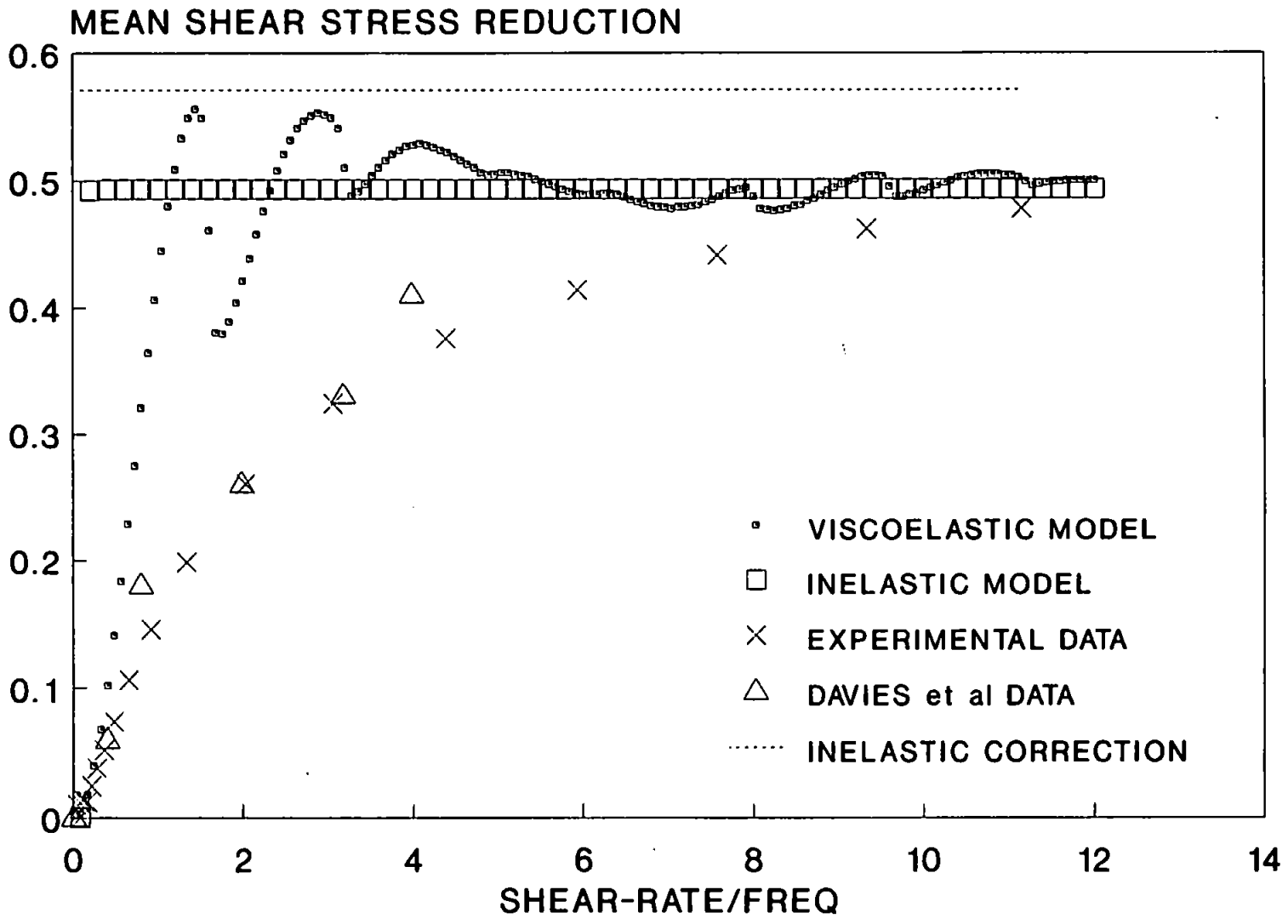
MEAN SHEAR STRESS REDUCTION
0.6
0.5
0.4
0.3
0.2
0.1
0
0
2
4
6
8
10
12
14
SHEAR-RATE/FREQ
VISCOELASTIC MODEL
INELASTIC MODEL
EXPERIMENTAL DATA
DAVIES et al DATA
INELASTIC CORRECTION

FIGURE (5.6)

Combined Steady and Oscillatory Shear Flow.

Variation of mean shear stress reduction $(\sigma_s - \sigma_m)/\sigma_s$ with $\dot{\gamma}_m/\omega$, (ϵ = 2.0; freq = 1 Hz).

(i). Experimental data (cone and plate geometry, $\theta_0 = 1^\circ$, a = 2 cm).

(ii). Goddard-Miller model (viscoelastic).

(iii). Generalised Newtonian model (inelastic).

(iv). Controlled stress inelastic correction.

Model constants (based on Carreau fit to shear viscosity curve), (n=0.35; $\lambda = 4.5\ s^{-1}$).

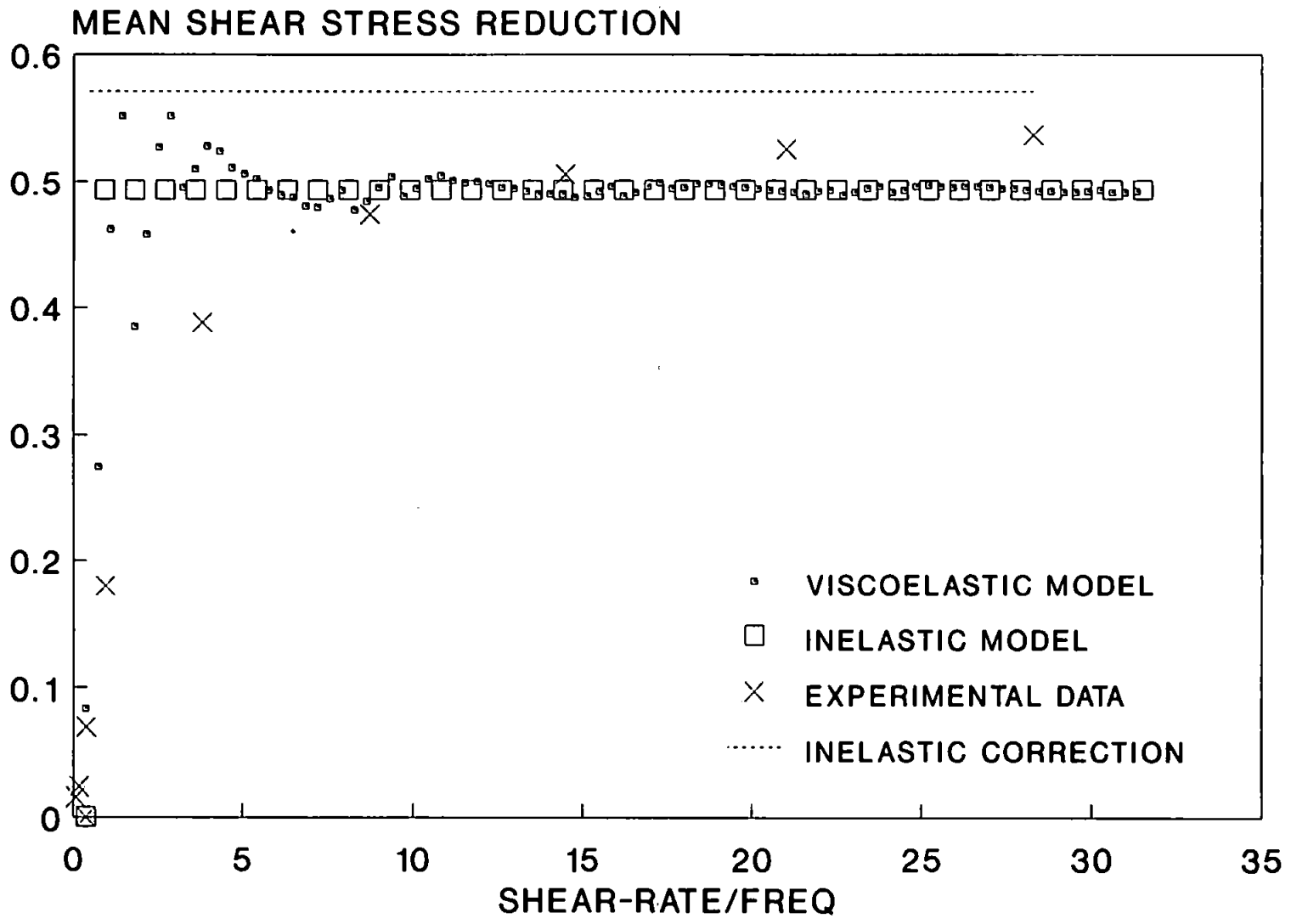
MEAN SHEAR STRESS REDUCTION
0.6
0.5
0.4
0.3
0.2
0.1
0
0
5
10
15
20
25
30
35
SHEAR-RATE/FREQ
VISCOELASTIC MODEL
INELASTIC MODEL
EXPERIMENTAL DATA
INELASTIC CORRECTION

FIGURE (5.7)

Combined Steady and Oscillatory Shear Flow.

Variation of mean shear stress reduction $(\sigma_s - \sigma_m)/\sigma_s$ with ϵ, ($\dot{\gamma}_m = 6.28\ s^{-1}$; freq = 1 Hz).

(i). Experimental data (cone and plate geometry, $\theta_0 = 1^{\circ}$, a = 2 cm).

(ii). Goddard-Miller model (viscoelastic).

(iii). Generalised Newtonian model (inelastic).

Model constants (based on Carreau fit to shear viscosity curve), (n=0.35; $\lambda = 4.5\ s^{-1}$).

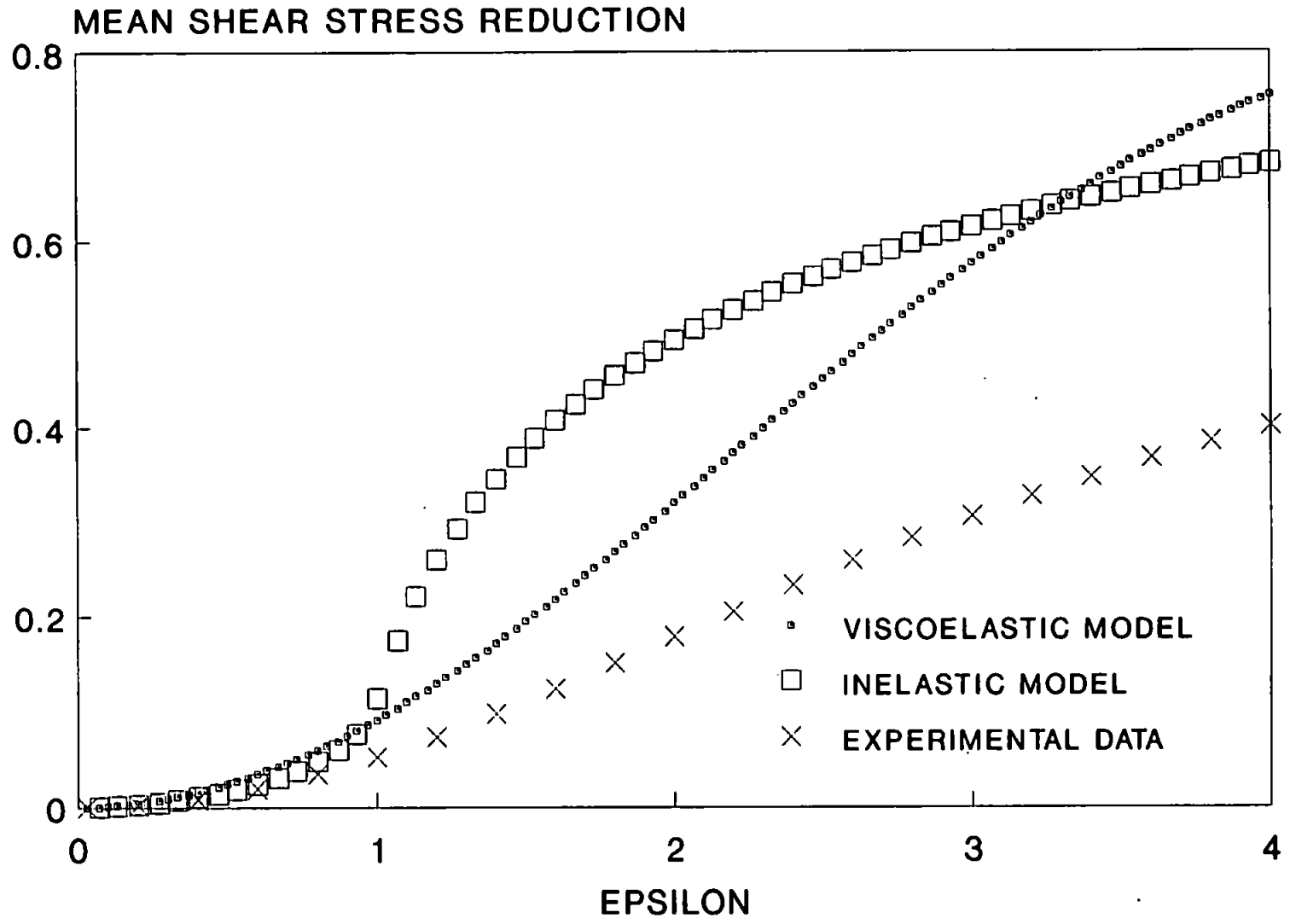
MEAN SHEAR STRESS REDUCTION
0.8
0.6
0.4
0.2
0
0
1
2
3
4
EPSILON
VISCOELASTIC MODEL
INELASTIC MODEL
EXPERIMENTAL DATA

FIGURE (5.8)

Combined Steady and Oscillatory Shear Flow.

Variation of mean shear stress reduction $(\sigma_s - \sigma_m)/\sigma_s$ with ϵ, ($\dot{\gamma}_m = 6.28\ s^{-1}$; freq = 1 Hz).

(i). Inelastic power law model (for small ϵ [ ]).

(ii). Controlled strain inelastic model.

(iii). Controlled stress inelastic model.

Model constants (based on Carreau fit to shear viscosity curve), ($n=0.35$; $\lambda = 4.5\ s^{-1}$).

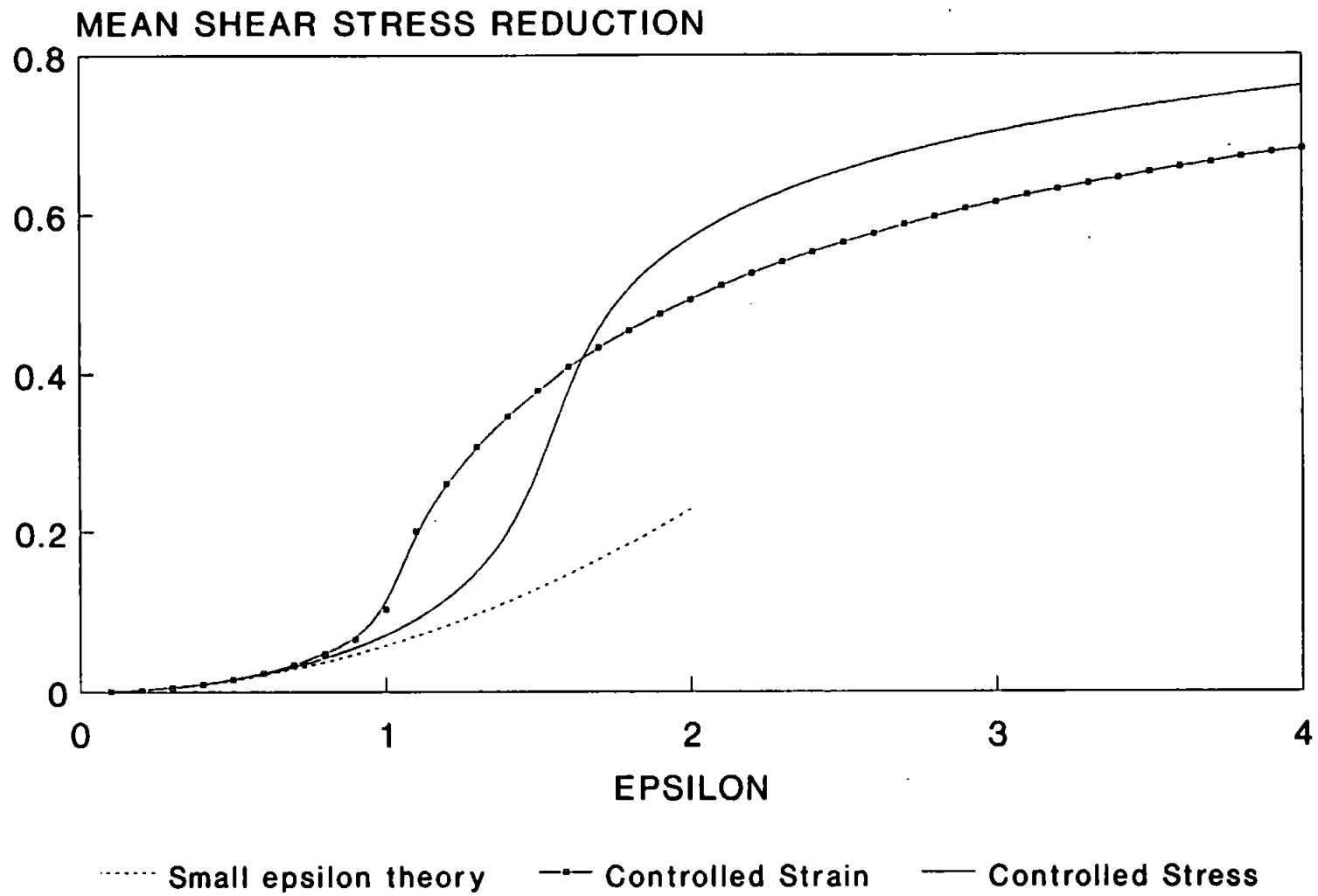
MEAN SHEAR STRESS REDUCTION
0.8
0.6
0.4
0.2
0
0
1
2
3
4
EPSILON
Small epsilon theory
Controlled Strain
Controlled Stress

FIGURE (5.9)

Combined Steady and Oscillatory Shear.

Shear rate waveform for an inelastic power law fluid (n = 0.35) subjected to a combined steady and oscillatory shear stress.

(i). $\delta = 2.885$.

(ii). $\epsilon = 2.0$

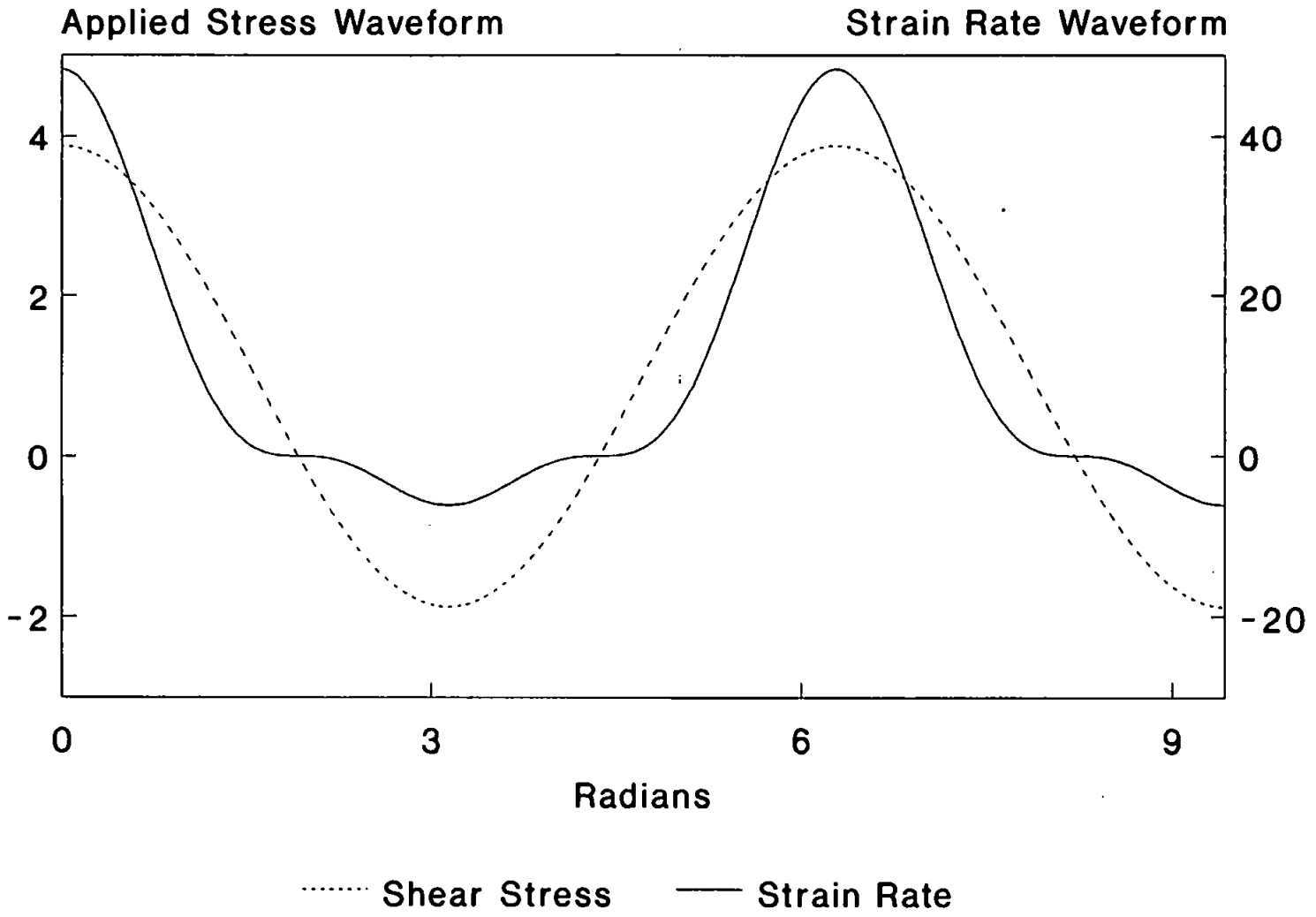
Applied Stress Waveform
Strain Rate Waveform
4
2
0
-2
40
20
0
-20
0
3
6
9
Radians
Shear Stress
Strain Rate

FIGURE (6.1)

Fluid inertia effects on the parallel plate geometry.

This figure shows a plot of the complex fluid inertia parameter $(\alpha h)^2$.

(i). X-axis; $Re(\alpha h)^2$, $Re(\alpha_0 h)^2$, $Re(\alpha_1 h)^2$, $Re(\alpha_2 h)^2$.

(ii). Y-axis; $Im(\alpha h)^2$, $Im(\alpha_0 h)^2$, $Im(\alpha_1 h)^2$, $Im(\alpha_2 h)^2$.

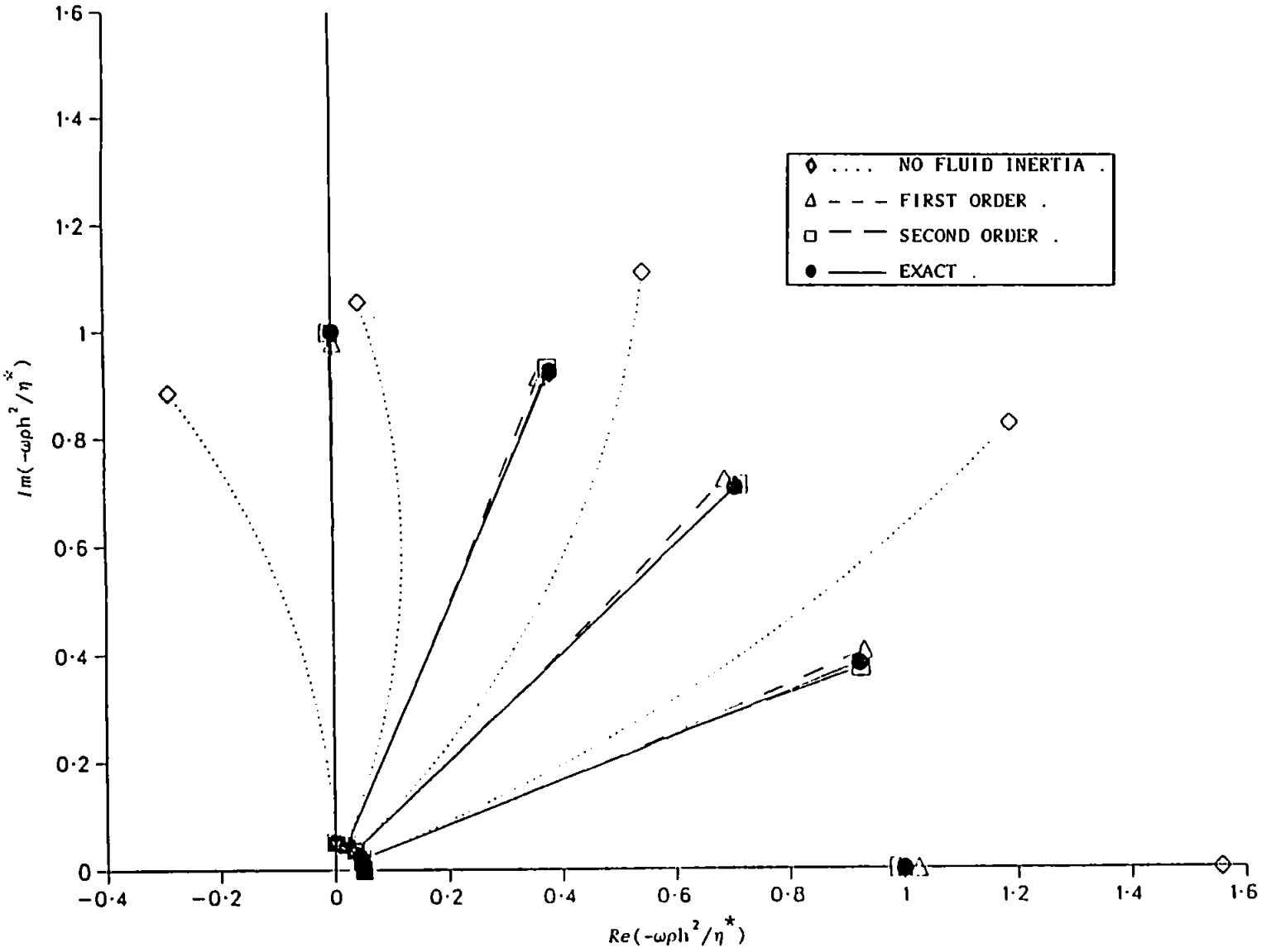
NO FLUID INERTIA .
FIRST ORDER .
SECOND ORDER .
EXACT .
1·6
1·4
1·2
1
0·8
0·6
0·4
0·2
0
−0·4
−0·2
0·2
0·4
0·6
0·8
1·2
1·4
1·6
$Im(-\omega\rho h^2/\eta^*)$
$Re(-\omega\rho h^2/\eta^*)$

FIGURE (6.2)

Fluid inertia effects on the parallel plate geometry.

This figure shows a plot of the complex fluid inertia parameter $(\alpha h)^2$.

(i). X-axis; $Re(\alpha h)^2$, $Re(\alpha_1 h)^2$, $Re(\alpha_2 h)^2$.

(ii). Y-axis; $Im(\alpha h)^2$, $Im(\alpha_1 h)^2$, $Im(\alpha_2 h)^2$.

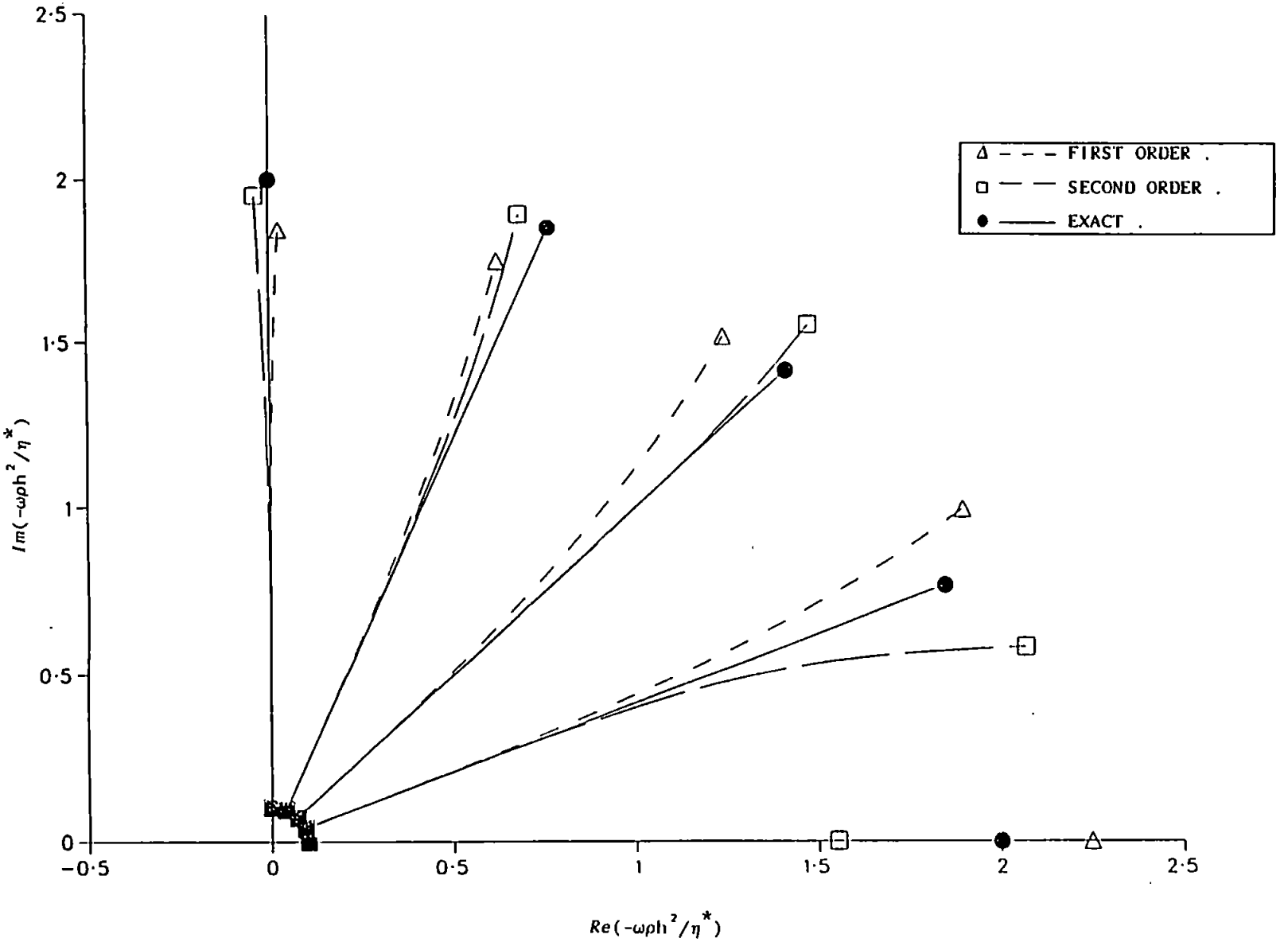
2·5
2
1·5
1
0·5
0
−0·5
0
0·5
1
1·5
2
2·5
Im(−ωρh²/η*)
Re(−ωρh²/η*)
FIRST ORDER .
SECOND ORDER .
EXACT .

FIGURE (6.3-5)

Fluid inertia effects on the parallel plate geometry.

These figures show the effect of fluid inertia on the complex fluid inertia parameter $(\alpha h)^2$.

(i). X-axis; $Re(\alpha h)^2$, $Re(\alpha_0 h)^2$.

(ii). Y-axis; $Im(\alpha h)^2$, $Im(\alpha_0 h)^2$.

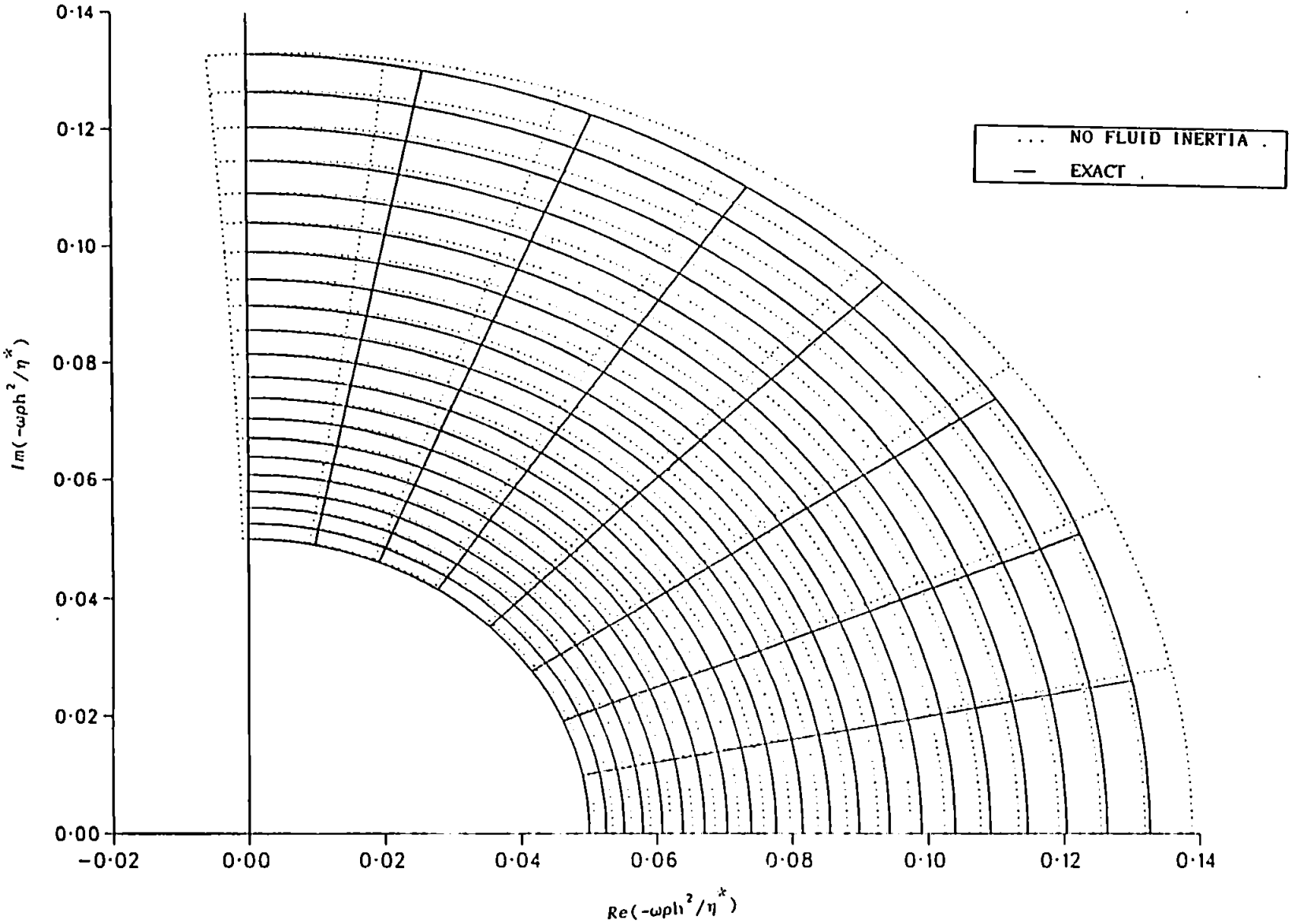
0·14
0·12
0·10
0·08
0·06
0·04
0·02
0·00
−0·02
0·00
0·02
0·04
0·06
0·08
0·10
0·12
0·14
Im(−ωρh²/η*)
Re(−ωρh²/η*)
NO FLUID INERTIA
EXACT

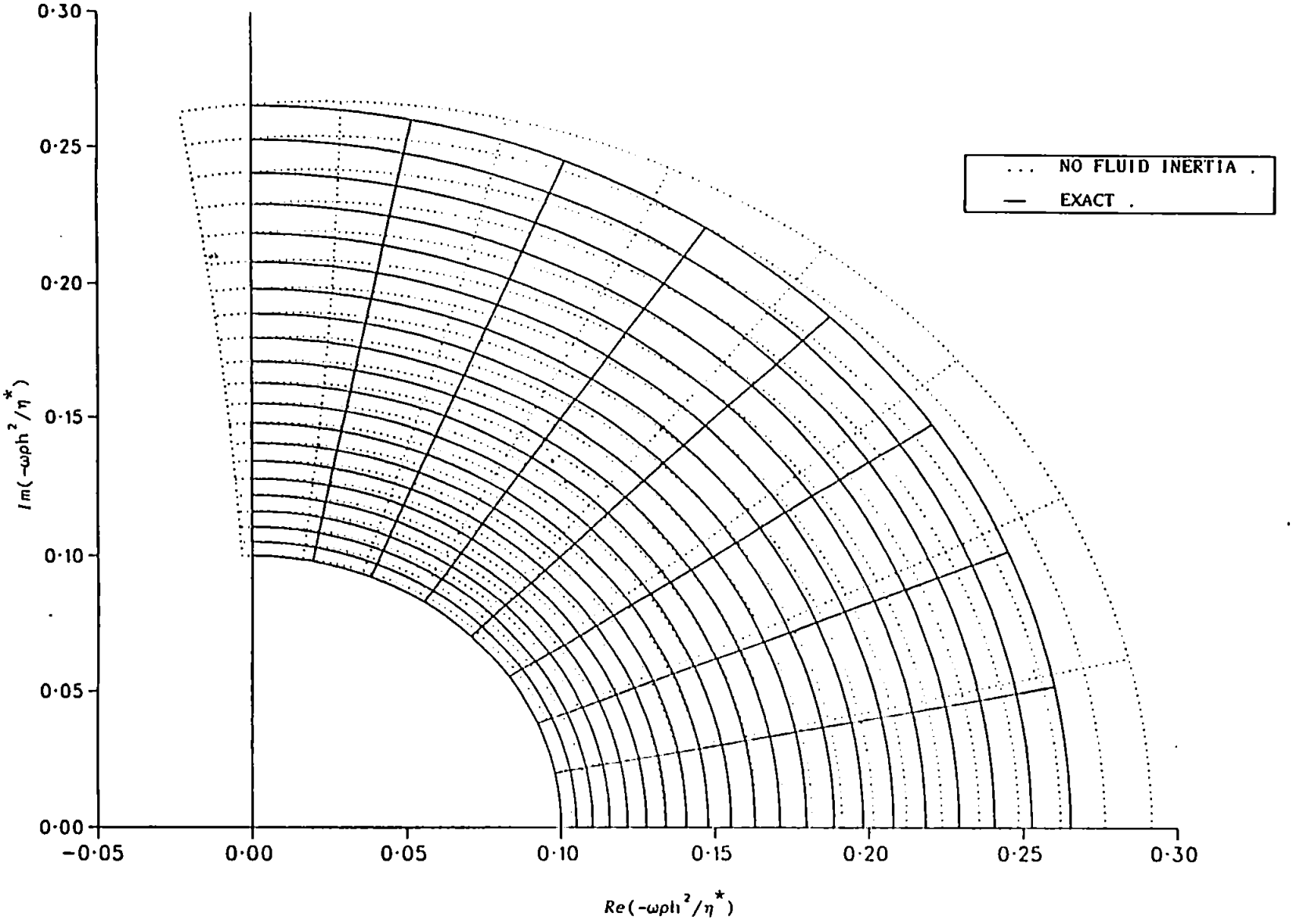
0·30
0·25
0·20
0·15
0·10
0·05
0·00
−0·05
0·00
0·05
0·10
0·15
0·20
0·25
0·30
Im(−ωρh²/η*)
Re(−ωρh²/η*)
... NO FLUID INERTIA .
— EXACT .

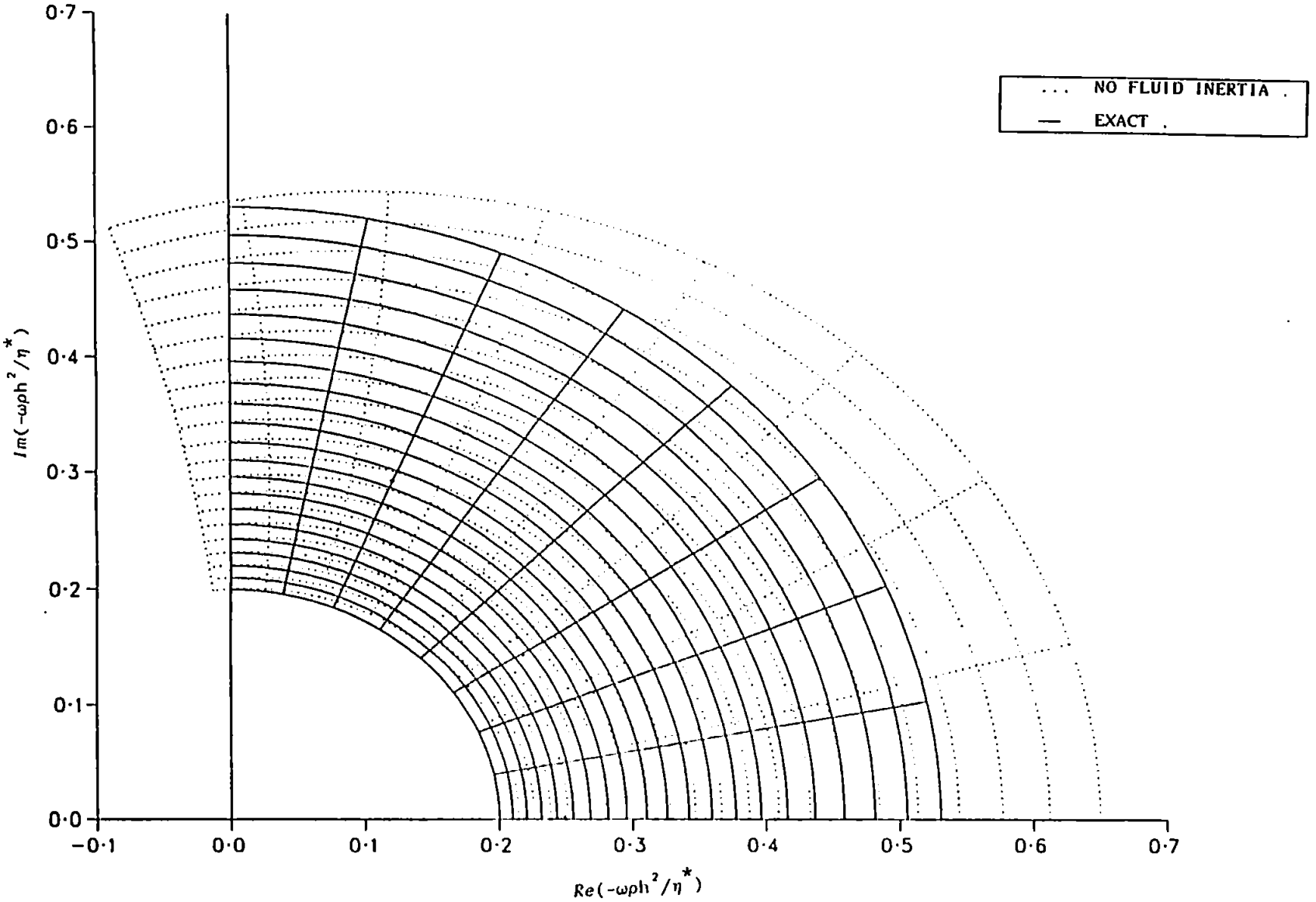
NO FLUID INERTIA
EXACT
0·7
0·6
0·5
0·4
0·3
0·2
0·1
0·0
−0·1
0·0
0·1
0·2
0·3
0·4
0·5
0·6
0·7
Im(−ωρh²/η*)
Re(−ωρh²/η*)

FIGURES (6.6-8)

Fluid inertia effects on the parallel plate geometry.

These figures compare the first order fluid inertia parameter $(\alpha_1 h)^2$ with $(\alpha h)^2$.

(i). X-axis; $Re(\alpha h)^2$, $Re(\alpha_1 h)^2$.

(ii). Y-axis; $Im(\alpha h)^2$, $Im(\alpha_1 h)^2$.

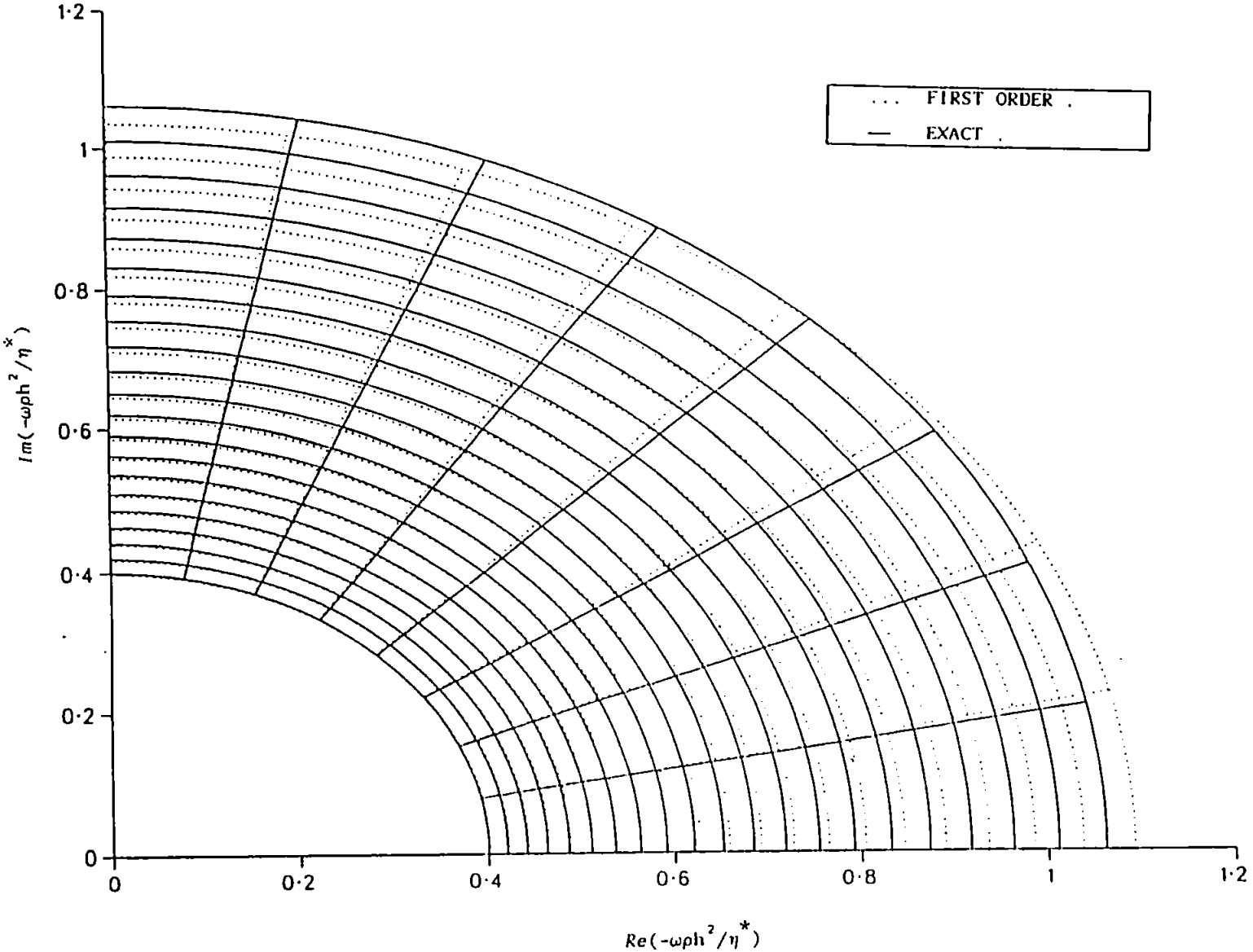
FIRST ORDER
EXACT
1·2
1
0·8
0·6
0·4
0·2
0
0·2
0·4
0·6
0·8
1
1·2
$Im(-\omega\rho h^2/\eta^*)$
$Re(-\omega\rho h^2/\eta^*)$

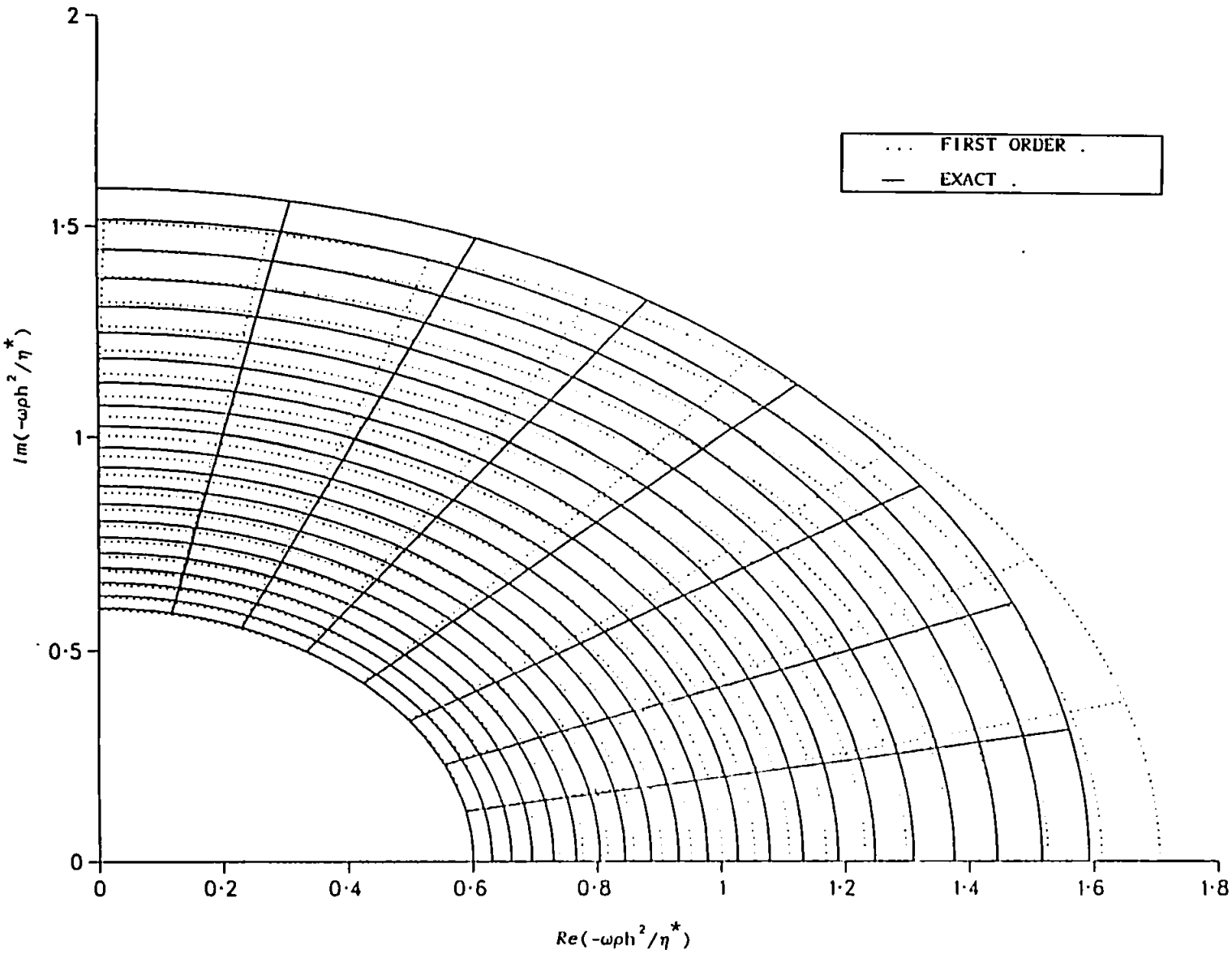
FIRST ORDER
EXACT
2
1·5
1
0·5
0
0
0·2
0·4
0·6
0·8
1
1·2
1·4
1·6
1·8
Im(-ωρh²/η*)
Re(-ωρh²/η*)

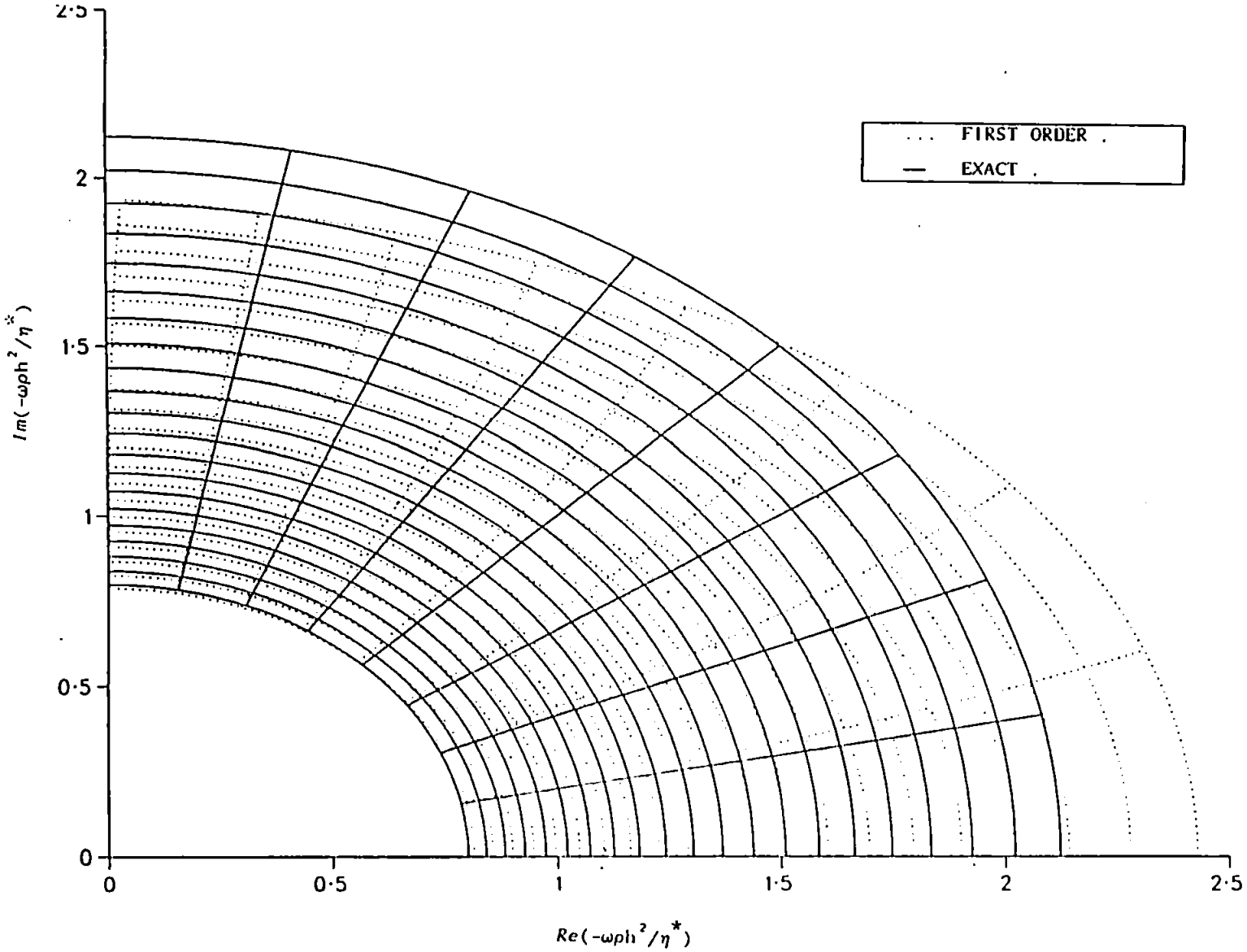
FIRST ORDER .
EXACT .
2·5
2
1·5
1
0·5
0
0
0·5
1
1·5
2
2·5
Im(-ωρh²/η*)
Re(-ωρh²/η*)

FIGURES (6.9-11)

Fluid inertia effects on the parallel plate geometry.

These figures compare the second order fluid inertia parameter $(\alpha_2 h)^2$ with $(\alpha h)^2$.

(i). X-axis; $Re(\alpha h)^2$, $Re(\alpha_2 h)^2$.

(ii). Y-axis; $Im(\alpha h)^2$, $Im(\alpha_2 h)^2$.

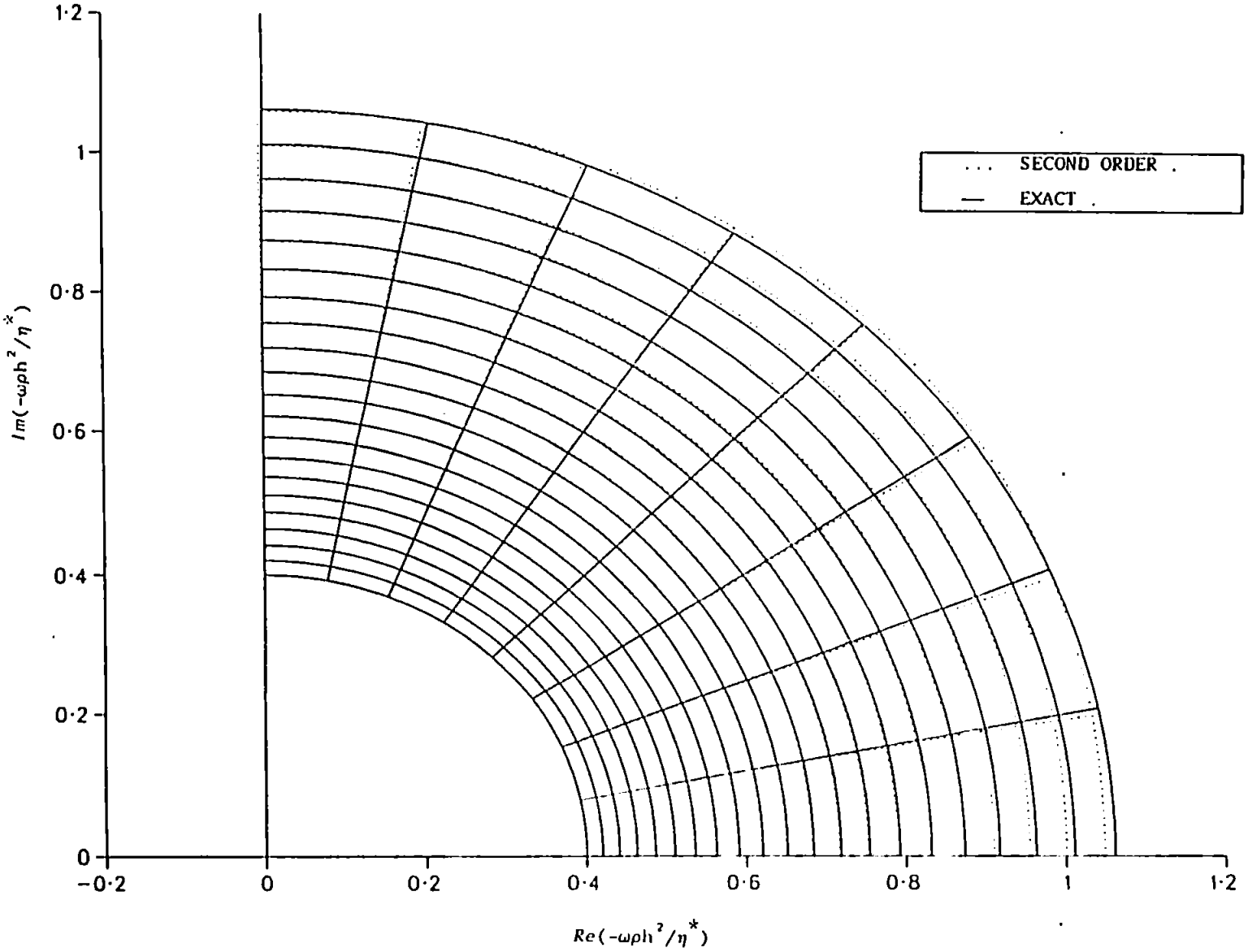
1·2
1
0·8
0·6
0·4
0·2
0
−0·2
0
0·2
0·4
0·6
0·8
1
1·2
Im(−ωρh²/η*)
Re(−ωρh²/η*)
... SECOND ORDER
— EXACT

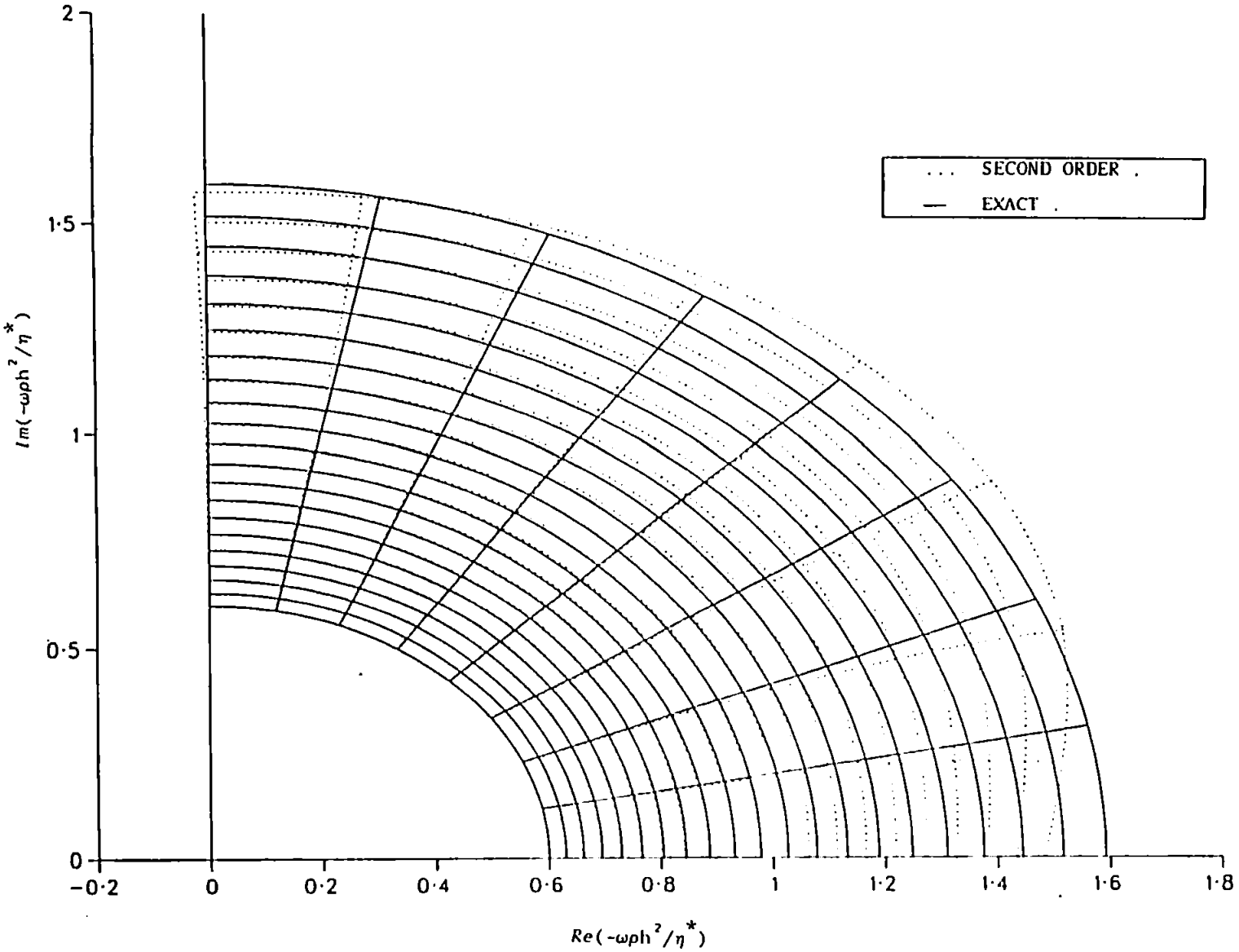
... SECOND ORDER .
— EXACT .
2
1·5
1
0·5
0
−0·2
0
0·2
0·4
0·6
0·8
1
1·2
1·4
1·6
1·8
Im(−ωρh²/η*)
Re(−ωρh²/η*)

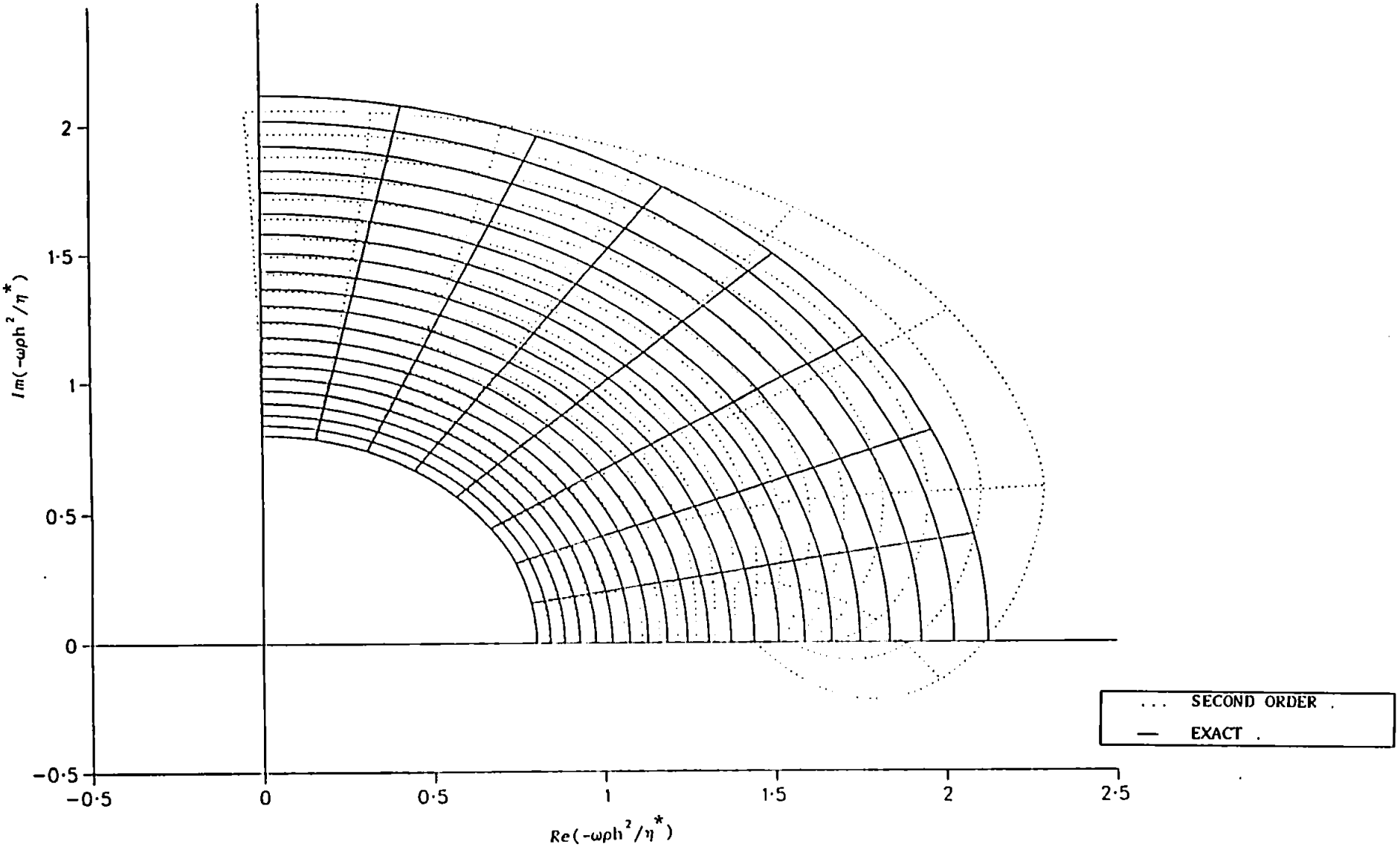
2
1·5
1
0·5
0
−0·5
−0·5
0
0·5
1
1·5
2
2·5
$Im(-\omega\rho h^2/\eta^*)$
$Re(-\omega\rho h^2/\eta^*)$
... SECOND ORDER
— EXACT

FIGURES (6.12-13)

Fluid inertia effects on the cone and plate geometry.

These figures show the effect of fluid inertia on the complex fluid inertia parameter $(\alpha\theta_0 a)^2$.

(i). X-axis; $Re(\alpha\theta_0 a)^2$, $Re(\alpha_0\theta_0 a)^2$.

(ii). Y-axis; $Im(\alpha\theta_0 a)^2$, $Im(\alpha_0\theta_0 a)^2$.

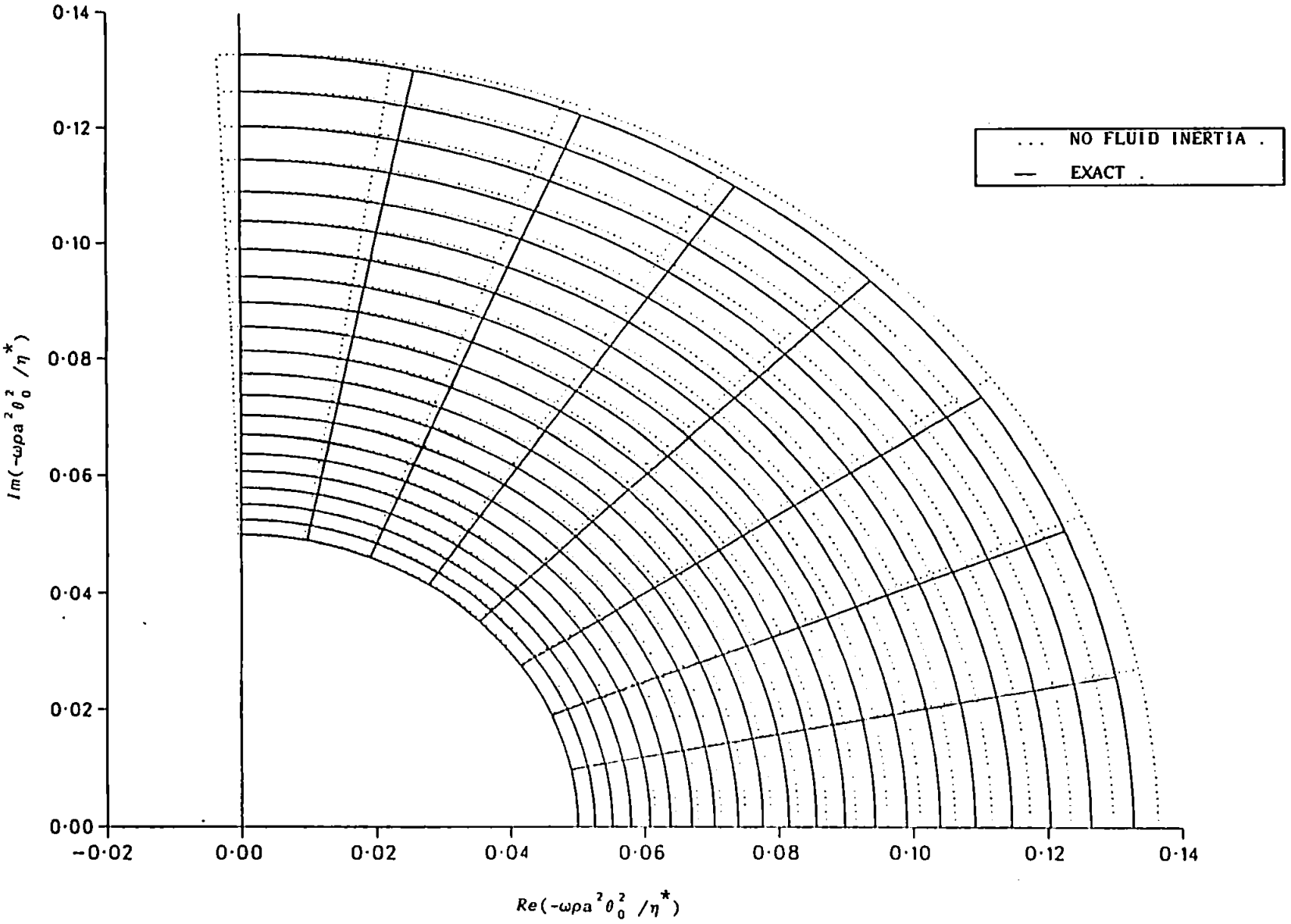
0·14
0·12
0·10
0·08
0·06
0·04
0·02
0·00
−0·02
0·00
0·02
0·04
0·06
0·08
0·10
0·12
0·14
Im(−ωρa²θ₀²/η*)
Re(−ωρa²θ₀²/η*)
... NO FLUID INERTIA .
— EXACT .

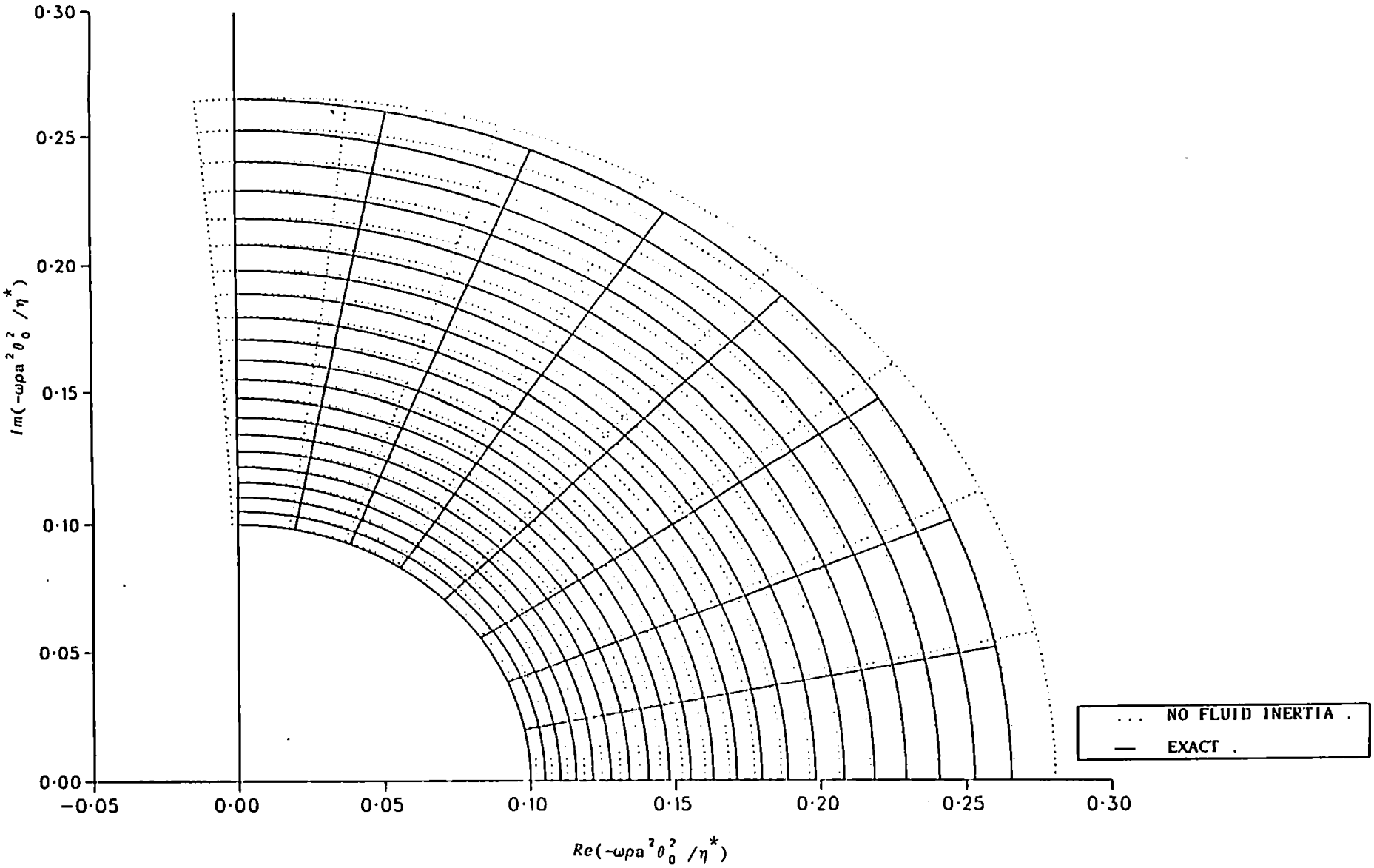
0·30
0·25
0·20
0·15
0·10
0·05
0·00
−0·05
0·00
0·05
0·10
0·15
0·20
0·25
0·30
Im(−ωρa²θ₀² /η*)
Re(−ωρa²θ₀² /η*)
... NO FLUID INERTIA .
— EXACT .

FIGURE (6.14)

Fluid inertia effects on the cone and plate geometry.

This figure compares the first order fluid inertia parameter $(\alpha_1 \theta_0 a)^2$ with $(\alpha \theta_0 a)^2$.

(i). X-axis; $Re(\alpha \theta_0 a)^2$, $Re(\alpha_1 \theta_0 a)^2$.

(ii). Y-axis; $Im(\alpha \theta_0 a)^2$, $Im(\alpha_1 \theta_0 a)^2$.

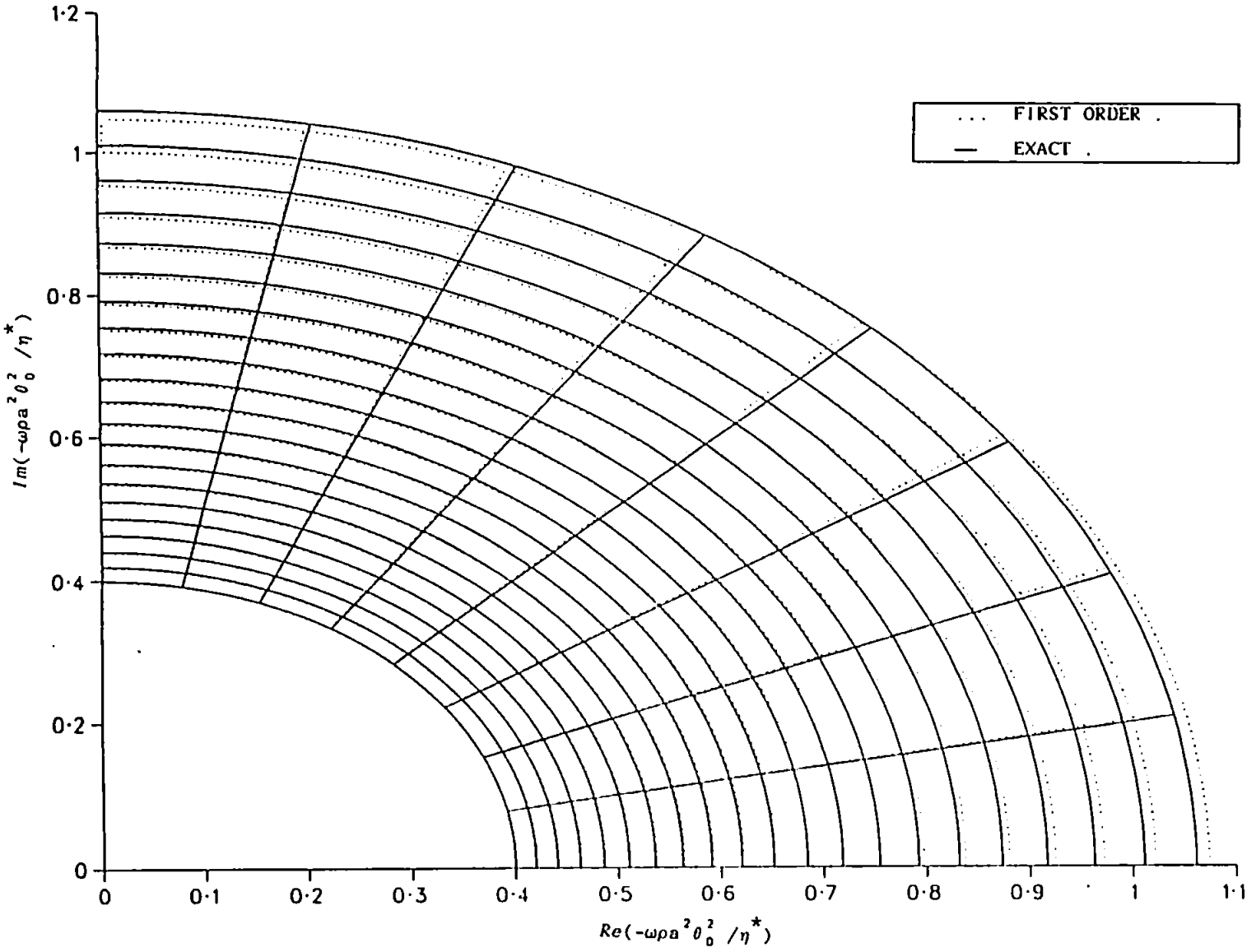
... FIRST ORDER .
— EXACT .
1·2
1
0·8
0·6
0·4
0·2
0
0
0·1
0·2
0·3
0·4
0·5
0·6
0·7
0·8
0·9
1
1·1
Im(-ωρa²θ₀²/η*)
Re(-ωρa²θ₀²/η*)

FIGURE (6.15)

Fluid inertia effects on the concentric cylinder geometry.

These figures show the effect of fluid inertia on the complex fluid inertia parameter $(\alpha(r_o - r_i))^2$.

(i). X-axis; $Re(\alpha h)^2$, $Re(\alpha_0(r_o - r_i))^2$.

(ii). Y-axis; $Im(\alpha h)^2$, $Im(\alpha_0(r_o - r_i))^2$.

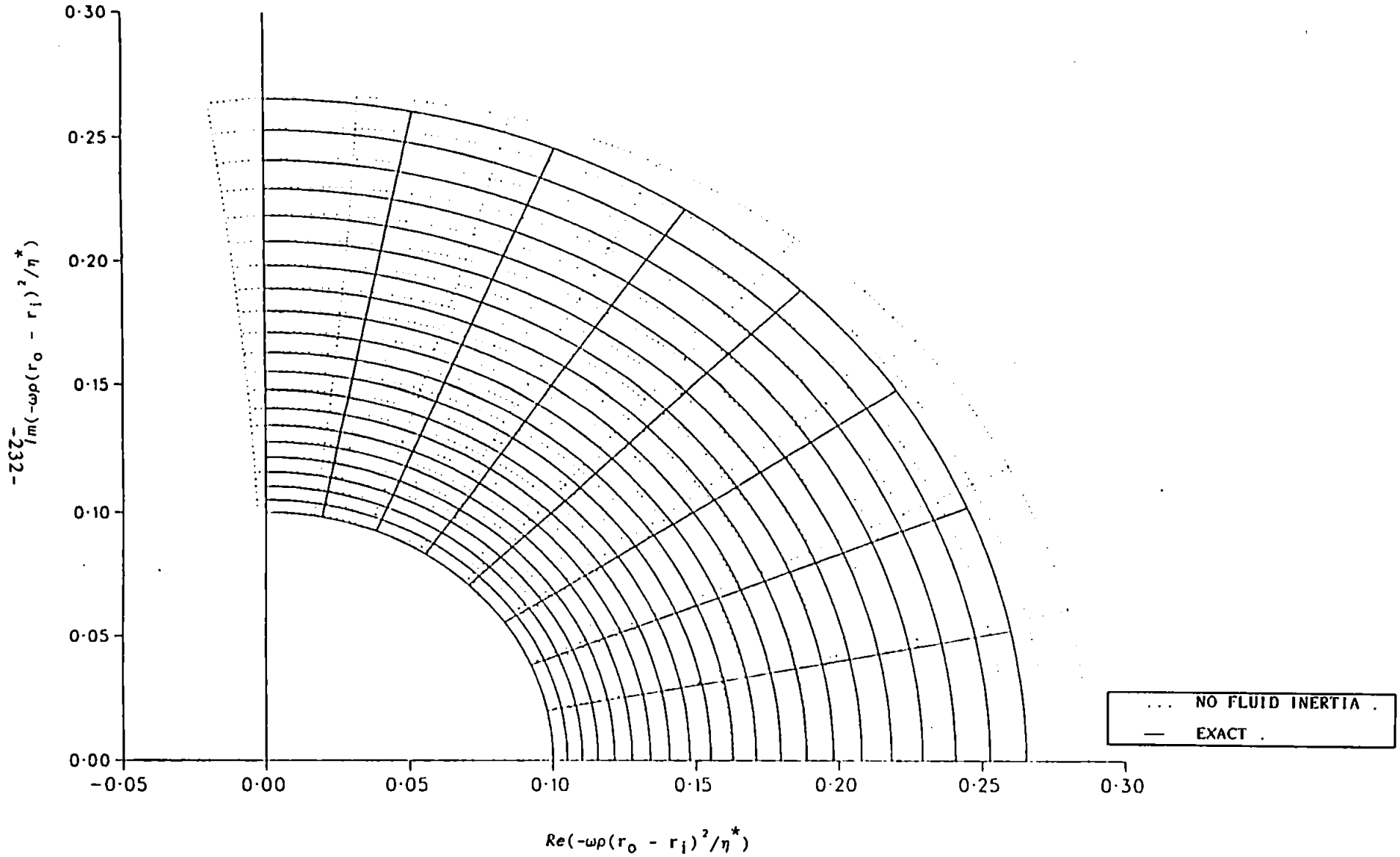
0·30
0·25
0·20
0·15
0·10
0·05
0·00
−0·05
0·00
0·05
0·10
0·15
0·20
0·25
0·30
$Im(-\omega\rho(r_o - r_i)^2/\eta^*)$
$Re(-\omega\rho(r_o - r_i)^2/\eta^*)$
... NO FLUID INERTIA .
— EXACT .

FIGURE (7.1)

Oscillatory Shear Experiments.

Dynamic data for a 2% solution of polyisobutylene in dekalin.
Experimental conditions (Temp = 20 °C; ρ = 0.88 gm/cm^3).

Measurement system;

(i). Cone and plate (gap angle=2°; cone radius=2 cm)

(ii). Parallel plate (gap=0.25 mm; radius=2 cm)

(iii). Concentric cylinder (r_i=18.5 mm, r_o=20.75 mm, cylinder height=50 mm).

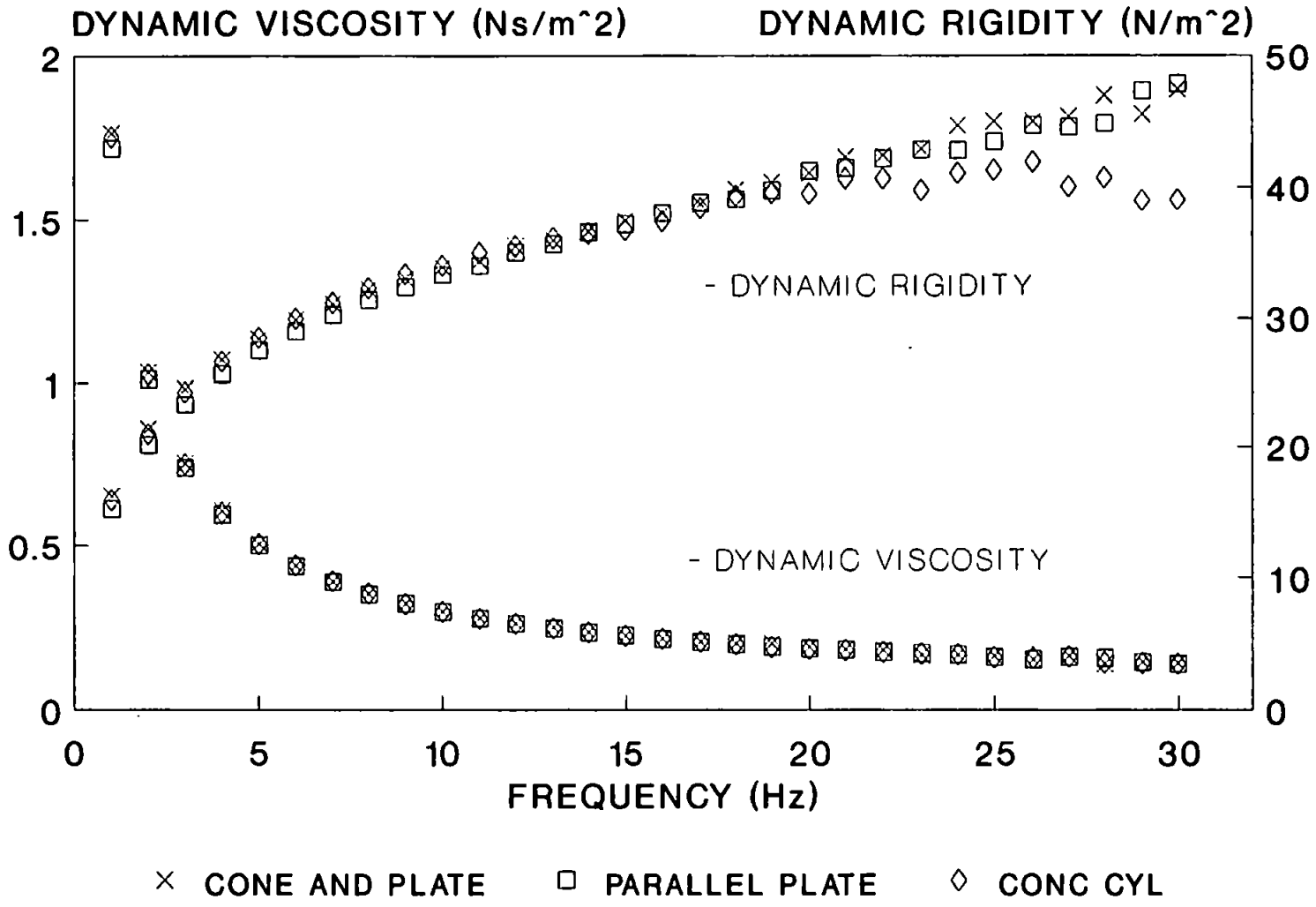
DYNAMIC VISCOSITY (Ns/m^2)
DYNAMIC RIGIDITY (N/m^2)
2
1.5
1
0.5
0
50
40
30
20
10
0
- DYNAMIC RIGIDITY
- DYNAMIC VISCOSITY
0
5
10
15
20
25
30
FREQUENCY (Hz)
× CONE AND PLATE
□ PARALLEL PLATE
◇ CONC CYL

FIGURE (7.2)

Oscillatory Shear Experiments.

Dynamic data for a 2% solution of polyisobutylene in dekalin.
Experimental conditions (Temp = 20 C; ρ = 0.88 gm/cm^3),

Measurement system; concentric cylinder geometry (r_o=20.75 mm, cylinder height = 50mm).

(i). r_i=18.5 mm.
(ii). r_i=15.0 mm.
(iii). r_i=12.5 mm.

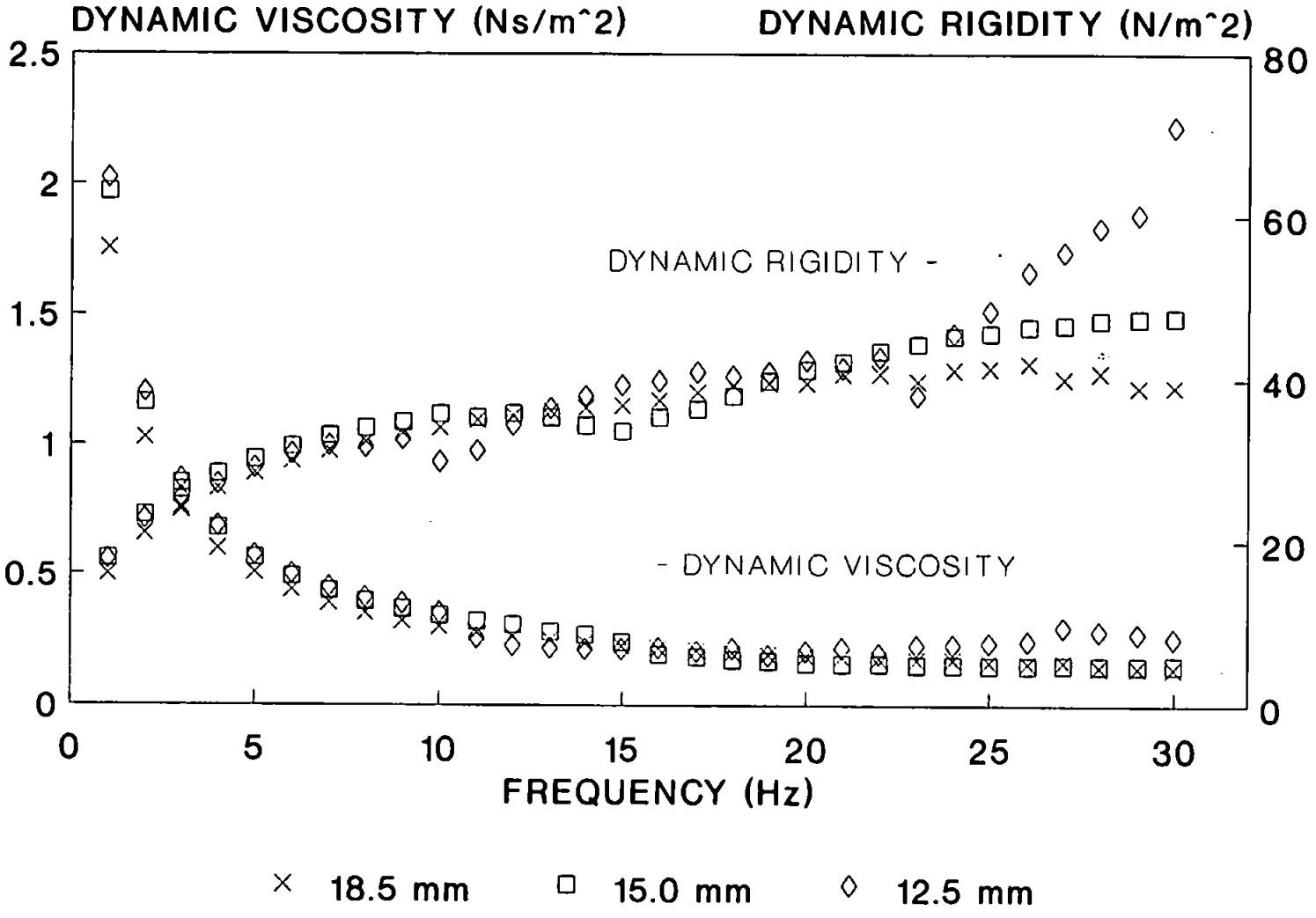
DYNAMIC VISCOSITY (Ns/m^2)
DYNAMIC RIGIDITY (N/m^2)
2.5
2
1.5
1
0.5
0
80
60
40
20
0
DYNAMIC RIGIDITY -
- DYNAMIC VISCOSITY
0
5
10
15
20
25
30
FREQUENCY (Hz)
× 18.5 mm
□ 15.0 mm
◇ 12.5 mm

FIGURE (7.3)

Oscillatory Shear Experiments.

Effect of fluid inertia on dynamic viscosity of a 2% solution of polyisobutylene in dekalin.

Experimental conditions (Temp = 20° C; ρ = 0.88 gm/cm^3).

Measurement system; concentric cylinder geometry (r_o=20.75 mm; r_i=12.5 mm; cylinder height=50 mm).

(i). Exact.

(ii). Fluid inertia ignored.

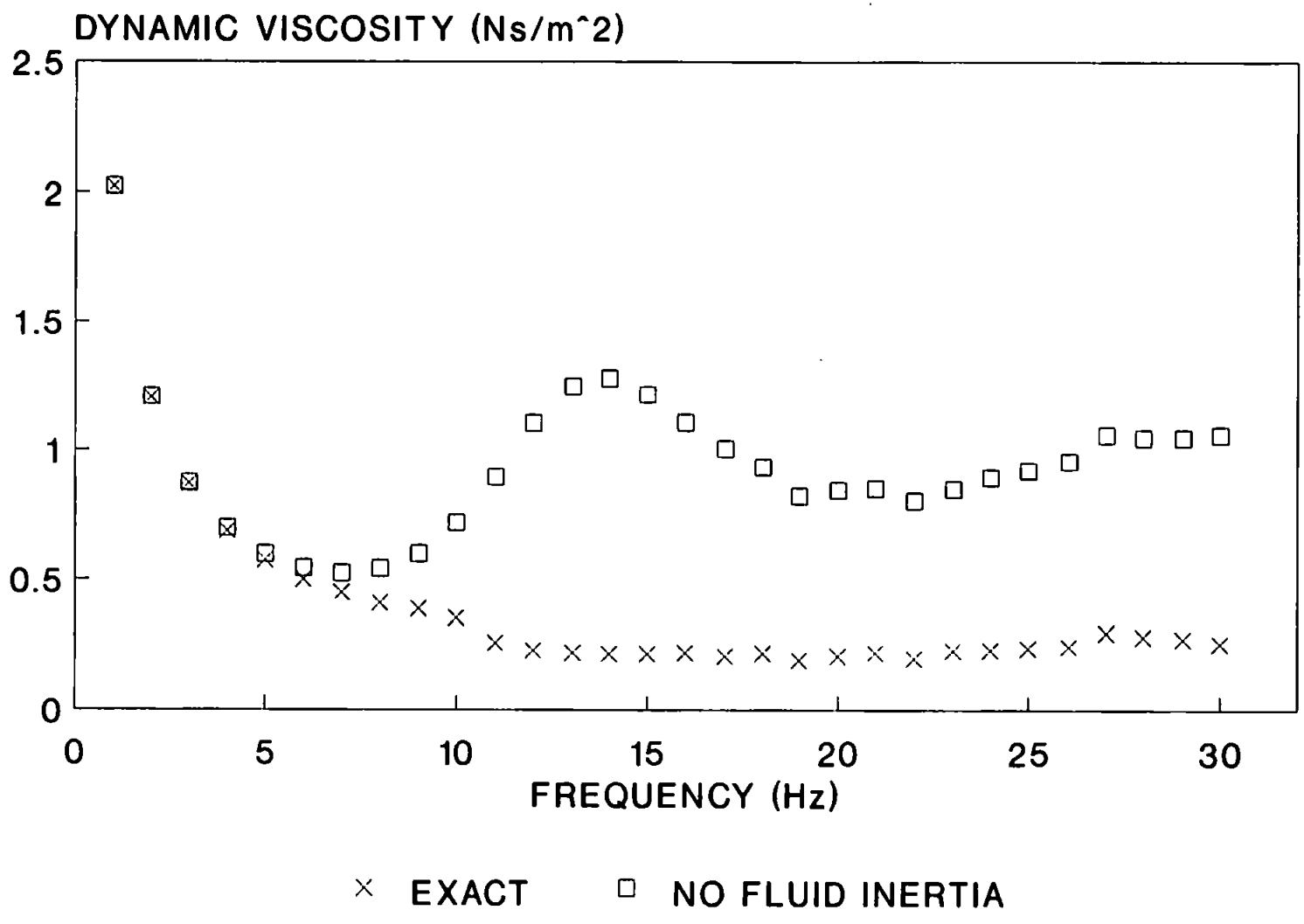
DYNAMIC VISCOSITY (Ns/m^2)
2.5
2
1.5
1
0.5
0
0
5
10
15
20
25
30
FREQUENCY (Hz)
EXACT
NO FLUID INERTIA

FIGURE (7.4)

Oscillatory Shear Experiments.

Effect of fluid inertia on dynamic rigidity of a 2% solution of polyisobutylene in dekalin.

Experimental conditions (Temp = 20° C; ρ = 0.88 gm/cm^3).

Measurement system; concentric cylinder geometry (r_o=20.75 mm; r_i=12.5 mm; cylinder height=50 mm).

(i). Exact.

(ii). Fluid inertia ignored.

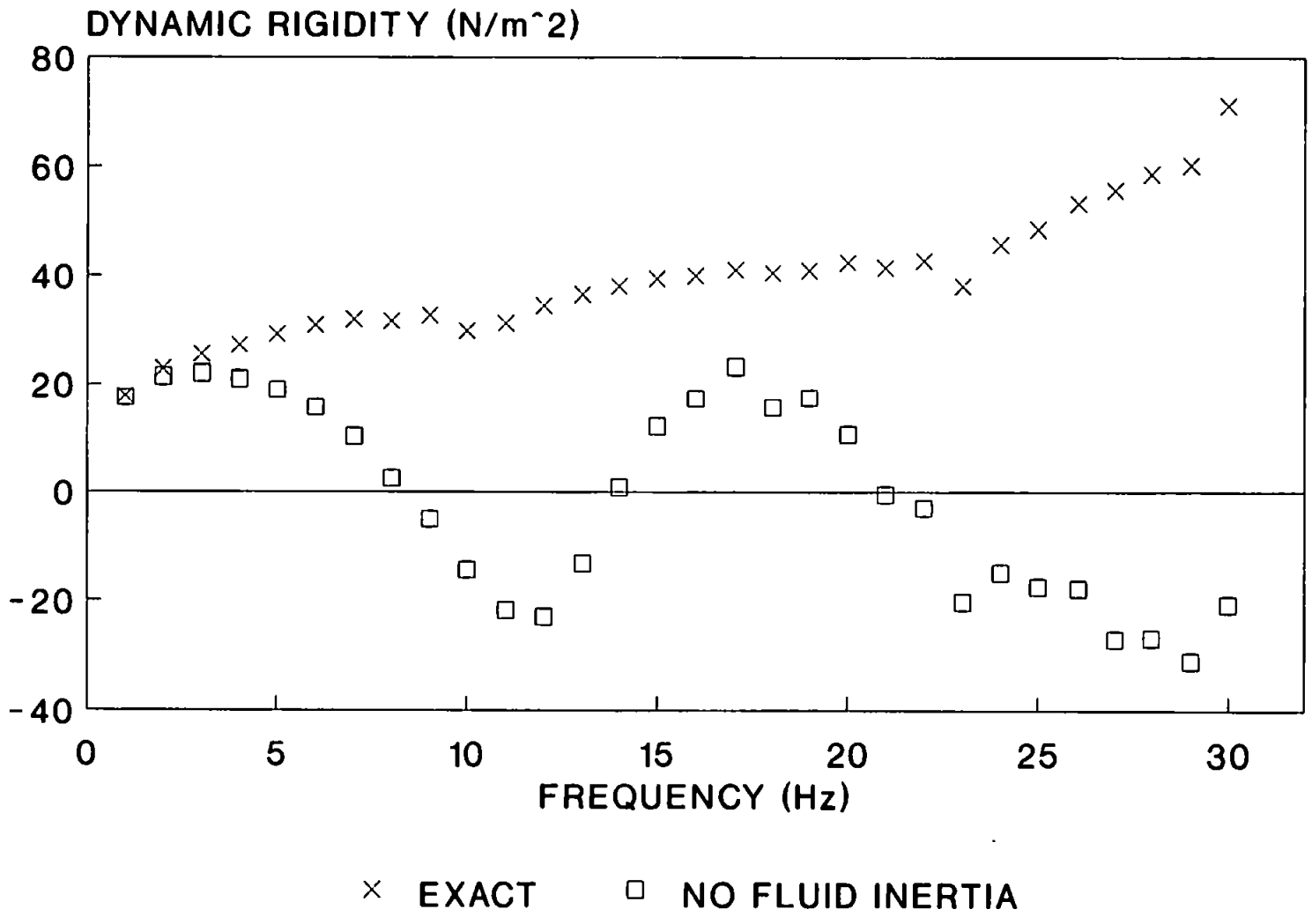
DYNAMIC RIGIDITY (N/m^2)
80
60
40
20
0
-20
-40
0
5
10
15
20
25
30
FREQUENCY (Hz)
EXACT
NO FLUID INERTIA

FIGURE (7.5)

Oscillatory Shear Experiments.

Effect of fluid inertia on dynamic viscosity of a 2% solution of polyisobutylene in dekalin.

Experimental conditions (Temp = 20° C; ρ = 0.88 gm/cm^3).

Measurement system; concentric cylinder geometry (r_o=20.75 mm; r_i=15.0 mm; cylinder height=50 mm).

(i). Exact.

(ii). Fluid inertia ignored.

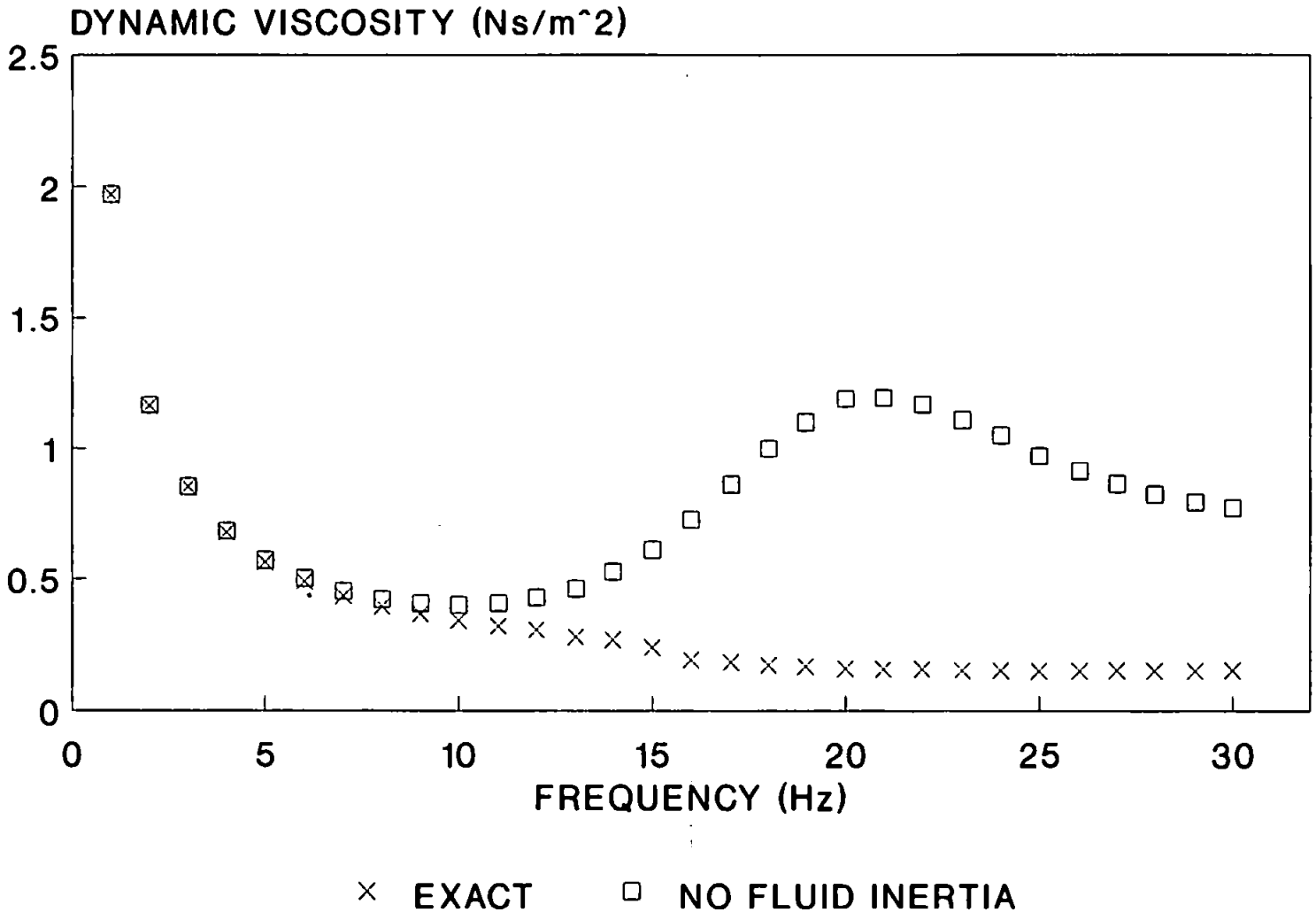
DYNAMIC VISCOSITY (Ns/m^2)
2.5
2
1.5
1
0.5
0
0
5
10
15
20
25
30
FREQUENCY (Hz)
EXACT
NO FLUID INERTIA

FIGURE (7.6)

Oscillatory Shear Experiments.

Effect of fluid inertia on dynamic rigidity of a 2% solution of polyisobutylene in dekalin.

Experimental conditions (Temp = 20° C; ρ = 0.88 gm/cm^3).

Measurement system; concentric cylinder geometry (r_o=20.75 mm; r_i=15.0 mm; cylinder height=50 mm).

(i). Exact.

(ii). Fluid inertia ignored.

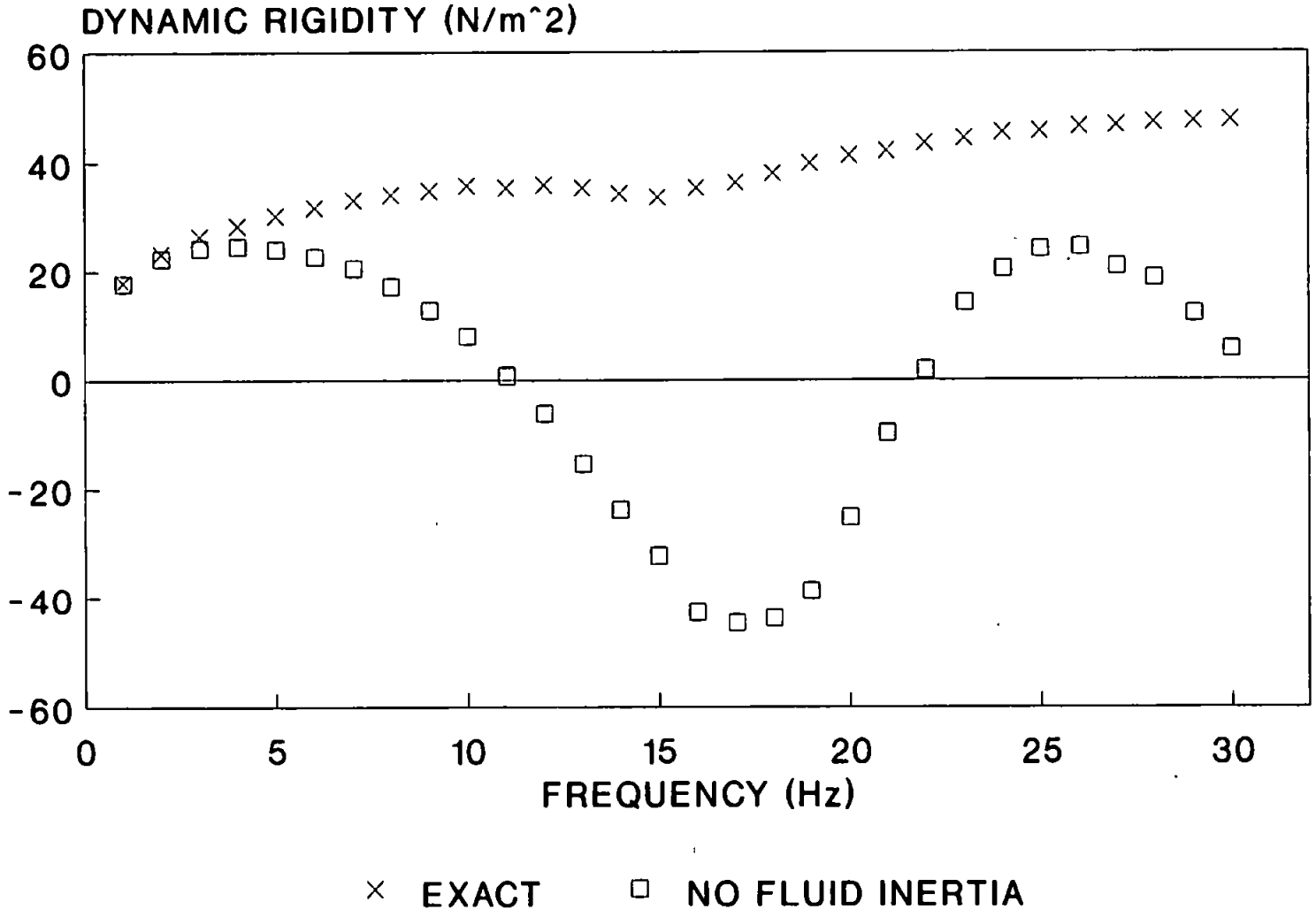
DYNAMIC RIGIDITY (N/m^2)
60
40
20
0
-20
-40
-60
0
5
10
15
20
25
30
FREQUENCY (Hz)
× EXACT
□ NO FLUID INERTIA

FIGURE (7.7)

Theoretical prediction of the effect of fluid inertia on the dynamic viscosity of a 2% solution of polyisobutylene in dekalin, (ρ=0.88 gm/cm^3).

Measurement system; concentric cylinder (r_o=20.75 mm, cylinder height = 50mm).

(i). r_i=18.5 mm.

(ii). r_i=15.0 mm.

(iii). r_i=12.5 mm.

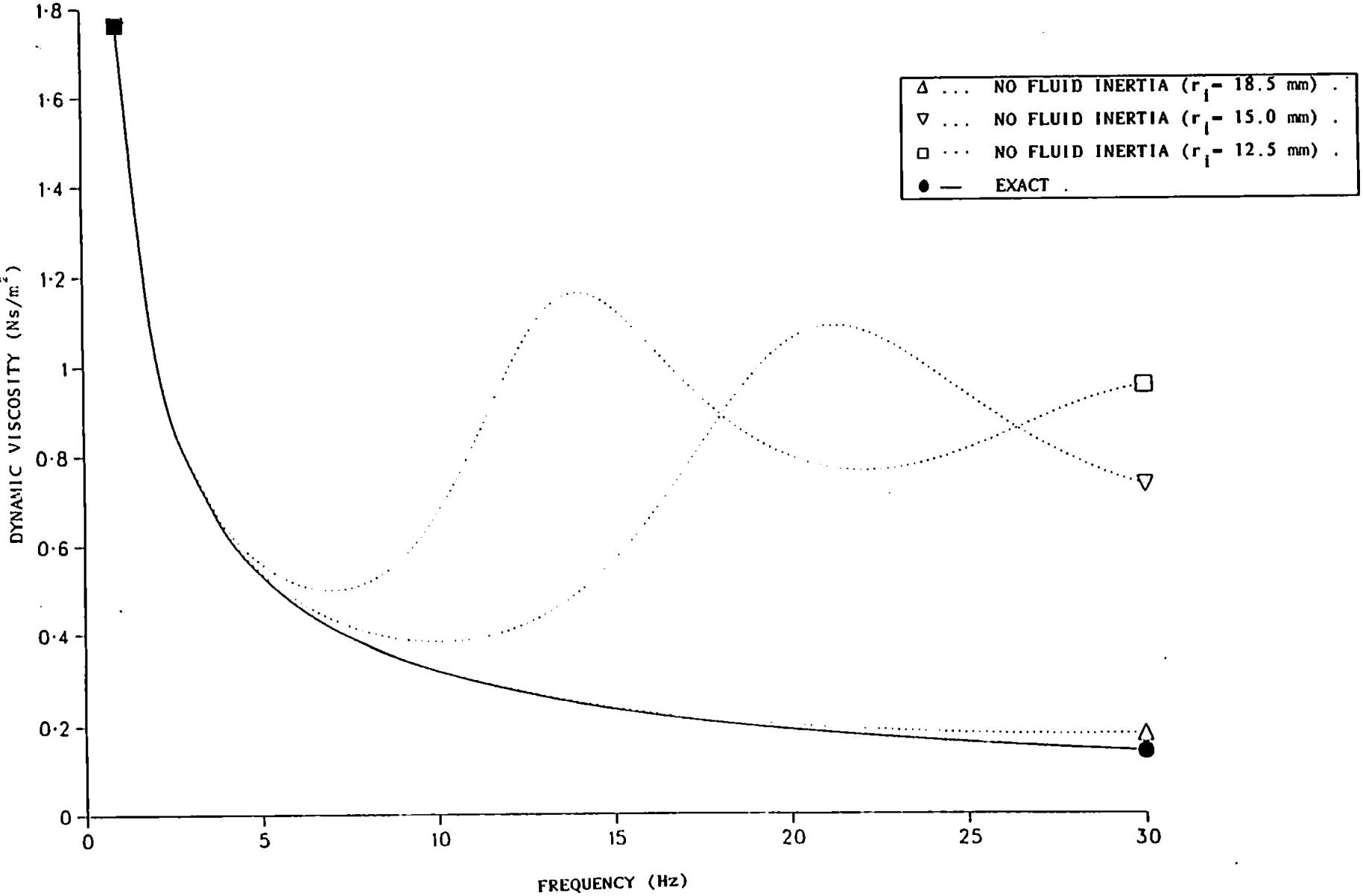
Δ ... NO FLUID INERTIA (r_i = 18.5 mm) .
▽ ... NO FLUID INERTIA (r_i = 15.0 mm) .
□ ··· NO FLUID INERTIA (r_i = 12.5 mm) .
● — EXACT .
DYNAMIC VISCOSITY (Ns/m²)
1·8
1·6
1·4
1·2
1
0·8
0·6
0·4
0·2
0
0
5
10
15
20
25
30
FREQUENCY (Hz)

FIGURE (7.8)

Theoretical prediction of the effect of fluid inertia on the dynamic rigidity of a 2% solution of polyisobutylene in dekalin, (ρ=0.88 gm/cm^3).

Measurement system; concentric cylinder (r_o=20.75 mm, cylinder height = 50mm).

(i). r_i=18.5 mm.

(ii). r_i=15.0 mm.

(iii). r_i=12.5 mm.

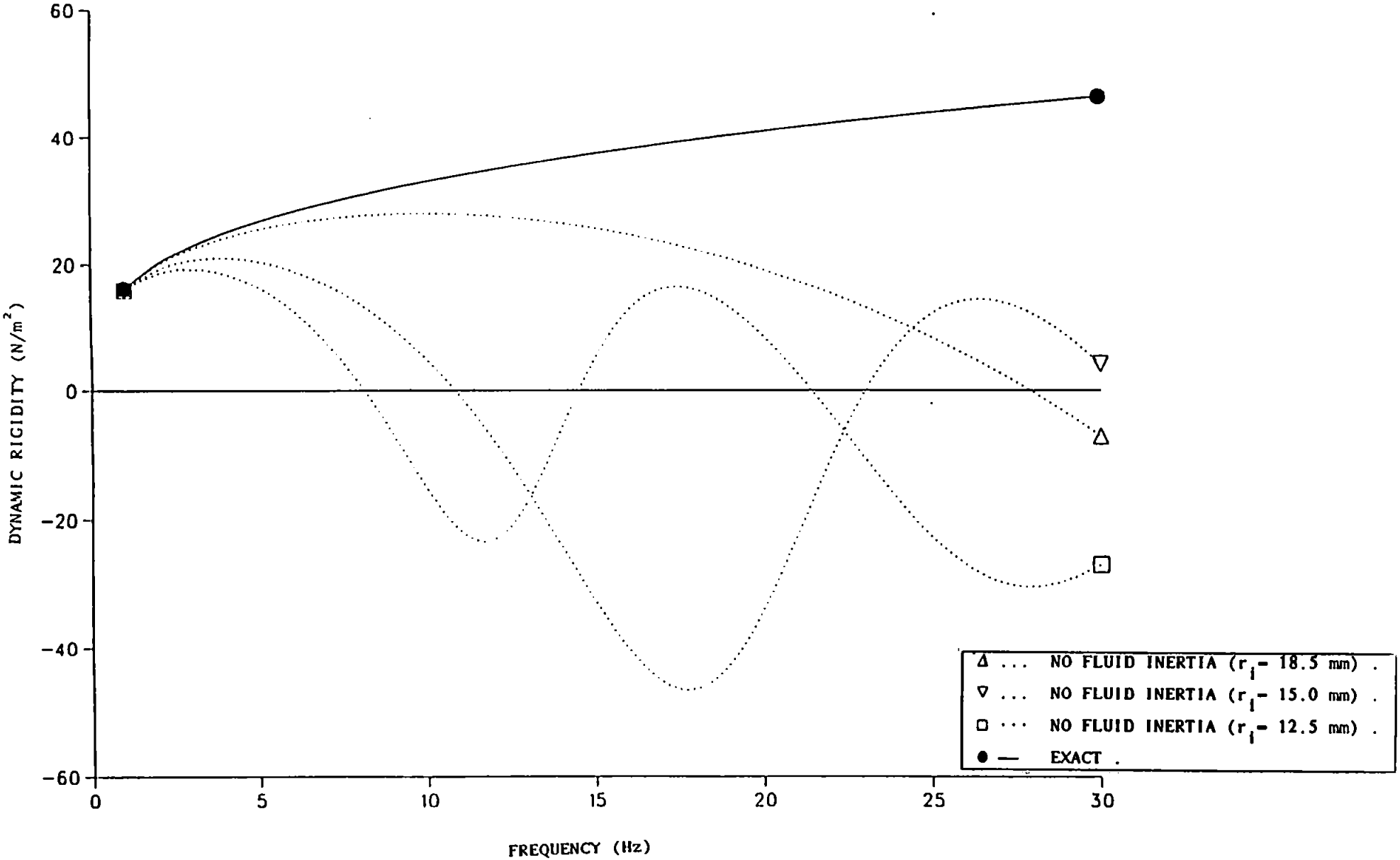
60
40
20
0
-20
-40
-60
0
5
10
15
20
25
30
DYNAMIC RIGIDITY (N/m²)
FREQUENCY (Hz)
Δ ... NO FLUID INERTIA (r_i = 18.5 mm) .
▽ ... NO FLUID INERTIA (r_i = 15.0 mm) .
□ ··· NO FLUID INERTIA (r_i = 12.5 mm) .
● — EXACT .

FIGURE (7.9)

Power law fit to dynamic data for a 2% solution of polyisobutylene in dekalin. Model constants,

(i). Dynamic viscosity (n=0.269; m=6.355).

(ii). Dynamic rigidity (n=1.292; m=10.076).

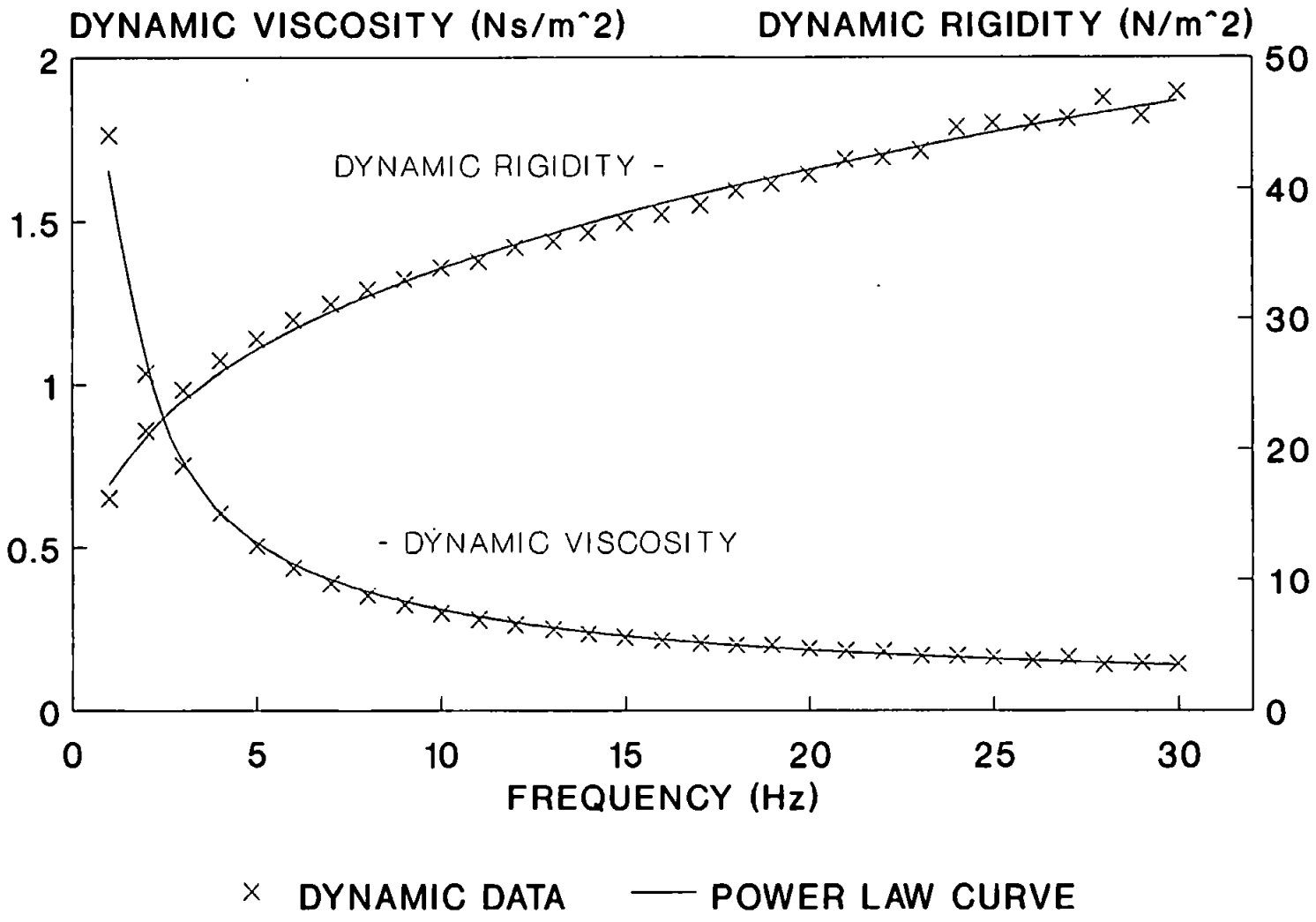
DYNAMIC VISCOSITY (Ns/m^2)
DYNAMIC RIGIDITY (N/m^2)
2
1.5
1
0.5
0
50
40
30
20
10
0
DYNAMIC RIGIDITY -
- DYNAMIC VISCOSITY
0
5
10
15
20
25
30
FREQUENCY (Hz)
× DYNAMIC DATA
POWER LAW CURVE

FIGURE (7.10)

Oscillatory Shear Experiments.

Effect of fluid inertia on dynamic viscosity of a 2% solution of polyisobutylene in dekalin.

Experimental conditions (Temp = 20° C; ρ = 0.88 gm/cm^3).

Measurement system; concentric cylinder geometry (r_o=20.75 mm; r_i=18.5 mm; cylinder height=50 mm).

(i). Exact.
(ii). Fluid inertia ignored.
(iii). First order fluid inertia correction.
(iv). Second order second fluid correction.

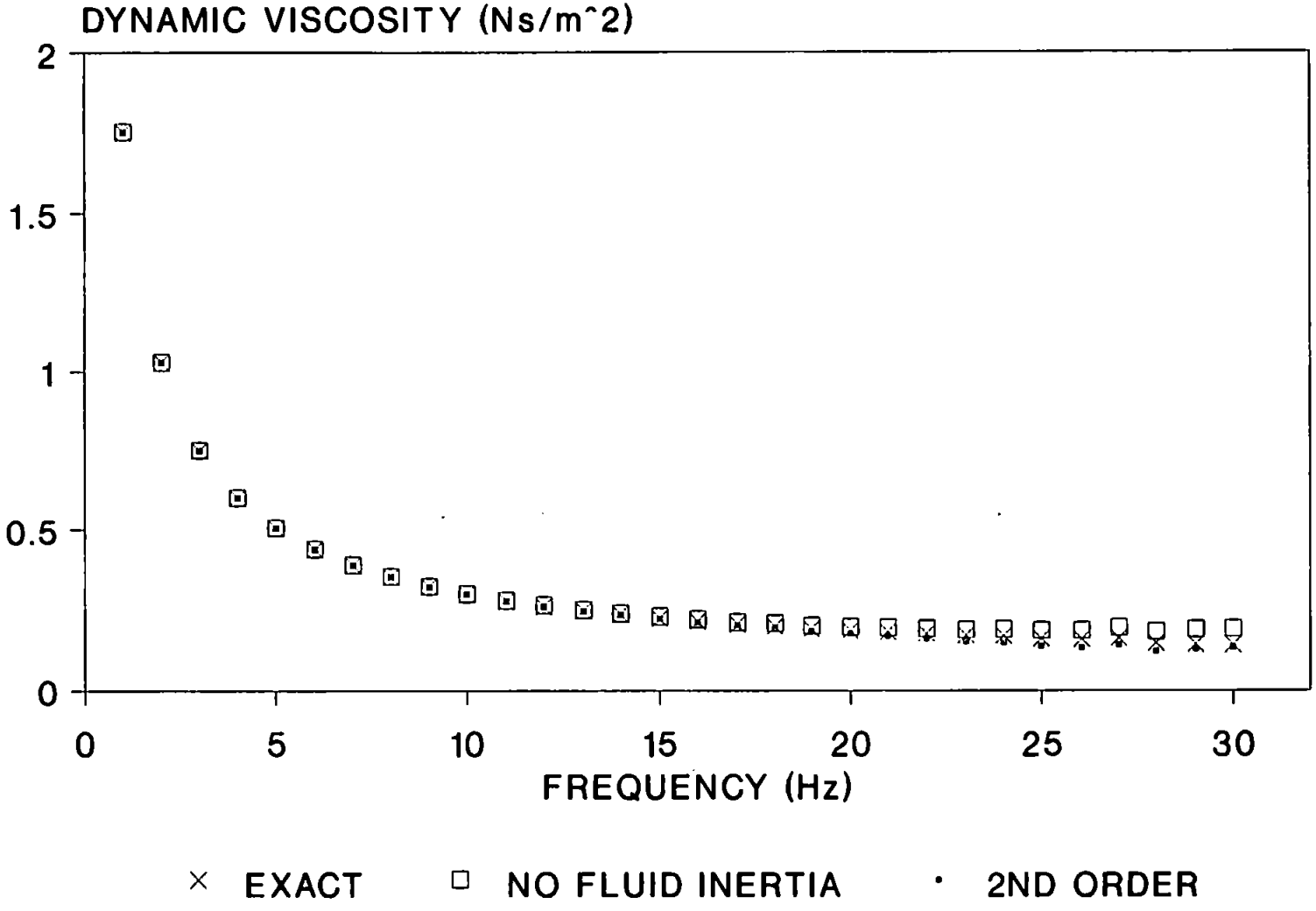
DYNAMIC VISCOSITY (Ns/m^2)
2
1.5
1
0.5
0
0
5
10
15
20
25
30
FREQUENCY (Hz)
× EXACT
□ NO FLUID INERTIA
· 2ND ORDER

FIGURE (7.11)

Oscillatory Shear Experiments.

Effect of fluid inertia on dynamic rigidity of a 2% solution of polyisobutylene in dekalin.

Experimental conditions (Temp = 20° C; ρ = 0.88 gm/cm^3).

Measurement system; concentric cylinder geometry (r_o=20.75 mm; r_i=18.5 mm; cylinder height=50 mm).

(i). Exact.
(ii). Fluid inertia ignored.
(iii). First order fluid inertia correction.
(iv). Second order fluid inertia correction.

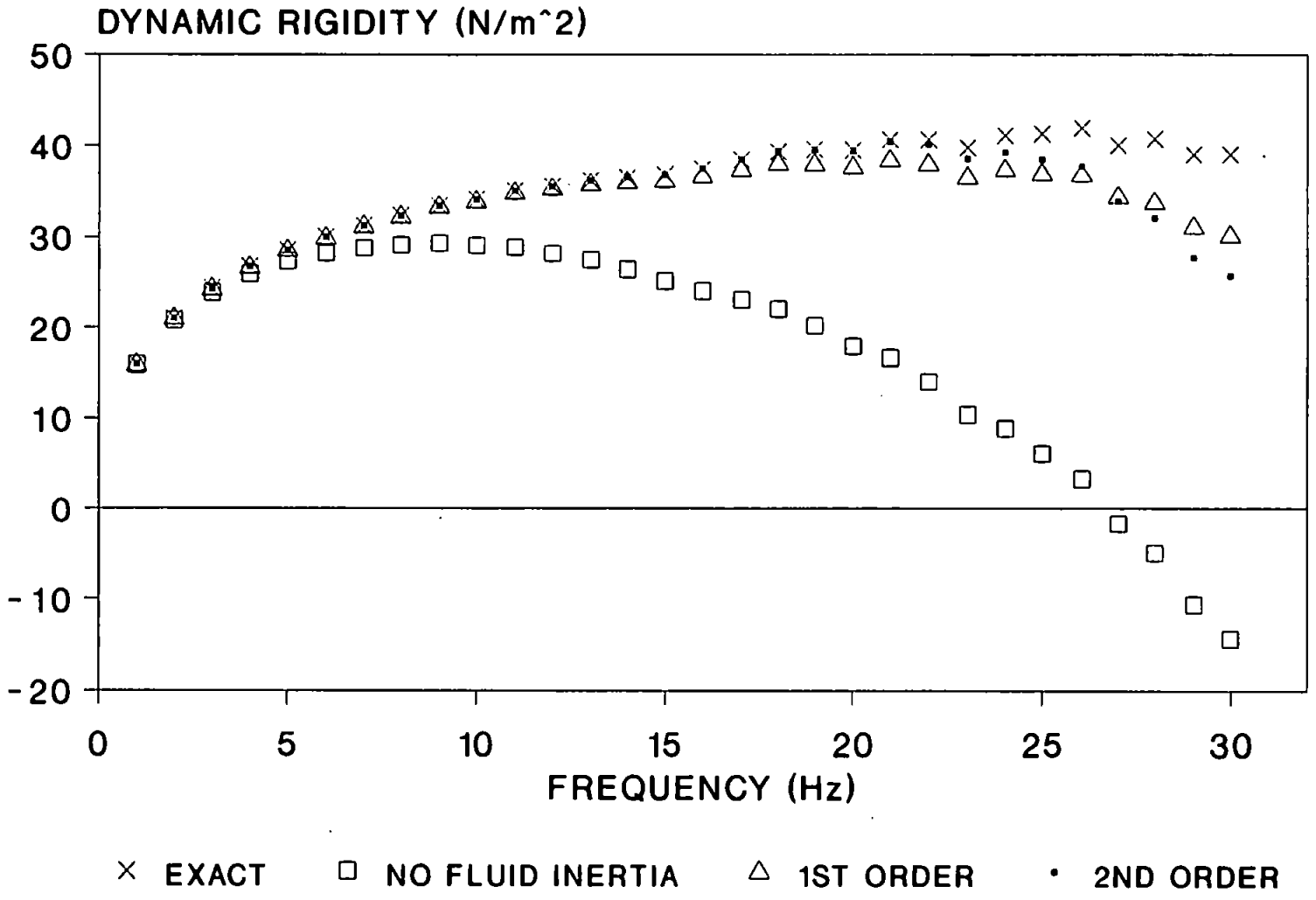
DYNAMIC RIGIDITY (N/m^2)
50
40
30
20
10
0
-10
-20
0
5
10
15
20
25
30
FREQUENCY (Hz)
EXACT
NO FLUID INERTIA
1ST ORDER
2ND ORDER

FIGURE (7.12)

Oscillatory Shear Experiments.

Dynamic data for a 2% solution of polyisobutylene in dekalin.
Experimental conditions (Temp = 20 C; ρ = 0.88 gm/cm^3),

Measurement system; parallel plate geometry (radius = 2 cm).

(i). gap = 0.25 mm.

(ii). gap = 0.5 mm.

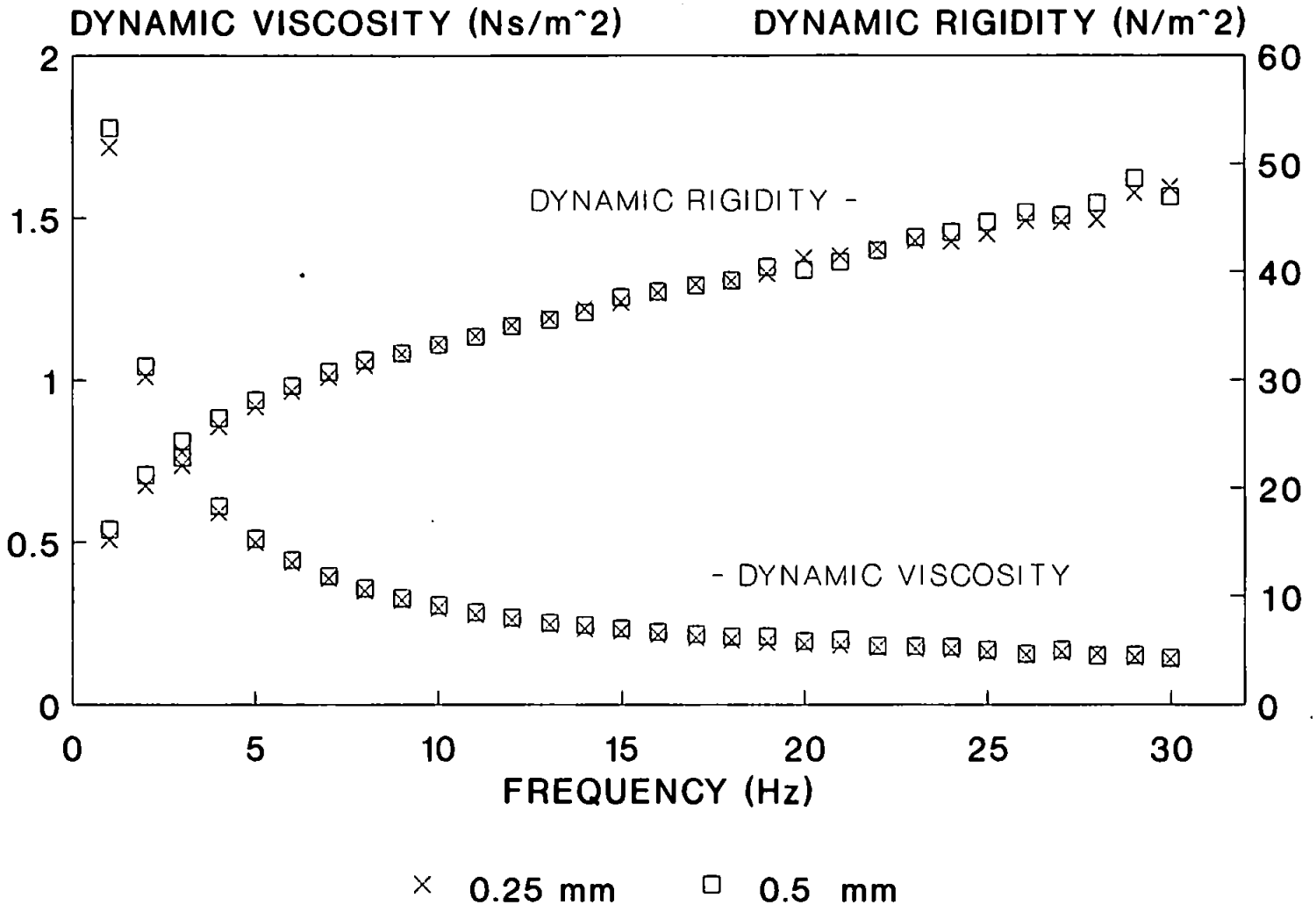
DYNAMIC VISCOSITY (Ns/m^2)
DYNAMIC RIGIDITY (N/m^2)
2
1.5
1
0.5
0
60
50
40
30
20
10
0
DYNAMIC RIGIDITY -
- DYNAMIC VISCOSITY
0
5
10
15
20
25
30
FREQUENCY (Hz)
× 0.25 mm
□ 0.5 mm

FIGURE (7.13)

Oscillatory Shear Experiments.

Effect of fluid inertia on dynamic data for a 2% solution of polyisobutylene in dekalin.
Experimental conditions (Temp = 20° C; ρ = 0.88 gm/cm^3),

Measurement system; parallel plate geometry (radius = 2 cm; gap = 0.5 mm).

(i). Exact.
(ii). Fluid inertia ignored.
(iii). First order fluid inertia correction.

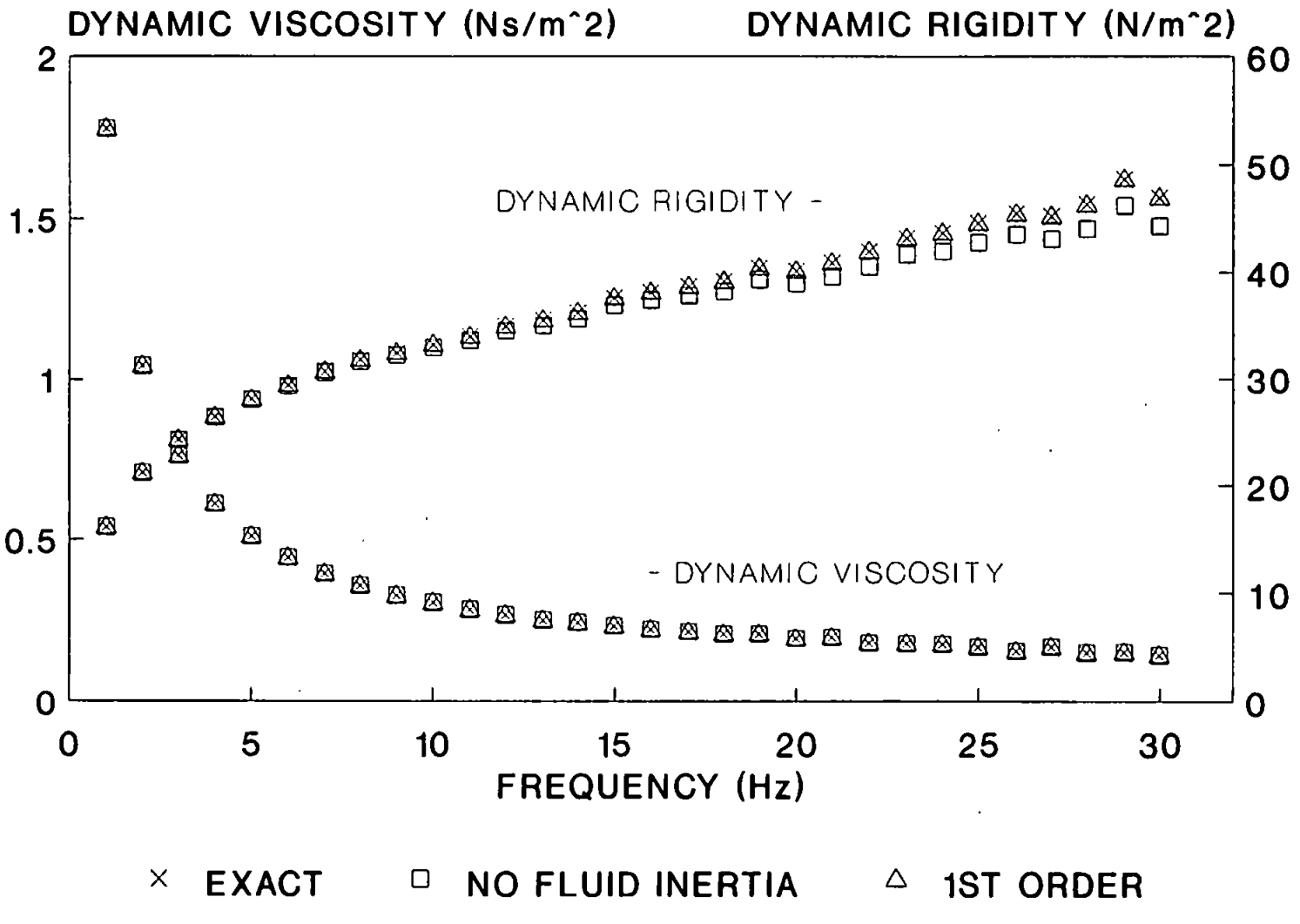
DYNAMIC VISCOSITY (Ns/m^2)
DYNAMIC RIGIDITY (N/m^2)
2
1.5
1
0.5
0
60
50
40
30
20
10
0
DYNAMIC RIGIDITY -
- DYNAMIC VISCOSITY
0
5
10
15
20
25
30
FREQUENCY (Hz)
× EXACT
□ NO FLUID INERTIA
△ 1ST ORDER

FIGURE (7.14)

Oscillatory Shear Experiments.

Effect of fluid inertia on dynamic data for a 2% solution of polyisobutylene in dekalin.

Experimental conditions (Temp = 20°C; ρ = 0.88 gm/cm^3),

Measurement system; cone and plate geometry (gap angle=2°; cone radius=2cm).

(i). gap = 0.25 mm.

(ii). gap = 0.5 mm.

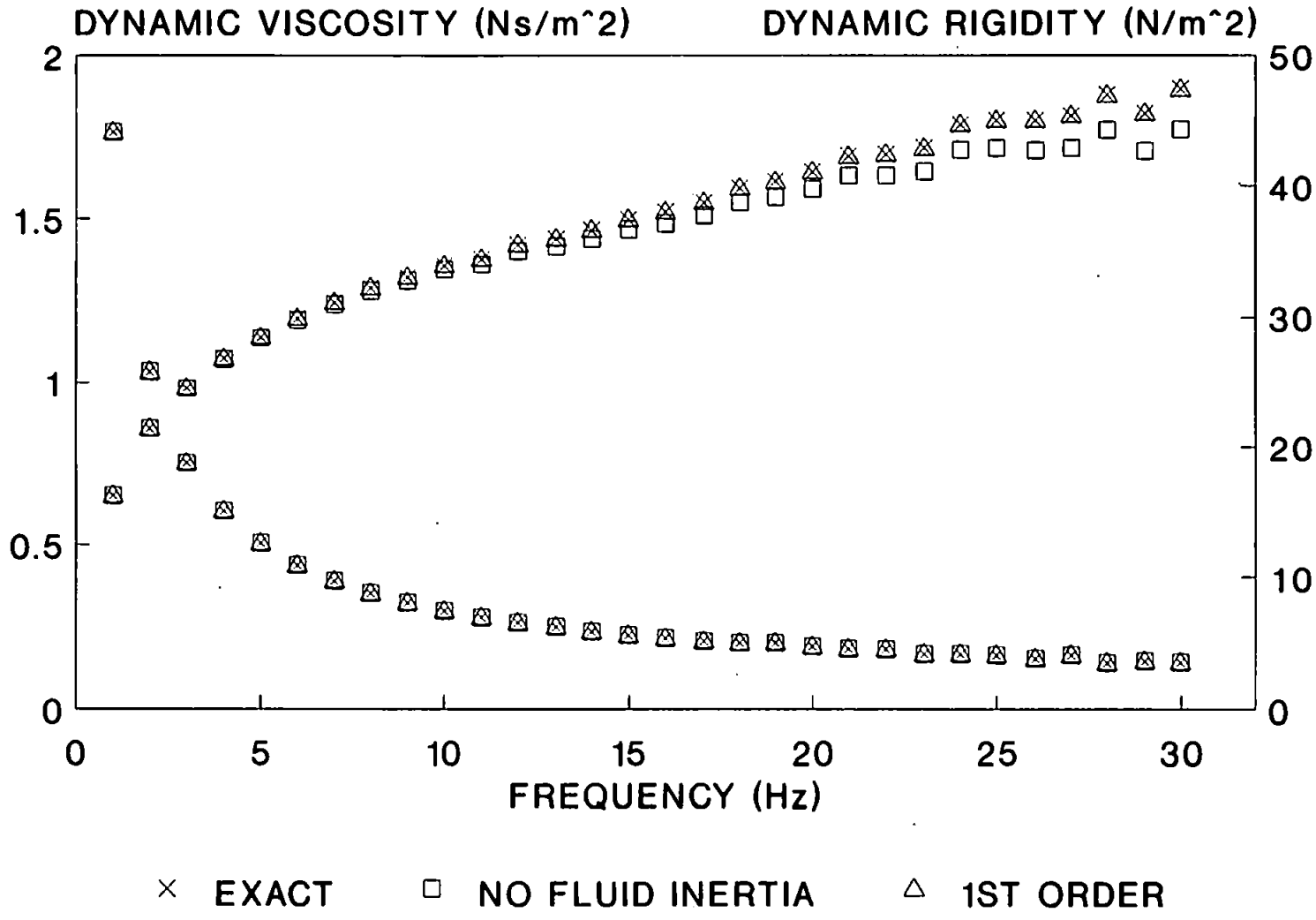
DYNAMIC VISCOSITY (Ns/m^2)
DYNAMIC RIGIDITY (N/m^2)
2
1.5
1
0.5
0
50
40
30
20
10
0
0
5
10
15
20
25
30
FREQUENCY (Hz)
× EXACT
□ NO FLUID INERTIA
△ 1ST ORDER

FIGURE (7.15)

Oscillatory Shear Experiments.

Dynamic data for silicone (30 Ns/m^2).

Experimental conditions (Temp = 25 °C; ρ = 0.9 gm/cm^3).

Measurement system;

(i). Cone and plate (gap angle=2°; cone radius=2 cm)

(ii). Parallel plate (gap=0.25 mm; radius=2 cm)

(iii). Concentric cylinder (r_i=18.5 mm, r_o=20.75 mm, cylinder height=50 mm).

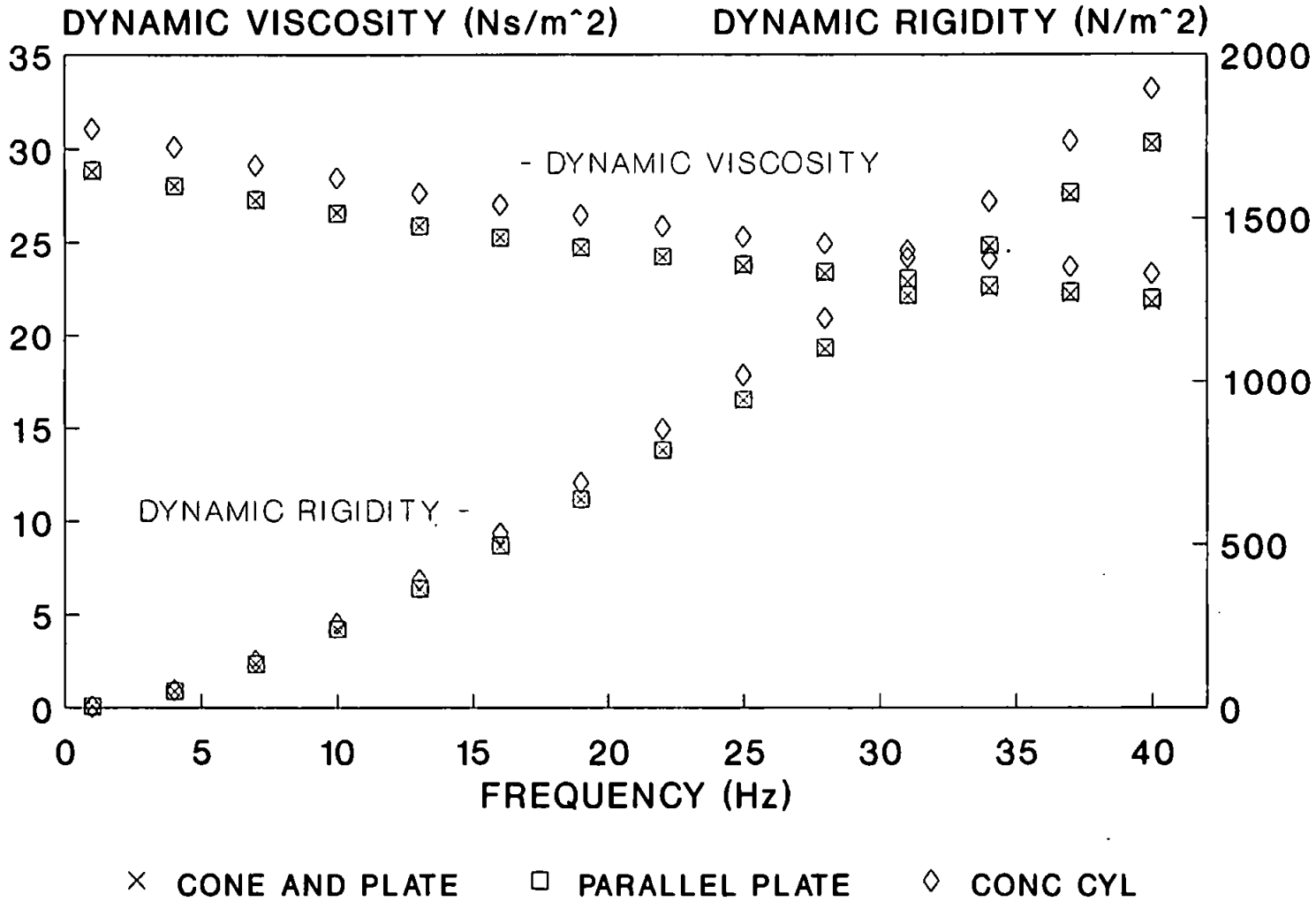
DYNAMIC VISCOSITY (Ns/m^2)
DYNAMIC RIGIDITY (N/m^2)
35
30
25
20
15
10
5
0
2000
1500
1000
500
0
- DYNAMIC VISCOSITY
DYNAMIC RIGIDITY -
0
5
10
15
20
25
30
35
40
FREQUENCY (Hz)
× CONE AND PLATE
□ PARALLEL PLATE
◇ CONC CYL

FIGURE (7.16)

Oscillatory Shear Experiments.

Dynamic data for silicone (30 Ns/m^2).

Experimental conditions (Temp = 25 C; ρ = 0.9 gm/cm^3),

Measurement system; concentric cylinder geometry (r_o=20.75 mm, cylinder height = 50mm).

(i). r_i=18.5 mm.

(ii). r_i=15.0 mm.

(iii). r_i=12.5 mm.

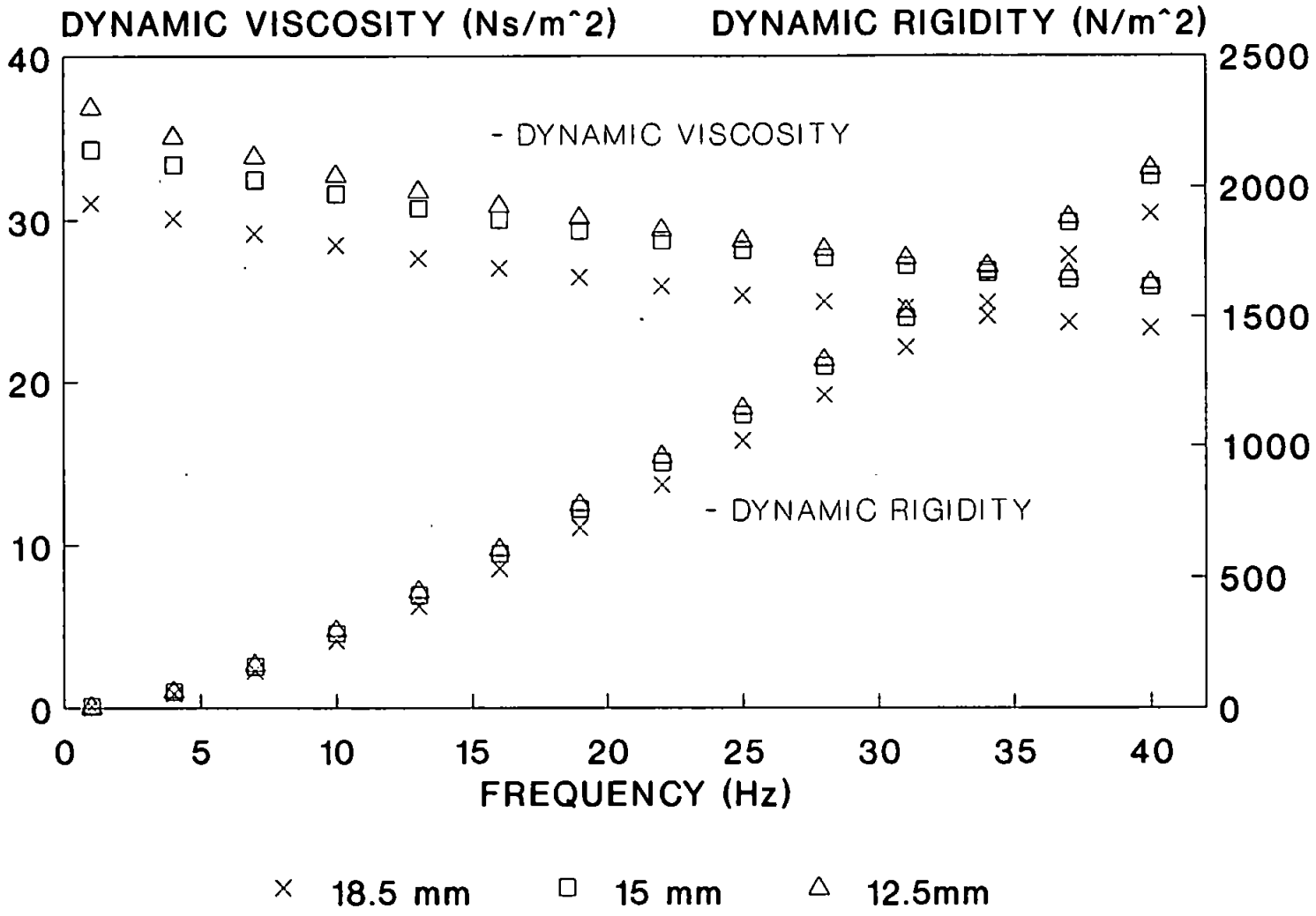
DYNAMIC VISCOSITY (Ns/m^2)
DYNAMIC RIGIDITY (N/m^2)
40
30
20
10
0
2500
2000
1500
1000
500
0
- DYNAMIC VISCOSITY
- DYNAMIC RIGIDITY
0
5
10
15
20
25
30
35
40
FREQUENCY (Hz)
× 18.5 mm
□ 15 mm
△ 12.5mm

FIGURE (7.17)

Oscillatory Shear Experiments.

Dynamic data for silicone (30 Ns/m^2).

Experimental conditions (Temp = 25 C; ρ = 0.9 gm/cm^3),

Measurement system; parallel plate geometry (radius = 2 cm).

(i). gap = 0.25 mm.

(ii). gap = 0.5 mm.

(iii). gap = 1.0 mm.

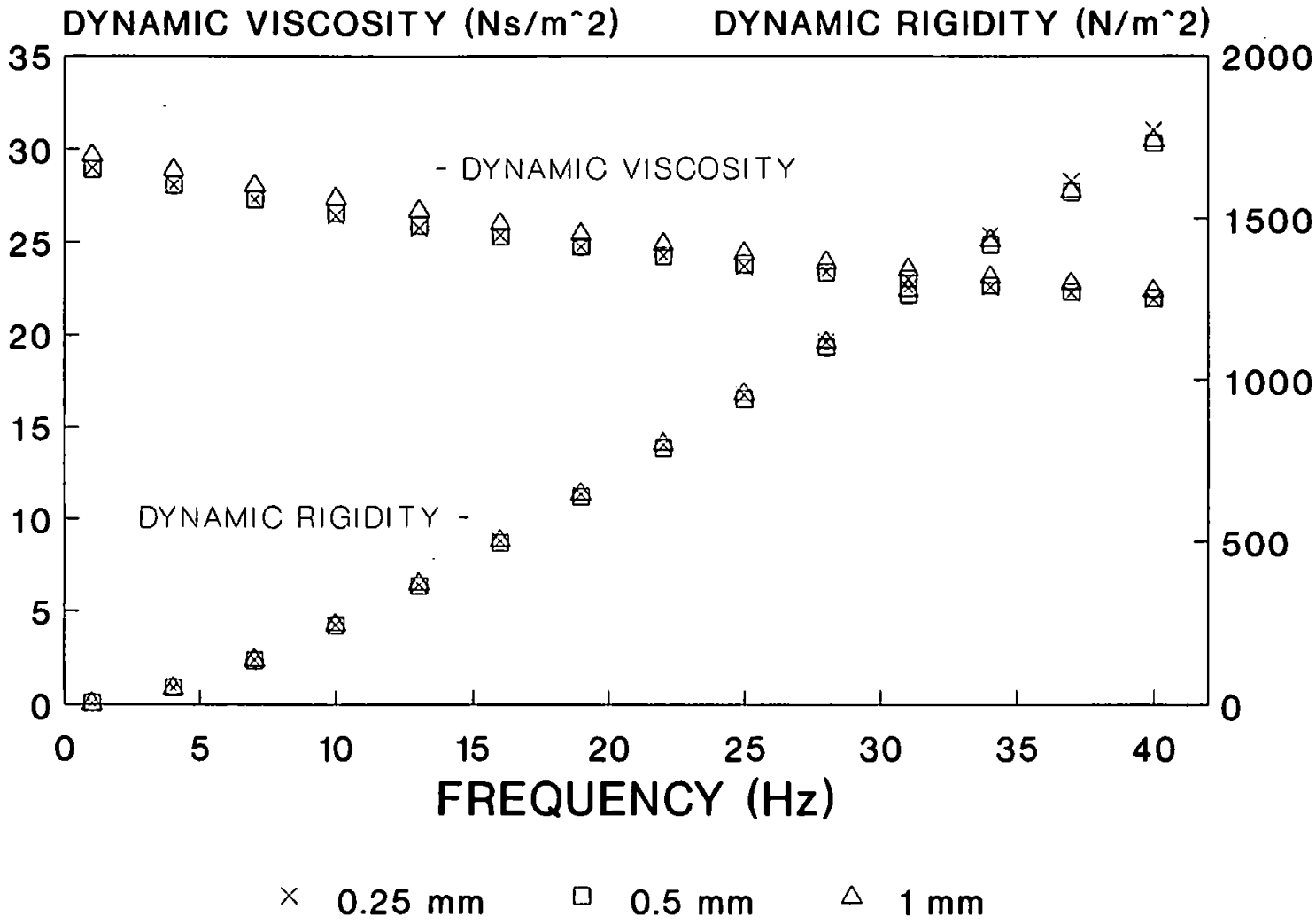
DYNAMIC VISCOSITY (Ns/m^2)
DYNAMIC RIGIDITY (N/m^2)
35
30
25
20
15
10
5
0
2000
1500
1000
500
0
- DYNAMIC VISCOSITY
DYNAMIC RIGIDITY -
0
5
10
15
20
25
30
35
40
FREQUENCY (Hz)
× 0.25 mm
□ 0.5 mm
△ 1 mm

FIGURE (7.18)

Oscillatory Shear Experiments.

Effect of fluid inertia on dynamic data for silicone (30 Ns/m^2).

Experimental conditions (Temp = 25 °C; ρ = 0.9 gm/cm^3).

Measurement system; concentric cylinder geometry (r_o=20.75 mm; r_i=12.5 mm; cylinder height=50 mm).

(i). Exact.

(ii). Fluid inertia ignored.

(iii). First order fluid inertia correction.

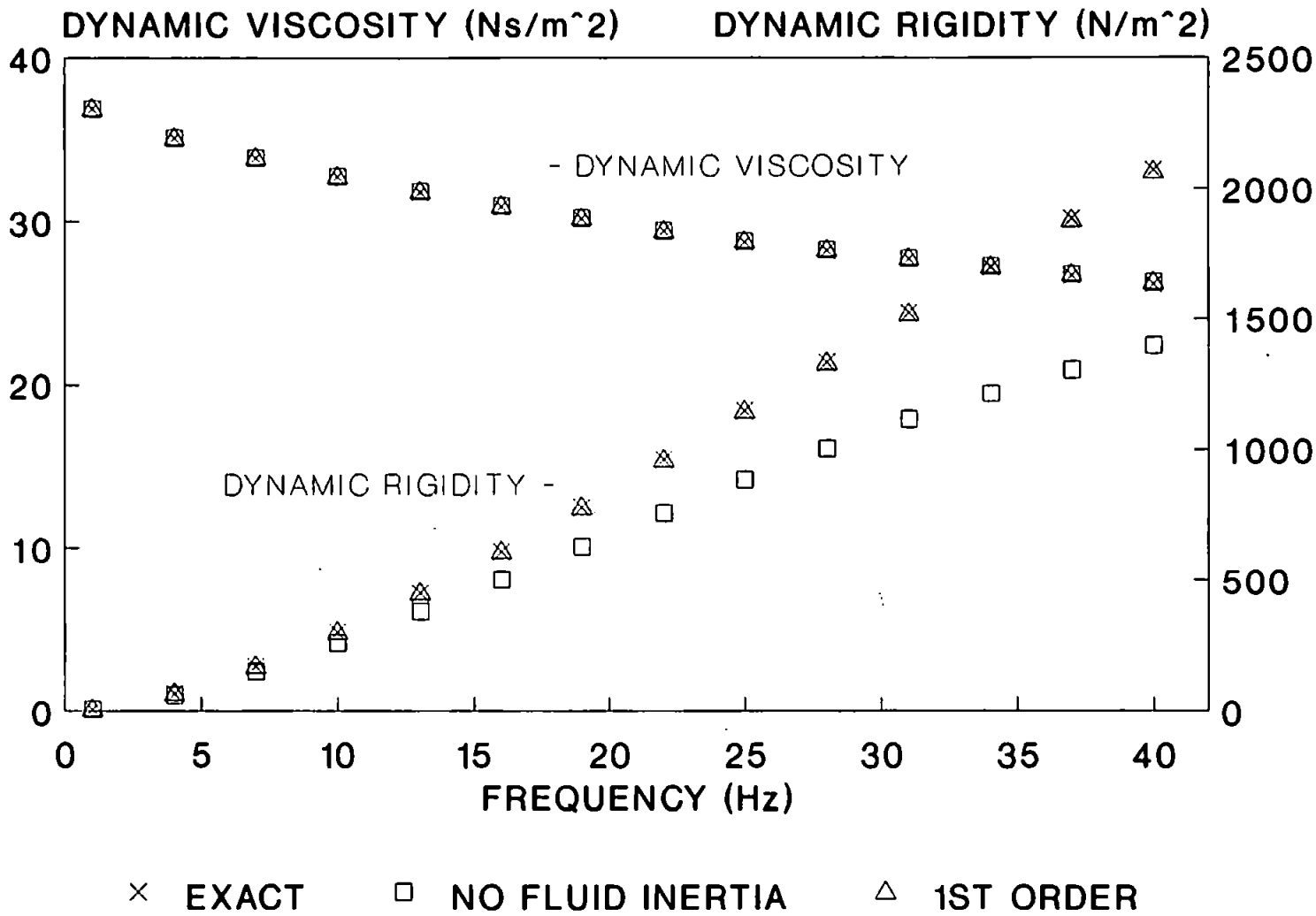
DYNAMIC VISCOSITY (Ns/m^2)
DYNAMIC RIGIDITY (N/m^2)
40
30
20
10
0
2500
2000
1500
1000
500
0
- DYNAMIC VISCOSITY
DYNAMIC RIGIDITY -
0
5
10
15
20
25
30
35
40
FREQUENCY (Hz)
× EXACT
□ NO FLUID INERTIA
△ 1ST ORDER

FIGURE (7.19)

Oscillatory Shear Experiments.

Effect of fluid inertia on dynamic data for silicone (30 Ns/m^2).

Experimental conditions (Temp = 25 $\dot{C}$; ρ = 0.9 gm/cm^3).

Measurement system; parallel plate geometry (radius = 2 cm; gap = 1 mm).

(i). Exact.

(ii). Fluid inertia ignored.

(iii). First order fluid inertia correction.

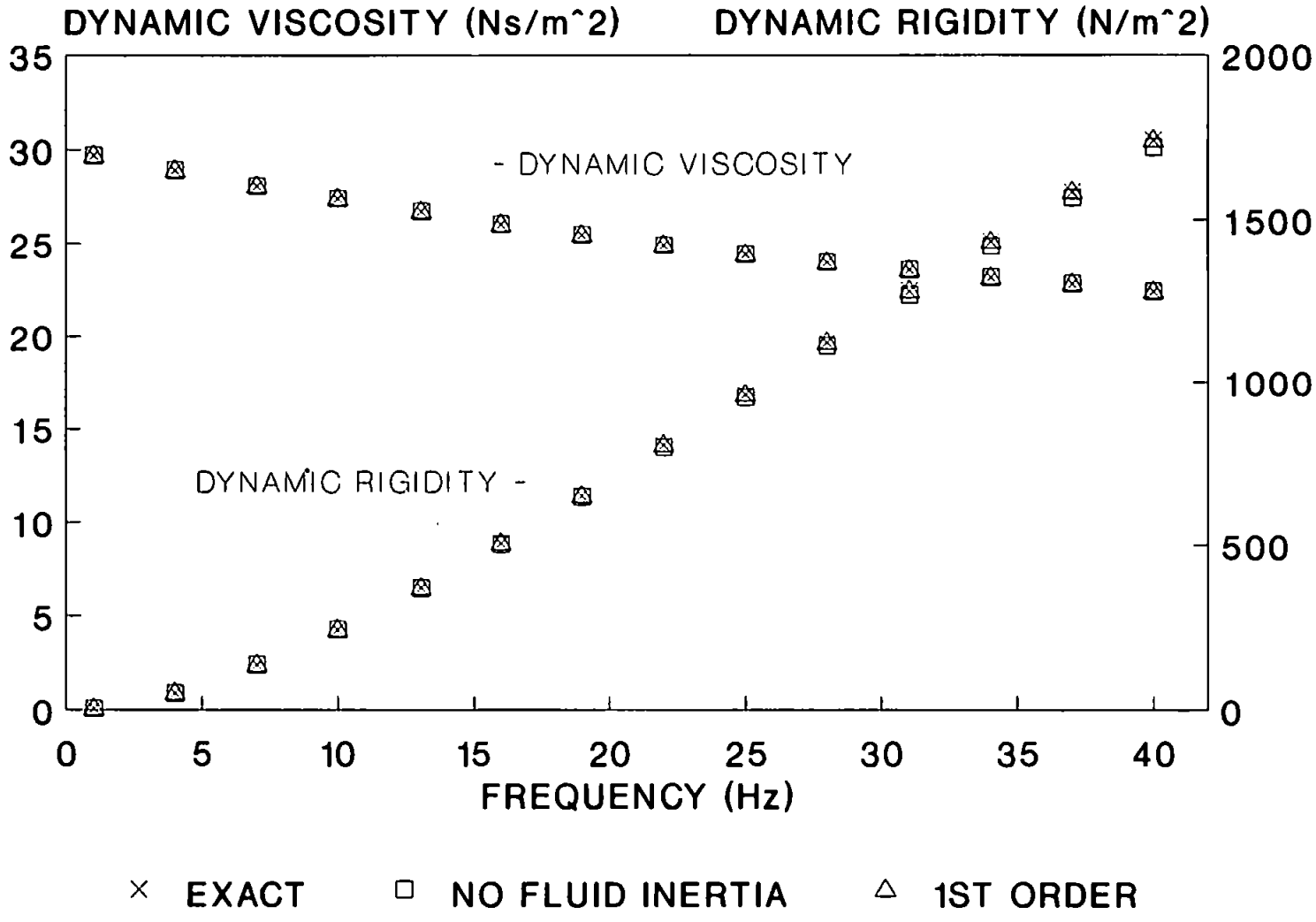
DYNAMIC VISCOSITY (Ns/m^2)
DYNAMIC RIGIDITY (N/m^2)
35
30
25
20
15
10
5
0
2000
1500
1000
500
0
- DYNAMIC VISCOSITY
DYNAMIC RIGIDITY -
0
5
10
15
20
25
30
35
40
FREQUENCY (Hz)
× EXACT
□ NO FLUID INERTIA
△ 1ST ORDER

FIGURE (7.20)

Oscillatory Shear Experiments.

Effect of fluid inertia on dynamic data for silicone (30 Ns/m^2).

Experimental conditions (Temp = 25° C; ρ = 0.9 gm/cm^3).

Measurement system; cone and plate geometry (gap angle = 2°; cone radius = 2 cm).

(i). Exact.

(ii). Fluid inertia ignored.

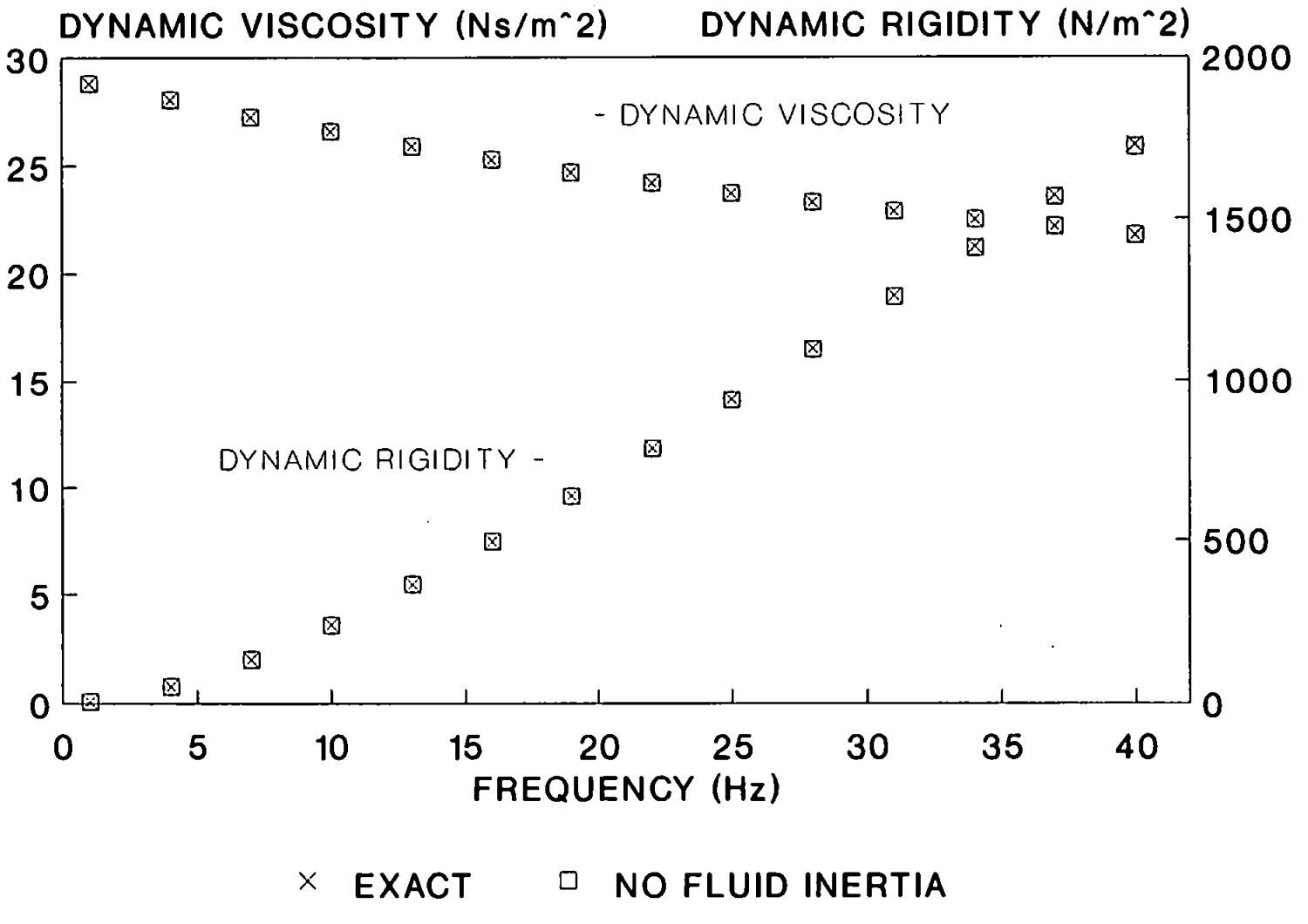
DYNAMIC VISCOSITY (Ns/m^2)
DYNAMIC RIGIDITY (N/m^2)
30
25
20
15
10
5
0
2000
1500
1000
500
0
- DYNAMIC VISCOSITY
DYNAMIC RIGIDITY -
0
5
10
15
20
25
30
35
40
FREQUENCY (Hz)
× EXACT
□ NO FLUID INERTIA

FIGURE (7.21)

Oscillatory Shear Experiments.

Dynamic data for polybutene.

Experimental conditions (Temp = 20° C; ρ = 0.9 gm/cm^3).

Measurement system;

(i). Cone and plate (gap angle = 2°; cone radius = 2 cm).

(ii). Parallel plate (radius = 2 cm; gap = 1 mm).

(iii). Parallel plate (radius = 2 cm; gap = 0.5 mm).

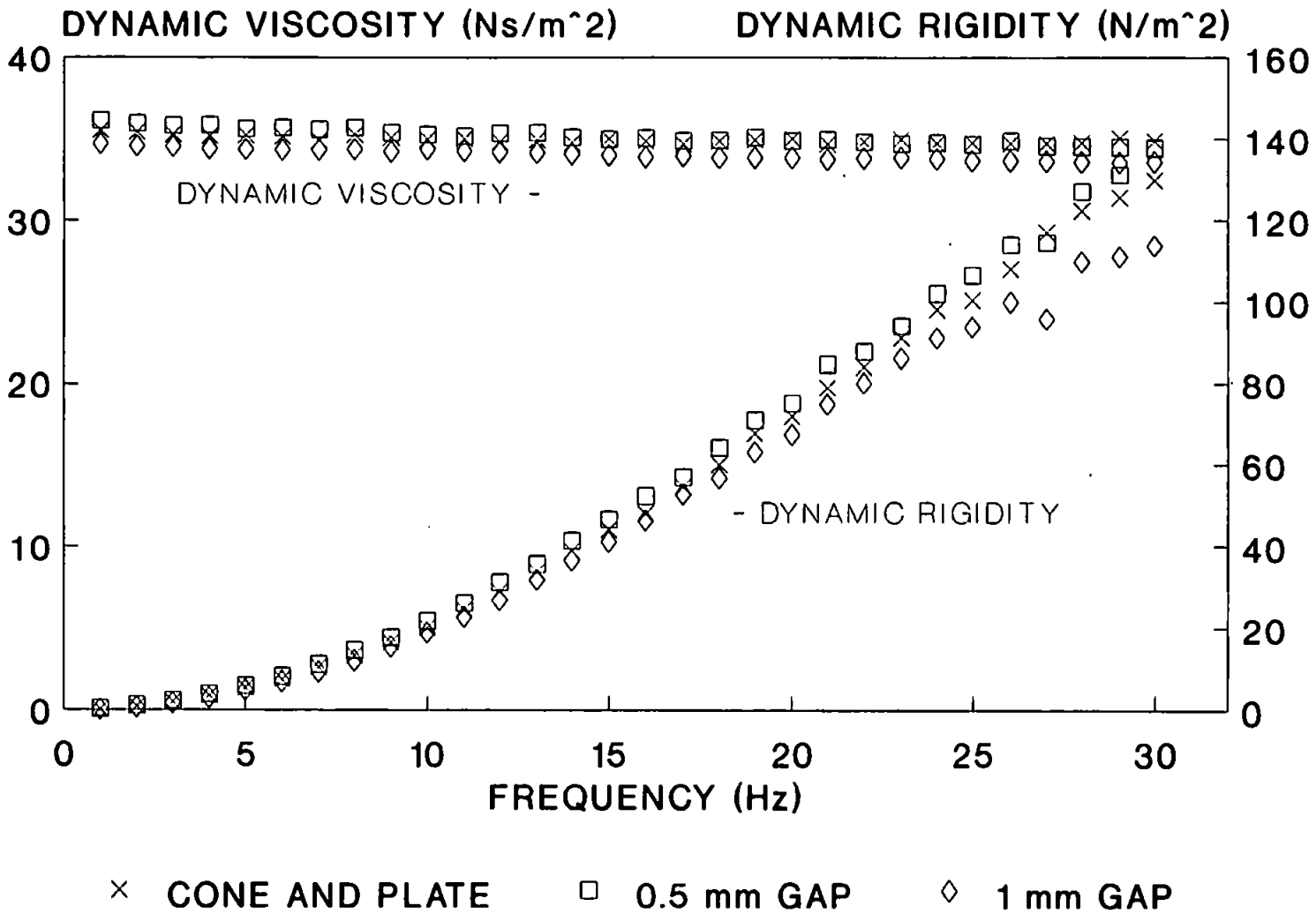
DYNAMIC VISCOSITY (Ns/m^2)
DYNAMIC RIGIDITY (N/m^2)
40
30
20
10
0
160
140
120
100
80
60
40
20
0
DYNAMIC VISCOSITY -
- DYNAMIC RIGIDITY
0
5
10
15
20
25
30
FREQUENCY (Hz)
× CONE AND PLATE
□ 0.5 mm GAP
◇ 1 mm GAP

FIGURE (7.22)

Oscillatory Shear Experiments.

Effect of fluid inertia on dynamic data for polybutene.

Experimental conditions (Temp = 20°C; ρ = 0.9 gm/cm^3).

Measurement system; parallel plate geometry (radius = 2 cm; gap = 0.5 mm).

(i). Exact.

(ii). Fluid inertia ignored.

(iii). First order fluid inertia correction.

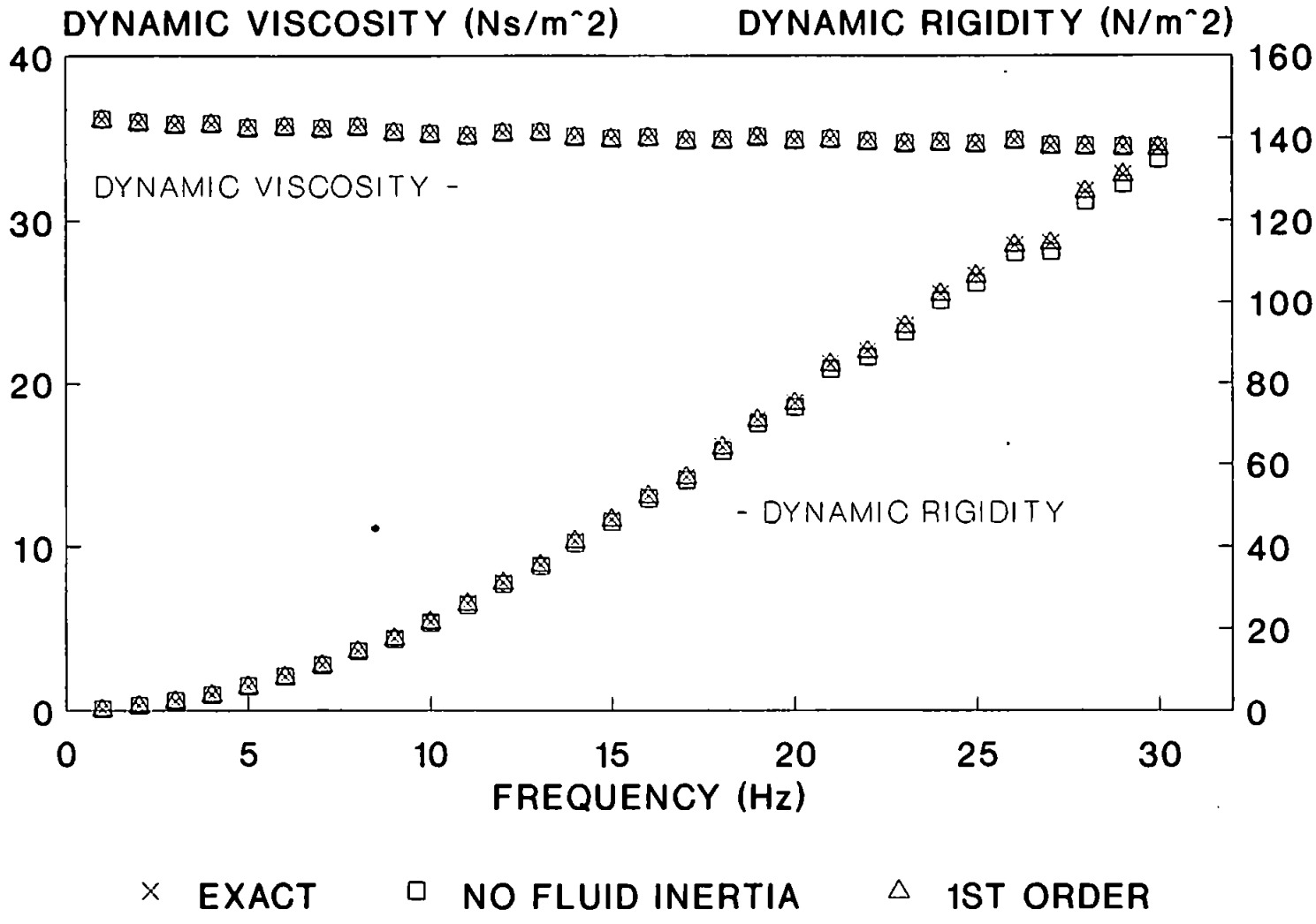
DYNAMIC VISCOSITY (Ns/m^2)
DYNAMIC RIGIDITY (N/m^2)
40
30
20
10
0
160
140
120
100
80
60
40
20
0
DYNAMIC VISCOSITY -
- DYNAMIC RIGIDITY
0
5
10
15
20
25
30
FREQUENCY (Hz)
× EXACT
□ NO FLUID INERTIA
△ 1ST ORDER

FIGURE (7.23)

Oscillatory Shear Experiments.

Effect of fluid inertia on dynamic data for polybutene.

Experimental conditions (Temp = 20°C; ρ = 0.9 gm/cm^3).

Measurement system; cone and plate geometry (gap angle = 2°; cone radius = 2 cm;).

(i). Exact.

(ii). Fluid inertia ignored.

(iii). First order fluid inertia correction.

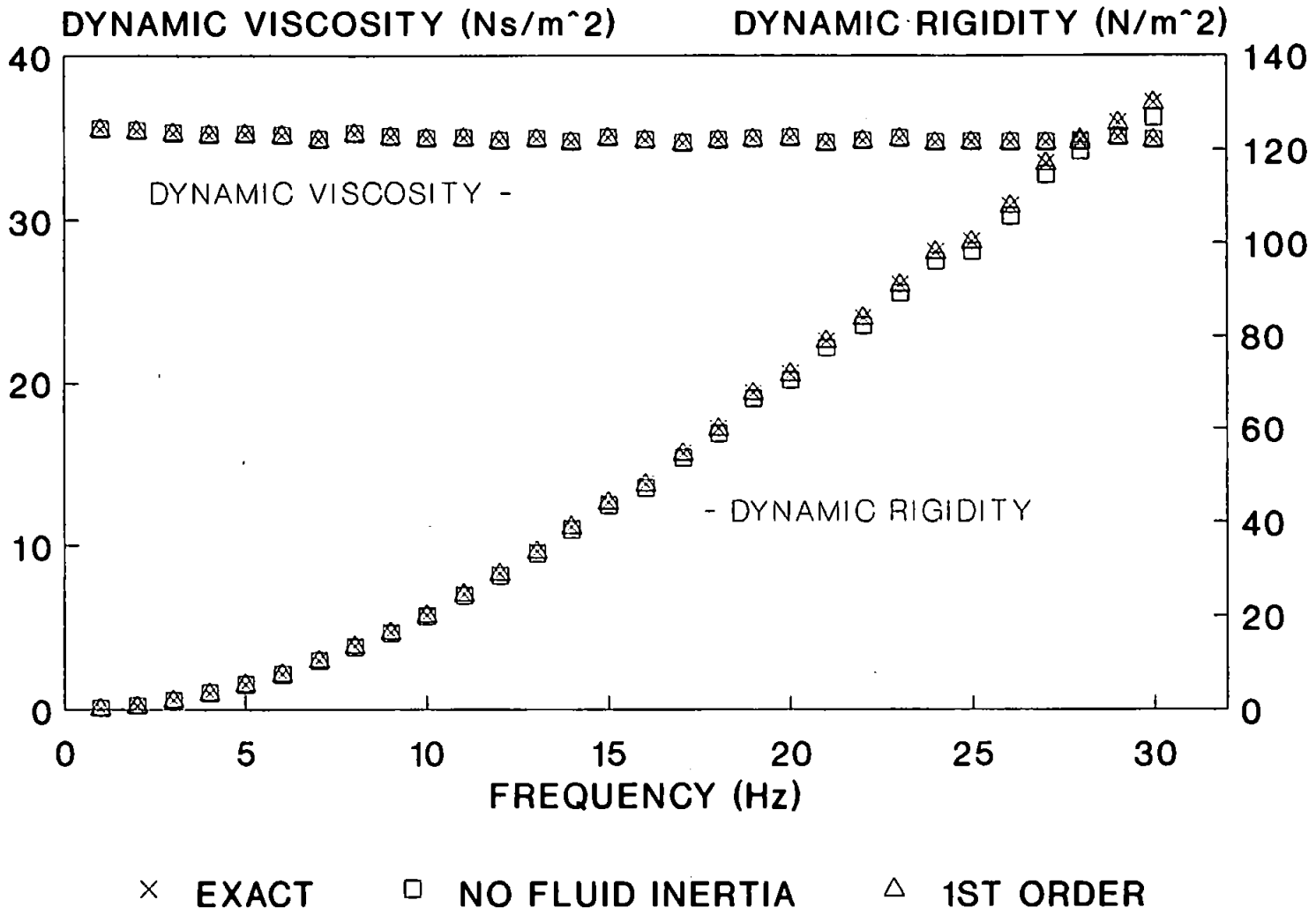
DYNAMIC VISCOSITY (Ns/m^2)
DYNAMIC RIGIDITY (N/m^2)
40
30
20
10
0
140
120
100
80
60
40
20
0
DYNAMIC VISCOSITY -
- DYNAMIC RIGIDITY
0
5
10
15
20
25
30
FREQUENCY (Hz)
× EXACT
□ NO FLUID INERTIA
△ 1ST ORDER

FIGURE (8.1)

Typical experimental strain waveform for a 'yield stress' material undergoing a sinusoidal oscillatory stress. Test fluid is a water absorbant gel (Sanwet 2500) with a 1% concentration by weight.

Measurement system, cone and plate geometry (gap angle = 2°; radius = 2cm).

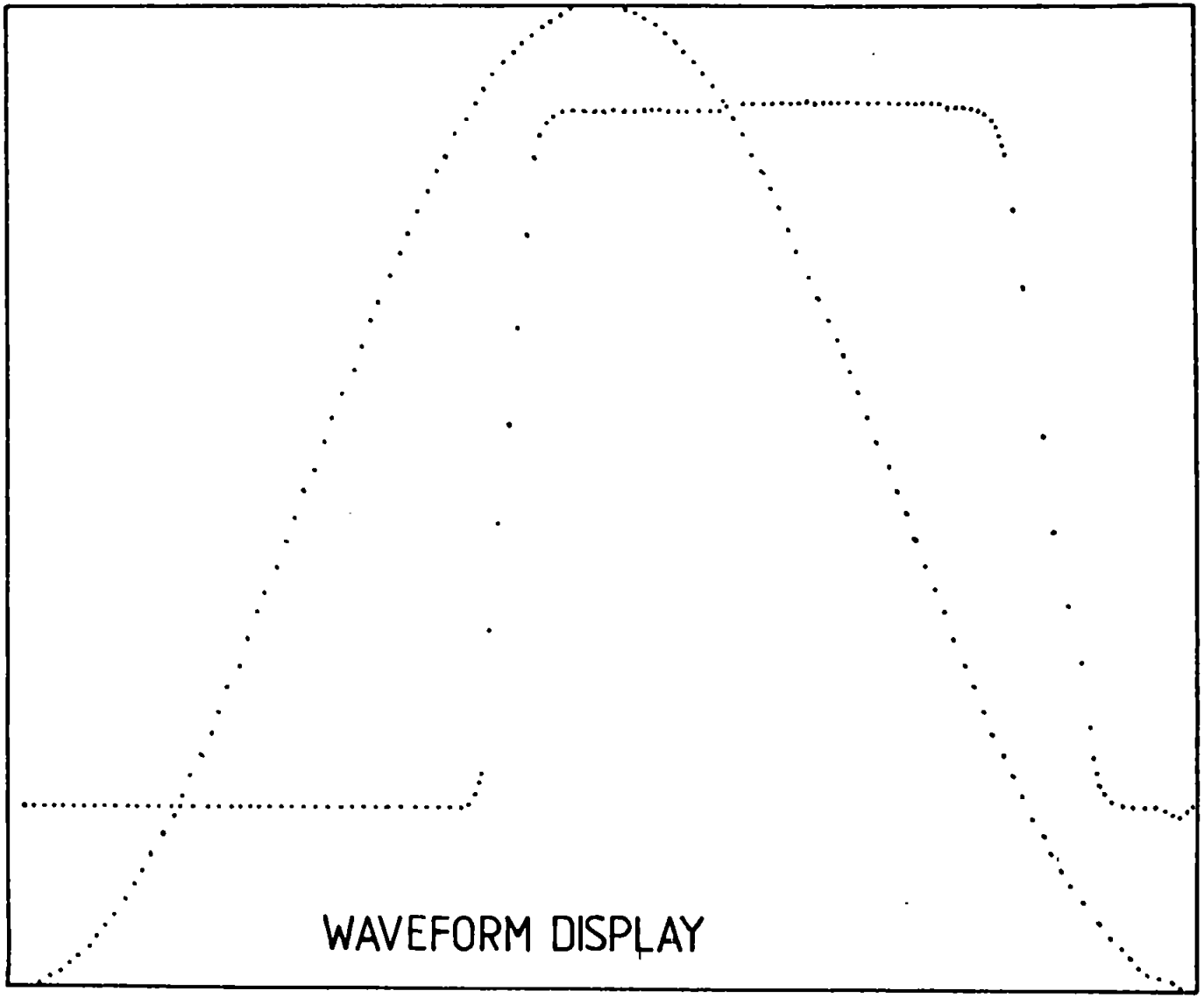
WAVEFORM DISPLAY

FIGURE (8.2)

Variation of complex viscosity data with torque amplitude for a water absorbant gel (Sanwet 2500) with a 1% concentration by weight.

Measurement system, cone and plate geometry (gap angle = 2°; radius = 2cm).

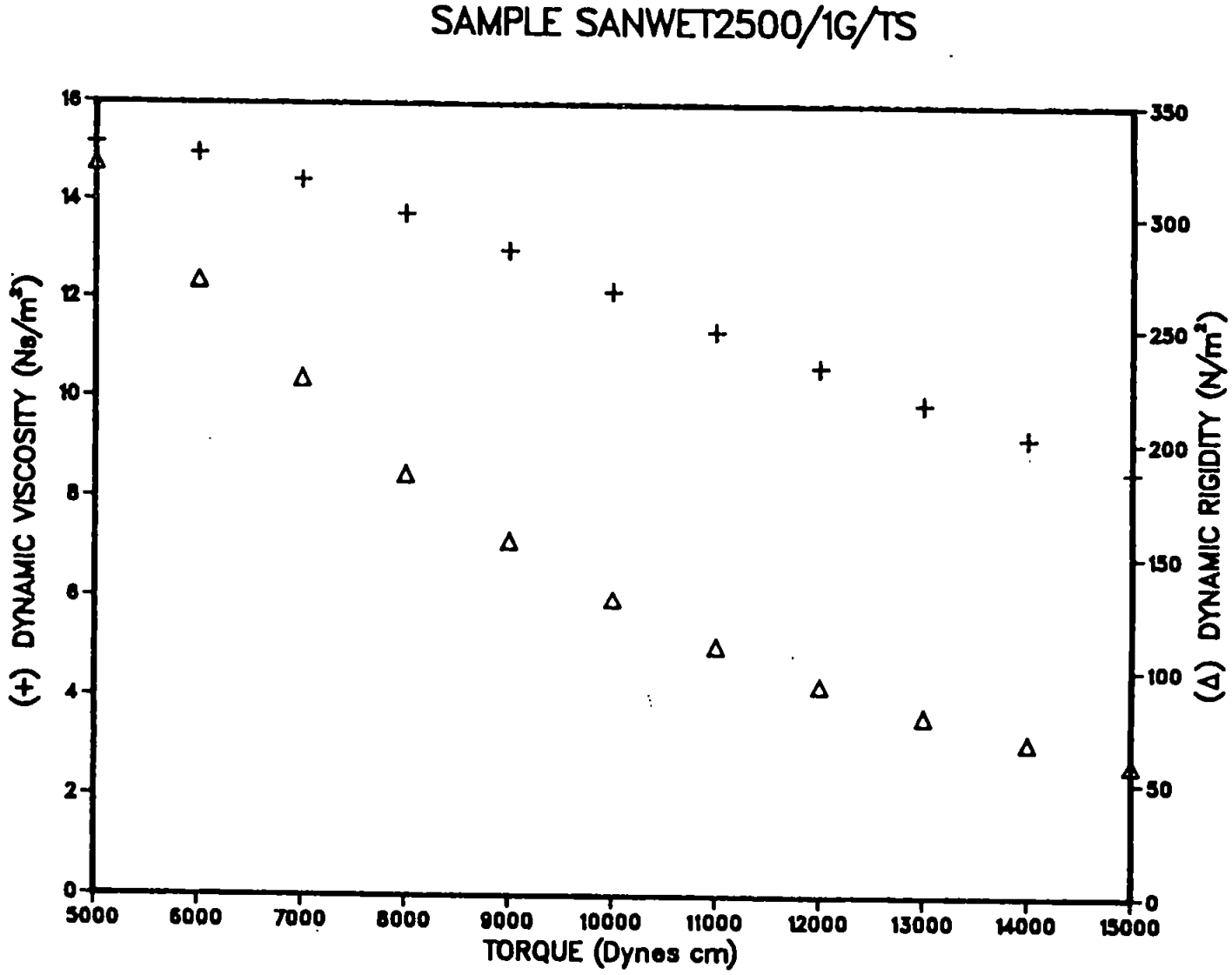
SAMPLE SANWET2500/1G/TS
(+) DYNAMIC VISCOSITY (Ns/m²)
(Δ) DYNAMIC RIGIDITY (N/m²)
TORQUE (Dynes cm)
0
2
4
6
8
10
12
14
16
0
50
100
150
200
250
300
350
5000
6000
7000
8000
9000
10000
11000
12000
13000
14000
15000

FIGURE (8.3)

Modified Generalised Maxwell Model.

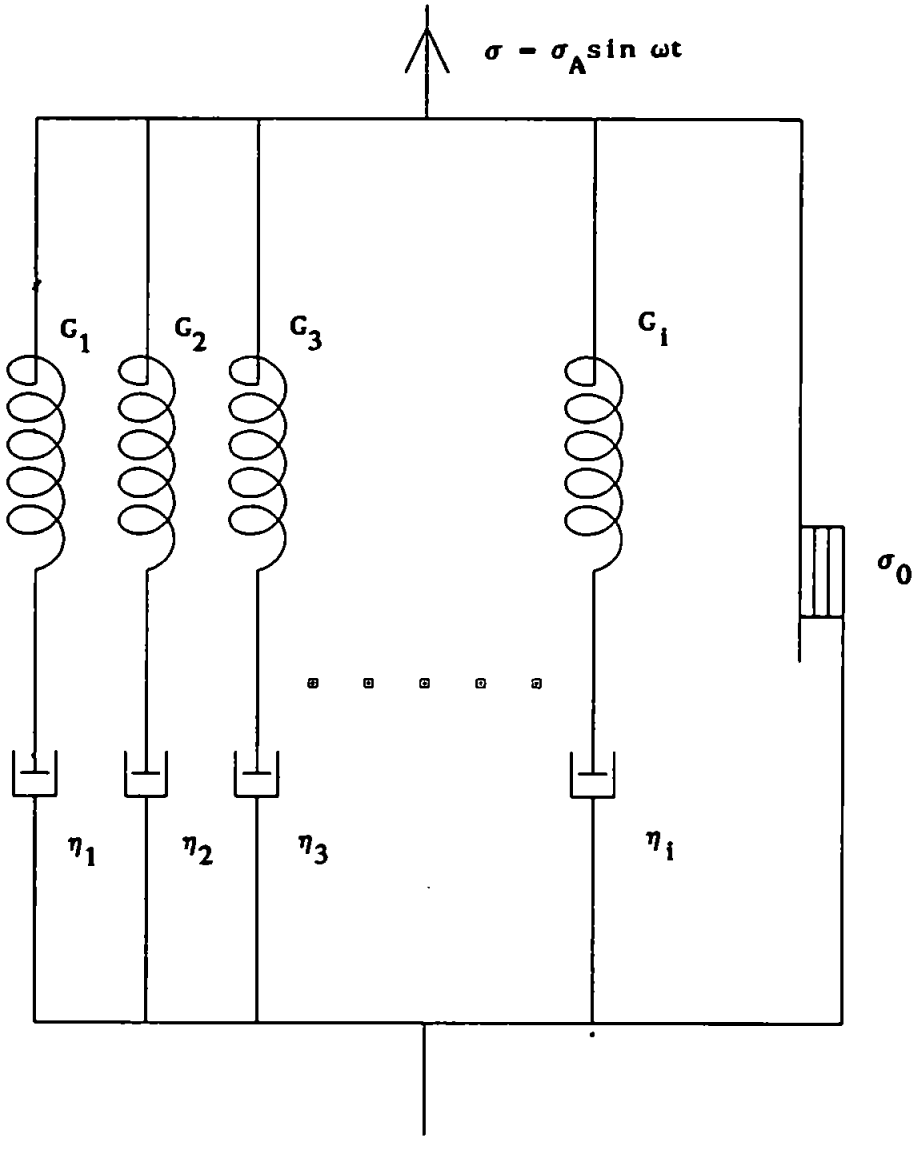
$\sigma = \sigma_A \sin \omega t$
G_1
G_2
G_3
G_i
σ_0
η_1
η_2
η_3
η_i

FIGURE (8.4)

Typical strain rate response of a single element modified Maxwell model to an applied sinusoidal oscillatory stress.

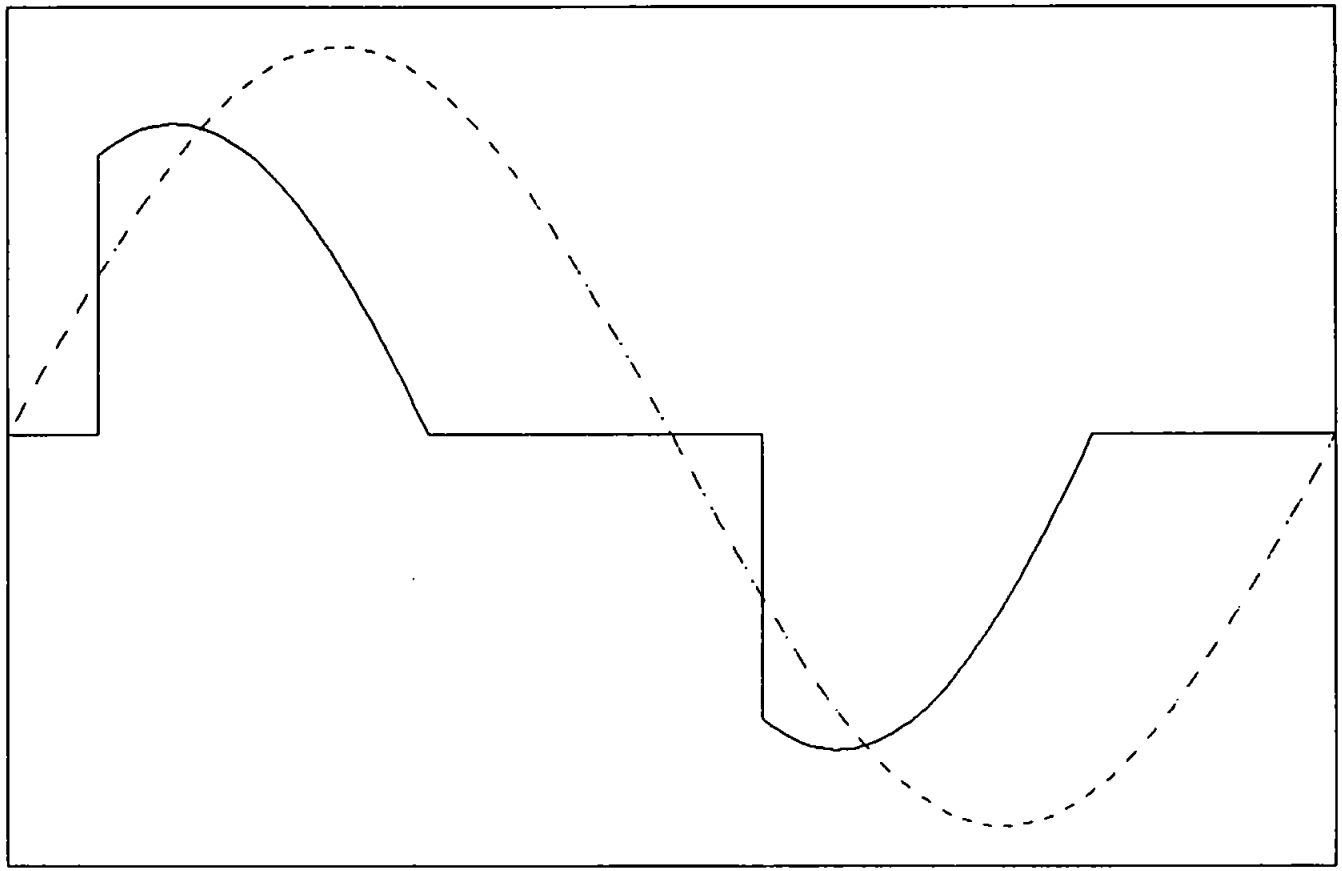

Applied Stress Strain Rate

FIGURE (8.5)

Typical strain response of a single element modified Maxwell model to an applied sinusoidal oscillatory stress.

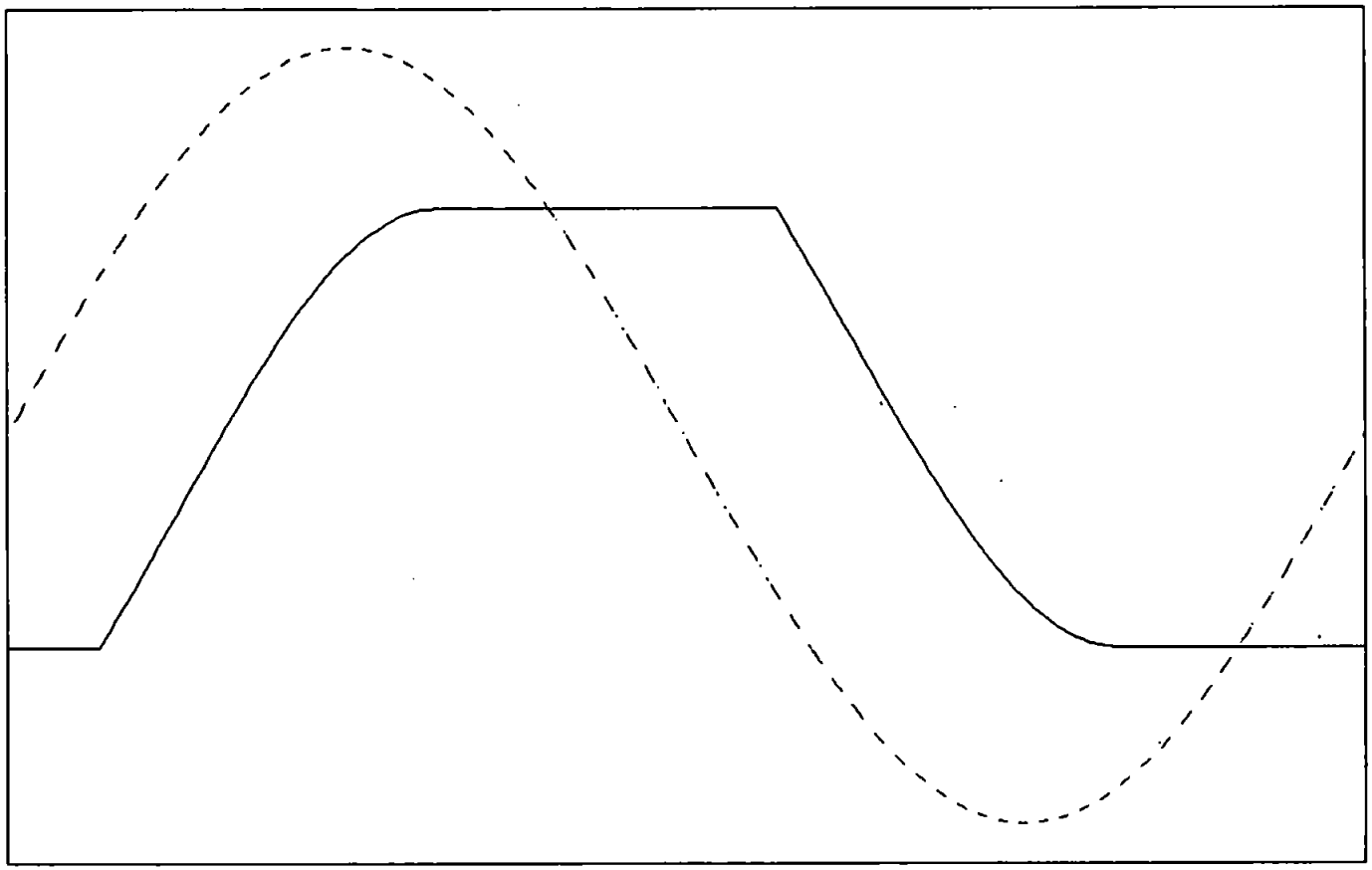
Applied Stress
Strain

FIGURE (8.6)

Variation of normalised dynamic viscosity with normalised frequency for a range of values of Δ (0, 0.2, 0.5).

where,

$$\Delta = \frac{\sigma_0}{\sigma_a}$$

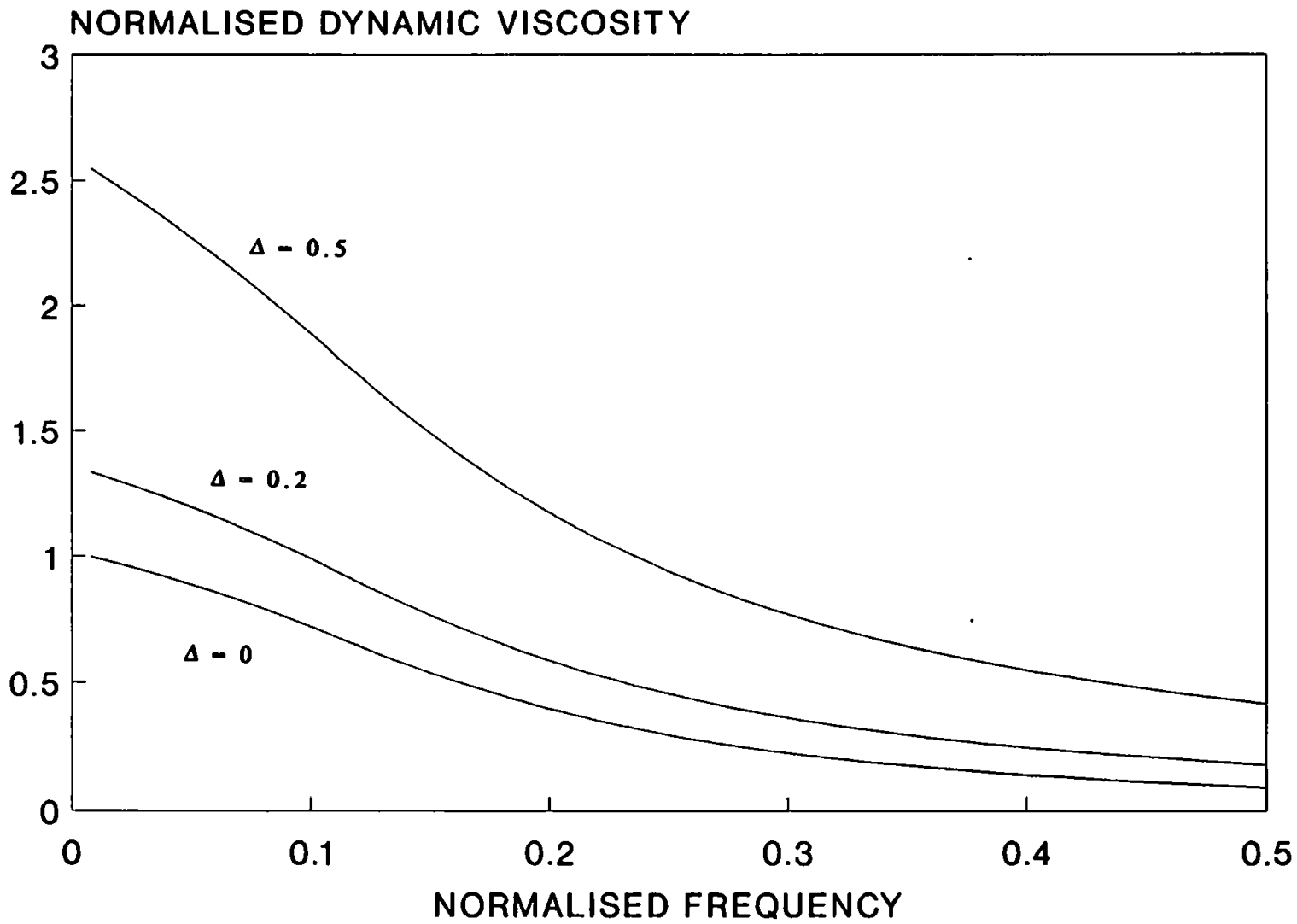
NORMALISED DYNAMIC VISCOSITY
3
2.5
2
1.5
1
0.5
0
Δ = 0.5
Δ = 0.2
Δ = 0
0
0.1
0.2
0.3
0.4
0.5
NORMALISED FREQUENCY

FIGURE (8.7)

Variation of normalised dynamic rigidity with normalised frequency for a range of values of Δ (0, 0.2, 0.5).

where,

$$\Delta = \frac{\sigma_0}{\sigma_a}$$

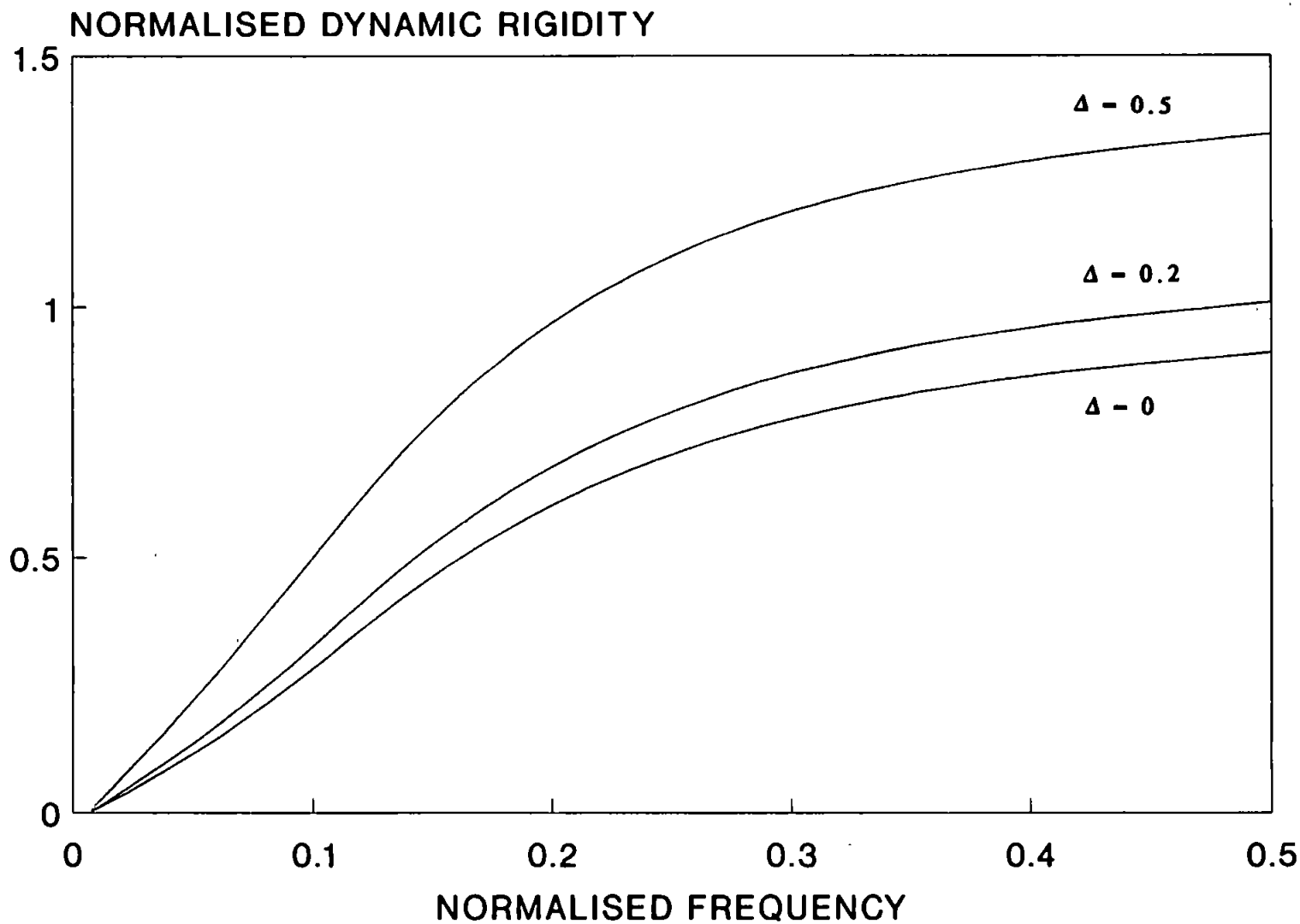
NORMALISED DYNAMIC RIGIDITY
1.5
1
0.5
0
Δ = 0.5
Δ = 0.2
Δ = 0
0
0.1
0.2
0.3
0.4
0.5
NORMALISED FREQUENCY

FIGURE (8.8)

Variation of normalised dynamic viscosity with normalised stress amplitude for a range of values of values of $\lambda\omega$ (0, 2.0, 5.0)

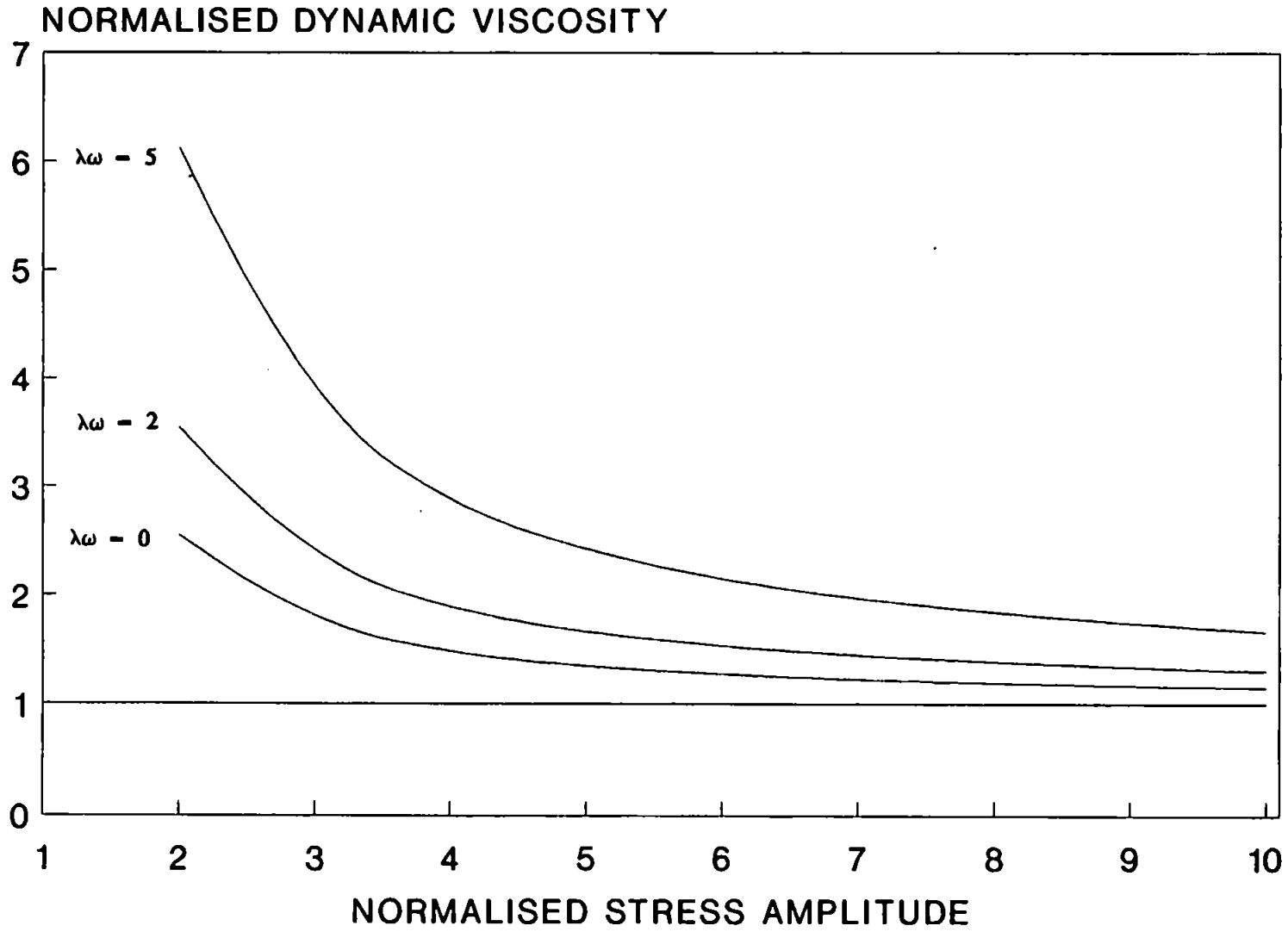
NORMALISED DYNAMIC VISCOSITY
7
6
5
4
3
2
1
0
λω = 5
λω = 2
λω = 0
1
2
3
4
5
6
7
8
9
10
NORMALISED STRESS AMPLITUDE

FIGURE (8.9)

Variation of normalised dynamic rigidity with normalised frequency for a range of values of Δ (0, 0.2, 0.5).

where,

$$\Delta = \frac{\sigma_0}{\sigma_a}$$

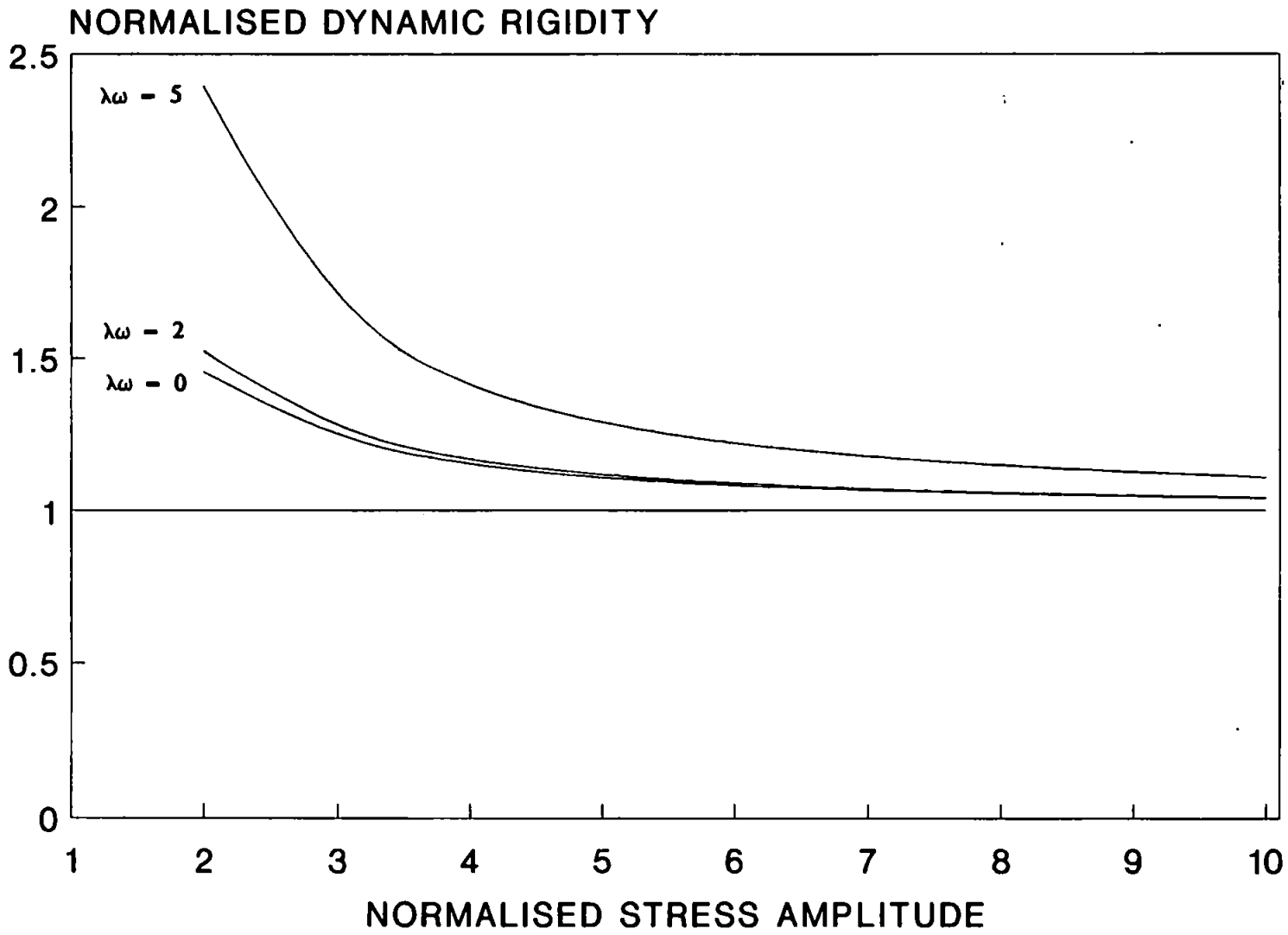
NORMALISED DYNAMIC RIGIDITY
2.5
2
1.5
1
0.5
0
λω = 5
λω = 2
λω = 0
1
2
3
4
5
6
7
8
9
10
NORMALISED STRESS AMPLITUDE